Aus dem Bereich der Molekularen Zellbiologie Theoretische Medizin und Biowissenschaften der Medizinischen Fakultät der Universität des Saarlandes Homburg/Saar

Ca²⁺-entry into Red Blood Cells: Channel Mediated Influx and its Detection

Dissertation zur Erlangung des Grades: Doktorin der Naturwissenschaften (Dr. rer. nat.) der Medizinischen Fakultät

> der Universität des Saarlandes 2025

vorgelegt von: Min Qiao

geb.am: 22.03.1994 in Shanxi, China

Tag der Promotion: 15. September 2025

Dekan: Prof. Dr. med. dent. Matthias Hannig

Berichterstatter: Prof. Dr. Lars Kaestner

Prof. Dr. Hermann Eichler

Contents

Abbreviations									
М	Mathematical notations								
ΑI	Abstract V								
Ζι	ısamı	menfassung	IX						
1	Intr	oduction	1						
	1.1	Overview of Blood	1						
	1.2	Erythrocytes (RBCs)	2						
		1.2.1 Physiology of RBCs	2						
		1.2.2 Ion Regulation in RBCs	4						
	1.3	Fluorescence	25						
		1.3.1 Overview of Fluorescence	25						
		1.3.2 Fluorescence Lifetime	27						
		1.3.3 Fluorophores	28						
2	Mat	erials and Methods	35						
_	2.1	Preparation of Chemicals and Solutions	35						
	2.2	Cell Preparation	35						
		2.2.1 RBCs Collection and Washing	35						
		2.2.2 ATP-depleted RBCs Preparation	36						
		2.2.3 Fluorescence Probe Loaded RBCs	37						
		2.2.4 Cell Lysis and Ghost RBCs Preparation	38						
	2.3	Flow Cytometry	40						
	2.4	Membrane Potential Measurements According to the Method of Macey,							
		Bennekou, and Egee (MBE-method)	42						
	2.5	Microscopy	43						
		2.5.1 Fluorescence Microscopy	43						
		2.5.2 Confocal Microscopy	43						
		2.5.3 Fluorescence Lifetime Imaging Microscopy (FLIM)	44						
	2.6	Western Blot	47						
		2.6.1 Protein Quantification	47						
		2.6.2 Sodium Dodecyl Sulfate Polyacrylamide Gel Electrophoresis (SDS-							
		PAGE)	48						
		2.6.3 Western Blot	50						
	27	Data Analysis	50						

<u>II</u> Contents

3	Resu	ılts	51		
	3.1	Piezo 1 Channel Investigation	51		
		3.1.1 Wild Type Piezo 1 Channel Activation	51		
		3.1.2 Genetic Variants of the Piezo 1 Channel	62		
	3.2	Gárdos Channel Activation and Intracellular Ca ²⁺	65		
	3.3	Transient Receptor Potential Vanilloid Type 2 (TRPV2) Channel	67		
		3.3.1 Influence of Long-term Cannabis Consumption on TRPV2 Channel			
		Function in RBCs	67		
		3.3.2 Effects of TRPV2 Activation on Sickle Cells	72		
	3.4	Calcium Quantification by Fluorescence Lifetime Image Microscopy (FLIM)	77		
		3.4.1 Hemoglobin Concentration Influence on Fluorescence Intensity De-			
		pendent Semi-quantification of Calcium Concentration	77		
		3.4.2 FLIM Measurement of Intracellular Ca^{2+} Concentration	78		
4	Disc	eussion 1	105		
•	4.1		105		
	4.2		114		
		3			
Α			123		
	A.1	1	123 127		
	A.2 Supplementary Figures				
	A.3		141		
	A.4		144		
	A.5	Information of Used Equipment	146		
Lis	t of	Publications 1	149		
Eid	lesst	attliche Erklärung 1	150		
Ac	know	vledgements 1	151		
Bil	Bibliography 1				

Abbreviations

 Δ^9 -THC (-)-trans- Δ^9 -tetrahydrocannabidol

 Δ^9 -THCV Δ^9 -tetrahydrocannabivarin 1-EBIO 1-ethylbenzimidazolinone

1PE 1-photon excitation 2PE 2-photon excitation AA Healthy controls

AFFM Advanced FLIM fitting method

AM-esters Acetoxymethyl esters

AMPK 5'AMP-activated protein kinase

ATP Adenosine triphosphate BSA Bovine serum albumin

Ca-CaM Calcium-calmodulin complex

CAM Calmodulin
CBD Cannabidiol
CBN Cannabinol

CCCP Carbonyl cyanide m-chlorophenylhydrazone

ChTX Charybdotoxin DMSO Dimethylsulfoxide

EDTA Ethylenediaminetetraacetic acid

EGTA Ethylene glycol-bis-(2 aminoethylether)-N,N,N',N'-tetraacetic acid

ER Endoplasmic reticulum

EtOH Ethanol

FLIM Fluorescence lifetime imaging microscopy

Hb Haemoglobin

HEK cells Human embryonic kidney cells

IF Immunofluorescence

 $\begin{array}{ll} \text{IRF} & \text{Instrument response function} \\ \text{IP}_3 & \text{Inositol 1,4,5-trisphosphate} \\ \text{LPC} & \text{Lysophosphatidylcholine} \\ \end{array}$

MBE Method of Macey, Bennekou, and Egee
MELT Maximum entropy lifetime method

MEM Maximum entropy method MPE Multiple photon excitation

MS Marijuana smokers NP-40 Nonidet P 40 NS Non-smoker

OGB-1 Oregon Green 488 BAPTA-1

PAGE Polyacrylamide gel electrophoresis

IV Abbreviations

PBS Phosphate-buffered saline
PET Photoinduced electron transfer

PKA Protein kinase A PKC Protein kinase C

PMCA Plasma-membrane Ca²⁺ ATPase

PpIX Protoporphyrin IX
PS Phosphatidylserine
RBCs Red blood cells

RET Resonance energy transfer

RT Room temperature SCD Sickle cell disease

SD Spinning-disk confocal microscope

SDE sequence Stomatocyte - discocyte - echinocyte sequence

SDS Sodium dodecyl sulfate

SDS-PAGE Sodium Dodecyl Sulfate Polyacrylamide Gel Electrophoresis

SEM Standard error of mean

SERCA Sarcoendoplasmic reticulum calcium ATPase

SNARE Soluble N-ethylmaleimide-sensitive-factor attachment protein receptor

SS Sickle cell patients

TBST Tris-Buffered Saline with Tween-20 TCSPC Time-correlated single photon counting

TIRF Total internal reflection fluorescence microscope

TRP Transient receptor potential

TRPA Transient receptor potential ankyrin
TRPC Transient receptor potential canonical
TRPM Transient receptor potential melastatin
TRPML Transient receptor potential mucolipin
TRPP Transient receptor potential polycystin
TRPV Transient receptor potential vanilloid

TRPV2 Transient receptor potential vanilloid type 2

VGCC Voltage-gated calcium channel VRL-1 Vanilloid receptor-like protein-1

WB Western blot
WBCs White blood cells

Mathematical notations

Bispectral luminous radiance factor	$\beta_{L,\lambda}(\mu,\lambda)$
Decay rate constant	k
Dissociation constant	K_{d}
Emission spectrum	$M(\lambda)$
Emission wavelength parameter	λ
Excitation spectrum	$X(\mu)$
Excitation wavelength	μ
Excitation wavelengths	λ
Extracellular concentrations of the relevant ions	$[X]_{out}$
Extracellular pH	$\mathrm{pH_o}$
Faraday constants	\mathbf{F}
Fixed emission wavelength	λ_0
Fixed excitation wavelength	μ_0
Fluorescence lifetime	τ
Fluorescence lifetime amplitude	a_{x}
Fluorescence lifetime compounent	$ au_{\mathbf{X}}$
Fluorescence signal from a blank sample	I_0
Fluorescence signal from the analyte	${ m I_S}$
Gas constants	R
Hyperpolarization magnitudes	$\Delta({ m Vm_{Max}}$ - ${ m E_m})$
Intensity	I
Intracellular concentrations of the relevant ions	$[X]_{\mathrm{in}}$
Intracellular pH	$\mathrm{pH_{i}}$
Ion activity	a_{x}
Ion activity coeffeicent	γ_{x}
Ion concentrition	$C_{\mathbf{x}}$
Ionic valence	${f Z}$
Maximal hyperpolarization	$ m Vm_{Max}$
Permeability coefficients of the relevant ions	$P_{\mathbf{X}}$
Plasma membrane potential variation	$\Delta \psi$
Relative fluorescence intensity	${ m I_f}$
Resting membrane potential	E_{m}
Temperature	Τ
The decay rate constant	k
Transmembrane potential	ψ

Abstract

Blood is an essential connective tissue that performs several critical functions in the human body. Red blood cells (RBCs), constituting around 45% of the blood volume, are responsible for gas exchange and nutrient transport. Mature RBCs have a unique biconcave shape and are filled with hemoglobin (Hb), but they lack a nucleus and organelles. Because of their structure, RBCs rely on ion regulation as one of the key factors influencing cell behavior. Ion transport across RBC membranes occurs through a combination of passive channels, transporters and active pumps.

 ${\rm Ca^{2+}}$, as a universal signalling molecule, plays an essential role in RBCs to regulate cellular activities. Due to the large gradient across the membrane, a small number of channel openings can lead to acute and severe changes in free ${\rm Ca^{2+}}$ levels. The plasma membrane ${\rm Ca^{2+}}$ -ATPase (PMCA) is one of the key factors in maintaining the ${\rm Ca^{2+}}$ gradient in RBCs. In addition, several channels have been identified as sources of ${\rm Ca^{2+}}$ entry in erythrocytes, including Piezo 1, transient receptor potential vanilloid type 2 (TRPV2) and ${\rm Ca_{v}2.1}$ channels. Piezo 1 channels, which are sensitive to mechanical stimuli, help regulate RBC volume and contribute to RBC deformability. TRPV2 and ${\rm Ca_{v}2.1}$ channels in RBCs support RBC adaptability under physiological and pathological conditions. When the intracellular free ${\rm Ca^{2+}}$ concentration changes, it can trigger several downstream pathways to regulate cell behavior. For example, the Gárdos channel regulates ${\rm K^{+}}$ efflux in response to ${\rm Ca^{2+}}$ levels, affecting cell volume and shape.

To understand the Ca^{2+} -related pathways in RBCs, it is important to quantify the Ca^{2+} concentration in RBCs under different conditions. However, current methods based on fluorescence intensity can only provide semi-quantification, because of a strong influentially by the hemoglobin. Fluorescence lifetime is one of the intrinsic properties of fluorophores that is independent on fluorophore concentration, initial disturbance conditions and fluorescence intensity. The characteristics of fluorescence lifetime provide a potential method for the quantification of Ca^{2+} .

This study outlines the methods for studying RBCs under different experimental conditions. Blood samples from different sources, including healthy individuals, marijuana smokers and patients with specific diseases, were processed to isolate RBCs. Isolated RBCs were subjected to further steps for Ca^{2+} measurement based on fluorescence intensity. Immunofluorescence and western blot techniques were used to detect and quantify specific proteins within the RBC samples. In addition, the Ca^{2+} indicator-loaded RBCs were imaged using fluorescence lifetime imaging microscopy (FLIM).

The data presented in the results part shows that an activation of the Piezo 1 channel caused by the application of Yoda 1, one of Piezo 1 activators, leads to an increase of intracellular Ca^{2+} in two phases, which can be regulated by multiple factors. Measurements of RBCs from people with spectrin mutation or thalassemia β mutation provide evidence

VIII Abstract

that membrane and cytoskeletal structure may influence Piezo 1 channel function, causing a different Yoda 1-induced intracellular Ca²⁺ increase. PMCA show strong inhibitory effects on the first phase of Yoda 1-induced Ca²⁺ increase. Cl⁻ conductance has a positive influence on Yoda 1-induced Ca²⁺ entry and maintenance of high free Ca²⁺ levels. However, the pathway involved is still unknown. The Gárdos channel not only induces K⁺ efflux and hyperpolarization in response to a Yoda 1-induced Ca²⁺ increase, its opening probability can also influence the Ca_v2.1 channel activity involved in Yoda 1-induced Ca²⁺-entry. TRPV2 is a non-selective cation channel recently discovered in RBCs. RBCs show a heterogeneous response to activation of TRPV2 with an increase of free Ca²⁺ concentration. In marijuana consumers and sickle cell patients, after application of Δ^9 -Tetrahydrocannabinol (Δ^9 -THC), a TRPV2 activator, RBCs have a higher induced Ca²⁺ concentration, a higher number of responding RBCs, and even hyperpolarization. It is indicating that these RBCs are more sensitive to Δ^9 -THC. Sickle RBCs have an enhanced response to Δ^9 -THC in the deoxygenated condition. This suggests that oxidative stress may alter the activity of the channels. In addition, the studies of patient RBCs also suggest that the cell age may influence channel activity and sensitivity.

The analysis of FLIM images of X-Rhod-1-loaded RBCs with low or high intracellular $\mathrm{Ca^{2+}}$ shows different lifetimes with the lowest fluorescence signal originating in the RBC itself. The number of fitted lifetime components is different between 1-photon excitation and 2-photon excitation. The environment and the concentration of Hb in RBCs can influence the lifetime components and the amplitude-averaged lifetime of X-Rhod-1. Other factors such as excitation wavelength, acquisition time, use of CellTak and $\mathrm{Ca^{2+}}$ -ionophore Bromo-A23187 show no effect on the lifetime parameters of X-Rhod-1. With the chosen measurement parameters, the normalized amplitude-average lifetime is a promising parameter to be used to establish a calibration curve for $\mathrm{Ca^{2+}}$ -quantification.

Zusammenfassung

Blut ist ein wichtiges flüssiges Bindegewebe, das im menschlichen Körper mehrere wichtige Funktionen erfüllt. Die roten Blutzellen (Erythrozyten), die etwa 45% des Blutvolumens ausmachen, sind für den Gasaustausch und den Nährstofftransport verantwortlich. Vollständig ausgebildete Erythrozyten haben eine einzigartige bikonkave Form und sind mit Hämoglobin (Hb) gefüllt, besitzen jedoch keinen Zellkern und keine Organellen. Aufgrund dieser Struktur sind die Erythrozyten auf die Ionenregulierung als einen der Schlüsselfaktoren zur Steuerung des Zellverhaltens angewiesen. Der Ionentransport durch die Erythrozytenmembranen erfolgt durch eine Kombination aus passiven Transporteren, Kanälen und aktiven Pumpen.

Ca²⁺ als universelles Signalmolekül spielt in Erythrozyten eine wesentliche Rolle bei der Regulierung der zellulären Aktivitäten. Aufgrund des großen Gradienten über die Membran kann bereits eine kleine Anzahl von Kanalöffnungen zu akuten und signifikanten Veränderungen der freien Ca²⁺-Konzentration führen. Die Plasmamembran-Kalzium-ATPase (engl. PMCA) ist einer der wichtigsten Faktoren für die Aufrechterhaltung des Ca²⁺-Gradienten in Erythrozyten. Darüber hinaus wurden in der Vergangenheit mehrere Kanäle als Quellen für den Ca²⁺-Eintritt in Erythrozyten identifiziert, darunter Piezo 1, der Transient-Receptor-Potential-Vanilloid-Kanal Typ 2 (TRPV2) und Cav2.1-Kanäle. Piezo 1-Kanäle, die empfindlich auf mechanische Reize reagieren, helfen bei der Regulierung des Volumens der Erythrozyten und tragen zur Verformbarkeit der Erythrozyten bei. TRPV2 und Ca_v2.1 in Erythrozyten vermitteln zelluläre Reaktionen auf mechanische und thermische Belastungen und unterstützen so ihre Anpassungsfähigkeit unter physiologischen und pathologischen Bedingungen. Wenn sich die intrazelluläre freie Ca²⁺-Konzentration ändert, kann dies verschiedene nachgeschaltete Signalwege zur Regulierung des Zellverhaltens auslösen. So reguliert der Gárdos-Kanal beispielsweise den K⁺-Efflux als Reaktion auf den Ca²⁺-Spiegel und beeinflusst folglich auch das Zellvolumen und die Zellform.

Um die Ca^{2+} -abhängigen Signalwege in Erythrozyten zu verstehen, ist es wichtig, die Ca^{2+} -Konzentration im Zellinnern unter verschiedenen Bedingungen zu quantifizieren. Die derzeitigen Methoden, die auf der Fluoreszenzintensitätsmessungen basieren, können jedoch nur eine Semiquantifizierung liefern, da die Messungen durch das Hämoglobin stark beeinflusst werden. Die Fluoreszenzlebensdauer ist eine der intrinsischen Eigenschaften von Fluorophoren, die unabhängig von deren Konzentration, anfänglichen Störungsbedingungen und der Fluoreszenzintensität ist. Die Eigenschaften der Fluoreszenzlebensdauer bieten ein potentielles Maß zur Quantifizierung der Ca^{2+} -Konzentration.

In dieser Studie werden die Methoden zur Untersuchung von Erythrozyten unter verschiedenen Versuchsbedingungen beschrieben. Blutproben unterschiedlichen Ursprungs, darunter gesunde Personen, Marihuana-Raucher und Patienten mit bestimmten Krankheiten, wurden zur Isolierung der Erythrozyten aufbereitet. Die isolierten Erythrozyten wurden

X Zusammenfassung

weiteren Schritten zur Kalziummessung anhand der Fluoreszenzintensität unterzogen. Immunfluoreszenz- und Western-Blot-Techniken wurden eingesetzt, um spezifische Proteine in den Erythrozytenproben nachzuweisen und zu quantifizieren. Darüber hinaus wurden die mit $\mathrm{Ca^{2+}}$ -Indikatoren beladenen Erythrozyten mittels Fluoreszenzlebensdauer-Mikroskopie (engl. FLIM) abgebildet.

Die im folgenden Kapitel vorgestellten Daten zeigen, dass die Aktivierung des Piezo 1-Kanals durch den Piezo 1-Aktivator Yoda 1 zu einem zweiphasigen intrazellulären Ca²⁺-Anstieg führen kann, der durch mehrere Faktoren gesteuert werden kann. Untersuchungen an Erythrozyten von Menschen mit einer Spektrin- oder einer Beta-Thalassämie-Mutation liefern Beweise dafür, dass die Membran- und Zytoskelettstruktur die Funktion des Kanals Piezo 1 beeinflussen kann. Dies hat unterschiedliche Yoda 1-induzierte intrazelluläre Ca²⁺-Anstiege zur Folge. Die PMCA zeigt starke hemmende Effekte auf die erste Phase des Yoda 1-induzierten Ca²⁺-Anstiegs. Die Cl⁻-Leitfähigkeit hat einen positiven Einfluss auf den Yoda 1-induzierten Ca²⁺-Anstieg und die Aufrechterhaltung eines hohen freien Ca²⁺-Spiegels. Der beteiligte Signalweg ist jedoch noch unbekannt. Der Gárdos-Kanal induziert nicht nur den K⁺-Efflux und die Hyperpolarisation als Reaktion auf den Yoda 1-induzierten Ca²⁺-Anstieg, sondern seine Öffnungswahrscheinlichkeit kann auch die Aktivierung des Ca_v2.1-Kanals beeinflussen, der am Yoda 1-induzierten Ca²⁺-Anstieg beteiligt ist. TRPV2 ist ein kürzlich in roten Blutzellen entdeckter nicht-selektiver Kationenkanal. Erythrozyten zeigen eine heterogene Reaktion auf die Aktivierung von TRPV2 durch eine erhöhte freie Ca²⁺-Konzentration. Nach Zugabe von Δ^9 -Tetrahydrocannabinol (Δ^9 -THC), einem TRPV2-Aktivator, wiesen die Erythrozyten von Marihuana-Konsumenten und Sichelzellpatienten eine höhere induzierte Ca²⁺-Konzentration, eine höhere Anzahl reagierender Erythrozyten und sogar eine Hyperpolarisation auf. Dies deutet darauf hin, dass diese Erythrozyten empfindlicher auf Δ^9 -THC reagieren. Außerdem reagieren sichelförmigen Erythrozyten im desoxygenierten Zustand verstärkt auf Δ^9 -THC. Somit gibt es Hinweise, dass oxidativer Stress die Aktivität der Kanäle verändern kann. Darüber hinaus legen die Studien mit Erythrozyten von Patienten nahe, dass das Alter der Erythrozyten die Aktivität und Empfindlichkeit der Kanäle beeinflussen kann.

Die Analyse der FLIM-Bilder von mit X-Rhod-1 gefärbten Erythrozyten mit niedrigem oder hohem intrazellulärem $\mathrm{Ca^{2+}}$ zeigt unterschiedliche Lebensdauern, wobei das Fluoreszenzsignal geringster Intensität von den Erythrozyten selbst ausgeht. Die Anzahl der per Regression angepasster Lebensdauerkomponenten ist zwischen 1-Photonen-Anregung und 2-Photonen-Anregung unterschiedlich. Eine unzureichende Fokussierung während der Ablichtung kann die Auflösung der Anzahl der angepassten Lebenszeitkomponenten beeinflussen. Auch die Umgebung und die Hb-Konzentration in den Erythrozyten können die Lebenszeitkomponenten und die amplitudengemittelte Lebensdauer von X-Rhod-1 beeinflussen. Andere Faktoren wie Anregungswellenlänge, Aufnahmezeit und die Verwendung verschiedener Farbstoffe wie CellTak und $\mathrm{Ca^{2+}}$ -Ionophor Bromo-A23187 haben keinen Einfluss auf die Lebenszeitparameter von X-Rhod-1. Mit den im Zuge dieser Analyse bestimmten Messparametern ist die normalisierte amplitudengemittelte Lebensdauer ein vielversprechender Parameter, der zur Erstellung einer Kalibrierungskurve für die $\mathrm{Ca^{2+}}$ -Quantifizierung verwendet werden kann.

1.1 Overview of Blood

Blood is a liquid tissue in the body and has important functions such as transport, defence and maintenance of homeostasis [1]. Primarily, it delivers oxygen, nutrients and hormones to the body's cells and removes carbon dioxide, cellular waste and by-products to target organs for exhalation and excretion. In addition, it could protect the body against external and internal threats through peripheral blood leukocytes, antibodies and immunoglobins. It could also protect against blood loss by platelets and certain proteins. It participates in homeostasis maintenance. It has a colloidal osmotic pressure of around 25 mmHg. The average temperature is around 37°C and the pH is between 7.35 and 7.45. Blood consists of liquid part, (i) plasma and cellular elements including (ii) erythrocytes, (iii) leukocytes and (iv) platelets (Fig. 1.1) [1, 2].

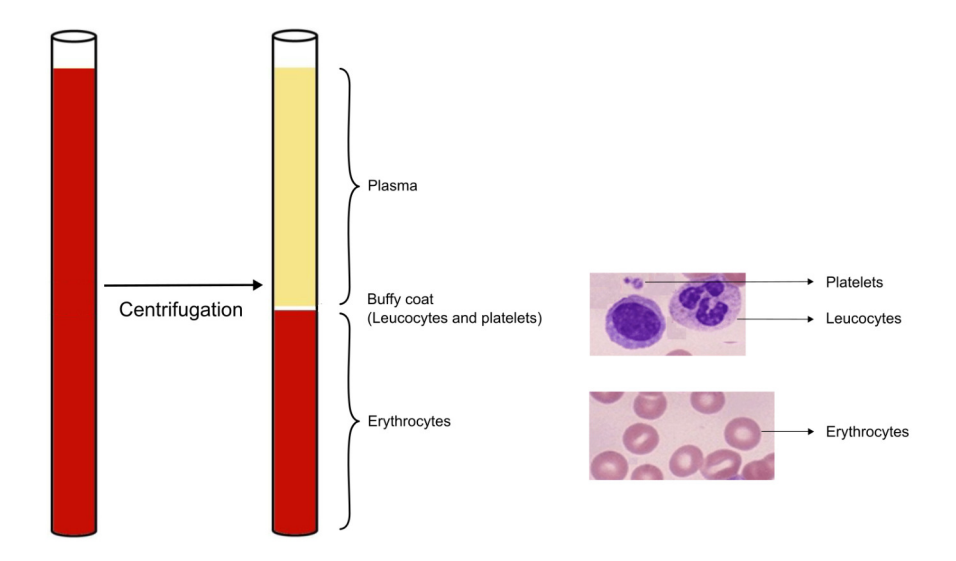


Fig. 1.1: Blood components and representative cell images from stained blood smear. The whole blood after centrifugation could be divided into plasma, buffy coat (including leukocytes and platelets) and erythrocytes. The representative cells are shown with an arrow. Image adapted from Acharya et al. and Mondal et al. [3,4].

(i) Plasma is the liquid part of the blood, accounting for about 54% of the total blood. It contains about water (90%), small and large molecular weight components, ions and gases. It alone transports the blood cells throughout the body with several

substances such as immunoglobulins, antibodies, clotting proteins, nutrients, messenger molecules, gases, by-products and wastes. It also participates in maintaining homeostasis such as body temperature, acid-base balance and osmotic pressure [2,5,6].

- (ii) Erythrocytes, also known as red blood cells (RBCs), are the major cellular component of blood (approximately 45%). It is the functional component of blood for the transport of gases and nutrients. The unique biconcave shape, full of haemoglobin and lack of nucleus allow these cells to perform the essential functions [7].
- (iii) Leukocytes, also known as white blood cells (WBCs), come in a variety of sizes and shapes with different functions and account for less than 1% of the total blood volume. WBCs can be divided into granulocytes, which include neutrophils, eosinophils and basophils, and agranulocytes, which include lymphocytes and monocytes. They play a role in defence against pathogens by removing damaged cells, toxins and waste products [8].
- (iv) Platelets are also known as thrombocytes. They play an essential role in haemostasis and thrombosis. They accumulate at the site of vascular injury, initiate the coagulation cascade and form the fibrin plug to stop bleeding. They are also important players in a number of pathophysiological processes such as inflammation, haematogenic metastasis and atherogenesis [9–11].

1.2 Erythrocytes (RBCs)

1.2.1 Physiology of RBCs

RBCs were first described by Jan Swammerdam in approximately 1660 and since then there have been various investigations of RBCs [12,13]. The number of RBCs in a man is approximately 4.5 - 6.3 million cells per microlitre of blood and in a woman 4.2 - 5.5 million per microlitre of blood [8]. The main physiological role of the RBCs is to transport gases (O₂ and CO₂) between the lungs and tissues and also to maintain systematic acid-base balance [7,8,14]. Mature RBCs have a specific shape of a biconcave disc with 2.6 µm at the thickest part and 0.8 µm in the middle. The diameter of the cells is approximately 7.8 µm (Fig. 1.2 A) [8]. They are anucleate and lack of organelles but have a large amount of hemoglobin (Hb) [7,8]. However, they lack organelles for the repair of the metabolic and physical damage, such as membrane vesiculation, antioxidant defences, cellular homeostasis and so on. After differentiation in the bone marrow and release into the peripheral blood, RBCs in a normal individual can remain in circulation for approximately 120 days before being removed by mononuclear phagocytes in the spleen, liver and bone marrow [8,15–18].

The unique biconcave shape of RBCs is ideal for enlarging the surface area to volume ratio to increase the gas exchange efficiency [7,14,21]. The cell membrane plays an important role in framing the shape which is composed of three parts: the phospholipid bilayer, the cytoskeleton and membrane proteins (Fig. 1.2 B) [14,21]. The lipids bilayer is composed of cholesterol and phospholipids [22]. Cholesterol is considered to be evenly distributed, whereas the 4 main phospholipids are asymmetrically distributed. Sphingomyelin and phosphatidylcholine are located in the outer layer while phosphatidylserine and phos-

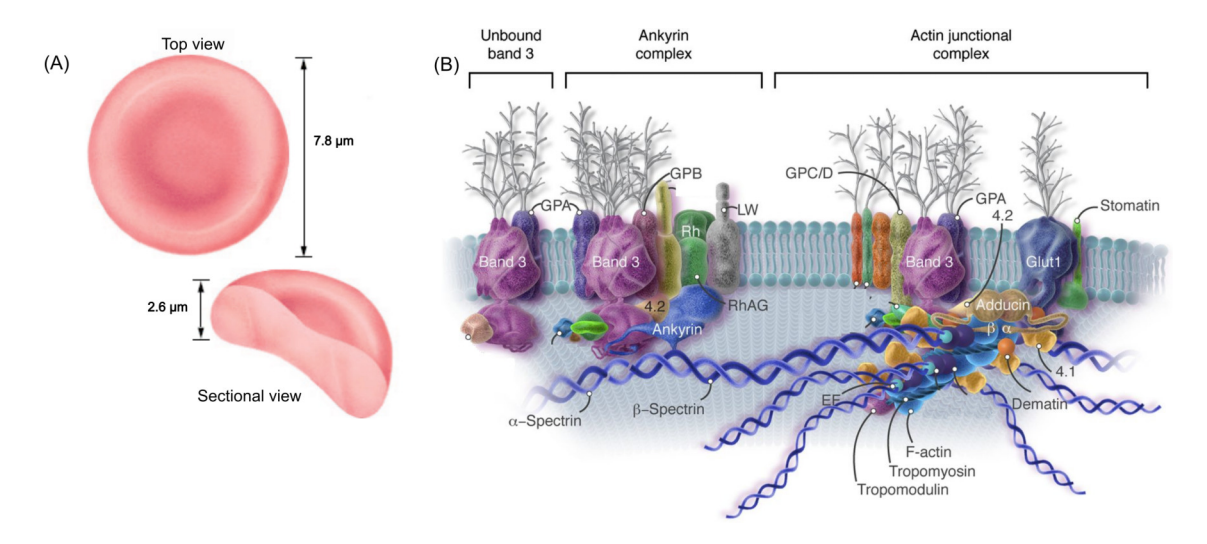


Fig. 1.2: RBCs shape and the structure of RBC membrane and cytoskeleton. (A) Biconcave shape of RBCs in top view and sectional view. Image adapted from Sonker [19]. (B) The current theoretical structure of RBC membrane and cytoskeleton with a few transmembrane proteins as representative. Image adapted from Lux [20].

phatidylethanolamine form the inner layer [23,24]. The loss of the asymmetric distribution of the phospholipids could cause the lipid in the inner side such as phosphatidylserine (PS) to be exposed at the surface and cause the functional consequences. Lipid rafts involved in cell signaling as well [25].

The major components of the cytoskeleton are several proteins, including α - and β -spectrin, actin, protein 4.1, adducin, tropomyosin and tropomodulin (Fig. 1.2 B) [20, 26]. It is a two-dimensional network based on five- or six-sided polygons formed by five or six spectrin molecules attached to short actin filaments [26]. Other proteins either participate in the formation of spectrin-actin complexes or assist in the attachment of the cytoskeleton to the lipid bilayer [20, 27]. Interactions between the lipid bilayer and the cytoskeletal proteins are important in regulating the mechanical function and stability of the membrane [28–31].

There are also more than 50 transmembrane proteins, ranging in abundance from a few to millions of copies per cell (Fig. 1.2 B). These proteins have diverse functional heterogeneity, including transport, adhesion, receptors and other known or unknown functions [32–34]. Some proteins, such as the glycophorin family, are critical for membrane architecture and the linkage between lipid bilayers and the cytoskeletal network [32, 33]. Molecules with receptor function are involved in signal transduction and some pathogenesis of infectious diseases [35,36]. Proteins can act as transporters and channels, such as Band 3, aquaproin 1, Rhesus factor associated glycoprotein etc., transferring biologically important molecules in and out of cells, especially water-soluble molecules [37–41]. In addition, there are a few proteins having enzyme function and participating in biosynthesis in RBCs [32, 42]. For example, Kell proteins can work as a zinc metalloprotease and be involved in variety of physiological processes (pain, blood pressure, inflammatory responses, etc) by hydrolyzing hormone or bioactive peptide substrates [43,44]. Human RBCs express relatively large number of adhesion molecules in human although they are considered to be non-adhesive. These adhesion molecules are activated during normal erythropoiesis or during pathophysiologic processes [45, 46]. Additionally, more than 30 of them can act as antigens to define the blood groups [47–49].

The structural organization of the membrane allows mature RBCs to have an excessive surface area to volume ratio and high membrane elasticity, which enables the cell to respond rapidly to fluid stress in the circulation with mechanical membrane stability [27, 50, 51]. It also allows the RBCs membrane to remains intact and flexible as the cells face endogenous and exogenous chemical and biochemical challenges [21]. The structural changes could cause malfunction of RBCs leading to pathological conditions [52, 53].

Hemoglobin (Hb) constitutes up to 95% of the protein content of mature RBCs [54]. It is a tetramer consisting of two α -subunits and two β -subunits [55]. Each subunit binds to heam, which has a porphyrin ring with a central iron ion. The iron atom could form a coordinate covalent bond with O_2 , the globin fold provides the environment of reversible and selective binding [56–58]. The structure of hemoglobin allows each molecule to bind up to four O_2 molecules. As the number of O_2 molecules bound increases, the structure of hemoglobin changes, leading to an increase in O_2 affinity. If only the last O_2 molecule binds and releases oxygen from hemoglobin, the system is deficient [59]. These properties also make hemoglobin have a much higher O_2 capacity than plasma and transport about 98% of the total O_2 in the blood [60].

Although the majority of carbon dioxide CO₂ in the blood is in the form of the bicarbonate ions in and about 5% CO₂ is dissolved in plasma. Hemoglobin can form carbamino compounds and transport approximately 6% CO₂ [61]. Interestingly, Bohr et al. found that CO₂ uptake is unaffected by the presence of O₂, but O₂ uptake is reduced when a certain amount of CO₂ is present [62]. Beside that, hemoglobin can buffer the hydrogen ions and regulate in nitric oxide metabolism [63]. The normal structure of hemoglobin and certain concentration can help mature red blood cells to maintain their shape and volume [27,61].

Other ligands such as nitrite ion (NO²⁻), nitric oxide (NO), carbon monoxide (CO), cyanide (CN⁻), sulphur monoxide (SO), sulphide (S²⁻) could also bind to heme as competitive inhibitors. They will greatly reduce the oxygen capacity and cause cellular hypoxia [64–69]. The abnormal hemoglobin structure could lead to abnormal oxygen binding affinity, altered shape of RBCs and result in anemia as well as other pathological symptoms [70].

1.2.2 Ion Regulation in RBCs

1.2.2.1 Generalities of lons

Electrolytes are substances that have the ability to conduct an electric current when they dissolved in solution [71,72]. When the molecules have a net electrical charge, the term "ion" is used to describe these molecules [71]. There are two types of ions, cations and anions. Cations are positively charged ions and the anions are negatively charged ions [71,73]. Organisms contain a wide variety of ions. Ions play an essential role in basic life functions from the cellular level to the organismal level [74]. For a single cell, ions participate in many cellular activities including maintaining pH and osmotic homeostasis [75–77], maintaining electrical neutrality [74], generating and conducting membrane potentials [78], participating in cell volume changes [79], regulating metabolism [80], signal transduction [81].

Component	Intracellular Concentration*	Extracellular Concentration**	
Cation			
Na ⁺ K ⁺	$7.35 \pm 1.26 \mathrm{mmol/L}$ [83] $99.1 \pm 5.3 \mathrm{mmol/L}$ [83]	$140 \pm 2.38 \mathrm{mmol/L}$ [84] $4.6 \pm 0.5 \mathrm{mmol/L}$ [85]	
Ca^{2+}	$19 \pm 9 \mu \text{mol/L} [86]$	$2.44 \pm 0.1 \text{mmol/L} [87]$	
$\underline{\qquad \qquad Mg^{2+}}$	$2.3 \pm 0.17 \mathrm{mmol/L}$ [88]	$0.78 \pm 0.04 \mathrm{mmol/L}$ [88]	
Anion			
Cl-	$67.9 \pm 4.9 \text{mmol/L} [89]$	$103.7 \pm 1.9 \mathrm{mmol/L}$ [90]	

^{*} Intracellular concentration measured in RBCs from adults.

Tab. 1.1: Measured intracellular and extracellular concentration of major cations and anions in human.

RBCs, like other cells, have a non-equilibrium ion distribution across the cell membrane, which is important for cell survival and function. The difference in concentration of major ions between the intracellular cytosol and the extracellular environment is shown in (Tab. 1.1). In addition to the activities mentioned above, ions also have a significant influence on the physiological function of the RBCs. For example, ions can alter the affinity of haemoglobin for oxygen and the ability to transport oxygen [82]. Imbalances in ion distribution can lead to cell dysfunction and even cell death [74].

1.2.2.2 Important lons

Sodium Cation (Na⁺)

Sodium (Na⁺) is the most important extracellular cation. The concentration of Na⁺ in the extracellular fluid is approximately ten times higher than it in the cytosol (Tab. 1.1). As an osmotically active ion, the Na⁺ is responsible for maintaining the extracellular volume and osmosis pressure in cells [74,91]. Na⁺ is also involved in several cell signaling pathways and regulates cell functions. Intracellular fluctuations of Na⁺ influence several membrane exchangers and trigger enzymatic and translational responses [92]. Cross-link between Na⁺ and other electrolytes is used to generate cytosolic ionic signals to regulate cell function. For example, Na⁺ and Ca²⁺ are both important signaling molecules. Several intracellular signaling pathways mediated by Na⁺ and Ca²⁺ have been shown to be closely linked by a few pathways that generate Na⁺ and Ca²⁺ fluxes, which in turn are regulated by both ions [93, 94].

The activities Na⁺ participates mentioned above may also occur in RBCs. Except that, the Na⁺ concentration across the RBCs membrane helps to maintain the resting membrane potential [95]. It also has an impact on RBC hemostats [96]. Na⁺ also affects on hemoglobin function. In 1937, Sidwell et al. mentioned the Na⁺ could affect the hemoglobin-oxygen equilibrium [97]. Later, Vig et al. and Davis et al. confirmed the influence of Na⁺ on oxygen binding with hemoglobin [98, 99].

Unregulated Na⁺ could lead to a change in the osmolality relative to the environment, resulting in RBCs dehydration or overhydration. It will also affect RBCs activities. Abnormal Na⁺ transport could be seen in several diseases' states. Berkowitz et al.

^{**} Extracellular concentration measured in plasma or serum from adults.

describe how deoxygenation could cause unidirectional passive influxes of Na⁺ in sickle cells [100].

Potassium Cation (K⁺)

Unlike Na⁺, potassium (K⁺) is a major intracellular ion. The intracellular concentration is much higher than in the extracellular part (Tab. 1.1). In alliance with other ions (i.e., Na⁺ and Cl⁻), it contributes to overall electrolyte balance of cells [96, 101, 102]. K⁺ is also really important in regulation of cellular electrolyte metabolism, electric signaling, transport of nutrients, and enzymes functions [102].

As in other cells, due to the high intracellular concentration in RBCs (approximately 30 times higher than extracellular concentration) (Tab. 1.1), K⁺ can maintain the fluid balance and osmolarity of RBCs. Changes in K⁺ membrane permeability contribute to repolarization and hyperpolarization of the cell membrane in RBCs [103]. The change in cell membrane potential may cause voltage-gated channels to open, leading to a downstream cascade reaction [104]. K⁺ can also activate some enzymes to participate in metabolism, membrane phosphorylation or other cellular activities [105]. It also helps to maintain the RBC shape and the deformability [106]. In addition, an earlier study showed a small effect of K⁺ chloride on hemoglobin-oxygen equilibrium [97].

The loss of K⁺ could lead to RBC dehydration, impaired deformability and programmed cell death [107]. Abnormal K⁺ transport or imbalance has been observed in pathophysiological conditions such as sickle cell disease [100].

Calcium Cation (Ca^{2+})

Intracellular calcium (Ca^{2+}) exists in two states in cells. Most of the Ca^{2+} is buffered or bound by Ca^{2+} -binding proteins, phospholipids and inorganic phosphate and small amount exists as free Ca^{2+} [108]. Usually in cells, the intracellular Ca^{2+} concentration is much less then extracellular environment (Tab. 1.1). The gradient across the membrane is essential for signaling. Opening of Ca^{2+} -permeable channels can lead to more than ten-fold changes in the free levels in the sub-membrane space, causing acute changes in the activity of Ca^{2+} -sensitive organic molecules and triggering downstream cascades, which makes Ca^{2+} as a universal and ubiquitous signaling molecule [108].

Total intracellular Ca^{2+} in RBCs could reach 5.7 µM when basal free Ca^{2+} is estimated to be in the range of 30 to 60 nM [109,110]. As in other cells, Ca^{2+} in RBCs, is involved in the regulation of cell cycle and fate, transport, metabolism and structural integrity, motility and volume [108]. In RBCs, Ca^{2+} can activate protein kinase $C\alpha$ (PKC α) [111], which can phosphorylate target membrane proteins to regulate the associated cellular cytoskeleton [112,113]. Ca^{2+} also forms complexes with other proteins such as calmodulin, to stabilize cytoskeletal structure [114,115]. Ca^{2+} can also modulate the membrane lipid bilayer by regulating the bidirectional transmembrane movement of phospholipids via scramblase [116–118] and flippase [119,120]. The Ca^{2+} dependent cysteine protease μ -calpain (calpain-1) targets several transmembrane or membrane-associated proteins and regulates cell shape, deformability and filterability [121]. Expect to regulate cell shape and volume by modulating the cytoskeleton and membrane, Ca^{2+} mediates cellular volume

changes through Ca²⁺-dependent channel activities. The first recognized channel was the Gárdos channel, the Ca²⁺-dependent K⁺ channel [122–124]. Increased intracellular Ca²⁺ activates Gárdos channel and leads to loss of K⁺, Cl⁻ and water, resulting in reduced cell volume, also known as Gárdos effect [125, 126].

 ${\rm Ca^{2+}}$ is also essential for RBCs metabolism. The ${\rm Ca^{2+}}$ -activated PKC α as mentioned above can also regulate RBCs metabolism [127]. Several other proteins in cascades are also affected by ${\rm Ca^{2+}}$ [128–131]. The role of the calcium-calmodulin complex (Ca-CaM) system in the regulation of glycolytic enzymes has been reported [132, 133]. Ca-CaM complexes are also involved in the redox state of RBCs. The complexes are co-activators of endothelial NO synthase activity [134–137].

Ca²⁺ also affects RBC function. It could alter the protonation of deoxyhemoglobin and change the affinity of oxygen to hemoglobin to change the ability of RBCs to transport oxygen [138]. In addition to modulating hemoglobin function, Ca²⁺ is involved in aggregation. Besides acting as clotting factor IV to participate in the coagulation cascade [139], Ca²⁺ mediates aggregation of RBCs [140–143] and RBC adhesion to the endothelium [144–146]. Ca²⁺ is not only essential for mature RBCs, but also for hematopoiesis [147,148] and RBC clearance [149–151]. High intracellular Ca²⁺ dysregulates cellular functions in the long term. Ca²⁺ overload leads to the formation of polymeric protein complexes and induces cytoskeletal remodeling and associated changes in cell shape and membrane plasticity [152]. Elevated intracellular Ca²⁺ levels are also implicated in several pathophysiological conditions such as sickle cell disease (SCD) [153], β-thalassemia [154] and hereditary hemolytic anaemia [110].

Some chemicals can act as ionophores for Ca²⁺. Ionophores are types of molecules that could form complexes with target ions and transport them across the membrane [155–159]. The use of Ca²⁺ ionophores has been effective in increasing the intracellular Ca²⁺ concentration in *in vitro* experiments. The most commonly used Ca²⁺ ionophores are Ionomycin [160] and calcimycin (A23187) [161,162]. Based on A23187, a halogenated non-fluorescent analogue has been developed for use in combination with fluorescent probes, named Bromo-A23187 [163].

Proton (H⁺)

Protons are important ions for basic biological process including pH homeostasis, synaptic transmission, generation and conversion of energy, and protein ioization state in cells [164]. Thus, proton in both intracellular and extracellular are really important for organism. For pH homeostasis of extracellular environment, especially plasma, RBCs are rally important regulation factors. RBCs can regulate the acid-base balance in the plasma by two key elements, hemoglobin and anion exchanger, including anion exchangers 1 (AE1), also known as band 3 [165]. Band 3 is a Cl^-/HCO_3^- exchanger facilitated by cytoplasmic carbonic anhydrase, an enzyme that catalyses the reversible hydration of carbon dioxide $(CO_2 + H_2O \leftrightarrows HCO_3^- + H^+)$. Band 3 activity could efficiently produce transport CO_2 and thus regulate plasma pH [166, 167]. Meanwhile, hemoglobin acts as a proton buffer [168]. While the modulating role of RBCs in plasma pH has been studied extensively [169, 170], the importance and function of intracellular proton dynamics in RBCs is gaining attention. In 1909, the quantity of pH defined by Sørensen as the negative logarithm of the hydrogen

ion activity [171]. Thus, the intracellular $\rm H^+$ concentration also influences the intracellular pH (pH_i) regulation in RBCs. The resting pH_i is about 7.25 [172–175] and pHi is tightly regulated by multiple systems, including AE1-linked $\rm CO_2/HCO_3^-$ -dependent buffering [166, 167], hemoglobin buffering [168] and intrinsic (non- $\rm CO_2/HCO_3^-$ -dependent) buffering [176]. In the early 20th century, some studies showed that pH_i could affect Hb-O₂ binding [62,177]. Besides affecting hemoglobin, intracellular pH could modulate various cellular processes, including metabolism, membrane potentials, and ion transport [178,179]. The pH change could also regulate membrane excitability, signal transduction, cytoskeletal dynamics and even apoptosis via pH-sensitive proteins [178,180,181]. There are some chemicals that can act as H⁺ ionophores, also known as protonophores, H⁺ translocators or uncouplers, which increase the proton conductivity of lipid membranes [182]. The most commonly used protonophores include carbonyl cyanide m-chlorophenylhydrazone (CCCP) [183] and 2,4-dinitrophenol [184].

Chloride Anion (CI⁻)

Chloride (Cl⁻) is one of the most essential anions in both extracellular environment and cytosol. Similar to Na⁺, the concentration of Cl⁻ in extracellular is much higher than cytosol. It is the major anion for neutralizing the positive charges of cations in the extracellular fluid [185]. It is the most abundant electrolyte in plasma after Na⁺ to regulate extracellular fluid volume [186], osmotic equilibrium, electrolyte balance [187], and acid-base status [188]. It plays an essential role in cell functions and activities in general. The intracellular Cl⁻ could be involved in multiple cation transport via Cl⁻-cation cotransporters [189]. The Cl⁻-dependent cation conductance is involved in several cell activities, such as reducing impact of cell shrinkage [190]. Cl⁻ also acts as a signaling effector or modulator to regulate cell volume [191] and intracellular pH [192]. It can also act as second messenger to affect the activity of channels [193] and enzymes [194]. Cl⁻ conductance contributes to the resting membrane potential of cells [195]. For RBCs, Cl⁻ conductance is the main factor to determine resting membrane potential [78, 196].

In addition to the general role of Cl⁻ mentioned above, Cl⁻ is also important for RBCs to transport oxygen and the CO₂ capacity in cells and blood [188]. RBCs have a special chloride movement based on a relatively higher intracellular chloride concentration than other cells, called 'chloride shift', which could move Cl⁻ from plasma to RBCs via the bicarbonate chloride carrier protein band 3 in the RBCs membrane. It will restore the equal Donnan ratio for Cl⁻ and HCO₃⁻ and increase the carrying HCO₃⁻-capacity of the blood. The internal Cl⁻ exchange could also reduce intracellular pCO₂ to increase the CO₂ diffusion into RBCs [197, 198]. Additionally, exchange affects intracellular pH which could regulate the efficiency of oxygen-hemoglobin binding [199]. Nigen et al. found an oxygen-linked binding site for chloride to hemoglobin suggesting allosteric effects of Cl⁻ to haemoglobin affinity for oxygen [200]. More recently, the study of chloride shift shows that influxes of Cl⁻ are important for oxygen unloading [198].

Some pharmaceutical Cl⁻ blockers are available. For example, 2-(((3-(trifluoromethyl) anilino) carbonyl) amino) benzoic acid, as known as NS1652, is one of the reversible Cl⁻ transport blockers. A study showed the IC₅₀ of NS1652 is about 1.3 mM [201]. Another compound N-[4-Bromo-2-(1H-tetrazol-5-yl-phenyl]-N'-[3-(trifluoromethyl) phenyl]-urea,

also called NS3623, is a more long-lived member of the same class of compounds as NS1652. NS3623 has a higher affinity than NS1652 [202].

1.2.2.3 Ion Transportation Transportation

As mentioned in the generalities of ions in RBCs, there is an enormous gradient of ions across the cell membrane. Initially, it was postulated that non-equilibrium distribution of ions in RBCs is only possible if the cell membrane is impermeable to ions [203]. However, in 1923, van Slyke et al. showed RBCs have the high permeability to Cl⁻ [170]. Later, several studies showed that the RBC membrane is permeable to Na⁺ and K⁺ [204, 205]. Some studies of ion permeation through pure lipid bilayers, as the hydrophobic interior, revealed that lipid bilayers are high permeability barriers for ions [206, 207]. High-throughput physicochemical screening also demonstrates the low permeability coefficient of artificial membranes for ions such as Na⁺ and K⁺ [208]. Thus, the permeability of the cell membrane to ions is not controlled by the lipid bilayer, there are other means of ion transport. After Krogh proposed of the existence of a Na⁺/K⁺ pump in the cell membrane by in 1946 [209], systematic investigations of ion transport across the RBC membrane started in 1950s [210, 211].

Because the lipid bilayer of cell membrane is impermeable to ions, cells, including RBCs, rely on transmembrane proteins to transport ions between cytosol and extracellular environment [212,213]. After years of study, three main types of ion transport, passive transport, active transport and semi-active transport, have been reported. Passive transport transports ions following gradient [214]. In cells, ion passive transport needs channel or simple carrier to participate [212,213]. Active transport is an energy-driven process across the cell membrane with direct ATP contribution. It allows transport against ion concentration or electrochemical gradient [215]. The proteins facilitated in active transport called pumps [212,213]. The semi-active transport usually requires the participation of two types of molecules. One is transported against the gradient and requires energy. Another type of molecule is transported following the gradient and it provides the energy required for the former molecule transport. The proteins participate in semi-active transport called cotransporters [216].

Channels (Fig. 1.3 A), can form a hydrophilic pore in the cell membrane that allows passive transmembrane movement [206]. According to the studies of Labara et al., there is a simple model of channel opening. Each channel opens independently of one another. Typical channels have a single open state and a single closed state. And the two conformations of the channel (open or closed) possess different dipole moments normal to the plane of the bilayer [217]. Some channels are gated, which means that some other factors can control the opening of the channel. Over years, studies have shown that ion channels in mammalian cells are regulated by many factors, including the signaling molecules [218,219], temperature [220], membrane potential changes [221–223] or mechanic stress [224]. When channels open, ions are allowed to diffuse through the channel following an electrochemical gradient. Most channels are selective for particular ions. Selectivity can be determined by hydration free energy [225], conformational flexibility, structural strain energy [226, 227], kinetic factors related to the multi-ion nature of the pore [228], conformational plasticity, as well as the conductive and non-conductive form of the pore [229]. Selectivity is important for multiple biological properties, including the excitability of biological membranes [229].

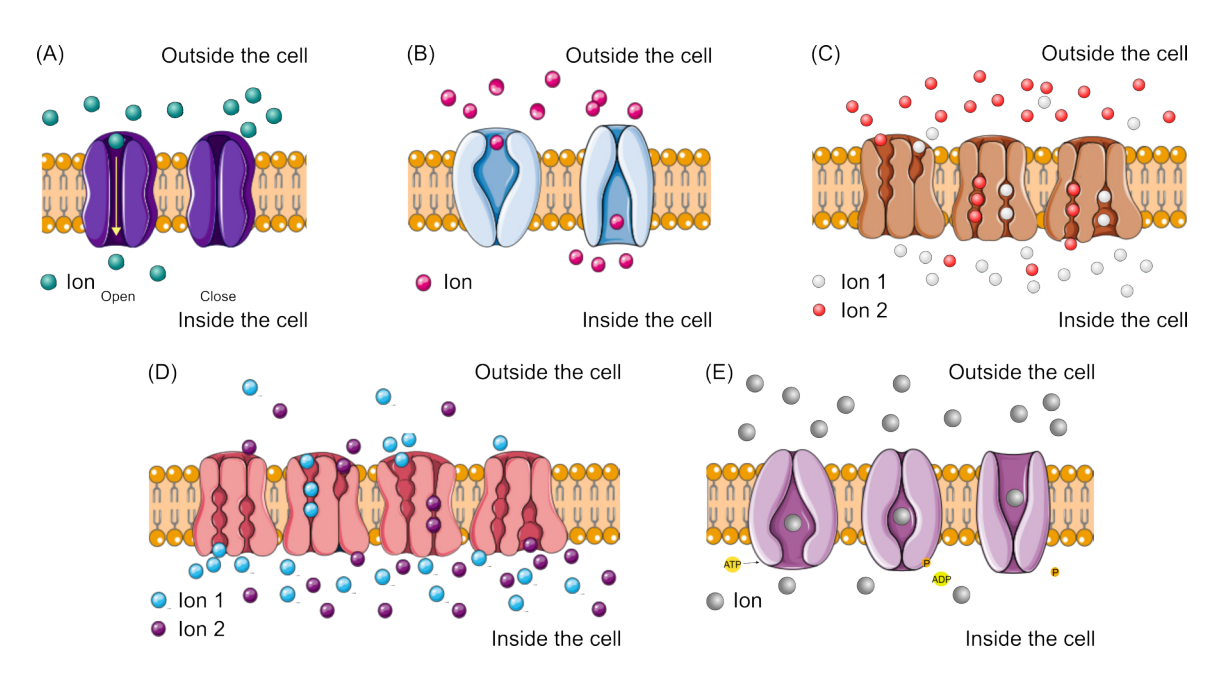


Fig. 1.3: Different types of ion transport proteins. (A) Ion channel protein. When the channel opens, it allows ions to move along a gradient. (B) Uniporter: it moves ions along a gradient with conformational changes. (C) Symporte: it can move two ions in the same direction. One ion is moved against the gradient and the other ion follows the gradient. (D) Antiporter: it could move two ions in opposite directions. One ion is moved against the gradient and the other is moved with the gradient. (E) Pump: it could move ions against a gradient with ATP consumption.

Proteins that has a moving part that moves ions back and forth across the membranes, called transporter (Fig. 1.3 B-E) [206]. Some of transporters can only bind one molecule or substrate at a time, which are called uniporters (Fig. 1.3 B) [216], or simple carriers. Simple carriers would undergo a reorientation or conformational change during the transmembrane movement of their substrate. These carriers exist in two conformational states: their binding sites for substrate are exposed alternately on one and then the other side of the membrane [230]. Typically, carriers move solutes following a concentration or electrical gradient. No energy is required for this process. It is therefore a type of passive transport [212]. Some of transporters could bind more than one type substrate or molecule during the movement, called cotransporters. If the transporters can move two types of molecules in the same direction, they are called symporters (Fig. 1.3 C). If the transporters move two types of molecules in opposite directions, they are called countertransporters or antiporters (Fig. 1.3 D) [212,231]. Cotransporters, can also be considered as secondary active transport or semi-active transport, couple the free energy of the electrochemical potential or gradient of one solute to the transmembrane movement of another and resulting in an uphill flux of the latter [212, 213, 232]. Secondary active transport requires the simultaneous binding of two or more substrates to the transporters to induce conformational change [230, 233]. Different to carriers and cotransporters, ion pumps are pure energy-driven transporters, which can transport ions against the gradient (Fig. 1.3 E) [234–237]. Pumps carry out active transport in two main ways: ATP-driven pumps [233,238], and light-driven pumps [239]. However, the light-driven pumps are not common in mammalian cells [212]. ATP-driven pumps directly hydrolyze ATP to drive uphill transport, also known as primary active transport or direct active transport [240]. When primary active transport happens, the

conformational changes of the pump occur when the substrate is bound. The ATP consumption takes place during the transport cycle (Fig. 1.3 E) [230].

The function of ion transport proteins can be regulated by multiple factors, including temperature, membrane potential, number of the transport proteins, ion gradient and molecular regulators. Specific molecules that can open channels, prolong their open state duration, or increase the activity of transporters, are called activators [241,242]. Ligands that can prevent channel opening or prevent substrate binding to transport proteins are called inhibitors or blockers [243]. Based on the whether the inhibition is permanent, inhibitors can be classified as irreversible and reversible inhibitors. Based on the binding behavior of inhibitors, they can be classified as competitive and non-competitive inhibitors. The former can block the substrate binding site and the latter can bind to the transport protein at another site to stop the function [230, 243]. Activators and inhibitors are essential for studying of transport protein function.

In the following part, the most important ion channels in RBCs for mythesis and the Ca²⁺-pump are briefly introduced.

Piezo 1 Channel

The Piezo 1 channel was first identified as a potential channel in the Neuro2A cell line by the Patapoutian group in 2010. Coste et al. mechanically stimulated the model cell and measured evoked currents. They also found that the currents were rapidly inactivated. They identified the gene family with sequence similarity 38 A (Fam38A) as responsible for the current [244]. The protein encoded by Fam38A consists of approximately 2500 amino acids and contains numerous transmembrane regions (Fig. 1.4 A). According to several published cryo-EM studies, the murine Piezo 1 (mPiezo 1) protein has a homotrimeric structure resembling a three-bladed propeller-shaped configuration. This structure consists of a central cap, three peripheral blade-like formations on the extracellular side, three elongated beams on the intracellular side connecting the blades to the cap, and a transmembrane region positioned between these components (Fig. 1.4B) [245–249]. Since the activation of the channel required pressure, the channel was named Piezo 1 by Coste et al. from the Greek "πιεση" (piesi), meaning pressure [244]. Additionally, another gene Fam38B was detected by a homology search and the channel encoded by this gene called Piezo 2 [244, 250]. Only Piezo 1 chennel occurs in human RBCs with a few hundred copies per cell [251, 252].

The kinetics of the Piezo 1 channel can be effectively represented by a three-state model, including open, closed, and inactivated states. Collectively, these states constitute a critical mechanism for the functionality of the Piezo 1 channel [255]. Research suggests that the Piezo 1 channel is directly regulated by bilayer tension, which can be modulated by cytoskeletal proteins and connections to the environment (Fig. 1.4 C) [256–258]. Thus, Piezo 1 channels can be activated by a variety of mechanical cues related to lipid bilayer tension [259], including membrane stretching, cell indentation [244], fluid shear flow [260, 261], osmotic stress [258], substrate stiffness [262], matrix roughness [263] and environmental confinement [264]. In addition, Piezo 1 channels show rapid activation and voltage-dependent inactivation [265]. When Piezo 1 channels open, their structure allows cation-selective permeation. Thus, Piezo 1 channels are classified as non-selective cationic

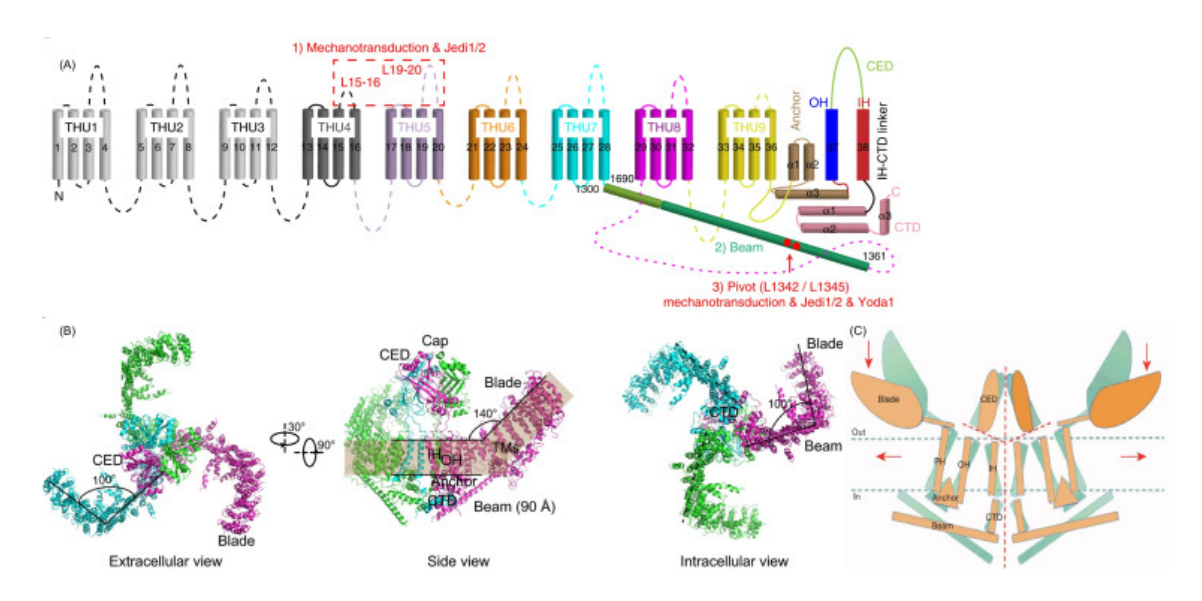


Fig. 1.4: Topological and structural illustration and mechanical activation model of Piezo 1. (A) Structural model of mPiezo 1 protein. (B) Atomic model of mPiezo 1 channel structure in extracellular view, side view and intracellular view. (C) Model of the lever-like mechanotransduction model of Piezo 1. Image adapted from Fang et al. and Wang et al [253, 254].

mechanosensitive channels [249]. Human Piezo 1 channels are permeable for monovalent ions (such as alkali ions, K^+ , Na^+ , and Cs^+), divalent ions (Ba^{2+} , Ca^{2+} , Mg^{2+} , and Mn^{2+}), and several organic cations (tetramethyl ammonium, tetraethyl ammonium), with selectivity sequence of $Ca^{2+} > K^+ > Na^+ > Mg^{2+}$ [244, 266].

In anticipation of mechanical stimuli, several relevant proteins have been reported to regulate Piezo channels, such as endoplasmic reticulum (ER) Ca²⁺ pump sarco/ER Ca²⁺ ATPase (SERCA) [267], polycystin 2 [268], Stomatin-like protein 3 [269], trefoil factor family 1 [270] and E-cadherin [271]. Through these proteins, Piezo could be involved in multiple cellular dynamics [272]. In vitro, there are also small peptides that can regulate the function of piezo channels. A comprehensive compound screening investigation revealed a small synthetic molecule known as Yoda 1 (2-[5-[[(2,6-dichlorophenyl)methyl]thio]-1,3,4thiadiazol-2-yl]-pyrazine) as the first chemical activator for both human and mouse Piezo 1 channels. Mechanistically, Yoda 1 acts as an agonist and affects the sensitivity and inactivation kinetics of the mechanically induced responses of Piezo 1 channels [273]. Through further investigation of the Yoda 1 analogue, a new modulator with a 4-benzoic acid modification was found and named as Yoda 2. It was found to have equivalent or improved reliability, efficacy and potency compared to Yoda 1 [274]. A spider venom peptide named GsMTx4, which selectively inhibits cationic mechanosensitive channels [265], is an antagonist that inhibits Piezo 1 channels [275]. The mechanism could be related to the penetration of GsMTx4 upon membrane expansion, which leads to partial relaxation of the outer monolayer of the plasma membrane and reduces the effective magnitude of the stimulus acting on the mechano-gating of the Piezo channel [265, 276].

In RBCs, Piezo 1 channels are critical for maintaining RBC volume homeostasis and deformability [277]. It has been proved to be involved in RBCs volume regulation via downstream activation of Gárdos channels [278]. Piezo 1 channels are also important for shear-induced ATP release and shear-dependent nitric oxide production in RBCs, in order to regulate microvascular tone and participate the in vascular pathophysiology [279, 280].

Recent studies have shown that Piezo 1 channels play an essential role in early erythropoiesis. Piezo 1 early expressed and activated in progenitor stages are important for both the proliferation and the differentiation kinetics of erythroid cells [281]. In addition, Piezo 1 is also involved in programmed RBC death by participating in iron metabolism [282, 283]. Mutations in genes encoding Piezo 1 channels are responsible for several inherited human diseases, including hereditary xerocytosis, myelodysplastic syndromes and congenital lymphatic dysplasia [284, 285].

Transient Receptor Potential Vanilloid Type 2 (TRPV2) Channel

The "transient receptor potential" gene was first identified in Drosophila fly in 1989 [286]. Six years later, the first molecule of the mammalian transient receptor potential (TRP) family was identified and its function was characterized [287,288]. After years of research, an understanding of the molecular structure, the biophysical properties, functional role and the pathophysiological impacts of 28 mammalian (27 human) members has been developed. Transient receptor potential (TRP) cation channels have been extensively studied and characterized as polymodal cell sensors [289–292]. Based on amino acid sequence identity and similarity, the mammalian TRP channel superfamily is categorized into six subfamilies: TRPV (vanilloid), TRPC (canonical), TRPA (ANKTM1), TRPP (polycystin), TRPM (melastatin) and TRPML (mucolipin) [292–294].

Transient receptor potential vanilloid type 2 (TRPV2), is a calcium-permeable cation channel belonging to the TRPV channel family. TRPV2 was identified in 1999 as vanilloid receptor-like protein-1 (VRL-1), a molecule structurally related to vanilloid receptor TRPV1 [295]. Similar to other members of the TRP superfamily, the TRPV2 protein has six putative transmembrane spans (S1–S6) and a cation-permeable pore region between S5 and S6 (Fig. 1.5 A) [296]. TRPV2 proteins form a homo-tetramer and function as a cation channel (Fig. 1.5 B), mediating cation currents with a permeability sequence of $Ca^{2+}>Mg^{2+}>Na^{+}\approx Cs^{+}>K^{+}$ [295]. This channel can be activated by heat (>52 °C). Thus, it has been termed a thermosensitive TRP channels or Thermo-TRP [297, 298]. Additionally, numerous studies have indicated that TRPV2 channel is regulated by mechanical stress. Muraki et al. showed that TRPV2 is involved in the elevation of intracellular calcium concentration induced by membrane stretch [299].

In addition, TRPV2 can be regulated by various ligands. Cannabinoids are a broad class of compounds derived from the plant Cannabis sativa. Qin et al. showed TRPV2 can be activated by cannabinoids [301]. (-)-trans- Δ^9 -tetrahydrocannabidol (Δ^9 -THC), cannabidol (CBD), cannabinoid (CBN), and Δ^9 -tetrahydrocannabivarin (Δ^9 -THCV) are well characterized cannabinoids. In studies using HEK293 cells expressing TRPV2, the rank order of potency is Δ^9 -THC >CBD > Δ^9 -THCV >CBN [302]. However, cannabioids are not specific to TRPV2 activation. In addition to the natural compounds, several pharmacological activators can be used for regulate TRPV2 channels, such as 2-aminoethoxydiphenyl borate [303], diphenylborinic anhydride [304], probenecid [305], lysophosphatidylcholine [306]. However, most of these activators lack specificity for TRPV2 channel and may even be species dependent [304, 307]. In contrast to the aforementioned activators, a few compounds can inhibit TRPV2 channel opening, including ruthenium red [303, 308], N-(2-Furanylmethyl)-3-[[4-(methylpropylamino)-6-(trifluoromethyl)-2-pyrimidinyl|thio|propenamide (SET2) [246],

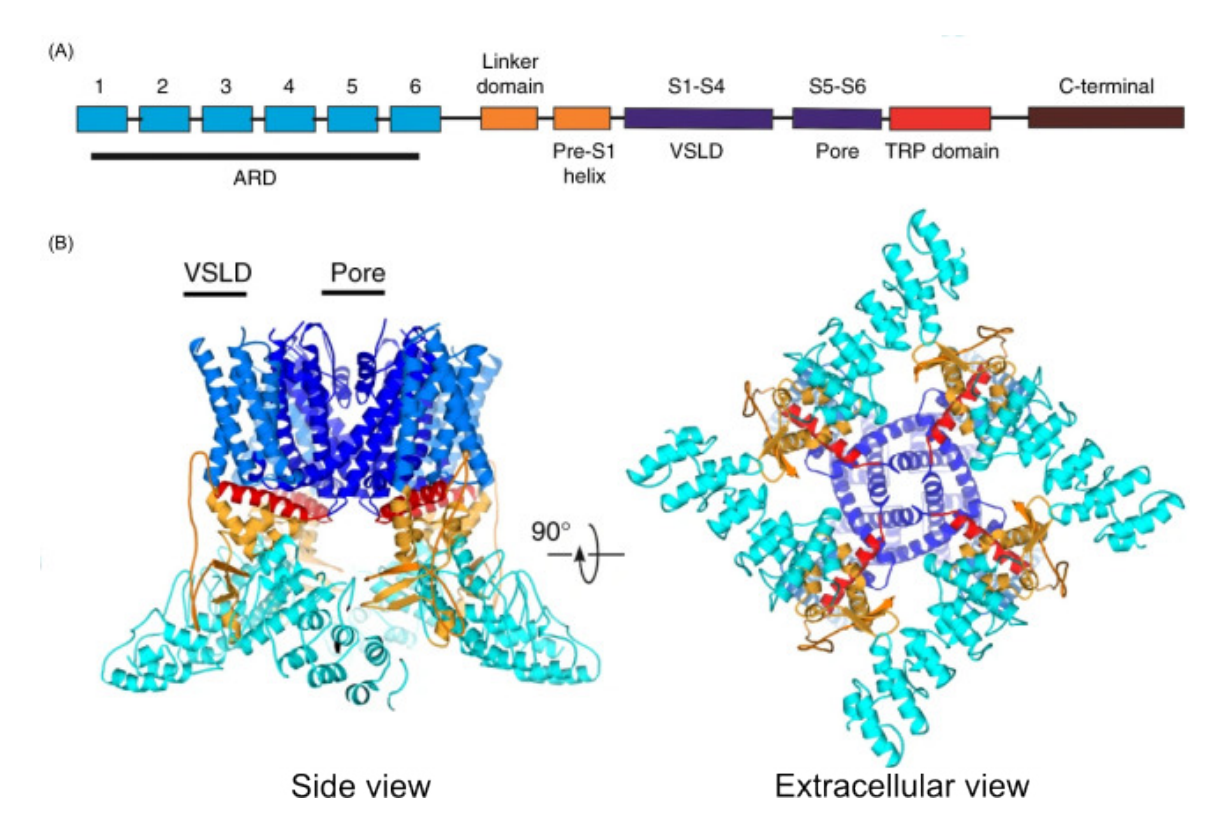


Fig. 1.5: Topological and structural representation of TRPV2. (A) Linear model of the TRPV2 protein with the domain architecture delineated by different colors. (B) Atomic model of the TRPV2 channel structure in different views, with domains colored as in (A). Image adapted from Zubcevic et al [300].

tranilast, lumin [306], linoleoyl ethanolamide and arachidonoyl ethanolamide [309] and 1-(β-[3-(4-methoxyphenyl)propoxy]-4-methoxyphenethyl)-1H-imidazole hydrochloride (SKF96365) [304]. Unfortunately, the majority of these inhibitors are not specific for TRPV2.

In 2021, Belkacemi et al. reported that TRPV2 channels are present in RBCs. It shows that TRPV2 channels are involved in the regulation of osmotic fragility in RBCs [310]. It is suggested that activated TRPV2 mediated Ca²⁺ entry activates the Gárdos channels followed by K⁺ loss and subsequent water loss, similar to Piezo 1 channel activation. If this is the case, the RBCs should be dehydrated/shrunk after TRPV2 activation [311]. However, Belkacemi et al. found cell overhydration/swelling instead, which is similar as previous investigation in 1979 (-detailed explanation seen section 4.1) [310,312]. The behavior of TRPV2 channels in RBCs is not yet fully understood. In addition, TRPV2 channel activators, CBD and THC, are used for medical purposes [313,314]. Altering the hydration status of RBCs may lead to further vascular complications, which also requires a deeper understanding of the function of TRPV2 channels in RBCs.

Gárdos Channel

In 1958, the Hungarian physiologist Gyorgy Gárdos reported Ca²⁺-dependent K⁺ loss from RBCs and the pathway was named the "Gárdos pathway" [122]. The "Gárdos pathway" is now known to be mediated by an intermediate conductance Ca²⁺-activated potassium

channel and named the Gárdos channel. This channel also known as KCNN4, IKCa, SK4, K_{Ca}3.1 [315,316]. The KCNN4 gene encoding was discovered and mapped in 1998 and the channel encoded by KCNN4 was identified as Gárdos channel in 2003 [123, 124, 317]. Later, cloning and functional expression of experiments showed that the channel is a tetrameric protein. Each subunit has six transmembrane segments, S1–S6, with a pore motif between segment S5 and S6 (Fig. 1.6 A) [316, 318, 319]. Functional studies show that the Gárdos channel displays a small unitary conductance and gated only influx of Ca²⁺. When the Gárdos channel activated, it could cause the K⁺-efflux and concomitant water efflux leads to cell volume reduction. Although channel activation is linked to Ca²⁺ concentration, the Gárdos channel itself does not directly bind Ca^{2+} . The Gárdos channel gains Ca^{2+} sensitivity through calmodulin (CAM), which remains constitutively bound (via its Clobe) to a domain in the membrane-proximal region of the intracellular C-terminus of the channel, thus acting as the channel's Ca^{2+} sensor (Fig. 1.6 B,C). Binding of Ca^{2+} to CAM leads to conformational changes in CAM, resulting in opening of the channel [320]. Weak activation was observed with Pb²⁺, Cd²⁺, Ba²⁺, and Sr²⁺, whereas Mg²⁺ acted as an antagonist. Subsequent studies revealed that Ca²⁺ enhances K⁺ permeability by increasing the frequency of channel openings rather than their open time [321].

Several studies have shown that gardos Gárdos channel activity is regulated by multiple cell signalling pathways. cAMP-activated protein kinase A (PKA) could modulate CAM binding affinity by regulating Gárdos channel phosphorylation [322]. Intracellular ATP could also positively modulate Gárdos channel. The region 355-368 at the C-terminal and multibasic 15RKR17 motif in the N-terminal region are both involved. Later, the ATP-binding region in the C terminal was found to be able to bind activated nucleoside diphosphate kinase B to increase the activity of the channel [323]. Interestingly, binding to phosphoinositol-3-phosphate, a membrane phospholipid continuously produced by the activity of phosphoinositide 3-kinases, is important for Gárdos channel activation. This activation could be downregulated by myotubularin-related protein 6 [324]. 5'AMP-activated protein kinase (AMPK) could inhibit Gárdos channel activity via AMPK activation. The AMPKγ subunit can interact with a leucine zipper domain in the C-terminal region of the Gárdos channel but how this interaction influences the Gárdos channel activation is not clear yet [325]. Dephosphorylation of H358 results in Gárdos channel inhibition, which is operated by the binding of histidine phosphatase [326].

In addition to the internal modulator of Gárdos channel, there are several pharmacology regulators of the Gárods channel available. For Gárdos channel activators, the 1-ethylbenzimidazolinone (1-EBIO) activates the channel, while the related molecule derivative of 1-EBIO exhibits ten-fold higher potency [327, 328]. Two more potent activators are the oxime NS309 and the benzothiazole SKA-31, with EC₅₀ approximately 250 nM [329, 330]. Nitrendipine may act as blocker by direct blockage of K⁺ flux through the Gárdos channel [331]. The peptidic toxins charybdotoxin (ChTx) and maurotoxin are high-affinity inhibitors of Gárdos channel [332–335]. Halothane has also been shown to inhibit the Gárdos channel in intact RBCs, but the mechanism is still poorly understood yet [336]. Small synthetic molecules have also been developed, mostly based on the clotrimazole template [337], the classical Gárdos blocker. The most widely used Tram-34 (1-((2-chlorophenyl)diphenylmethyl)-1H-pyrazole) inhibits Gárdos with an IC₅₀ approximately 20 nM, and displays high selectivity over the other K_{Ca} channels [338].

According to the previous studies, the number of Gárdos channels in RBCs is believed to be very low (on average, 2.6 channels per cell) [335, 339]. Even with low copy number, the Gárdos channel is still able to play an important role in regulation of cell death and volume homeostasis in RBCs [340]. Mutation of Gárdos channel could lead to diseases, such as Gárdos Channelopathy [341–344]

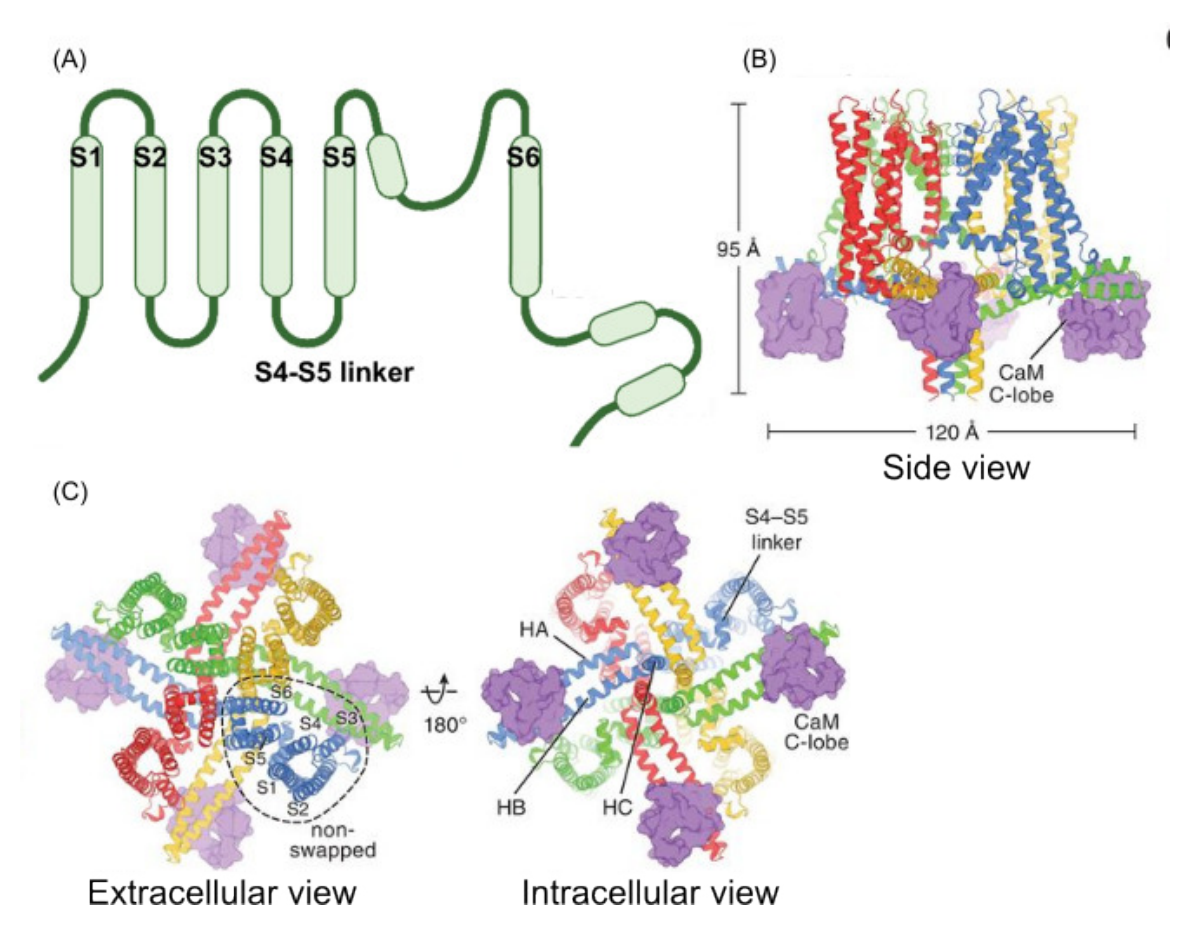


Fig. 1.6: Topological and structural representation of Gárdos channel. (A) Schematic representation of the Gárdos channel subunit. (B) Cryo-EM structure of the Ca²⁺-free Gárdos channel complex in side view. (C) Cryo-EM structure of the Ca²⁺-free Gárdos channel complex in extracellular and intracellular views. Images adapted from Nam et al. and Lee and Mackinnon [345, 346].

Ca_v2.1 Channel

The study of the voltage-gated calcium channel (VGCC) family started in 1953 when the first member was identified [347]. After 20 years, Hagiwara provided evidence that there was more than one type of calcium channel [348]. About ten years later, studies classified two current components in mammalian sensory neurons according to their biophysical properties and described these components as low- and high-voltage-activated channels. The studies also showed that the underlying individual channels had different conductance [349, 350]. Currently, six classes of VGCCs have been identified on the basis of membrane voltage activation, sensitivity to pharmacological antagonists and rate of inactivation, including transient (T)-type, long-lasting (L)-type, non-L and neuronal (N)-type, Purkinje (P)-type, Q-type and residual (R)-type channels [351–353]. Molecule

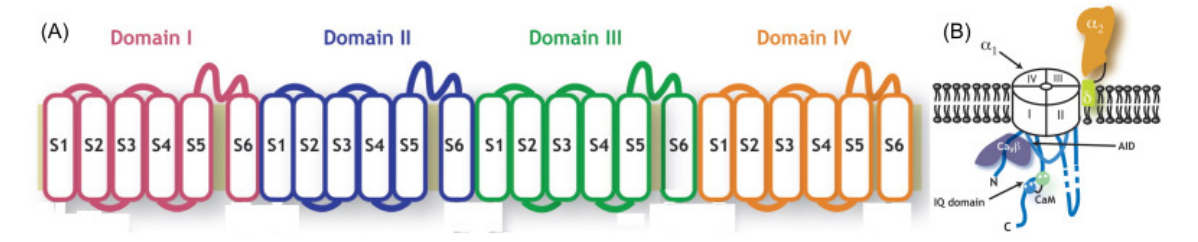


Fig. 1.7: Structure of a voltage-gated calcium channel. (A) Topology of the pore-forming $Ca_{\rm v}\alpha 1$ subunit. The $Ca_{\rm v}\alpha 1$ intracellular loops are drawn to scale according to the human $Ca_{\rm v}1.2$ sequence. (B) Cartoon representation of a $Ca_{\rm v}2$ channel. The four homologous transmembrane domains of $Ca_{\rm v}\alpha 1$ are indicated. $Ca_{\rm v}\beta$ is shown in dark blue. The membrane-associated $Ca_{\rm v}\alpha 2\delta$ subunit is shown in orange and green. Image adapted from Findeisen and Minor [361].

studies have identified five channel components in this family, which were termed $\alpha 1$, $\alpha 2$, β , δ and γ [354, 355]. Based on the differences in α 1 subunits, these channels are divided into three structurally and functionally related families (Ca_v1, Ca_v2, and Ca_v3) [356,357]. According to structural studies, VGCCs have a fourfold symmetrical structure (Fig. 1.7 B). The pore-forming subunit $\alpha 1$ in each unit consists of six transmembrane α helices (S1–S6) (Fig. 1.7 A,B) and a membrane-associated loop located between S5 and S6. The S4 segments within each homologous domain function as voltage sensors for activation and undergo outward movement and rotation in response to the electric field, thus initiating a conformational shift that leads to pore opening. The S5 and S6 segments and the membrane-associated pore loop between them form the pore lining of the voltage-gated ion channels. The narrow external end of the pore is lined by the pore loop, which contains a pair of glutamate residues in each domain that are required for Ca²⁺ selectivity [358–360]. Ca_v2.1, a member of VGCC, is also called P/Q type voltage-gated calcium channel. It is one of the high-voltage-gated calcium channels. The channel is encoded by the CACNA1A gene. It has $\alpha 1A$ to form the ion-conducting pore, with β and $\alpha 2\delta$ as accessory subunits to modulate channel kinetics and expression level [362]. Studies have shown that Ca_v2.1 can conduct a P-type Ca^{2+} current and a Q-type Ca^{2+} current [353, 363]. The current could be inactivated by a voltage- or Ca²⁺- mediated mechanism, or by a combination of the two [364]. In addition to changes in membrane potential and Ca²⁺, other signaling molecules could also modulate Ca_v2.1 activation. There is evidence that P/Q-type currents may be regulated by multiple G protein-coupled pathways [365]. The soluble N-ethylmaleimidesensitive-factor attachment protein receptor (SNARE) protein could also regulate the Ca_v2.1 channel. Coexpression of the plasma membrane SNARE proteins syntaxin or SNAP-25 with Ca_v2.1 channel reduces the level of channel expression and inhibits Ca²⁺ channel activity by shifting the voltage dependence of steady-state inactivation during long depolarizing prepulses towards more negative membrane potentials [366, 367]. In addition, CaM or Ca²⁺-related binding protein has been proven to regulate Ca_v2.1 by protein interaction [368–371]. Pharmaceutical regulators of Ca_v2.1 are also available, including peptide toxins and small molecular weight blockers [362]. Most of compounds are non-selective expect two peptide toxins. ω -agatoxin IVA and ω -agatoxin IVB, venoms from the American funnel-web spider Agelenopsis aperta, share the same specificity and affinity with different kinetics [372–376].

Most studies of $Ca_v 2.1$ channel function have been performed in other cell types, particularly neurons and cardiac cells [377]. In 2002, Andrews et al confirmed the presence of a ω -agatoxin-IVA–sensitive, $Ca_v 2.1$ -like calcium channel exists in the mature erythrocyte RBC membrane [128]. The hypothesis that the $Ca_v 2.1$ channel participates in multiple Ca^{2+} -triggered cellular functions such as programed cell death, deformation, and aging has often been mentioned, but further investigation is needed [378–381].

Plasma-membrane Ca²⁺ ATPase

The Plasma-membrane Ca²⁺ ATPase (PMCA) belongs to the family of P-type ATPases. PMCA is encoded by four different genes, PMCA1-4, giving rise to four isoforms of the pump, PMCA1-4 [382–384]. It was discovered in RBCs in 1966 by Schatzmann [385]. Later with successful purification and cloning, the primary structure of PMCA was reported [386–388]. Based on the structure of sarcoendoplasmic reticulum calcium ATPase (SERCA1a), the first structure-determined P-type ATPase, the predicted structure of PMCA was made. PMCA consists of 10 transmembrane domains, two large intracellular loops, and of amino- and carboxy-terminal cytoplasmic tails (Fig. 1.8 A,B) [389]. The first cytosolic loop between transmembrane domains two and three is considered as the "transducer domain". It contains one of the two sites that mediate the activation by acidic phospholipids and one of the two sites for the autoinhibitory interaction with the calmodulin binding domain (Fig. 1.8 A) [390, 391]. The cytosolic loop connecting transmembrane domains four and five contains the ATP-binding site. The carboxyterminal tail contains the main regulatory sites for the activity of the pump including: consensus sites for protein kinases A (PKA), and C (PKC) and high affinity allosteric Ca²⁺ binding sites (Fig. 1.8 A). Thus, PKA, PKC, Ca²⁺ and ATP could modulate the function of PMCA [390, 392, 393]. In addition, calmodulin could bind both the carboxy-terminal tail and the cytosolic loop to regulate the PMCA activation [394, 395]. Some evidence also showed that the PMCA dimerization mediated by the calmodulin-binding domain could activate the pump [396, 397].

PMCA has a high affinity but low capacity for Ca^{2+} transport [400]. The stoichiometry of PMCA is one Ca^{2+} transported for each ATP hydrolyzed. These pumps probably do not carry out bulk movements of Ca^{2+} but are most effective in maintaining very

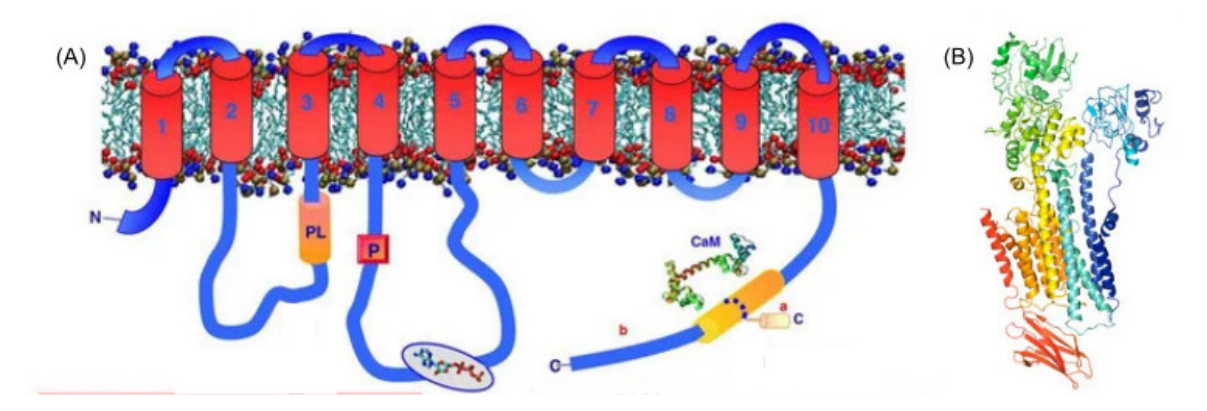
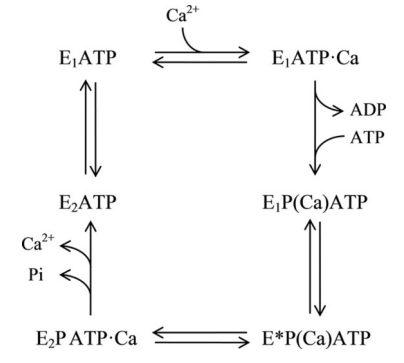


Fig. 1.8: The structure of PMCA. (A) Schematic topological model of PMCA. (B) Atomic model of the PMCA structure. Images taken from Krebs and Boczek et al [398, 399].

low concentrations of cytosolic Ca²⁺ in resting cells [400–403]. Acidic phospholipids can increase the Ca²⁺ affinity of the pump [404]. The current kinetic model for the PMCA proposes that the enzyme exists in three major conformations, E1, E* and E2 (Fig. 1.9) [405, 406]. E1 has a high affinity for Ca²⁺ and is readily binds ATP to form E1ATP [407–409]. When E1ATP binds to intracellular Ca²⁺, it could be phosphorylated by ATP with formation of the intermediate E1P(Ca) [406,408]. The E1P(Ca) could again bind to ATP and change to the conformation E*P(Ca)ATP, followed by a conformational change to E2P(Ca)ATP [406]. The E2 conformation has low Ca²⁺ affinity and can be dephosphorylated [406, 410]. The E2P(Ca)ATP would disassociated with Ca²⁺ and Pi and transition to E2ATP [405, 406, 411]. In its resting state, PMCA is predominantly in equilibrium as two intermediates, E1ATP and E2ATP [406]. Upon the signal of Ca²⁺ or calmodulin-Ca²⁺ signal, cation transport is initiated by ATP hydrolysis [409,412]. Under physiological conditions, characterized by a sufficiently high concentration of ATP and a large ATP/ADP ratio, the modulatory site becomes saturated with ATP [406, 407, 412]. This saturation allows the E2 state to bypass the E1Ca conformation and transition directly to the E1ATPCa (Fig. 1.9) [405–407, 413]

Fig. 1.9: Scheme of the PMCA functional reaction cycle. Image taken from Mangialavori et al [406].



There is no pharmacological inhibitor with high selectivity for the PMCA. La³⁺ is an inhibitor of PMCA activity [414]. Eosin may also act as a semi-selective PMCA blocker [415]. Recently, a bis-phenolic compound derived from the Australian native plant Grevillea striata, was found to be able to inhibit the PMCA [416]. Studies also showed vanadate can inhibit PMCA function, but it also shows a potent inhibition of many other phosphoenzymes [417–419]

In addition to their basic function as Ca²⁺ housekeeping enzymes, PMCAs may also work as a signaling molecule itself [390]. Abnormal PMCA could cause excessive levels of intracellular Ca²⁺ in RBCs, which could lead to cell death and PMCA defects have been described in different diseases, such as chronic kidney disease, hypertension [420–423].

1.2.2.4 Membrane Potential of RBCs

Cell membrane acts functional as a biophysical barrier and the ionic composition of the cytosol and extracellular fluid is very different in cells. This could lead to charge differences between the two sides of the membrane. Previous investigations showed that the difference is caused by three factors: (1) the intrinsic selective permeability of the membrane to ions and charged molecules present in both the cytoplasm and the extracellular space; (2) charged molecules incorporated into the plasma membrane (found in both the inner and

outer leaflets of the bilayer); and (3) osmotic equilibrium [210, 424–426]. The difference in electrical charge between two sites separated by membrane could result in voltage gradients across the membrane and generate ionic currents via ion channels. The term is used to describe the differences in electrical potential across the membrane is the transmembrane potential (ψ) [427]. There are two terms used to describe transmembrane potential changing. One is hyperpolarization, and the other is depolarization. Hyperpolarization is used to describe the transmembrane potential of a cell becoming more negative. It is often caused by efflux of K⁺ or influx of Cl⁻. Conversely, depolarization means that the transmembrane potential becomes less negative or even positive. Influx of cations, most of the time Na⁺ could lead to depolarization. Activation and inhibition of ion channels and pumps could generate local change in the resting membrane potential, resulting in an electrical signal in cells [196, 428–431].

The transmembrane potential has two main functions in cell behavior and signaling. First, it could provide the energy to drive a variety of transmembrane transport. Second, it could transmit signals between different regions [429, 432, 433]. Molecule transport and signaling regulated by ψ may be involved in a variety of cellular activities. The plasma membrane potential variation ($\Delta\psi$) has been linked to multiple cellular processes in different cell types, including RBCs [196]. The standard expression for membrane potential (Vm) is given by the Goldman-Hodgkin-Katz equation (Eq. 1.1):

$$Vm = \frac{RT}{F} ln(\frac{P_{Na^{+}}[Na^{+}]_{out} + P_{K^{+}}[K^{+}]_{out} + P_{Ca^{2+}}[Ca^{2+}]_{out} + P_{Cl^{-}}[Cl^{-}]_{in}}{P_{Na^{+}}[Na^{+}]_{in} + P_{K^{+}}[K^{+}]_{in} + P_{Ca^{2+}}[Ca^{2+}]_{in} + P_{Cl^{-}}[Cl^{-}]_{out}})$$
(1.1)

where $[X]_{out}$ and $[X]_{in}$ are the extracellular and intracellular concentrations of the relevant ions. P_X are the permeability coefficients of the relevant ions. P_X and P_X are the gas and Faraday constants, and P_X is the temperature [434]. In normal condition, representative ions in cells contributed to membrane potential are P_X in P_X and P_X and P_X is much higher than other ions, the earliest studies of P_X were based on calculating the equilibrium P_X by the chloride concentration ratio in ideal conditions (Eq. 1.2):

$$\Delta \psi = \frac{RT}{zF} \ln\left(\frac{([Cl^-])_{in}}{([Cl^-])_{out}}\right)$$
 (1.2)

In this equation, $\Delta \psi$ is the potential (V), R is the gas constant (J mol⁻¹ K⁻¹), T is the absolute temperature (°K), z is the ionic valence, F is the Faraday constant (C mol⁻¹) and [Cl⁻]_{out} and [Cl⁻]_{in} are the extracellular and intracellular Cl⁻ concentrations. This equation requires at least two primary conditions to be correct: (1) a passive bidirectional chloride flux and (2) the activity coefficients for chloride ions being equal in the two phases [78,435,436]. In addition, the unequilibrium of any other ions through transport or coupling with other compounds would introduce an error to the calculation [196]. Tosteson demonstrated the high membrane permeability for Cl⁻ in RBCs and it fulfilled the primary condition (1). However, because of anionic hemoglobin in RBCs, the coefficient for water and solutes, including Cl⁻ has different values on either side of the membrane due to the Donnan effect [437–439]. Thus, estimation of $\Delta \psi$ is impossible by solely from Cl⁻

concentration as the calculation mentioned above (Eq. 1.2). The upgraded method was used to determine $\Delta \psi$ by measuring the activity distribution of the dominant permeable ions in a steady cell. In RBCs, the dominant ion is Cl⁻ [78]. With measured distribution of the activity of Cl⁻ at equilibrium, the $\Delta \psi$ can be calculated with equation following (Eq. 1.3) [196]:

$$\Delta \psi = \frac{RT}{zF} \ln\left(\frac{(a_{Cl^-})_{in}}{(a_{Cl^-})_{out}}\right) \tag{1.3}$$

where a_{Cl}^- is Cl^- activity in RBCs, which is based on Cl^- activity coeffeicent (γ_{Cl}^-) and Cl^- concentration (C_{Cl}^-) as following (Eq. 1.4) [440]:

$$a_{Cl} = \gamma_{Cl} \times C_{Cl} \tag{1.4}$$

The Cl⁻ activity is easily influenced by other factors, such as the exact volume in which these milliequivalents are found, and the extracellular water that forms part of the pellet, among others. These factors are usually measured or assumed, introducing errors into final calculation of $\Delta\psi$ [196,441]. In addition, to determine the accurate activity of Cl⁻, nuclear magnetic resonance or fluorinated probes or other advanced but complicated methods need to be applied. These factors makes determining membrane potential by Cl⁻ is difficult. In 1978, Macey et al. proposed to use the H⁺ distribution instead of Cl⁻ with H⁺ ionophore (CCCP) help and developed the equation as follows [442]:

$$\Delta \psi = \frac{RT}{F} \ln \frac{a_{H_{\text{out}}}^{+}}{a_{H_{\text{in}}^{+}}}$$
 (1.5)

$$\Delta \psi = 2.303 \frac{RT}{F} (pH_{in} - pH_{out}) \tag{1.6}$$

$$Vm = 61.5mV \times (pH_{in} - pH_{out})$$
(1.7)

In this method, the H⁺ ionophore bring the H⁺ activity coefficient to ideal condition [442]. According to the theory mentioned above, the microeletrode method can be used to determine $\Delta \psi$ in RBCs in a direct and apparently accurate manner in single cells by measuring and calculating different ion distributions [438, 443]. With the development of probes, voltage-sensitive dyes or potentiometric probes are available for optical measurement of $\Delta \psi$ [444–447]. Based on the response speed, the probe can used for detect possible transient changes in microsecond or average membrane potential with additional calibration by an independent measurement of $\Delta \psi$ [448–451]. The measurements performed with different methods showed that RBCs, as non-excitable cells, maintain a relatively constant resting membrane potential around $-10 \, \text{mV}$ [95, 452].

1.2.2.5 RBC Morphology

Overview of RBC Morphology

Because mature RBCs lack nuclei and organelles, their size, shape, volume, structure or color are easier to be changed with internal or external factors [453,454]. As mentioned in previous section 1.2.1, healthy mature RBCs in stasis have biconcave disc shape. Under physiological and experimental conditions with changes in external factors, such as changes in osmolarity amphipaths, extracellular ionic strength or pH, the transformation of RBCs has been described as the stomatocyte - discocyte - echinocyte (SDE) sequence [455–457]. In diseases, additional morphological abnormalities of RBCs appear, such as sickle cells in sickle cell disease, keratocytes in thalassemia, spherocytes in hereditary spherocytosis and acanthocytes in neuro-acanthocytosis disease [137,457–459]. Thus, the morphology of RBCs is used to monitor the functioning of many organs to assess the general health condition and the physiological progress of their body. The morphology can be used as laboratory hematologic diagnosis parameter to understand clinical diseases and pathological processes [453,458,460,461]. The investigation of RBC morphology for the clinical diagnosis relies on the visual examination of blood smears under microscope [457]. Some types of normal and abnormal RBCs are shown in Figure 1.10.

Stomatocyte - discocyte - echinocyte (SDE) Sequence

Overview of SDE Sequence

Many physical and chemical conditions can transform normal biconcave RBC into stomatocytes or echinocytes [463–465]. These shape changes are reversible to the stage where sphero-stomatocyte and sphero-echinocyte become smooth spheres when small interior buds and vesicles are pinched off from the RBC surface [456, 457, 466]. These reversible RBC shape changes from biconcave shape to-and-from stomatocyte and echinocyte shapes are widely known as SDE shape transformations [456, 457, 467]. SDE shape transformations have a universal nature for the resultant shape and do not depend on the engaged shape-transforming agent [456, 457, 463]. The SDE transformation can be explained through the bilayer-couple hypothesis, and any change in relaxed area-difference between bilayer-leaflets is the necessary and sufficient factor for shape changes [456, 457, 468].

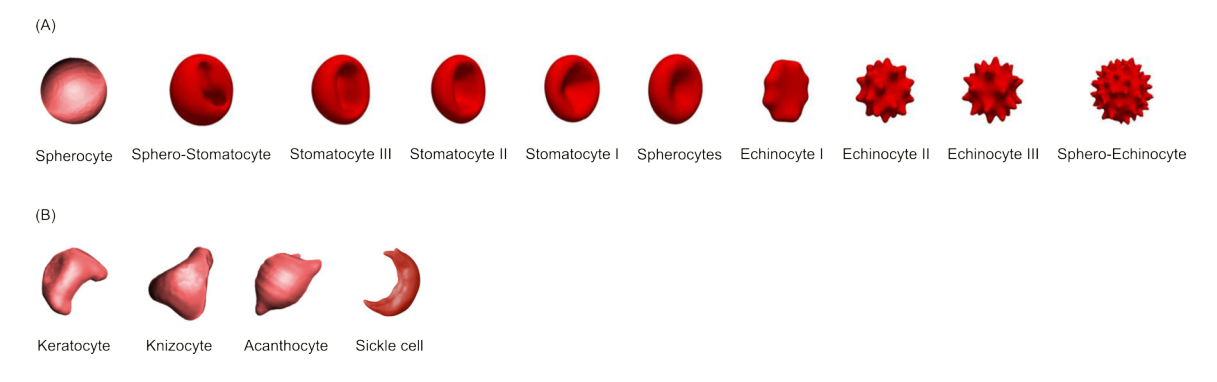


Fig. 1.10: Example 3D images of RBCs morphology. (A) Example of SDE shapes. (B) Example of abnormal RBCs shapes. Images adapted from Simionato et al. and Karandeniya et al [457, 462].

Echinocytes

Echinocytes is a type of RBCs that has a membrane charactered with many small, evenly spaced thorny projections (Fig. 1.10 A) [123]. The cause of echinocytes usually is a change in the extracellular environment. Echinocytes shapes can be further categorized into subclasses I, II, III and IV considering different stages of concavity and crenation. Echinocyte I is a disc with several undulations around its rim. Echinocyte II is a flattened elliptical body with rounded spicules distributed more or less uniformly over its surface. Echinocyte III is an ovoid or spherical body with sharper and more numerous (30–50) spicules distributed evenly over its surface. Echinocyte IV (sphero-echinocyte) is a sphere with small sharp projections still attached to its surface (Fig. 1.10 A) [456, 462, 465, 469]. In vitro, echinocytes can be produced by anionic amphipaths, high salt, high pH, ATP depletion, cholesterol enrichment [463,464]. They could also be found after incubation in high calcium medium, or medium with reduced albumin, exposure to glass as well as in prolonged storage blood [470]. In addition to these factors, diseases can also lead to echinocyte formation, such as burns, uremia, malnutrition, pyruvate kinase deficiency, hypomagnesemia, hypophosphatemia, hemodialysis [471], parenteral fish oil [472], end-stage renal disease [470, 473, 474], liver diseases [475], vitamin E deficiency [476].

Stomatocyte

Stomatocytes are derived from genetic defects in membrane proteins that result in "leakiness" of cations and fluid [477,478]. The cells appear cup-shaped with a central pallor in the form of a slit, sometimes referred to as a "fish mouth" (Fig. 1.10 A) [479]. In certain physiological and experimental conditions, such as cationic amphipaths, non-penetrating anions low salt, low pH and cholesterol depletion can transform normal biconcave RBC into stomatocytes [463,464,480,481], which belongs to SDE sequence. Similar as echinocytes, stomatocyte shapes can also be categorized into four subclasses. Stomatocyte I is a cup shape with a deeper invagination, still at least approximately circular. Stomatocyte III is a cup shape with a deep invagination, often elongated into a mouth-like slit and sometimes accompanied by other pit-like invaginations. Stomatocyte IV (sphero-stomatocyte) is a spherical shape with small interior buds still attached to the membrane (Fig. 1.10 A) [441,456,465].

However, the term was initially coined to characterize the morphology of certain cells observed in a rare type of hemolytic anemia known as hereditary stomatocytosis [482]. The hereditary variant of stomatocytosis typically follows an autosomal dominant pattern of inheritance. Additionally, stomatocytes are often found in individuals with south-east Asian ovalocytosis. Notably, they have been reported to be especially prevalent in the blood films of Australians of Mediterranean descent [483,484]. The basic defect in stomatocytosis is believed to be a dysregulation of fluid and cation movement into the cells. *Piezo 1* encodes a transmembrane protein that is thought to establish "mechanosensitive currents" across the RBCs membrane [341,485]. Piezo 1 mediates Ca²⁺ movement and acts as a primary regulator of volume [477]. Variations in the red blood cells presentation are explained by differences in prevalence of *Piezo 1* gene mutations [478]. Stomatocytes were also identified in acquired conditions, where they occasionally become prominent. They have been observed in liver disease, alcoholism [486], myelodysplastic syndromes, obstructive lung disease [480]

Pathological RBCs

Sickle Cell

Sickle cell disease (SCD) is an autosomal recessive genetic disorder [487]. SCD is a term for all mutations in the β -globin gene that results in the same clinical syndrome of abnormal sickling of red blood cells, altered blood rheology, and subsequent tissue damage [488, 489]. Mutation of the β -globin gene results in the replacement of a hydrophilic glutamic acid (Glu) residue with a hydrophobic valine (Val) residue at the sixth position in the β -globin chain, resulting in a mutant hemoglobin tetramer HbS [490, 491]. Under certain conditions, such as low oxygen tension or dehydration, HbS crystallises to form long, rigid crystals within the red blood cells [488, 490]. Crystallization of HbS results in the deformation of red blood cells into a sickle shape (Fig. 1.10 B). Sickled red blood cells are rigid, less deformable, and prone to hemolysis. These cells cannot flow smoothly through blood vessels, that might lead to vaso-occlusion and tissue ischemia [488, 492].

Thalassemia

Thalassemia defines a complex of various hereditary disorders of haemoglobin with impaired synthesis of the hemoglobin protein components [493]. These disorders have two features: a mutation interferes with amount of hemoglobin produced (thalassemias) and the production of a variant protein due to a structural change in the hemoglobin molecule (hemoglobinopathies) [494]. Depending on which globin chain of the hemoglobin molecule is inadequately produced, thalassemias can be divided into various categories, including α -, β -, γ -, σ -, $\sigma\beta$ -, and ε $\gamma\sigma\beta$ -thalassaemias [493–495]. The reduced production of one of the globin chains could lead to an accumulation of the normally produced chains due to the failure to find the equivalent amount heterologous partner to assemble into the normal heterotetramer [496–498]. The excess unpaired and insoluble α-globin chains will cause apoptosis of red cell precursors, resulting in ineffective erythropoiesis. If the excess unpaired and insoluble globin chains are non-α-globin chains, the irregular tetramers are formed. These tetramers have high oxygen affinity to be poor oxygen carriers [494, 497, 499, 500]. Both insoluble α-globin chains and irregular tetramers can precipitate to the RBCs membrane surface causing oxidative damage, altered deformability and hemolysis. The membrane defect makes these RBCs easily trapped by the spleen and destroyed by macrophages. In addition, some of the immature RBCs can enter the circulation. Those immature RBCs are fragile and prone to hemolysis due to their membrane defect. Ineffective erythropoiesis, removal of abnormal RBCs by the spleen and hemolysis all contribute to an anemia of variable severity [494, 495]. Thalassemia patients have many abnormal RBC shapes in blood smear, including stomatocytes (Fig. 1.10 A), keratocytes (Fig. 1.10 B), and schizocytes (fragments of red blood cells) [501, 502].

1.3 Fluorescence 25

1.3 Fluorescence

1.3.1 Overview of Fluorescence

The study of light began around eighth century B.C [503]. However, the understanding of light is still considered the least certain [503]. Luminescence is one subfield of light research. The term "luminescence" originates from the Latin root "lumen," meaning light. It was first introduced as "luminescenz" by the German physicist and science historian Eilhard Wiedemann in 1888 for all phenomena of light. Unlike incandescence, luminescence does not depend on temperature rise [504]. With further studies on luminescence, the modern definition has been changed to "a spontaneous emission of radiation from an electronically excited (or vibrationally excited) species that is not in thermal equilibrium with its environment" [504, 505]. The different types of luminescence are classified according to the mode of excitation. Photoluminescence, for instance, results from direct photoexcitation of the emitting species. Well-known forms of photoluminescence include fluorescence, phosphorescence, and delayed photoluminescence [504, 505]. G. G. Stokes was first to introduced the term "fluorescence" in the mid-19th century [506, 507]. Initially, the distinction between fluorescence and phosphorescence based on the duration of emission after excitation ceased. Fluorescence was characterized by the cessation of emission simultaneously with the end of excitation, whereas phosphorescence showed persistent emission after excitation [504]. But such a criterion proved insufficient with the discovery of long-lived fluorescence (e.g., divalent europium salts) and short-lived phosphorescence (e.g., violet luminescence of zinc sulfide) [508, 509]. In 1929, Francis Perrin proposed an intermediate stable or metastable state between the absorption and the emission states. The excited electron could transit to a third state and change spin multiplicity value. This process requires additional energy from the environment to generate emission light. This discovery led to a more precise distinction between fluorescence and phosphorescence [510]. In excited singlet states, the electron in the excited orbital is paired with the second electron (with opposite spin) in the ground-state orbital. Consequently, the return to the ground state occurs rapidly by emission of a photon, resulting in fluorescence. Phosphorescence, on the other hand, involves the emission of light from triplet excited states, where the electron in the excited orbital has the same spin orientation as the ground-state electron. Transitions to the ground state are forbidden, leading to slow emission rates [510, 511].

The transition between absorption and emission of light is illustrated in a diagram (Fig. 1.11), named after Alexander Jablonski, the father of fluorescence spectroscopy [512–514]. The diagram (Fig. 1.11) depicts the singlet ground, first, and second electronic states as S_0 , S_1 , and S_2 , respectively. Each electronic energy level can accommodate fluorophores in various vibrational energy levels denoted by 0, 1, 2, etc. The transitions between these states are shown as vertical lines to illustrate the instantaneous nature of light absorption. The transition time is too short for any significant displacement of nuclei to occur, which is the Franck-Condon principle [512,514–517]. A fluorophore is usually excited to a higher vibrational level of either S_1 or S_2 . This is followed by a rapid relaxation to the lowest vibrational level of S_1 , known as internal conversion, which is usually complete before emission. Thus, fluorescence emission generally results from a thermally equilibrated excited state - the lowest energy vibrational state of S_1 [518].

26 1 Introduction

Return to the ground state typically occurs to a higher excited vibrational ground state level, which then quickly reaches thermal equilibrium. Electronic excitation does not significantly alter the nuclear geometry. Additionally, the spacing of the vibrational energy levels of the excited states is similar to that of the ground state. As a result, the vibrational structures seen in the absorption and the emission spectra are similar [518].

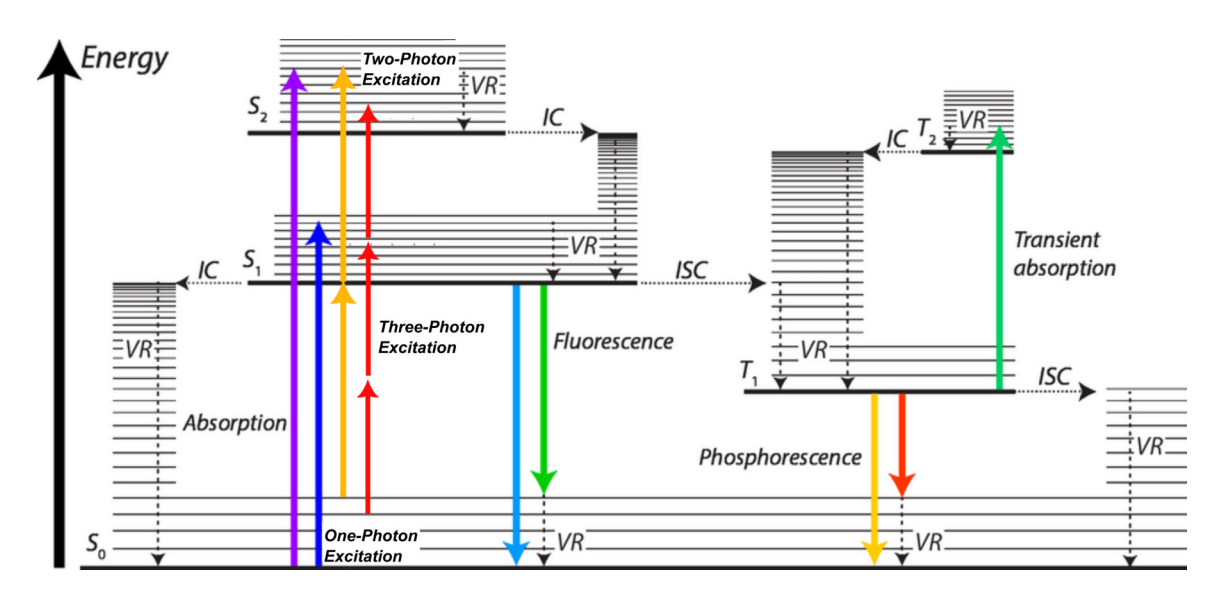


Fig. 1.11: Jablonski diagram. The vertical arrows represent the energy. The colors indicates different energy level. More purple means higher energy and more red means less energy. The thick horizontal lines represent the electronic singlet (S_n) and triplet (T_n) levels while the thin horizontal lines represent vibrational levels.VR means vibrational relaxation. IC means internal conversion. ISC meand inter system crossing. Images adapted from Dzebo [519].

During excitation, energy can be supplied by one photon (one-photon excitation, 1PE) or by multiple photons (multiphoton excitation, MPE). In 1PE, irrespective of the excitation wavelength, the fluorophore has reached the excited state by absorption of a single photon. MPE uses longer-wavelength excitation to avoid the much stronger single-photon absorption of the fluorophore, so that multiple photons are required to reach the same energy level. Both 1PE and MPE can be illustrated using Jablonski diagram (Fig. 1.11). Unlike 1PE, MPE involves the simultaneous absorption of multiple photons to eliminate intermediate states. Moreover, MPE requires high illumination intensities because multiple photons must interact with the fluorophore simultaneously, making it a nonlinear process. The magnitude of the MPE is proportional to the intensity raised to the second or third power for 2-photon excitation (2PE) and 3-photon excitation (3PE) respectively. Thus far, all fluorophores examined with MPE have exhibited emission spectra and lifetimes similar to those excited by one-photon absorption [520].

In fluorescence measurements for analytical purposes, the parameter being measured is often referred to as the intensity, denoted as I. This intensity serves as a measure of the signal detected by the fluorescence instrument. The specific quantity being measured may include spectral radiance, spectral radiant flux, photon flux, or the number of photons, depending on the measurement geometry and the detector used. Typically, the intensity values are expressed in arbitrary units (A.U.). To ensure accuracy, these intensity values require background correction. This correction involves measuring the signal from a blank

1.3 Fluorescence 27

sample, denoted as I_0 , and subtracting this "blank" determination from the measured signal from the analyte, denoted as, I_s . Thus, the relative fluorescence intensity attributable to the analyte, I_f , can be calculated as follows [521]:

$$I_{f} = I_{s} - I_{0} \tag{1.8}$$

The intensity of fluorescence can be influenced by other factors in the environment. The decrease in intensity are called quenching and is the result of several mechanisms. Collisional quenching occurs when the excited-state fluorophore loses its activation upon coming into contact with another molecule in the solution, known as the quencher. In the progress, the fluorophore returns to its ground state as it diffusively encounters the quencher. Importantly, no chemical changes occur to either molecule during this process [518]. Resonance energy transfer, also known as fluorescence resonance energy transfer, is a distance-dependent physical process in which energy is transferred non-radiatively from an excited molecular fluorophore (named the donor) to another fluorophore (called the acceptor) via long-range intermolecular dipole-dipole coupling. The energy transfer result in a decrease in the fluorescence intensity of the donor molecule, which could be one of the mechanisms of quenching [518,522–524].

1.3.2 Fluorescence Lifetime

The fluorescence lifetime τ of the excited state is defined by the average time the molecule spends in the excited state before returning to the ground state. As mentioned above, the fluorescence occurs with a certain probability, which can be defined as the decay rate constant (k). Then the average time τ for the molecules to transition from one state to another is inversely related to the decay rate:

$$\tau = 1/k \tag{1.9}$$

The lifetime also indicates the duration time taken for a population of N electronically excited molecules to decrease by a factor of e. e can be defined as following:

$$e^{-t/t} = 1/e$$
 (1.10)

The fluorescence lifetime represents the time taken for a population of excited fluorophores to decrease exponentially to N/e through the emission of energy via fluorescence and other non-radiative mechanisms [518, 525].

Fluorescence lifetime is an intrinsic property of a fluorophore, which remains unaffected by the method of measurement [525]. It can be considered as a state function, as it is independent of initial perturbation conditions such as single- or multiphoton excitation, excitation wavelength and duration of light exposure. Fluorescence lifetime is also not affected by photobleaching [525, 526]. In addition, it is a parameter that is largely independent of the fluorescence intensity and fluorophore concentration. As this process is affiliated with an energetically unstable state, fluorescence lifetime is sensitive to various internal factors variety of internal factors defined by the fluorophore structure, as well

28 1 Introduction

as external factors like temperature, polarity, and the presence of fluorescence quenchers. The combination of environmental sensitivity and independence from intensity-based parameters makes fluorescence lifetime a potent measure complementary to conventional fluorescence intensity [525].

1.3.3 Fluorophores

1.3.3.1 Overview of Fluorophores

A fluorophore, also known as a fluorochrome, refers to a molecule or a segment of a molecule that is capable of generating fluorescence [527]. They are generally classified into two main classes: intrinsic and extrinsic. Intrinsic fluorophores are naturally occurring in the sample, whereas extrinsic fluorophores are intentionally introduced into the sample to induce fluorescence or alter its spectral properties. A notable subset of extrinsic fluorophores are fluorescent indicators, which are fluorophores whose spectral characteristics are sensitive to specific substances of interest [518,528].

The quantitative characterization of the optical properties of any fluorophore primarily involves the comparison of the incident radiation, which can be absorbed and converted, with the corresponding emission under defined instrumental and experimental conditions [521]. Since fluorescence measurements don't entail a straightforward radiometric assessment at the same wavelength, the spectral conditions of the measurement are crucial and need to be specified. The excitation wavelengths are represented by the symbol μ and the emission wavelengths are represented by the symbol λ [521].

When the emission wavelength parameter, λ , of the bispectral function that delineates the fluorescence characteristics of a material is fixed at a specified constant wavelength, λ_0 , and the excitation wavelength, μ , is the only spectral variable. The resulting function is called an excitation spectrum [521]. For example, if the applicable bispectral function is the bispectral luminous radiance factor, $\beta_{L,\lambda}(\mu,\lambda)$, an excitation spectrum $X(\mu)$ can be derived as:

$$X(\mu) = \beta_{L,\lambda} (\mu, \lambda_0)$$
 (1.11)

If the excitation wavelength is fixed at μ_0 , leaving the emission wavelength λ as the only spectral variable, the resulting function is known as the emission spectrum, denoted by $M(\lambda)$. For example, the emission spectrum $M(\lambda)$ can be derived from $\beta_{L,\lambda}(\mu,\lambda)$, as

$$M(\lambda) = \beta_{L},_{\lambda} (\mu_{0}, \lambda) \tag{1.12}$$

In both case, the fixed wavelength parameter is typically set to a value corresponding to a peak in the bispectral function. The excitation spectra and emission spectra of a fluorophore can be plotted after a given measurement under fixed environmental conditions [521].

Emission spectra exhibit considerable variability, contingent upon both the chemical composition of the fluorophore and the solvent in which it is dissolved. Certain compounds, such as perylene, have a pronounced spectral structure due to different vibrational energy

1.3 Fluorescence 29

levels in both the ground and excited states, whereas others, like quinine have spectra without vibrational features [518].

A fundamental property of fluorescence is that the emission spectrum remains constant regardless of the excitation wavelength, a principle known as Kasha's rule [529]. Examination of the Jablonski diagram (Fig. 1.11) reveals that the energy of the emission is typically less than that of absorption. Fluorescence generally manifests itself at lower energies or longer wavelengths, a phenomenon firstly observed by Sir. G. G. Stokes at the University of Cambridge in 1852 [506].

The discovery of fluorophores has introduced a novel method of observing molecules that are either too small to be seen with the naked eye or lack of distinguishing characteristics. The application of the fluorescence measurements can be broadly categorized into two areas: analytical and colorimetric. In analytical applications, fluorophores help to identify and/or quantify targets within the specimen. Conversely, in colorimetric applications, fluorophores facilitate the assessment of the radiative transfer properties of the specimen under examination to quantify its color appearance or color formulation using Kubelka-Munk analysis [521,530].

1.3.3.2 Ca²⁺ Indicators

Living organisms have complex system for regulating vital processes. Regulation of biological and chemical molecules inside of an organism is one of the important areas. However, most of biomolecules are too small to be observed with the naked eye, and they lack characteristics that allow them to be distinguished from each other. Therefore, scientists rely on special technologies to report the behavior of the molecules of interest, including optical observation. Fluorescence sensing is one of the active research areas for chemical and biochemical analytes [531–535]. Compared to radio traces, fluorescence sensing is a fast, inexpensive and relatively environmentally friendly method [536]. Fluorescence sensing requires a change in the response of the spectral properties to the analytes. The changes can occur in the intensity, excitation spectrum, emission spectrum or lifetime of the sensing probe. Fluorescent indicators, a class of fluorophores, have spectral properties that are sensitive to the substance of interest and are commonly used for fluorescence sensing. Fluorescent indicators are currently available for a variety of substances, including Ca^{2+} , Mg^{2+} , Na^+ , Cl^- , as well as pH [518,537].

As described in previous section 1.2.2.2, Ca²⁺ is an important intracellular messenger for the regulation of a diverse range of cellular processes. Therefore, the study of intracellular calcium concentration is an important area in cell biology. The discovery of Ca²⁺ indicators made it possible to report changes in Ca²⁺ concentration visually. In 1979, Roger Y. Tsien found the importance of new indicators for monitoring the kinetics of [Ca²⁺]_C during his membrane potential experiments with Ca²⁺ selective microelectrodes and fluorescent probes [538]. In 1980, Tsien published first Ca²⁺ indicator, 1,2-bis (2-aminophenoxy) ethane-N,N,N',N'-tetraacetic acid (BAPTA). BAPTA is a newly developed high-affinity buffer and optical indicator for Ca²⁺ [539]. After that, the development of Ca²⁺ indicators is booming, from synthetic Ca²⁺ indicators to genetically encoded Ca²⁺ indicators [540].

30 1 Introduction

Most Ca²⁺ probes are available in salt forms, lacking the ability to diffuse across cell membranes. Therefore, when the intracellular encoded Ca²⁺ concentration needs to be measured, the probes are attached to esterified carboxy groups, the so-called acetoxymethyl esters (AM esters). In this form, the probe is less polar and could passively diffuse across cell membrane. When the probe with the AM ester enters the cell, the AM ester is cleaved by ubiquitous cellular carboxy esterases. After that, the probe will again become polar and cannot leave the cytosol by diffusing across membrane [540–542]. A few of Ca²⁺ indicators will be introduced in following part.

Fura-2

Fura-2 is a wavelength-ratiometric probe, published by Tsien's group in 1985. It has an extended BAPTA core with a benzofuran fluorophore (Fig. 1.12 A) [543]. Fure-2 has The Ca²⁺ dissociation constant (K_d) of Fura-2 is 145 nM in vitro at 22 °C [544]. Binding to Ca²⁺ could lead to conformational rotation of the aniline (Fig. 1.12 A) and a shift in fluorescence spectrum between 300 and 400 nm (Fig. 1.12 B) [543,544]. There is also a shift in the emission spectrum, but it is relatively small compared to the shift in the absorption or excitation spectrum, allowing the excitation wavelength to be switched to alternatingly excite the Ca²⁺-bound form or the Ca²⁺-free form while monitoring the same emission band. Then based on the ratio of the emission intensity excited at the wavelengths corresponding to different Fura-2 forms, the actual Ca²⁺ concentration could be estimated [545–548].

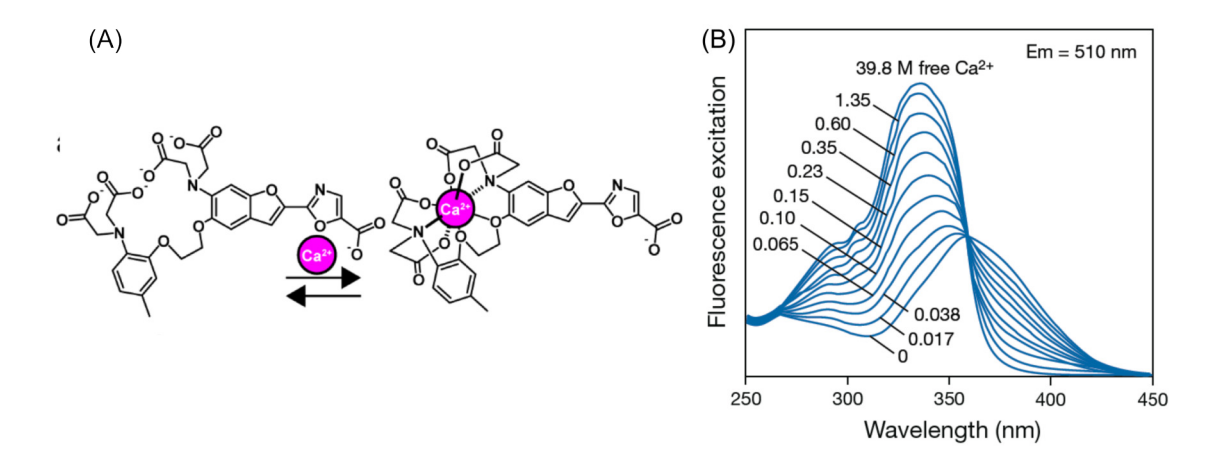


Fig. 1.12: Structure and excitation spectra of Fura-2. (A) Chemical structure of Fura-2 with and without Ca²⁺. (B) Excitation spectra of Fura-2 in solutions containing 0–39.8 μM free Ca²⁺ (emssion detection at 510 nm). Image adopted from Zhou et al. and *The Molecular Probes Handbook* [540, 544].

Fura-red

Fura-red is Fure-2-analogue in which an oxazole of the benzofuran fluorophore is replaced by thiohydantoin (Fig. 1.13 A) [549,550]. It is a visible-light-excitable ratio-metric Ca²⁺ indicator. The $\rm K_d$ of Fura-red is 140 nM in vitro at 22 °C [544]. As Fura-2, the excitation spectrum changes with or without Ca²⁺ binding. Fura-red could be excited by the 488 nm

1.3 Fluorescence 31

laser line in the absence of Ca²⁺, whereas the optimal excitation wavelength of the Ca²⁺-bound form shifts to 436 nm [551–553]. As Figure 1.13 B shows, fluorescence emission of Fura-red decreases once Fura-red bind Ca²⁺ [544]. Fura-red has long-wavelength emission maximum (approximately 660 nm) and the emission spectra are shown in Figure 1.13 C. Because of the long-wavelength emission, in theory, imaging with Fura-red does not interfere with haemoglobin. However, the low fluorescence quantum yield of Fura-red means that imaging process needs either high indicator concentration or impractically high laser power [549].

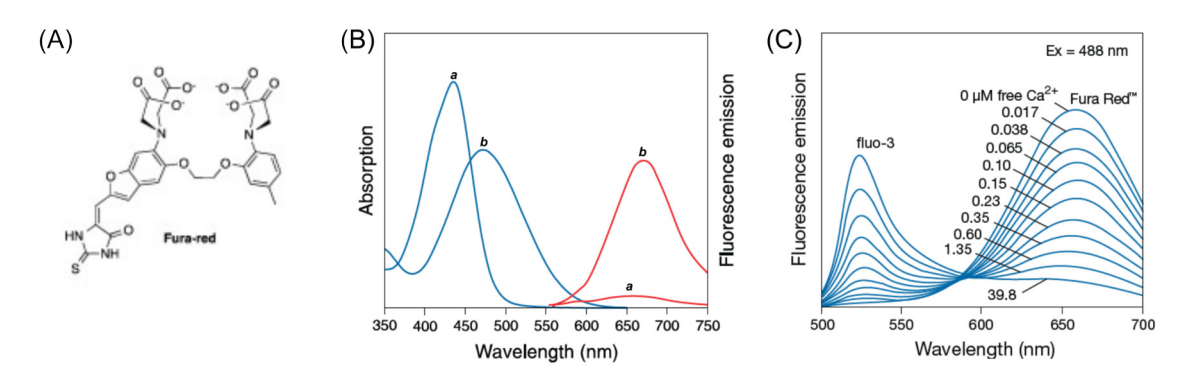


Fig. 1.13: Chemical structure and spectra of Fura-red. (A) Chemical structure of Fura-red. (B) Absorption and Fluorescence emission (excited at 488 nm) spectra of Ca^{2+} -saturated (a) and Ca^{2+} -free (b) Fura Red in pH 7.2 buffer. (C) Fluorescence emission spectra of a 1:10 (mole:mole) mixture of the Fluo-3 and Fura-red, simultaneously excited at 488 nm in solutions containing 0–39.8 μM free Ca^{2+} . Image adopted from Oheim et al. and *The Molecular Probes Handbook* [544, 549].

Fluo-3 and Fluo-4

Fluo-4 is a single wavelength, intensity-modulating dye modified from Fluo-3 by substituting two fluorines for the two chlorine substituents in the fluorophore (Fig. 1.14 A) [540]. Fluo-4 has similar K_d (345 nM) as Fluo-3 (390 nM) (both measured at 22 °C with designed buffer kit) [544, 554–556]. Fluo-3 is a Ca^{2+} -sensitive fluorophore in which BAPTA is attached to the pendant aryl ring of the fluorescein [540]. The mechanism of Fluo-3 involves photoinduced electron transfer (PET). PET is an interaction that causes quenching. Quenching results in the dissipation of the fluorophore's electronic energy of the fluorophore as heat, leading to a decrease in intensity [557]. Because of the PET, Fluo-3 will have increased fluorescence emission when it binds to Ca^{2+} . Like Fluo-3, Fluo-4 has little fluorescence in the absence of Ca^{2+} but the fluorescence emission of the Ca^{2+} -bound form is dramatically increased. Unlike the Fura dye family, Fluo-4 responds to binding without spectral shift [554]. But, the absorption maximum of Fluo-4 is blue-shifted about 12 nm compared with Fluo-3, indicating Fluo-4 has increased fluorescence excitation at 488 nm (Fig. 1.14 B), which benefits in higher signal levels for confocal microscopy [544].

X-rhod-1

X-rhod-1 is a BAPTA-based rhodamine calcium indicator, with Texas Red (sulforhodamine 101) attached to BAPTA (Fig. 1.15 A) [549, 559]. It has higher intensity when binding

32 1 Introduction

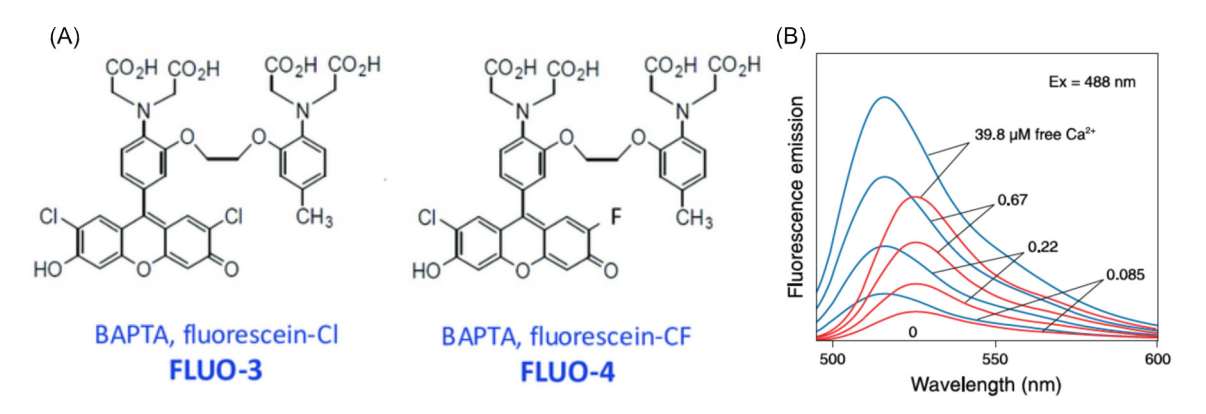


Fig. 1.14: Chemical structure and spectra comparison of Fluo-3 and Fluo-4. (A) Chemical structure of Fluo3 and Fluo-4. (B) Comparison of fluorescence emission spectra at equal concentrations of Fluo-4 (blue) and Fluo-3 (red) in solutions containing 0–39.8 μM free Ca²⁺. Image adopted from Byrnes et al. and *The Molecular Probes Handbook* [544, 558].

calcium than Fluo-4 due to PET. X-rhod-1 has longer excitation and emission wavelengths (excitation/emission maxima of approximately $580/602\,\mathrm{nm}$) compared to Fluo-4 (Fig. 1.15 B) [540, 544]. X-rhod-1 has a $\mathrm{K_d}$ for $\mathrm{Ca^{2+}}$ of $700\,\mathrm{nM}$ at $22\,^{\circ}\mathrm{C}$ with designed buffer kit [544].

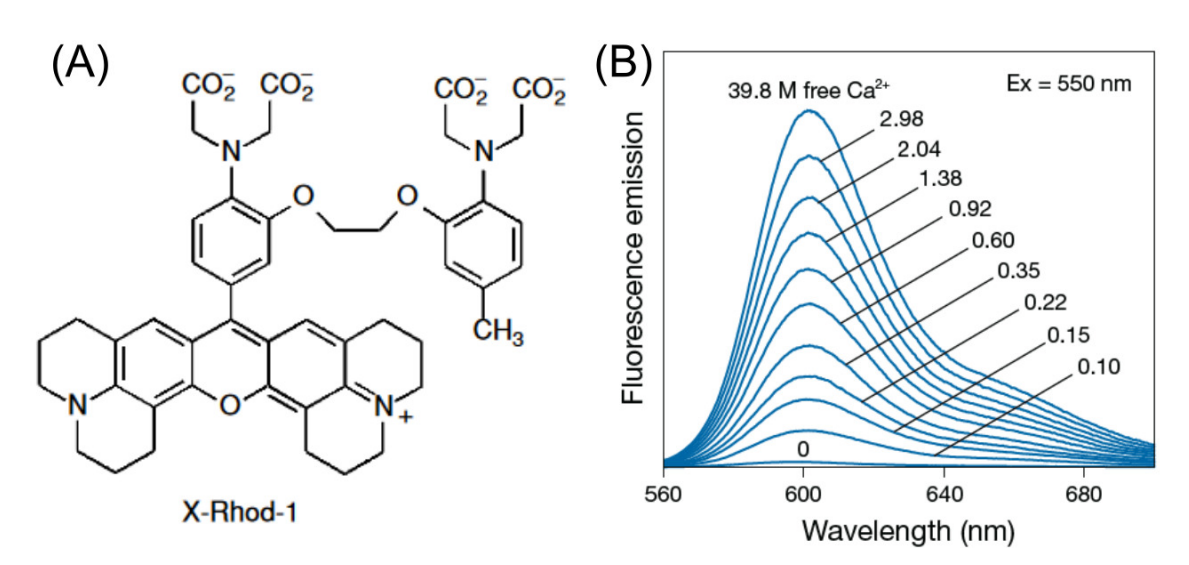


Fig. 1.15: Chemical structure and spectra of X-rhod-1. (A) Chemical structure of X-rhod-1. (B) Fluorescence emission spectra of the tripotassium salt of X-rhod-1 in solutions containing 0–39.8 µM free Ca²⁺. Image adopted from *Calcium Signaling* and *The Molecular Probes Handbook* [544,560].

Oregon Green 488 BAPTA-1

Oregon Green 488 BAPTA-1 (OGB-1) is a dye based on BAPTA to be sensitive to $\mathrm{Ca^{2+}}$ with a $\mathrm{K_d}$ for $\mathrm{Ca^{2+}}$ in the absence of $\mathrm{Mg^{2+}}$ of about 170 nM [544]. In OGB-1, a complete difluorofluorescein moiety is coupled to BAPTA via an amide bond (Fig. 1.16 A) [561]. As Fluo-4, the binding to $\mathrm{Ca^{2+}}$ could lead to a change in fluorescence intensity, increasing it approximately 14-fold (Fig. 1.16 B) [544, 560]. The absorptivity of Oregon Green 488

1.3 Fluorescence 33

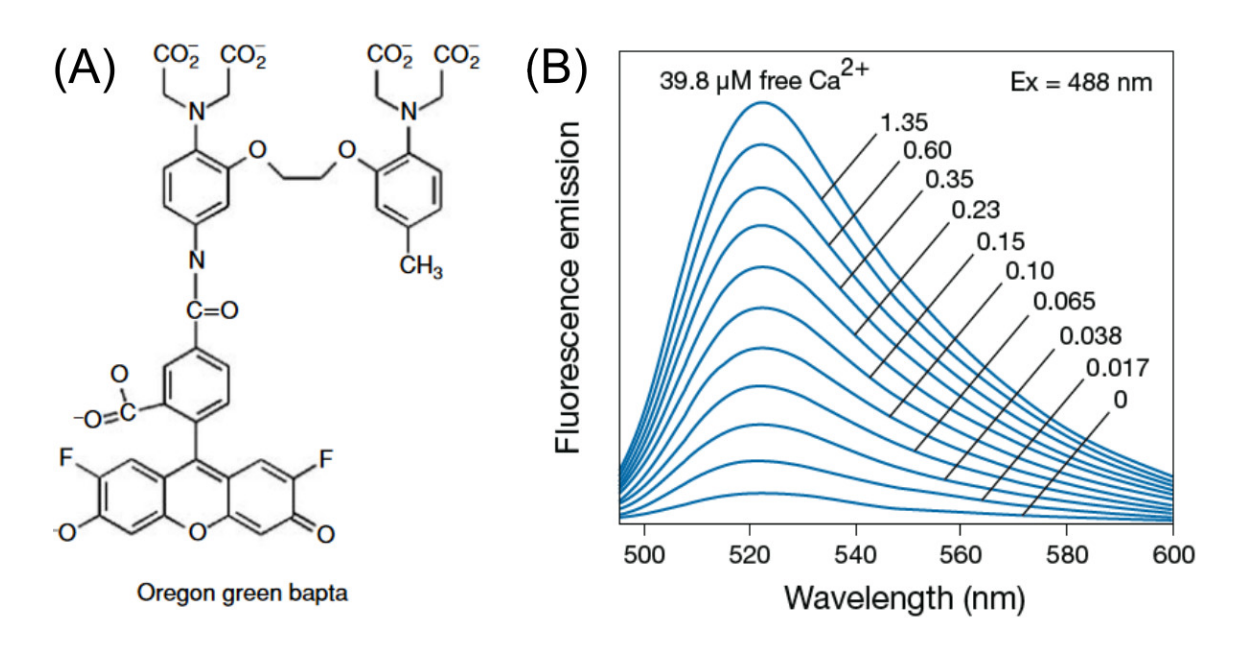


Fig. 1.16: Chemical structure and spectra of Oregon Green 488 BAPTA-1 (OGB-1). (A) Chemical structure of OGB-1. (B) Fluorescence emission spectra of the OGB-1. Image adopted from Calcium Signaling and The Molecular Probes Handbook [544,560].

BAPTA-1 at 488 nm is about 93% of its peak value, which makes excitation of Oregon Green 488 BAPTA-1 by the 488 nm spectral line of the argon-ion laser more efficiently [544].

1.3.3.3 Haemoglobin Fluorescence

Protoporphyrin IX (PpIX), the final intermediate in the heme biosynthetic pathway, is an intrinsic fluorophore [562]. PpIX can be excited in different spectral regions, ranging from violet (around 405 nm) to red (around 633 nm) light an emit pink to red light emits red to pink fluorescence [563,564]. Since PpIX is the precursor of heme and the structure of four pyrrole rings maintained in heme, the hemoglobin has been considered as an intrinsic fluorophore in humans. In 1934, Shenk et al. reported hemoglobin absorption spectrum of hemoglobin in beef [565]. In 1942, Horecker reported the absorption spectrum of hemoglobin could change with different modifications [566]. Since then, the fluorescence properties of hemoglobin have been studied. In 1980, a significant steady-state intrinsic fluorescence emission of Hb was discovered [567, 568]. Later with advanced optical equipment, the emitted fluorescence of hemoglobin was reported to be found in the wavelength range of 580nm-650nm [569]. Using two-photon excitation, the hemoglobin emission spectrum also be reported recently [570]. However, there was a theory that the emission was thought to be strongly quenched by energy transfer to heme [567, 571, 572] making the fluorescence difficult to detect under experimental conditions. There was a study showed the doubt of the fluorescence detected from RBCs or hemoglobin actually from heme. In the experiment, UV light induced auto-fluorescence from RBCs had similar spectral as bilirubin isomers by comparing the spectral of RBCs in the experiment with previous published data of bilirubin isomers [573–575]. Whether there is fluorescence from RBCs and the source of the fluorescence are still under investigation.

2 Materials and Methods

2.1 Preparation of Chemicals and Solutions

Details of the reagents and solutions used in the experiments are given in Appendix A.3 and A.4. All stock solutions of compounds were dissolved in distilled water or dimethyl sulfoxide (DMSO) or 20% pluronic F127 in DMSO according to the manufacturer's recommendations.

The pH and osmolarity of the solutions were checked and adjusted during preparation using a pH meter (SevenEasy S20) and an osmometer (Gonotec® Osmomat 3000 Basic or Automaticsemi-micro osmometer A0300).

Total calcium concentration and calcium chelator concentration were calculated using Ca-buf software based on the addition of 10 mM ethylene glycol-bis-(2-aminoethylether)-N,N,N',N'-tetraacetic acid (EGTA) or 10 mM ethylenediaminetetraacetic acid (EDTA).

A calcium electrode (perfectION comb CA) and an ion/pH meter (SevenCompact pH meter S220) were used to determine the solution-free calcium concentration.

Information on the equipment used for solution preparation and the experiments is given in Appendix A.5.

2.2 Cell Preparation

2.2.1 RBCs Collection and Washing

For all *in vitro* experiments, various blood samples were obtained either by venipuncture and collected in EDTA-coated or Na-Heparin-coated tubes or tubes with Li-heparin beads, or by finger prick and collected in Eppendorf tubes, as listed in Tab. 2.1. The research followed the guidelines of the Declaration of Helsinki and was approved by the local ethics committee ("Arztekammer des Saarlandes") for all blood sample analyses (permit number 51/18).

The protocol for isolating and washing the RBCs is illustrated in Figure 2.1. Detailed experiment protocol is given in Appendix A.1.

Sample type	Sample source	Acquiring methods	Number of donors
Marijuana smokers and matched con- trols	Universität des Saarlandes	Li-Heparin tubes	3 Smokers 4 Controls
Sickle cell disease patients	Hospices Civils de Lyon, Lyon/France	EDTA tubes for sickle cell patient Na-Heparin tubes for controls	65 Sickle cell patients 12 Controls
Patient with double mutations	Medizinische Universität Graz	Li-Heparin tubes	Double mutation patient and 2 family members 5 Controls
β-thalassemia patient with Piezo 1 channel mutation	Fondazione IRCCS Ca' Granda Ospedale Maggiore Policlinico	Li-Heparin tubes	1 Patient1 Healthy control1 Thalassemia control
Healthy RBCs	Universität des Saarlandes	Finger prick	8 Controls

Tab. 2.1: Blood sample information.

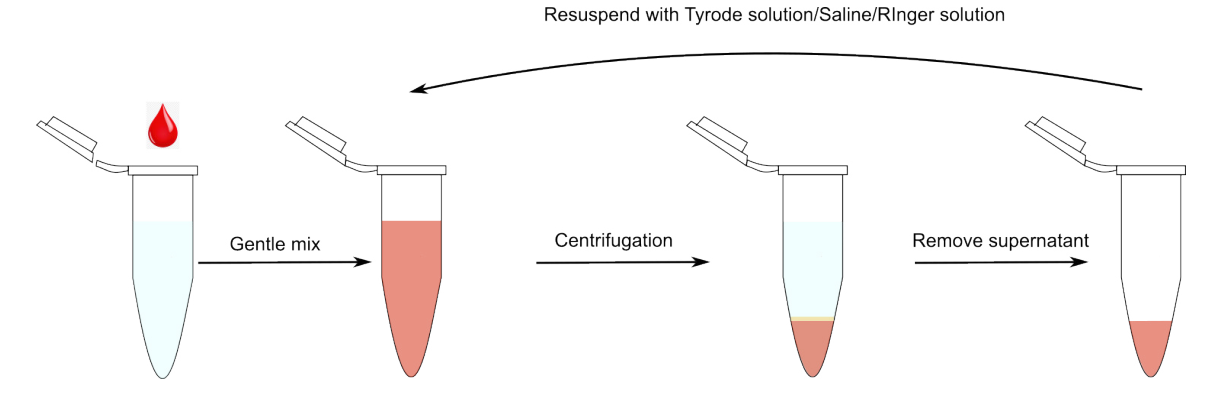


Fig. 2.1: Illustration of the blood washing process (from left to the right). The blood washing process involves taking a defined amount from the blood sample and adding it to the defined solution, followed by gentle agitation, centrifugation and resuspension in a buffer for three times. After the last centrifugation, the sedimented RBCs were ready for further steps.

2.2.2 ATP-depleted RBCs Preparation

In some conditions based on the experimental design, the RBCs required to deplete intracellular ATP storage to inhibit PMCAs activity. In the absence of a specific PMCA inhibitor, incubating RBCs in glucose-free medium for several hours is used to obtain reversibly metabolically depleted cells and this method has been suggested by several previous studies [576–578].

For calcium-imaging, the healthy RBCs were incubated in glucose-free medium for 16 hours at 4 °C for ATP depletion, one of most common suggestion of fasting time in literature. For fluorescence lifetime imaging, healthy RBCs were incubated in glucose-free medium

for 72 hours in room temperature (RT) to make sure ATP level was undetectable by ATP assay kit, which allowed inhibiting PMCA activity as much as possible. The protocol to prepare the ATP-depleted RBCs suspension is illustrated in Figure 2.2. The detailed protocol to prepare the ATP-depleted RBCs suspension is given in Appendix A.1.

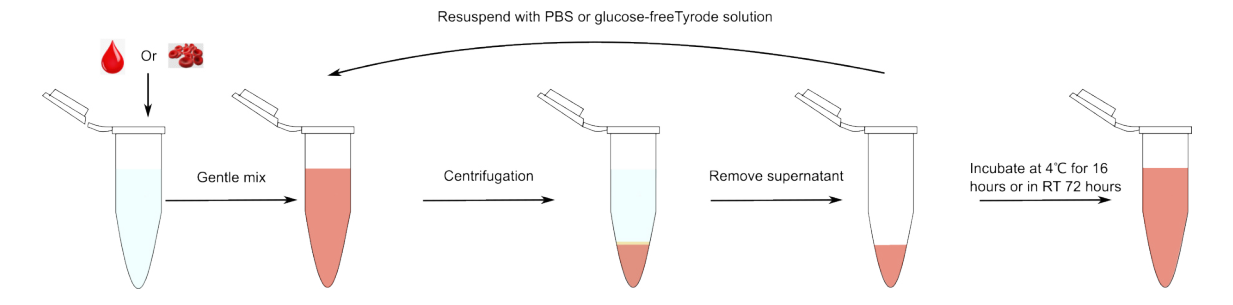


Fig. 2.2: The protocol for obtaining ATP-depleted RBCs (from left to the right). The designed amount was taken from the blood sample or washed RBCs and added to glucose-free medium (PBS or glucose-free Tyrode), followed by gentle agitation, centrifugation and resuspension in a buffer for three times. After the last centrifugation, the sedimented RBCs were incubated in at 4 °C or RT for the defined time.

2.2.3 Fluorescence Probe Loaded RBCs

Use of Calcium Indicators

As described in previous section 1.3.3.2, Ca²⁺ indicators are powerful tools for monitoring changes in Ca²⁺ concentration. Since Tsien used esterifying groups to mask Ca²⁺ chelators [542], the load of Ca²⁺-selective probes into the cytoplasm in suspension became easy. The AM-formed Ca²⁺ indicators could avoid perturb membrane integrity and soluble cytoplasmic contents. In experiments requiring Ca²⁺ detection, RBCs were loaded with Ca²⁺ indicators as follows (Fig. 2.3). The detailed protocol to prepare the Ca²⁺ indicator loaded RBCs is given in Appendix A.1.

Application of Fluorescent-dye-conjugated Antibody

In the 1940s and 1950s, Coons et al. successfully used antibodies labelled with fluorochrome groups, combining the high sensitivity of fluorescence microscopy with the strict specificity associated with immunological procedures, the antigen-antibody complex formation [579–581]. Immunofluorescence (IF), also called fluorescent antibody staining, became one of the efficient methods for detecting targeted molecules [582]. There are three methods to form a fluorescent antigen-antibody complex: the direct method [581,583]; the indirect method [584,585] and the complement method [586–589]. For the detection of transmembrane proteins in the experiment, IF with the indirect method was used. The indirect method means two or more layers in the fluorescent complexes. The formation of complexes requires an unlabeled antibody (primary antibody) that reacts with the target antigen, followed by the additional fluorescence-labeled antibody (secondary antibody) that reacts with primary antibody [584,585]. The detailed protocol of fluorescence-labeled RBCs is

illustrated in Figure 2.3. The detailed protocol to prepare fluorescence-labeled RBCs is given in Appendix A.1.

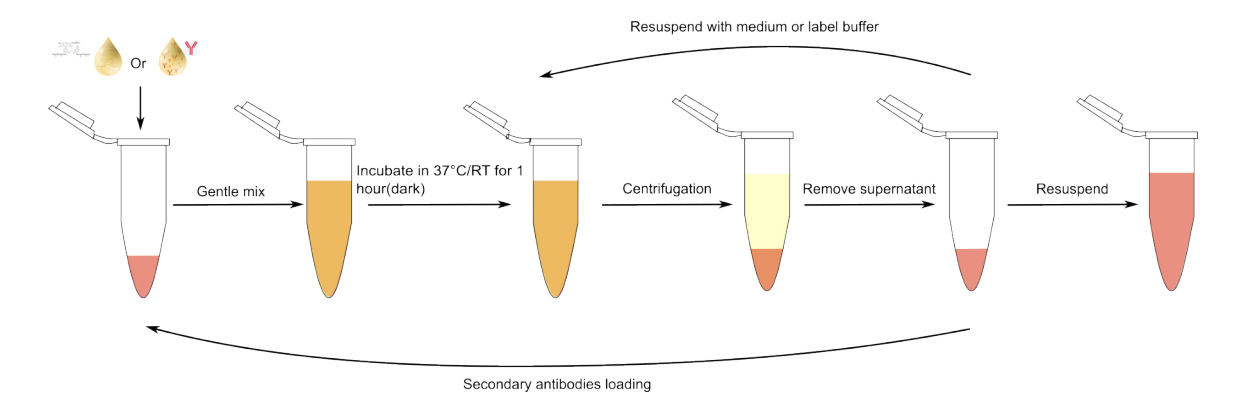


Fig. 2.3: Illustration of the loading of the fluorescent probe into RBCs (from left to the right). RBCs were washed and added to defined buffer or labeling buffer with fluorescent probe, followed by incubation for 1 hour at 37 °C or RT in dark with shaking at 400 rpm. Then gentle agitation and centrifugation were applied to the RBCs, followed by washing three times. After washing, the sedimented RBCs were resuspended for further steps. If secondary antibodies were required, the sedimented RBCs were resuspended in label buffer containing secondary antibody and incubated for 1 hour at RT at 400 rpm shaking in the dark. The same washing steps as after primary antibodies staining were applied. Finally, the RBCs were resuspended in 1 ml label buffer for further experiments.

2.2.4 Cell Lysis and Ghost RBCs Preparation

Cell lysis, or cell disruption, is a process in which the outer boundary or cell membrane is broken down to release intracellular materials. This process is a crucial unit operation in biomolecular analysis, including protein purification for structural and functional studies and composition of specific protein analysis [590]. Various methods have been developed over the past decades for different cell types, target molecules and the downstream techniques [591], including mechanical, physical, chemical and biological methods [590]. Non-ionic detergents are one of the most commonly used chemical detergents to achieve cell lysis with the least damage to proteins and enzymes. Nonidet-40 P (NP-40) is one of the mild non-ionic detergents that is good at isolating cytoplasmic proteins but not nuclear proteins [592, 593]. The detailed protocol of lysing cells by NP-40 is illustrated in Figure 2.4. The detailed protocol of lysing cells by NP-40 is given in Appendix A.1.

Pale RBCs with no internal content are called ghost RBCs and were first described by Dodge et al in 1963 [594]. Because RBCs lack of organelles and ghost RBCs have no internal cytosol content, the ghost RBCs have been considered as representative model to study plasma membrane properties, function and structural arrangement. The common technique used today to prepare erythrocyte ghost is the use of isoionic and isotonic solutions [595, 596]. The detailed protocol of harvesting ghost cells is illustrated in Figure 2.5. The detailed protocol of harvesting ghost cells is given in Appendix A.1.

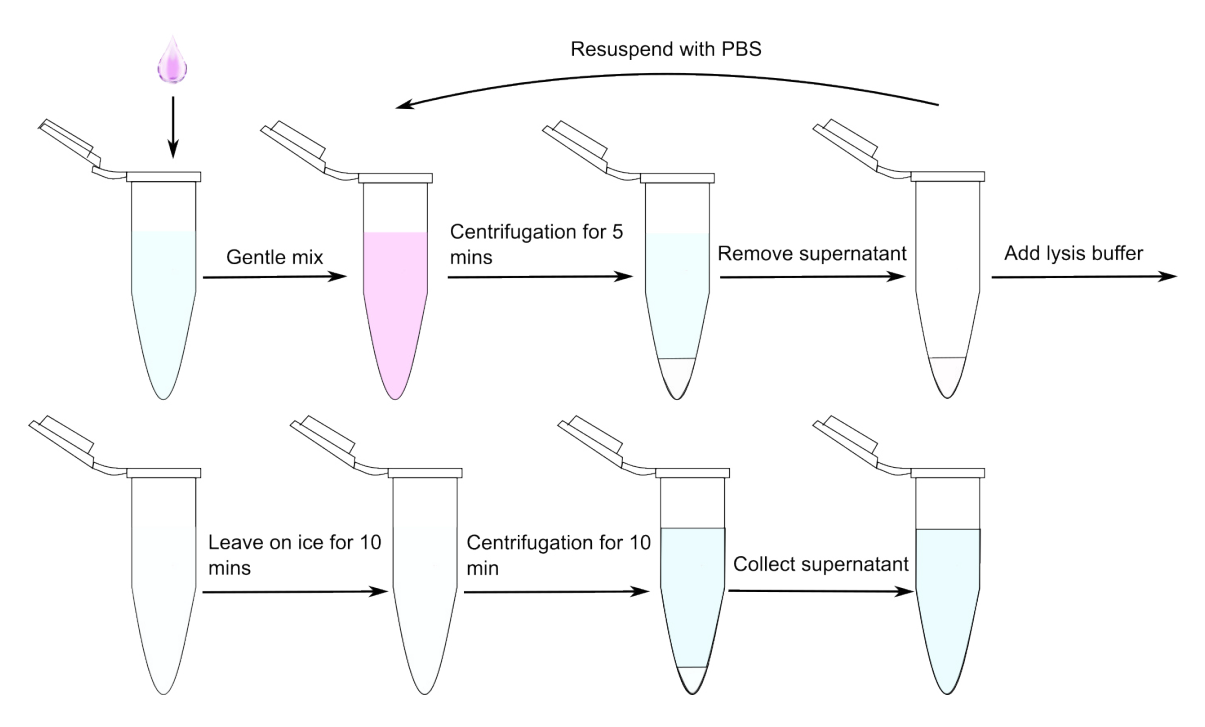


Fig. 2.4: Illustration of lysing cells (from left to the right). Cells were washed. Then the cells were lysed by applying defined lysis buffer to the cells on ice and incubate for 10 minutes. After that, the solution was centrifuged and the supernatant is collected.

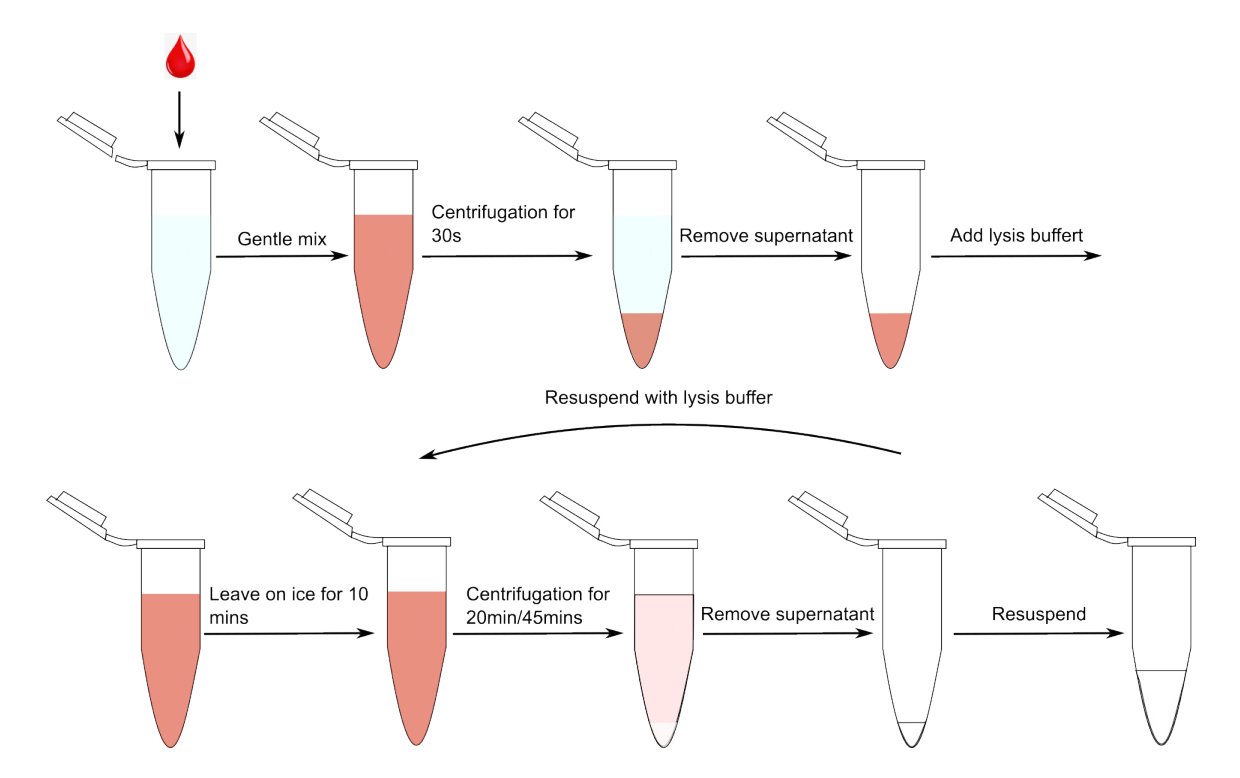


Fig. 2.5: Illustration of ghost RBCs preparation (from left to the right). RBCs were washed. Then the RBCs were lysed by applying defined lysis buffer to the RBCs on ice and incubate for 10 minutes. After that, the ghost RBCs were washed three times with the same lysis buffer and resuspended in the same lysis buffer for further experiments.

2 Materials and Methods

2.3 Flow Cytometry

Flow cytometry is a technique for the rapid analysis of single cells or particles with multiple parameters. The flow cytometers can utilize single or multiple lasers as light sources. When single cells or particles pass through the laser, the scattered or fluorescent light signal is produced and can be read by detectors. The light signals are converted into an electronic signal that can be analyzed by a computer and generated in to a standardized data file [597]. The basic configuration of a classical single laser flow cytometer is shown in Figure 2.6.

Flow cytometry measurements were performed on different models of flow cytometers (BD FACSCantoTM II or BD LSRFortessa). Blood samples were processed as described above according to different experimental aims. Data was recorded via BD FACSDivaTM software and the results were evaluated using FlowJo. The values were obtained from experiments with independent donors ($n_{cell} = 30,000$ for each measurement or time point).

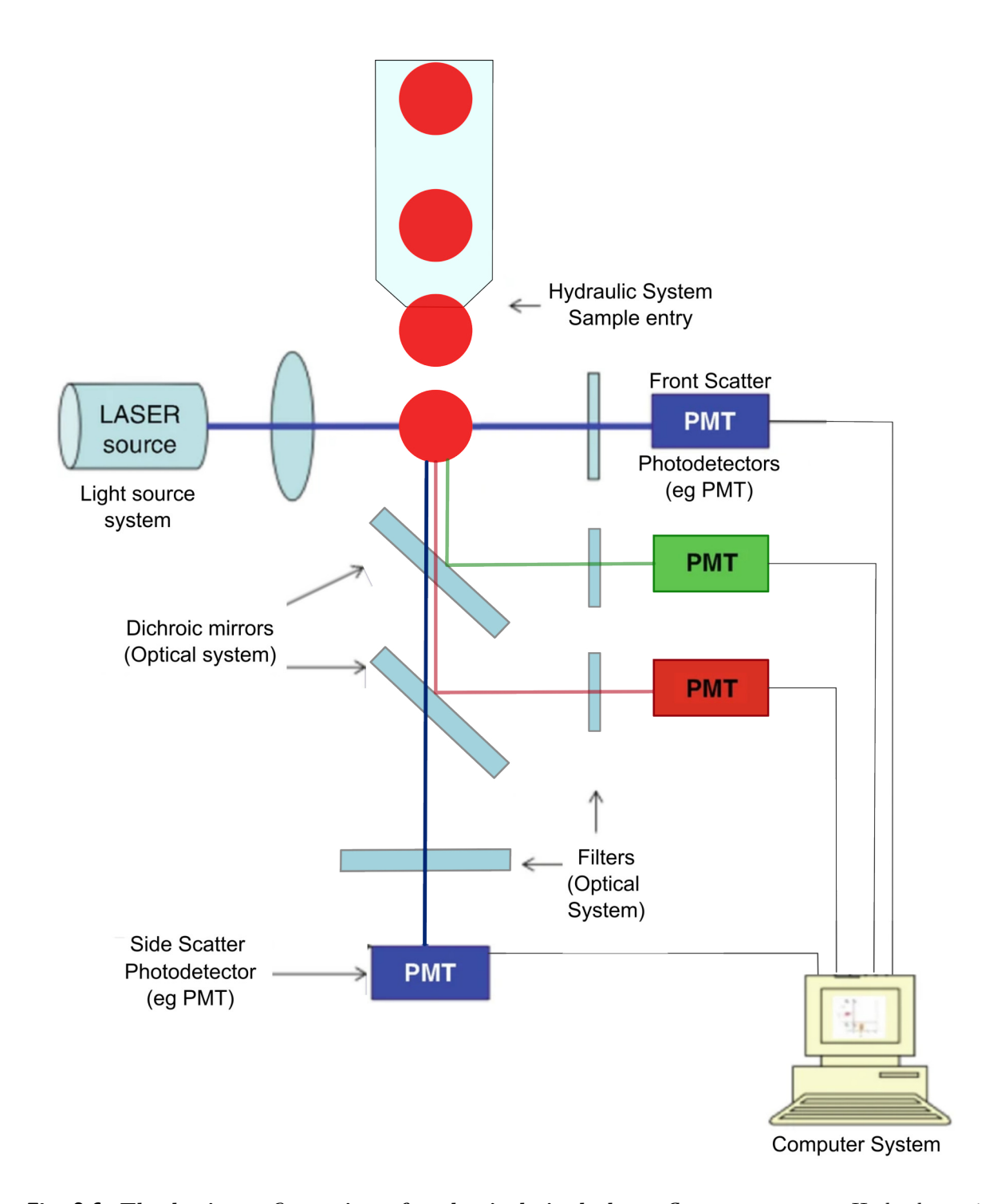


Fig. 2.6: The basic configuration of a classical single laser flow cytometer. Hydrodynamic system is used to force cells to flow one by one in front of a light beam. Optical system including dichroic mirrors, photodetectors and filters. Dichroic mirrors and filters are used to separate light by wavelength and collect the light signal within the wavelength range of interest. Photodetectors are used to collect signals. A computer system converts, processes and stores signals in a specific data format for further analysis. Image adapted from *Basic Principle of Flow Cytometry* [598].

2.4 Membrane Potential Measurements According to the Method of Macey, Bennekou, and Egee (MBE-method)

In order to measure the average membrane potential in a population of RBCs, the MBE method according to distribution of H⁺ was first described by Macey at al. and was later named as method of Macey, Bennekou, and Egee (MBE) method in 2021 [442,599].

The distribution of H^+ between RBCs membrane is at equilibrium. Across the membrane, there is an inward driving force for H^+ , the equilibration of H^+ can reflect the membrane potential. If H^+ equilibration raised, the H^+ conductance is increased. With help of CCCP, the ionophore of H^+ , the permeability of RBC membrane to H^+ is increased by orders of magnitude and keep the H^+ driving force only from membrane potential. The measurement is completed by lysing all RBCs and removing all plasma membrane, which lead to $Vm=0\,\text{mV}$ and $pH_{in}=pH_{out}$. Hence, the equation used to get the membrane potential (Vm) at 37 °C is the following equation:

$$Vm = 61.5mV \times (pH_{in} - pH_{out})$$
(2.1)

The general configuration for performing the MBE method is shown in Figure 2.7. The detailed protocol of the MBE method is given in Appendix A.1.

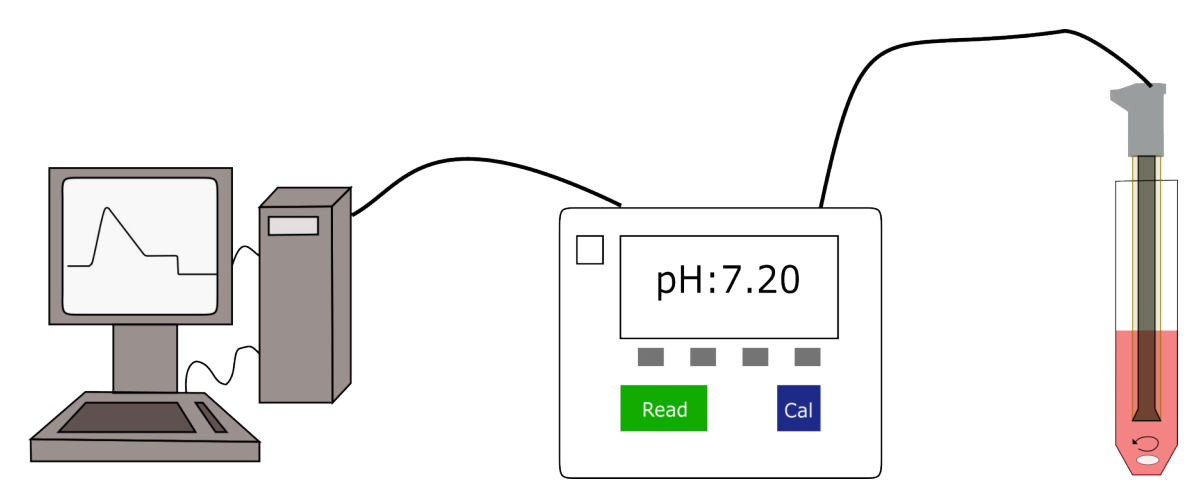


Fig. 2.7: The illustration shows the MBE measurement. The pH meter was used to measure the pH value of the RBC suspension and the computer was used for recording the pH value at an acquisition rate of 1 point/second.

In certain experimental settings, the inhibitors with a defined concentration was preapplied to ringer solution. When it is necessary to generate deoxygenated condition, the deoxygenated Ringer solution was obtained by continuously gassing 100% of nitrogen gas (N₂) into Ringer solution to expel oxygen away until the 10% of the initial partial pressure of O₂ (0.8 – 1.0 mg/L) was reached. The N₂ flow was maintained throughout the experiment.

Extracellular pH was measured using a PHM210 pH-meter coupled with a G200 pH electrode and a red Rod 200 reference electrode or a SevenCompact S210 pH-meter

2.5 Microscopy 43

coupled with an InLab Solids Pro-ISM electrode. Sampling and data acquisition were performed with an electrode amplifier connected to an AD LABQUEST Mini interface or the internal setup of the SevenCompact S210 pH-meter at a rate of 1 Hz with a resolution of 0.01 pH unit. The data were visualized and analyzed with the Logger Lite software or an internal house-made program. The data was processed by Matlab[®] 2022.

2.5 Microscopy

2.5.1 Fluorescence Microscopy

The resolution of human eyes alone is limited (about 200 µm between two points or lines) [600, 601]. In order to increases the resolution, additional help is needed. Since first compound microscope was invented by coincidence in in later sixteenth century, the observation with better resolution of small objects can be achieved [602–604]. Over the years, several methods have been developed to improve the resolution and contrast of microscope images [605]. Fluorescence microscopy was developed to reveal only the objects of interest against an otherwise black background. In the preferred fluorescence microscope setup, an epi-illumination is used to excite the fluorescence of fluorophores. Compared to a white light microscope, additional dichroic mirrors and filters are used to separate and filter excitation and emission light [606].

2.5.2 Confocal Microscopy

White light microscopy and fluorescence microscopy will also collect a considerable part of out-of-focus light during the imaging process. Thus, the captured images are composed of sharp features from the focal plane and blurred features from out of focus. Confocal microscopy could produce a point source of light and reject the out-of-focus light by introducing a spatial pinhole at the back focal plane in front of the detector, leading to a significant improvement in axial resolution [607].

As Figure 2.8 A shows, the essential component to the confocal is one or more placed pinhole apertures. When fluorescent molecules in a specimen are excited by the laser from laser beam, the emitted light is collected by the objective lens and focused by a second lens through the pinhole. The pinhole ensures that only fluorescence that originates at the focal point is captured by the detector and out-of-focus light is blocked. Additional scanning mirrors are used to sweep the laser beam across the specimen to generate an image pixel by pixel [608]. This could image with high resolution and provide a possible optical sectioning for 3D reconstructions of the imaged samples [608,609]. In order to capture fast dynamics in live specimens, small regions of interest or different confocal geometry needed, a spinning-disk confocal microscope (SD) cans be used. The SD illuminates the sample using an array of pinholes arranged in a special pattern on a disk. That could create hundreds of focused beam and effectively parallelize multiple confocal lightpaths of emitted fluorescence (Fig. 2.8 B) [608].

For calcium imaging, $50 \,\mu$ l of cell suspension was added to $950 \,\mu$ l Tyrode solution and transferred to μ -dishes. Ca²⁺ images were acquired by a spinning disk confocal microscope

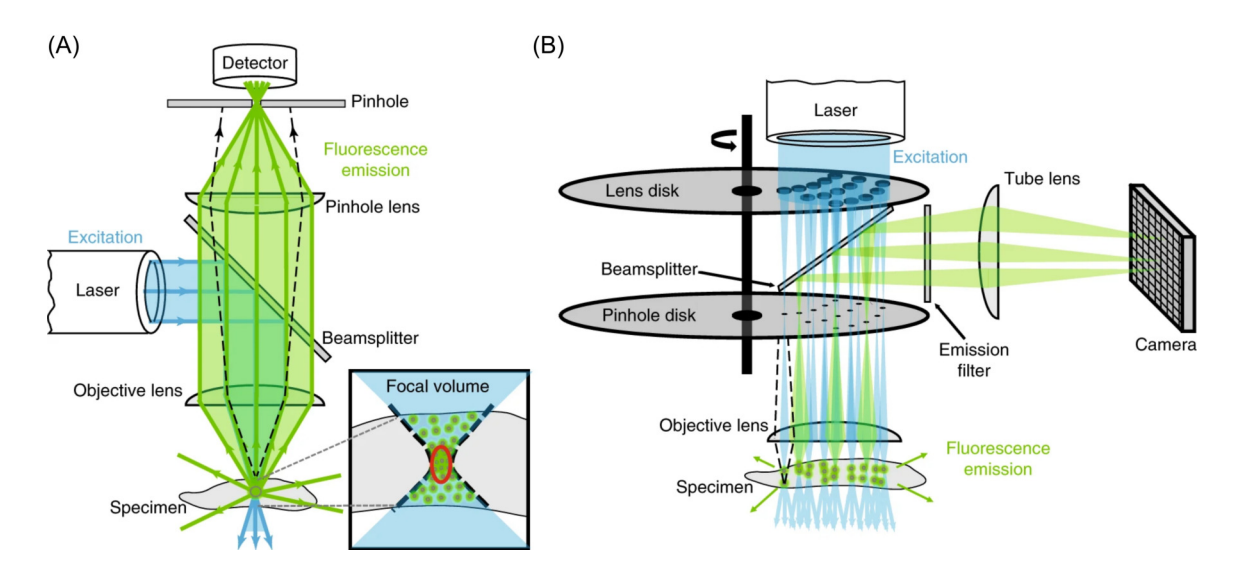


Fig. 2.8: Schematic of a classic confocal laser-scanning microscope (CLSM) and spinning disc confocal microscope (SD). (A) In the CLSM, a laser beam (blue lines) is focused into a specimen to excite fluorescent molecules throughout the entire cone of illumination. The emitted photons from excited fluorescent molecules in the focus plane (red oval) are collected by a detector through a pinhole. The out-of-focus emission fluorescence light (black dashed lines) does not reach the detector because it is not focused through the pinhole. (B) In the SD, the excitation laser beam (blue lines) hits a lens disk that splits the into smaller beams. The smaller laser beam pass through a matching pinhole disk and then are focused into the specimen, which excited fluorescent molecules throughout the focal volume as well as across the field of view as the rotating disk sweeps the pattern of laser beams. Fluorescence (green) generated from the many focal points passes back through the pinholes and is reflected by a beam splitter to a digital camera. Similar to CLSM, the light emitted from outside of the focus (black dashed lines) cannot be detected by camera because it cannot pass through the pinhole disk. Image taken from Jonkman et al. [608].

attached to an Eclipse Ti fluorescence microscope with an S Fluor 40× oil objective or Plan Apoc VC 60× oil objective or Plan Apo TIRF 100× oil objective. Acquisition was performed with a 488 nm laser. Depending on experimental purpose, either time-lapse acquisition with designed time intervals or single image acquisition was performed. Images were processed by Fiji.

2.5.3 Fluorescence Lifetime Imaging Microscopy (FLIM)

2.5.3.1 FLIM Measurement

Fluorescence lifetime imaging microscopy exploits the lifetime property of fluorescence to provide high-resolution images of molecular contrast. It has high sensitivity to molecular environment and changes in molecular conformation. There are two methods to determining the fluorescence lifetime of fluorophores. One of the method is time-domain acquisition [525,610]. In time-domain acquisition involves using a short pulse of light for excitation (short compared to the lifetime of the sample) and subsequently capturing the exponential decay of the fluorescent molecules. This decay is recorded either directly by gated detection or pulse sampling, or by employing time-resolved electronics that categorize photons based on their arrival times [611–614]. Time-correlated single photon count (TCSPC) is the most common time-domain measurement using fast-electronic method. In TCSPC, the

2.5 Microscopy 45

time between an excitation pulse and an emitted photon is measured, and the time defines the arrival time of each emission photon (Fig. 2.9 A) [610]. The times of arrival of the emission photons are collected and stored in a histogram with the time difference as the x-axis and the number of photons detected for that time difference as the y-axis (Fig. 2.9 B). The global histogram represents the waveform of the decay, called fluorescence decay, F(t) (Fig. 2.9 B) [615]. Later the global decay could be used to generate a lifetime image [616,617]. Fluorescence decay is often adequately described by modeling it as a combination of first-order kinetic processes. Mathematically, it is represented as a sum of exponentials:

$$F(t) = \sum_{i} a_{i} \exp(t/\tau_{i})$$
 (2.2)

where τ_i is the lifetime of component i and a_i its intensity contribution to the fluorescence decay [618].

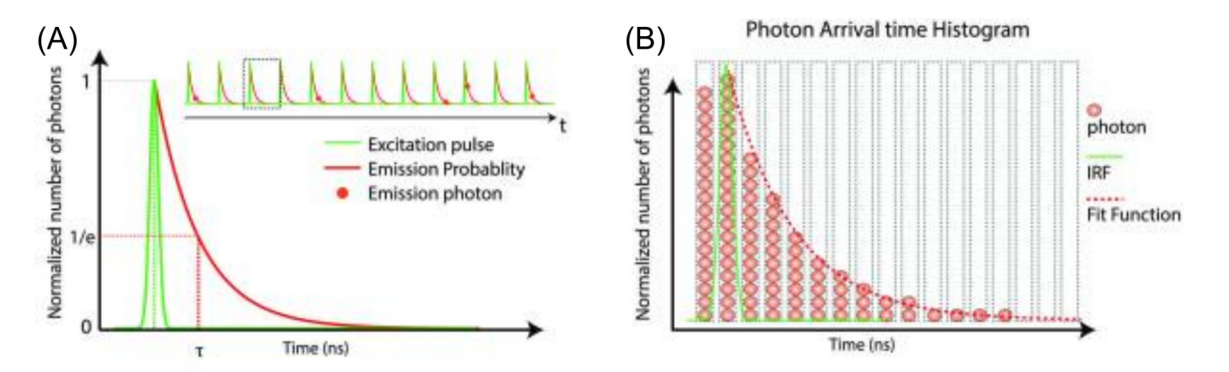


Fig. 2.9: Schematic of FLIM microscopy and time-domain (TCSPC) FLIM. (A) TCSPC FLIM acquisition includes the short excitation pulse, the single exponential fluorescence decay curve, and lifetime (τ) defined at the 1/e value. The inset shows detected single fluorescence photons (red circles) at different times within multiple excitation pulses. (B) Photon time-of-arrival histogram constructed from multiple fluorescence photon detection times (red circles), where the green line represents the instrument response function (IRF) and the dotted red line represents the fit function. Image taken from Datta et al [610].

Additionally, the instrument response function (IRF) is measured in the response of the instrument to a zero lifetime sample for the temporal response of the optical system [619]. The instrument response of the system need to be deconvoluted from the measured fluorescence decays [610, 620].

2.5.3.2 FLIM Data Analysis Strategies

FLIM Lifetime Histogram Data Treatment

Fluorescence lifetime imaging involves scanning a sample area and retrieving spatially resolved photon statistics. Therefore, the sample area is divided into a grid, and during scanning each grid element results in a finite time interval, during which photons from that element, i.e., pixel, are collected. Consequently, the storage data structure of FLIM can be represented by a three-dimensional array containing a histogram of photon arrival times for each pixel, with a fixed number of bins. Since the dye at each location is excited

repeatedly by equal laser pulses, emitted photons from previous excitation lead to an overcounting in the histogram after the current pulse. This overcounting is corrected by a subtraction of the extrapolated tail of each curve. To retrieve the tail, an initial best-fit of a redundant number of components, i.e., four in the case of three intrinsic components, is performed. The results also deliver starting values for the IRF parameters, the background noise, and the time shift.

Least Squares Curve Fitting

Least squares curve fitting is one of the most commonly used methods for analyzing FLIM data. The Chi-squared (χ^2) goodness-of-fit test is employed to assess the discrepancy between the fitted curve and the measured data. A mathematical procedure that identifies the best-fitting curve for a given set of points by minimizing the residuals, i.e. the sum of the squares of the deviations ("residuals") of the points from the curve [621, 622]. In FLIM data analysis, the model function is a superposition of multiple exponential decay components (a_i, τ_i) . The parameters of the model (a_i, τ_i) are iteratively adjusted to achieve a Chi-squared value as small as possible, indicating the best fit of the model to the experimental data. This method necessitates several prior assumptions, including that the uncertainty of the experimental data follows a Gaussian distribution [619,623,624], that the number of lifetime components is fixed a priori, that there is a temporal offset between the detected signal and the instrument response, and that there is background fluorescence. The accuracy of this method is also highly dependent on the number of photons detected per pixel: with higher photon counts leading to improved fitting accuracy following the Poisson statistics. The multicomponent exponential decay estimate is then convolved with the IRF in each iterative step and compared with the experimentally measured lifetime decay curve [610,619].

Advanced FLIM Fitting Method (AFFM)

The employed homemade fitting algorithm performs data corrections and includes the estimation of the generally unknown instrument response function, the impulse response of the entire optical system, rigorously including the optical effects of the sample itself. After corrections to the raw histogram, in each iteration, the instrument response function is fixed, and a least-squares fit of the convoluted exponential decay is performed. The IRF is assumed to be Gaussian. The overall parameter set that results in the smallest value of χ^2 is considered the best fit.

Maximum Entropy Method (MEM)

Entropy is a concept that originated in thermodynamics or statistical mechanics, and is used to measure the degree of disorder existing in a thermodynamic system. Recently, a more general concept of entropy has been described in information theory to measure the uncertainty of an information source. Based on this, new methods of statistical analysis have been incorporated into the modern concept of entropy, also known as information-theoretic entropy [617].

2.6 Western Blot

The maximum entropy method aims to find the one solution that leads to the maximum entropy among all possible solutions [617]. This requires a model of the entropy functional depending on the fit parameters. In FLIM analysis, MEM approaches to determine lifetime components treat the signal and noise as distinct entities, and select the solution with the least amount of false information from numerous possible solutions [625,626]. The method used aims at minimizing random errors and noise based on two criteria: firstly, an assumption is made about the shapes of the present peaks, and secondly, the best fit regarding noise is achieved by maximizing the configurational entropy [627–629].

The maximum entropy principle offers a powerful method for extracting model parameters and useful low-dimensional representations of complex, high-dimensional, and limited data [620].

Maximum Entropy Lifetime Method (MELT)

The maximum entropy lifetime method takes the corrected lifetime curve and an instrument response function as input data. The instrument response function is estimated using the AFFM. The entropy function favors a small number of components with high amplitudes while minimizing the deviation to experimental data χ^2 .

During the experiment, three FLIM microscopy systems were used, including (1) TauMap FLIM microscope with a high-NA objective and tunable titanium sapphire laser, (2) Axiovert 200 Fluorescence DIC Phase Contrast Inverted Microscope with a LCI Plan-NEOFLUAR objective and FemtoFiber pro TVISlaser and (3) Leica Fluorescence Lifetime Imaging Microscope. The FLIM data was recorded with a time correlated single photon counting (TCSPC) correspondingly by following equipment: (1) TCSPC card (SPC-150) and a PMT (PMH-100-0), (2) Photon counting module SPCM AQR-14 11206-1 with PicoHarp 300 TCSPC system and (3) 4Tune detectors. The data was processed by Matlab® 2022.

2.6 Western Blot

2.6.1 Protein Quantification

In order to accurately measure the concentration of protein harvested from the cell lysis or ghost preparation, Bradford method or NanoDrop technique was used. Based on the Lambert-Beer law, the absorbance of light with the known molar extinction coefficient of the protein could be used to accurately quantify the amount of protein. Most proteins have a characteristic UV absorption spectrum around 280 nm, predominately from the aromatic amino acids, tyrosine and tryptophan. Therefore, the 280 nm absorbance is commonly used for protein quantification [630,631]. M.M.Bradford found that an interesting property of Coomassie Brilliant Blue G-250 was that binding to proteins resulted in a shift of its absorption maximum to 595 nm. Based on this character of the dye, he developed a reproducible and rapid assay using Coomassie Brilliant Blue G-250 to perform the protein determination by measuring the absorbance of the solution at 595 nm [632,633].

2 Materials and Methods

Spectroscopy is the study of the interaction of light with matter, including reflection, refraction, elastic scattering, absorption, inelastic scattering, and emission [634]. Spectroscopy could be used directly to measure the absorbance of a specific protein solution at 280 nm directly or the absorbance of protein-bound Coomassie Brilliant Blue G-250 at 595 nm. The detailed measurement steps of the Bradford assay are described in Appendix A.1.

Traditional spectroscopy requires samples to be placed into cuvettes or capillaries, which require big measurement volume. In contrast, the NanoDrop technology uses the surface tension to hold and measure microvolume samples between two optical pedestals, allowing the measurement of $0.5 - 10\,\mu$ l volumes [635]. The detailed NanoDrop measurement steps are described in Appendix A.1.

The spectroscopy used for the Bradford assay was a SynergyTM 2 Spectrophotometer and the data was recorded by BioTek's Gen5. The NanoDrop used in the experiment was NanoDropTM 2000/2000c Spectrophotometer and data was recorded by NanoDrop 2000 software. The Protein concentration was calculated by Excel.

2.6.2 Sodium Dodecyl Sulfate Polyacrylamide Gel Electrophoresis (SDS-PAGE)

To detect the protein of interest from a mixture of proteins, the proteins are first separated by sodium dodecyl sulfate polyacrylamide gel electrophoresis (SDS-PAGE). SDS-PAGE can separate proteins according to their size, molecular weight and charges, which determine the speed at which protein molecules move under an electric current. There are two important parts to the SDS-PAGE technique. One is the denaturation of the protein with the detergent sodium dodecyl sulfate (SDS). During the boiling with SDS, protein molecules gain a negative charge proportional to their molecular size, which allows different protein molecules to have equal mobility in an electric field. Another one is polyacrylamide gel electrophoresis (PAGE), which uses an electric current to force protein through a polyacrylamide gel. The speed of protein molecule is inversely related to its size and molecular weight. The molecular weight of the unknown proteins can be estimated by comparing their migration distance with a molecular weight maker [636–639]. Illustrated steps of SDS-PAGE is shown in Figure 2.10. The detailed SDS-PAGE experiment protocol is given in Appendix A.1.

2.6 Western Blot

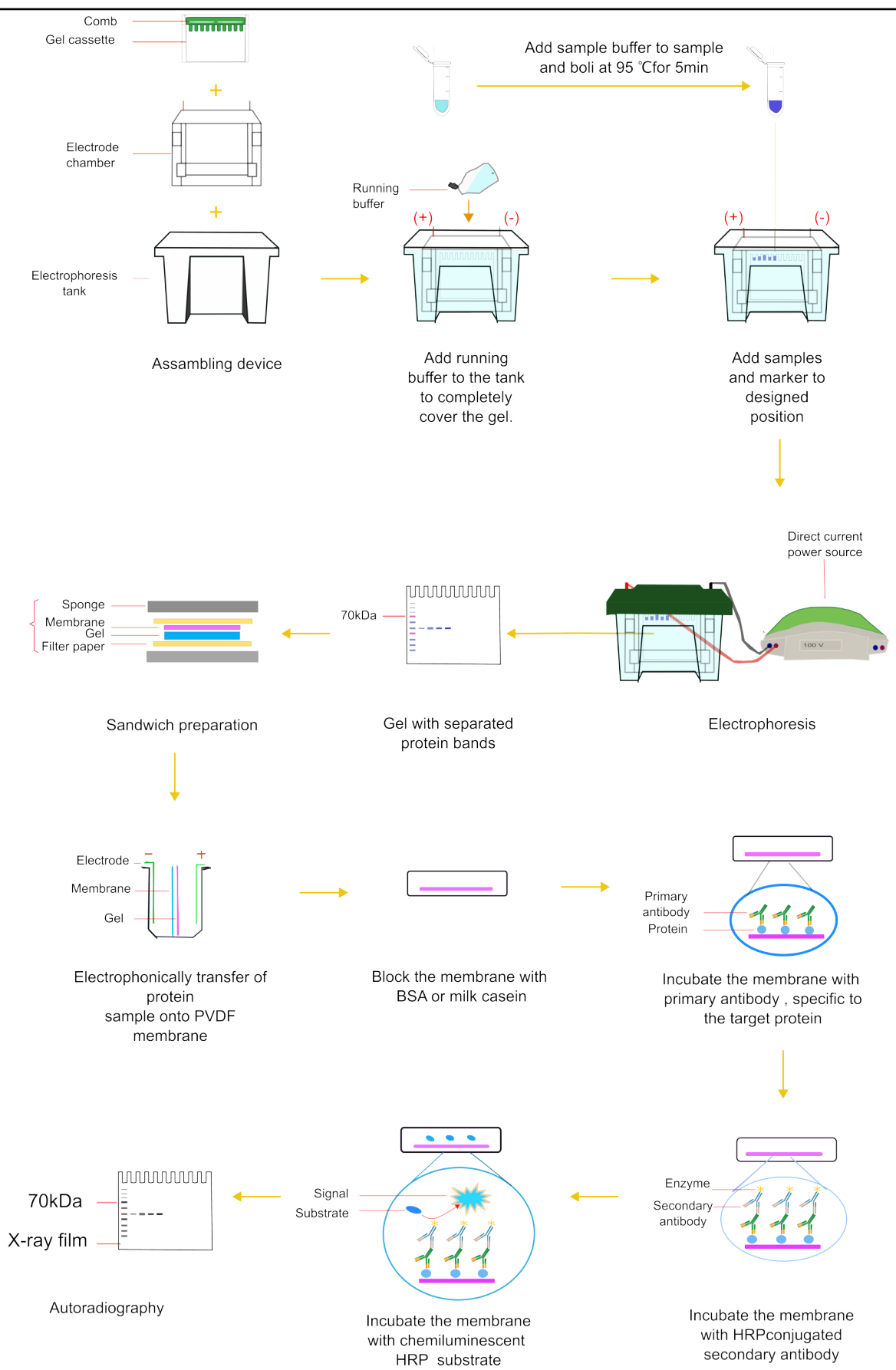


Fig. 2.10: The steps of SDS-PAGE and Western Blot. Proteins are denatured with SDS and separated by electrophoresis. Proteins are then transferred to a PVDF membrane. The membrane is blocked with protein to prevent nonspecific binding, followed by a primary antibody specific for the target protein. After that, a secondary antibody conjugated to a detection enzyme is applied. Then the protein can be visualized by chemiluminescence or colorimetric detection.

2.6.3 Western Blot

After electrophoresis, the separated proteins could be transferred to a membrane by electrophoretic blotting. This method could produce a band for each protein without losing the resolution of the original band pattern. The protein bands transferring allows detection of proteins by autoradiography. The method could also be used to detect specific proteins, when it is combined with immunological procedures. For specific protein detection, all the additional binding capacity of the nitrocellulose membrane must be blocked with excess proteins. Then the specific antibody for the target protein was applied after direct binding by second antibody labeled with a radioactive group or conjugated to fluorescein or to peroxidase. Finally, the complex formed with the target protein could be detected by autoradiography under UV light, or by the peroxidase reaction product [640,641].

The western blot protocol is illustrated in Figure 2.10. The detailed protocol of western blot is given in Appendix A.1. Blot in experiments was imaged with ChemDoc MP and analyzed by Fiji.

2.7 Data Analysis

GraphPad Prism version 10 was used for the statistical analysis and presentation of the data. If data followed a Gaussian distribution (Shapiro-Wilk test), paired t-test or ordinary one-way ANOVA with multiple comparison method was used to test for statistical significance. Data are presented as mean \pm standard error of the mean (SEM) or median \pm 95% CI. If data did not follow a Gaussian distribution, the Wilcoxon test was used for comparisons between two datasets and the Kruskal-Wallis test was used for multiple comparisons within the same dataset. p < 0.05 was considered as significant.

3 Results

3.1 Piezo 1 Channel Investigation

3.1.1 Wild Type Piezo 1 Channel Activation

Influence of Different Yoda 1 Concentration in RBCs

The first experiment was designed to test whether there is a difference in Ca²⁺ signaling upon stimulation with different concentrations of Yoda 1. RBCs from three healthy donors were exposed to 2 µM, 5 µM and 10 µM Yoda 1-containing Tyrode solution and the change in intracellular free Ca²⁺ was used as a read-out parameter. The results of the confocal microscopic measurements using the Ca²⁺-fluorophore Fluo-4 are summarized in Figure 3.1. Compared with the Tyrode solution-only control group, RBCs in the Yoda 1-stimulated groups have significantly higher Fluo-4 fluorescence intensity, indicating a higher intracellular free Ca²⁺ concentration (Fig. 3.1 A-D). The increase has two phases. In the approximately first 60 seconds after Yoda 1 application, there is a slow increase in Ca^{2+} . Subsequently, the Ca^{2+} concentration is increased to a maximum (Fig. 3.1 E). 2 μM and 5 μM Yoda 1 stimulation could reach twice and almost three times higher Fluo-4 intensity than 10 μM Yoda 1. In addition, 5 μM Yoda 1 application can cause higher Ca²⁺ influx than 2 µM Yoda 1, but there is no statistic significant difference (Fig. 3.1 E,F). In addition, the maximum Ca²⁺ concentration after Yoda 1 stimulation shows a bell-shaped relationship as a function of Yoda 1 concentration, and the maximum effect of Yoda 1 is around $5\,\mu\mathrm{M}$ (Fig. 3.1 F). Thus, $5\,\mu\mathrm{M}$ Yoda 1 was selected for further experiments.

Influence of ATP-depletion in Yoda 1-stimulated RBCs

Next, the experiments for testing whether the Ca^{2+} - signaling is altered by Yoda 1 application after plasma membrane Ca^{2+} -ATPase (PMCA) is blocked by ATP depletion. RBCs from healthy donors were kept in glucose-free solution for 16 hours at 4 °C to deplete intracellular ATP storage. According to reference mentioned in methods section 2.2.2, this could lead to reversible ATP depletion in RBCs [576,577,642,643]. In addition, residual ATP in RBCs after incubation was tested once by ATP detection assay, and the amount of residual ATP is below the sensitivity of the ATP detection assay (data not show). ATP depleted RBCs and normal RBCs were then challenged with 5 μ M Yoda 1. The results of the confocal microscopy measurements are shown in Figure 3.2. 5 μ M Yoda 1 can still increase intracellular Ca^{2+} concentration in ATP depleted RBCs (Fig. 3.2 B,D,E). The first phase of the Ca^{2+} increase is faster than it in normal RBCs (Fig. 3.2 E). The maximum Ca^{2+} level in ATP-depleted RBCs after Yoda 1 stimulation is higher than in normal RBCs which is significant (Fig. 3.2 C-F). In addition, the Ca^{2+} concentration decreased

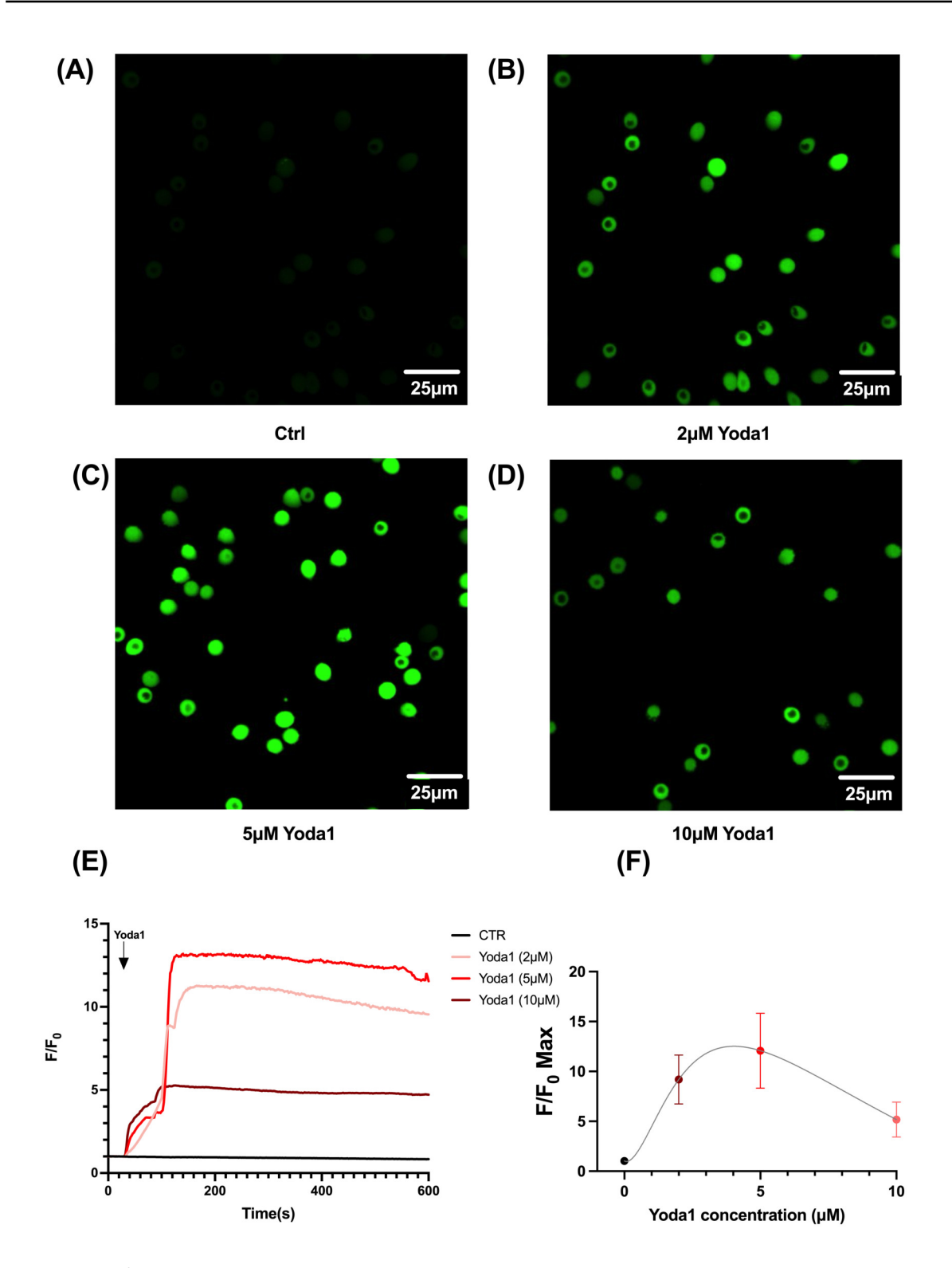


Fig. 3.1: Ca²⁺-signaling of healthy RBCs at different concentrations of Yoda 1 stimulation. (A)-(D) Example of confocal images at 120 seconds of recording with same display range: (A) Control, (B) 2 μM Yoda 1; (C) 5 μM Yoda 1, (D) 10 μM Yoda 1. (E) Cellular Ca²⁺-response is described as median fluorescence intensity trace (F/F₀) of the Ca²⁺-indicator Fluo-4 is plotted over time of all cells. The arrow indicates the time of solution change (30 seconds), (N_{donor}=3, n_{ce11}>50). (F) Analysis of the maximal cellular response (F/F₀). (N_{expeirment}=3). Black-control condition with Tyrode solution; rose: 2 μM Yoda 1; red: 5 μM Yoda 1; dark red: 10 μM Yoda 1. Data is shown as meidan with 95% CI in (F). Statistical differences were evaluated using mixed effect model with Tukey's multiple comparison method. p < 0.05 was deemed significant.

after reaching the plateau is seems slower in ATP-depleted RBCs than in normal RBCs (Fig. $3.2\,\mathrm{E}$). In addition, the ATP-depleted RBCs without Yoda 1 stimulation have slightly increased $\mathrm{Ca^{2+}}$ under the shear stress of the perfusion system compared to the normal RBCs without Yoda 1 stimulation. (Fig. $3.2\,\mathrm{A,B,F}$).

As Yoda 1 is one Piezo 1 agonist, its application could lead to Ca²⁺ entry and eventually the Ca²⁺ level will reach the threshold for Gárdos channel activation. The open probability of Gárdos channels depends on the intracellular Ca^{2+} concentration and a higher open probability leads to K⁺ efflux and hyperpolarization. The Gárdos effects in Yoda 1challenged normal and ATP-depleted RBCs were tested by the MBE-method and the results are shown in Figure 3.3. Yoda 1 stimulation results in hyperpolarization in both normal RBCs and ATP-depleted RBCs (Fig. 3.3 A). The resting membrane potential of ATP-depleted RBCs $(-17.2 \pm 1.6 \,\mathrm{mV})$ is slightly less negative than normal RBCs $(-19.7 \pm$ 0.3 mV) (Fig. 3.3 B). The ATP-depleted RBCs achieve a significantly higher maximum hyperpolarization $(-76.3 \pm 3.3 \,\mathrm{mV})$ and the slightly higher hyperpolarization magnitudes $(-59.1 \pm 4.1 \,\mathrm{mV})$ than normal RBCs $(-74.1 \pm 4.4 \,\mathrm{mV})$ for maximum hyperpolarization and $-54.4 \pm 4.1 \,\mathrm{mV}$ for hyperpolarization magnitudes) (Fig. 3.3 C,D). In addition, the ATPdepleted RBCs have an about 11% higher hyperpolarization rate (Fig. 3.3 E) and 8% shorter hyperpolarization time (Fig. 3.3 F). However, the normal RBCs stay longer in maximum hyperpolarization state than ATP-depleted RBCs (Fig. 3.3 G). When compared to the depolarized state, normal RBCs have a similar depolarization rate to ATP-depleted RBCs (Fig. 3.3 I), but ATP-depleted RBCs require more time to reach the new membrane potential plateau (Fig. 3.3 H). The results show that removing ATP storage in RBCs could increase the speed of first stage of Ca²⁺ entry and the maximum Ca²⁺ concentration in RBCs after Yoda 1 challenge. However, ATP depletion would neither influence the membrane potential change induced by Yoda 1 stimulation nor the resting membrane potential.

Influence of Gárdos Channel Inhibition in Yoda 1-stimulated RBCs

The effects of Gárdos channel inhibition on the Yoda 1-induced change in Ca²⁺-signaling were then tested with normal RBCs and ATP-depleted RBCs pre-treated with the Gárdos channel inhibitor Tram-34. After Gárdos channel inhibition, the rate of the first stages of the Ca²⁺ concentration increase is slower than in RBCs without Gárdos channel inhibition. But the rate of the second stages of the Ca²⁺ concentration increase shows opposite trend (Fig. 3.41). The first phase of the Yoda 1-induced increase in Ca²⁺ concentration is faster in Tram-34-pretreated ATP-depleted RBCs than in Tram-34-pretreated normal RBCs (Fig. 3.41). Gárdos channel-inhibited RBCs can also reach higher intracellular Ca²⁺ concentration after Yoda 1 stimulation, with about 2.5 times higher Fluo-4 intensity in normal RBCs and 1.5 times higher Fluo-4 intensity in ATP-depleted RBCs (Fig. 3.4 A,D,E,H,I). Compared to ATP-depleted RBCs and normal RBCs with Yoda 1 stimulation and Gárdos channel inhibition, there is a 35% increase in Fluo-4 intensity in ATP-depleted RBCs (Fig. 3.4). However, after reaching the highest intracellular Ca²⁺ concentration, the Ca²⁺ level in Gárdos channel-inhibited RBCs decreases more rapidly (Fig. 3.4 I). In addition, either normal RBCs or ATP depleted RBCs have a slightly increased intracellular Ca²⁺ concentration after Tram-34 application under shear stress from perfusion system (Fig. 3.4 C,G,I,J).

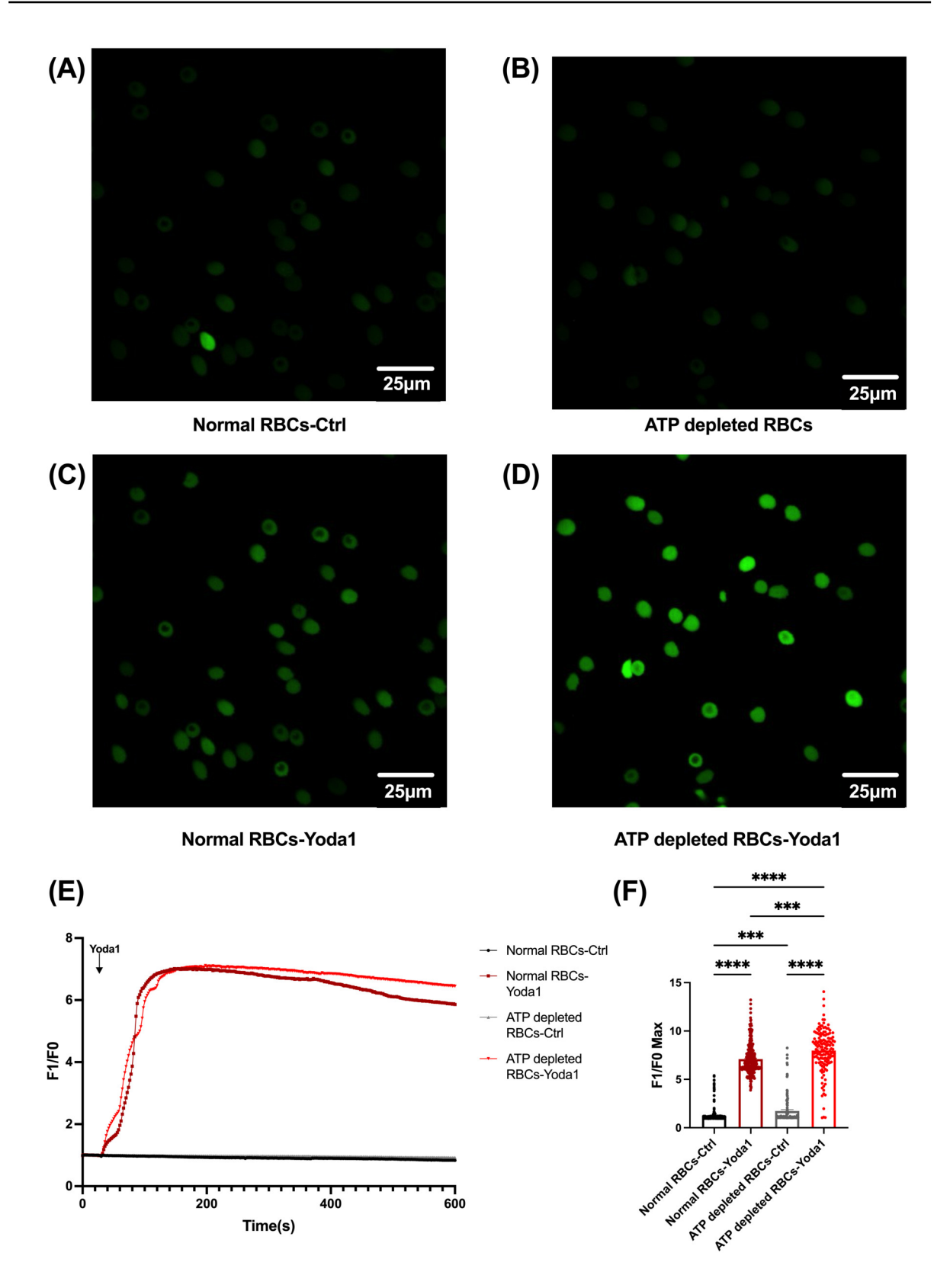


Fig. 3.2: Ca²⁺-signaling of healthy RBCs and ATP-depleted RBCs with 5 μM Yoda 1 stimulation. (A) –(D) Example of confocal images at 220 seconds recording with same display range in different conditions: (A) Normal RBCs, (B) Normal RBCs with 5 μM Yoda 1, (C) ATP-depleted RBCs, (D) ATP-depleted RBCs with 5 μM Yoda 1. (E) The median fluorescence trace (F/F₀) over time of all cells is depicted in different conditions. Yoda 1 was added at 30 seconds after the start of the recording as indicated by the arrow. (N_{expeirment}=6, n_{cell}>50). (F) Statistical analysis of cellular maximal response (F/F₀)(N_{expeirment}=6). Black: normal RBCs with Tyrode solution, dark red: normal RBCs with 5 μM Yoda 1, gray: ATP depleted RBCs with Tyrode solution, light red: ATP-depleted RBCs with 5 μM Yoda 1. Data is shown as means ± SEM in (F). Statistical differences were evaluated using mixed effect model with Tukey's multiple comparison method. p < 0.05 was deemed significant.

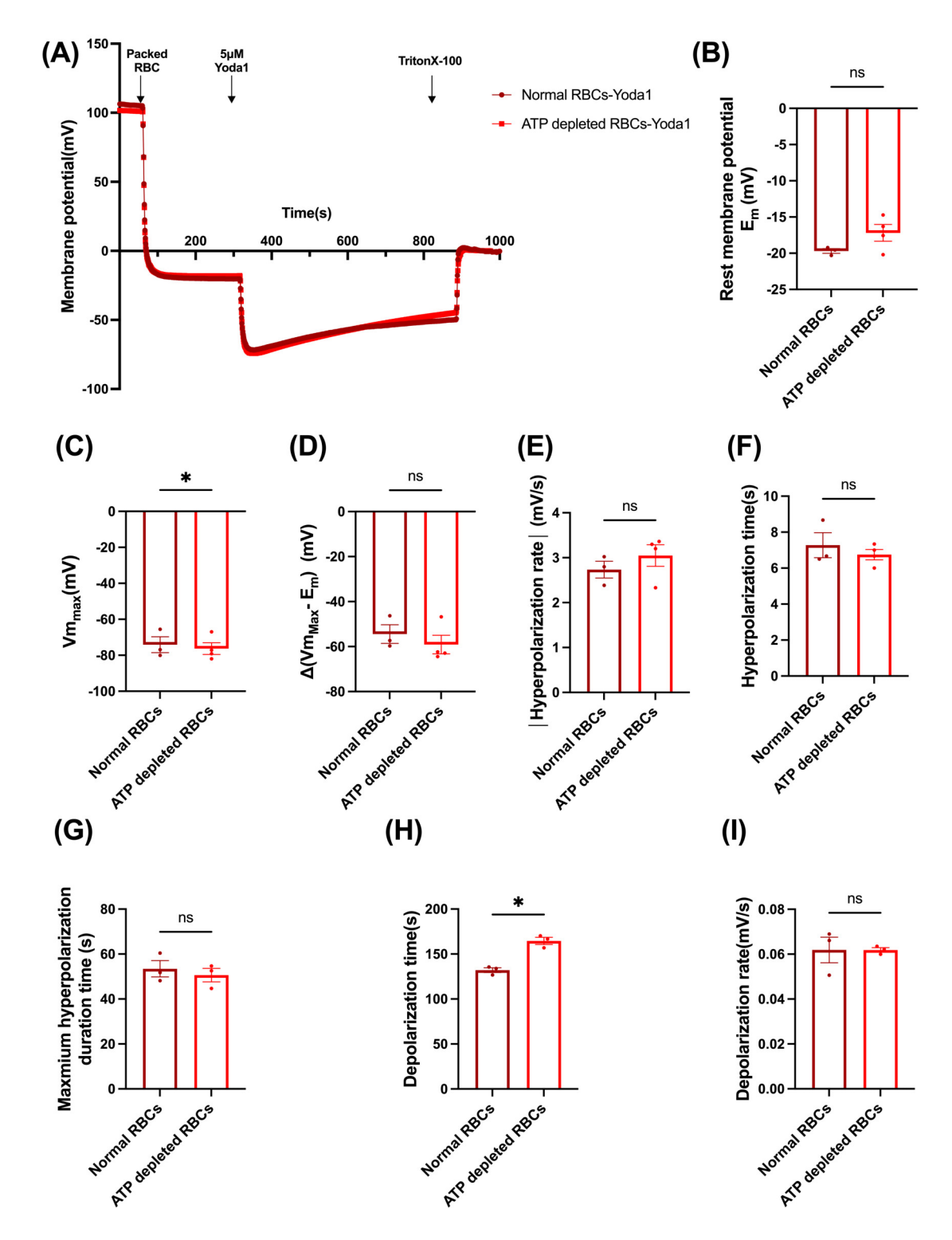


Fig. 3.3: Yoda 1 effects on membrane potential in normal RBCs and ATP-depleted RBCs. (A) Representative traces for the changes of membrane potential after application of $5\,\mu\mathrm{M}$ Yoda 1 in normal RBCs (dark red trace) and ATP-depleted RBCs (light red trace); Arrows indicate when packed RBCs, Yoda 1 and TritonX-100 were added to the measurement system. (B)-(I) Statistical comparison: (B) Resting membrane potential (E_{m}); (C) Maximal hyperpolarization (V_{Max}); (D) Hyperpolarization magnitudes ($\Delta(V_{\mathrm{Max}}^{-}-E_{\mathrm{m}})$) are obtained after subtracting the resting membrane potential (E_{m}) from the maximal hyperpolarization (V_{Max}) reached at each condition; (E) Absolute hyperpolarizing rate; (F) Hyperpolarizing time; (G) Duration time of hyperpolarization plateau; (H) Depolarization rate; (I) Depolarization time ($V_{\mathrm{Max}}^{-}-E_{\mathrm{m}}^{-}$). Data is shown as means \pm SEM in (B) - (F). Statistical differences were evaluated using paired T-tests. p < 0.05 was deemed significant.

Tram-34, as a Gárdos channel inhibitor, is able to reduce the maximal hyperpolarization induced by Yoda 1 application. There are two hyperpolarization peaks in Gárdos channel inhibited RBCs, a small quick hyperpolarization and a larger and slower hyperpolarization after (Fig. 3.5 A). The maximum hyperpolarization and hyperpolarization magnitudes in Tram-34 -treated group is much less than other groups (Fig. 3.5 A,C,D). Comparing the hyperpolarization rate in Tram-34 treated groups to the groups without Tram-34 inhibition, Tram-34-inhibited groups have hyperpolarization rate close to $0\,\mathrm{mV/s}$ (Fig. 3.5 E). In addition, Tram-34 pretreatment could cause resting membrane potentials slightly less electronegative but this is not statistically significant (Fig. 3.5 B).

The results show the inhibition of the Gárdos channel could lead to higher maximum concentration induced by Yoda 1 but the RBCs cannot maintain the high Ca²⁺ level for long time. The hyperpolarization caused by Yoda 1 application mainly rely on the Gárdos channel opening. But there seems to be some other factors contributing to the hyperpolarization.

Influence of CI⁻ Conductance Inhibition in Yoda 1-stimulated RBCs

The Cl⁻ conductance is very important in the regulation of cell volume and intracellular pH in RBCs. To investigate whether Cl⁻ conductance influences the Yoda 1 induced Ca²⁺signaling in normal and ATP-depleted RBCs. 10 µM NS3623, the Cl⁻ conductance inhibitor, was applied to normal RBCs and ATP-depleted RBCs 1 hour prior to Yoda 1 stimulation. As shown in the confocal images, Yoda 1 can still induce Ca²⁺ entry after Cl⁻ conductance inhibition in both normal RBCs and ATP-depleted RBCs (Fig. 3.6 A,D,E,H). However, instead of a two-phase Ca²⁺ increase in Ca²⁺ concentration with Yoda 1 stimulation alone, the increase in intracellular Ca²⁺ concentration in NS3623 treated RBCs is slower and there is only one phase (Fig. 3.61). The Yoda 1-only groups reach the maximum Ca²⁺ concentration around 120 seconds after the Yoda 1 application. However, it takes almost 360 seconds to reach the maximum Ca²⁺ concentration induced by Yoda 1 in NS3623 treated RBCs (Fig. 3.61). The maximum Ca²⁺ concentration induced by Yoda 1 in NS3623 treated groups is significantly lower than Yoda 1-only simulated groups with almost half Fluo-4 intensity (Fig. 3.6 B,D,F,H,I,J). When ATP depletion and Cl⁻ conductance inhibition are combined, the maximum Ca²⁺ concentration induced by Yoda 1 is higher than in NS3623-pretreated normal RBCs with a 23% increase in Fluo-4 intensity, and the highest Ca²⁺ concentration could be maintained for a longer time (Fig. 3.6 I,J). However, Cl⁻ conductance inhibition does not cause an increased intracellular Ca²⁺ under shear stress from perfusion system (Fig. 3.6 C,G,I,J).

The Cl⁻ is the dominating ion in RBCs for establishing the resting membrane potential and it is important for RBCs membrane potential changes as well. The effects of the Cl⁻ conductance on hyperpolarization induced by Yoda 1 were tested using the MBE-method. Yoda 1 could induce more hyperpolarization (qty-107.4 ± 0.9 mV) in Cl⁻ conductance inhibited normal RBCs compared to normal RBCs without NS3623 pretreatment ($-77.9 \pm 5.5 \,\text{mV}$). Similarly, the hyperpolarization ($-104.7 \pm 1.6 \,\text{mV}$) in ATP-depleted RBCs with Cl⁻ conductance inhibition is higer than ATP-depleted RBCs without NS3623 treatment (Fig. 3.7 C). The magnitude of hyperpolarization is higher in Cl⁻ conductance inhibited RBCs as well ($-93.7 \pm 1.1 \,\text{mV}$ in normal RBCs with NS3623 and $-91.9 \pm 0.7 \,\text{mV}$ in ATP-

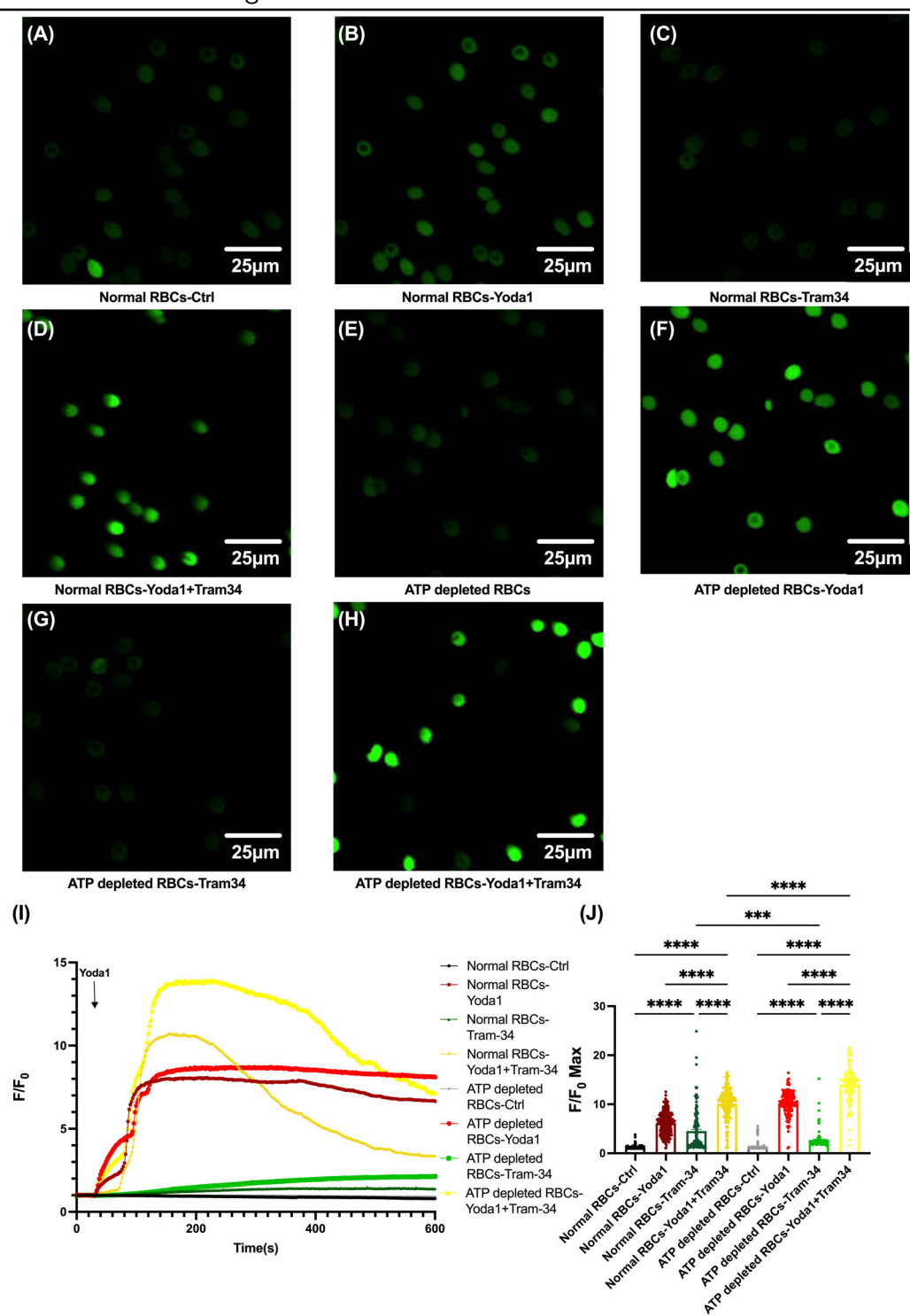


Fig. 3.4: Effects of Gárdos-channel pre-inhibition on Ca^{2+} -signaling of healthy and ATP-depleted RBCs with Yoda 1 stimulation. (A)-(H) Examples of confocal images at 160 seconds after recording started in different conditions: (A) Normal RBCs, (B) Normal RBCs with 5 μM Yoda 1, (C) Normal RBCs with 10 μM Tram-34, (D) Normal RBCs with 10 μM Tram-34 and 5 μM Yoda 1, (E) ATP-depleted RBC, (F) ATP-depleted RBCs with 5 μM Yoda 1, (G) ATP-depleted RBCs with 10 μM Tram-34, (H) ATP-depleted RBCs with 10 μM Tram-34 and 5 μM Yoda 1. (I) The median fluorescence traces (F/F₀) over time of all cells are shown. Yoda 1 was added 30 s after the start of the recording, as indicated by the arrow. (J) Statistical analysis of the maximum cellular response (F/F₀). Black: normal RBCs, dark red: normal RBCs with 5 μM Yoda 1, dark green: normal RBCs with 10 μM Tram-34, dark yellow: normal RBCs with 10 μM Tram-34 and 5 μM Yoda 1, gray: ATP-depleted RBC, light red: ATP-depleted RBCs with 5 μM Yoda 1, light green: ATP-depleted RBCs with 10 μM Tram-34, yellow: ATP-depleted RBCs with 10 μM Tram-34 and 5 μM Yoda 1, N_{donor}=3, n_{cell}>50). Data is shown as means \pm SEM in (F). Statistical differences were evaluated using mixed effect model with Tukey's multiple comparison test. p < 0.05 was deemed significant.

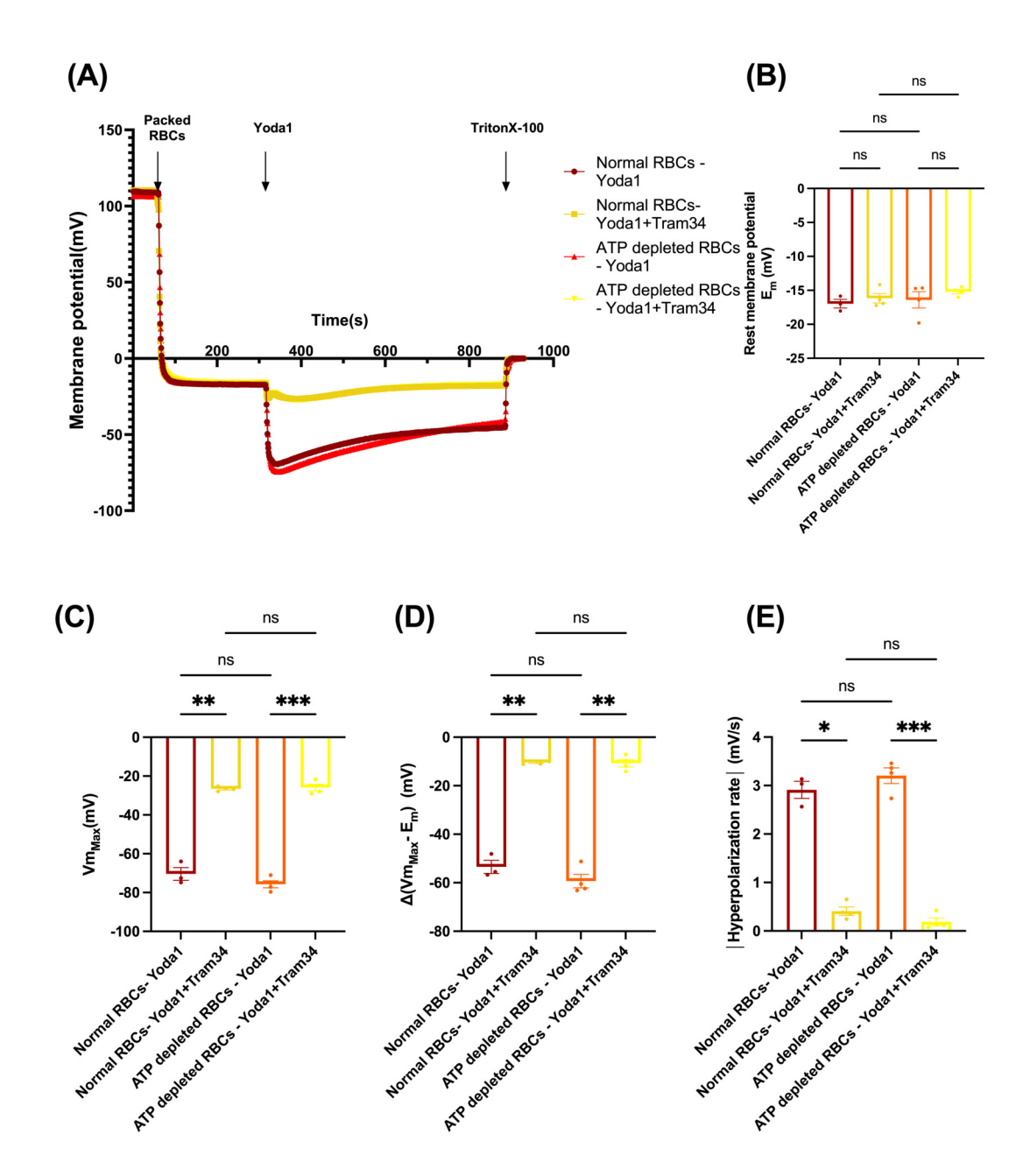


Fig. 3.5: Effects of pre-Gárdos-channel inhibition on membrane potential in normal and ATP-depleted RBCs. (A) Representative traces for the variations of membrane potential after injection of 5 μM Yoda 1 in normal RBCs (dark red), ATP-depleted RBCs (light red), Tram-34 pretreated normal RBCs (dark yellow) and Tram-34 pretreated ATP-depleted RBCs (yellow); Arrows indicate when packed RBCs, Yoda 1 and TritonX-100 were added into the measurement system. (B)-(E) Statistical comparison of multiple parameters at different conditions: (B) Resting membrane potential (E_m); (C) Maximal hyperpolarization (Vm_{Max}); (D) Hyperpolarization magnitudes ($\Delta(Vm_{Max}-E_m)$) are obtained by subtracting resting membrane potential (E_m) from the maximal hyperpolarization (Vm_{Max}) achieved at each condition; (E) Hyperpolarization rate ($N_{donor}=3$). Data is shown as means ± SEM in (B)-(E). Statistical differences were evaluated using mixed effect model with Tukey's multiple comparison method. p < 0.05 was deemed significant.

depleted RBCs with NS3623) (Fig. 3.7 D). However, when comparing Cl⁻ conductance inhibited normal and ATP-depleted RBCs with, there is no difference in either maximal hyperpolarization or hyperpolarization magnitude (Fig. 3.7 A,C,D).

The hyperpolarization rate is greater in NS3623 treated groups (65% faster in normal RBCs and 56% faster in ATP-depleted RBCs) (Fig. 3.7 E). In contrast, the rate of depolarization is slower in the NS3623 treated groups (20% slower in normal RBCs and approximately 30% slower in ATP-depleted RBCs) (Fig. 3.7 G). However, the hyperpolarizing time and depolarizing time does not differ with or without Cl⁻ conductance inhibition (Fig. 3.7 F,H). Furthermore, there is no difference in hyperpolarization rate, depolarization rate, hyperpolarizing time and depolarizing time between normal and ATP depleted RBCs (Fig. 3.7 E-H).

The results show the short time inhibition of Cl^- conductance can slow the Ca^{2+} entry into RBCs and decrease the maximum intracellular Ca^{2+} concentration induced by Yoda 1 stimulation. The inhibition of Cl^- conductance for short time does not change the resting membrane potential of RBCs yet but can enhance the hyperpolarization caused by Yoda 1 application.

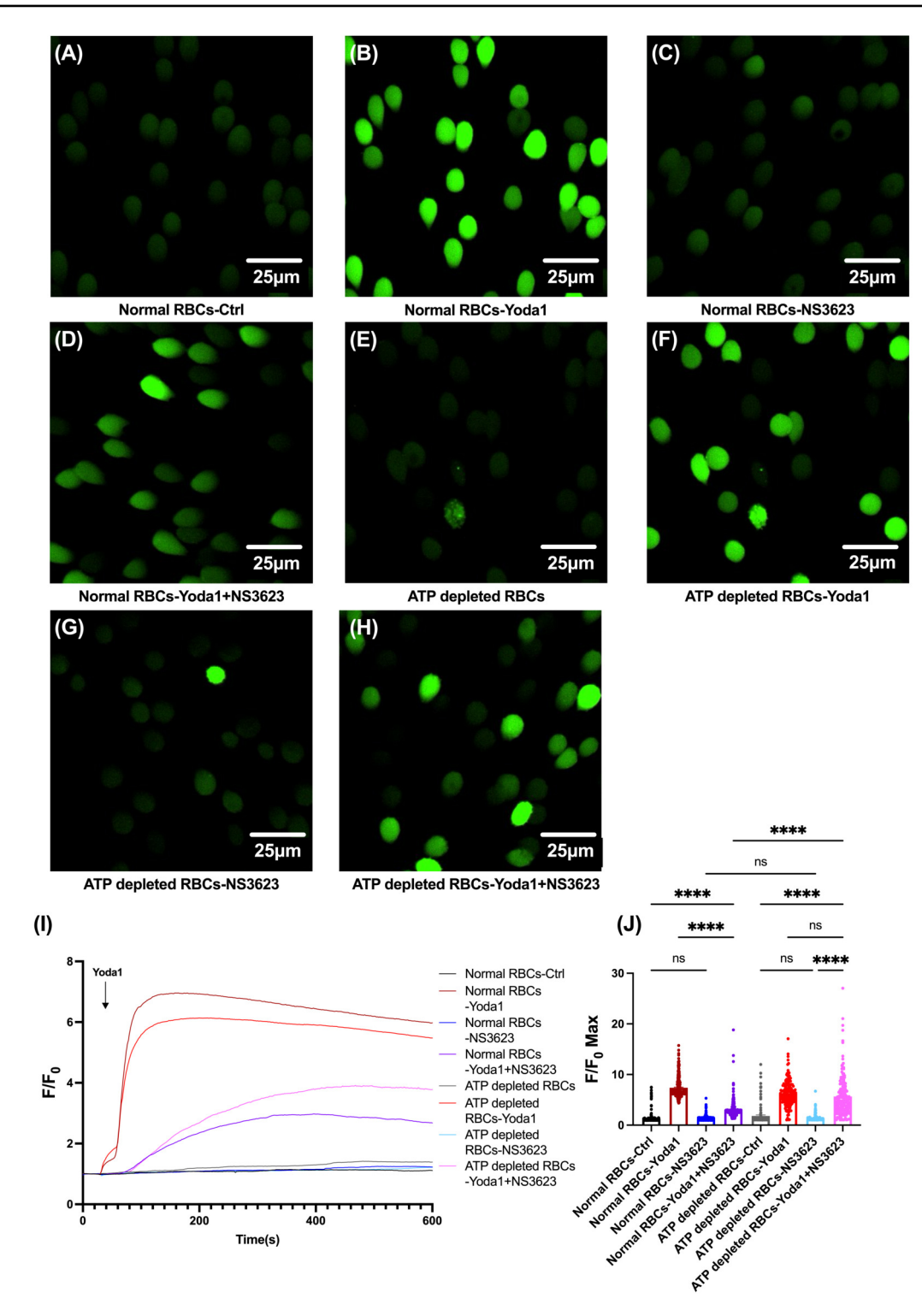


Fig. 3.6: Effects of pre-Cl¯-conductance inhibition influences on Ca²+-signaling of healthy RBCs and ATP-depleted RBCs with of Yoda 1 stimulation. (A)-(H) Example of confocal images at 400 seconds in different conditions: (A) Normal RBCs, (B) Normal RBCs with 5 μ M Yoda 1, (C) Normal RBCs with 10 μ M NS3623, (D) Normal RBCs with 10 μ M NS3623 and 5 μ M Yoda 1, (E) ATP-depleted RBC, (F) ATP-depleted RBCs with 5 μ M Yoda 1, (G) ATP-depleted RBCs with 10 μ M NS3623, (H) ATP-depleted RBCs with 10 μ M NS3623 and 5 μ M Yoda 1. (I) The median fluorescence traces (F/F0) over time of all cells are shown. Yoda 1 was added 30 seconds after the start of the recording, as indicated by the arrow. (J) Statistical analysis of maximum cellular response (F/F0). Black: normal RBCs, dark red: normal RBCs with 5 μ M Yoda 1, dark blue: normal RBCs with 10 μ M NS3623, dark purple: normal RBCs with 10 μ M NS3623 and 5 μ M Yoda 1, gray: ATP depleted RBC, light red: ATP-depleted RBCs with 10 μ M NS3623and 5 μ M Yoda 1. (Ndonor=3, ncell>50). Data is shown as means \pm SEM in (F). Statistical differences were evaluated using mixed effect model with Tukey's multiple comparison method. p < 0.05 was deemed significant.

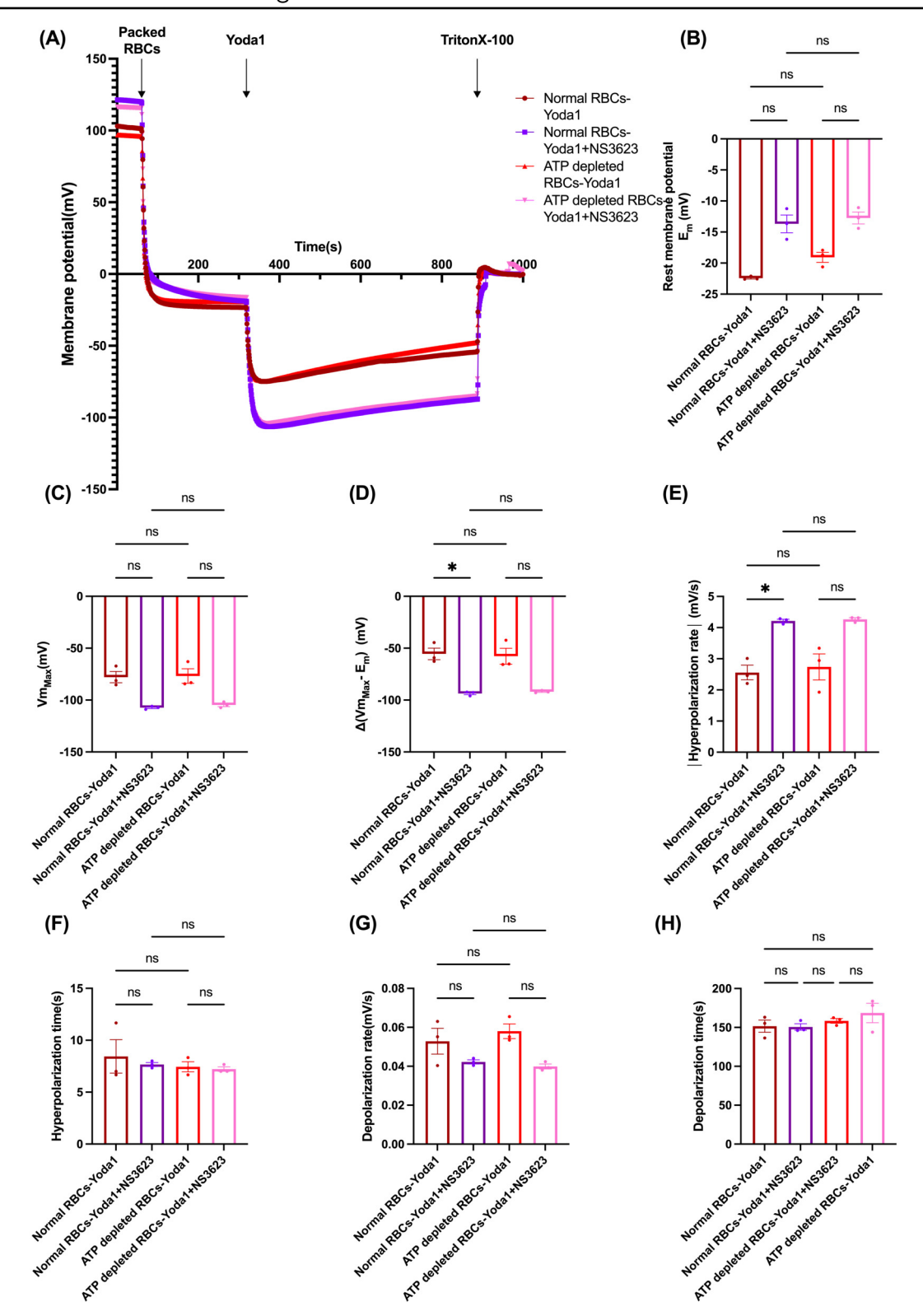


Fig. 3.7: Effects of pre-inhibition of the Cl⁻-conductance on membrane potential in normal and ATP-depleted RBCs. (A) Representative traces for the variations of membrane potential after injection of 5 µM Yoda 1 in normal RBCs (dark red), ATP depleted RBCs (light red), NS3623 pretreated normal RBCs (dark purple) and NS3623 pretreated ATP depleted RBCs (pink). Arrows indicate when packed RBCs, Yoda 1 and TritonX-100 were added into the measurement system. (B) Resting membrane potential (E_m); (C) Maximal hyperpolarization (Vm_{Max}); (D) Hyperpolarization magnitudes (Δ (Vm_{Max}-E_m)) are obtained after the deduction of resting membrane potential (E_m) from the maximal hyperpolarization (Vm_{Max}) reached at each condition; (E) Hyperpolarization rate; (F) Hyperpolarization time; (G) Depolarization rate; (H) Depolarization time. (N_{donor}=3). Data is shown as means ± SEM in (B)-(H). Statistical differences were evaluated using one-way ANOVA test with Tukey's multiple comparison method in (C)-(E). For (B), (F), (G) and (H), statistical differences were evaluated using one-way ANOVA test with Holm-Šídák multiple comparison method, p < 0.05 was deemed significant.

3.1.2 Genetic Variants of the Piezo 1 Channel

3.1.2.1 The Combination of Mutations of Piezo 1 and Spectrin

The female pediatric patient inherits the Piezo 1 mutation p.Asp710Asn from her mother and the spectrin alpha mutation p.Gln2002Ter from her father. The patient underwent splenectomy at the end of 2022. Blood samples were taken twice before and once after the date of splenectomy. Blood samples from these family members and healthy controls were transported to our laboratory and reached it within 10 hours after blood collection. To investigate the effects of these mutations on the physiological function of RBCs and the effects of splenectomy on the quality of RBCs, the Ca²⁺-signaling induced by Yoda 1 was measured using a flow cytometry and confocal microscopy (Fig. 3.8). Before the pediatric patient underwent splenectomy, the pediatric patient's Fluo-4 stained RBCs have different sizes and shapes and are brighter under the microscope compared to others (Fig. 3.8 Ba-Bd). The average basal Ca²⁺ level of the pediatric patient's RBCs is higher than that of the control or her parents. Her mother, who also has the Piezo 1 variant, has RBCs with a slightly higher basal Ca²⁺ than the controls and the father. The father, who has the spectrin mutation, has the lowest base Ca²⁺ (Fig. 3.8 Aa,Bi,Ca). With 1 μM Yoda 1 stimulation, before the surgery, the mean Ca²⁺ concentration of the pediatric patient's RBCs is higher than the others after 1 minute and 5 minutes and the father's RBCs have the lowest Ca²⁺ level (Fig. 3.8 Ac, Ae, Cb, Cc). After surgery, the basal Ca²⁺ level of the pediatric patient's RBCs is similar to that of the control and the parents, and the variation of the pediatric patient 's RBC size is smaller than before surgery (Fig. 3.8 Ab, Be-Bi, Ca). In contrast to the pre-surgery conditions, the pediatric patient's RBCs do not show much difference in intracellular Ca²⁺ concentration compared to the others after Yoda 1 stimulation (Fig. 3.8 Ad, Af, Cb, Cc). The samples were also challenged with 5 µM Yoda 1. The results showed similar trend (Fig. A.1).

The data shows the Piezo 1 mutation p.Asp710Asn only can cause the basal intracellular Ca²⁺ concentration increase but the spectrin alpha mutation p.Gln2002Ter alone seems to lead to decreased intracellular free Ca²⁺ in basal condition. The combination of two mutation in RBCs could lead to boost of basal intracellular Ca²⁺ and the bigger response to Yoda 1 stimulation. The spectrin alpha mutation can also lead to cell size and shape variations. With combination of Piezo 1 mutation, the variation of RBCs size and shape are bigger. After splenectomy, the effects of the double mutation on RBCs seem to be diminished.

3.1.2.2 A Piezo 1 Channel Mutation in a Thalassemia Patient

The patient has thal assemia β CD39 (C>T) variant and p.Arg1940Gln mutation in the Piezo 1 gene. The Piezo 1 mutation p.Arg1940Gln is a novel variant with unknown significance in Piezo 1 function. To understand how the Piezo 1 mutation affects on the Ca²⁺-signaling in thal assemia β RBCs, blood samples from the patient, 1 thal assemia β patient and 1 healthy control were shipped over night. The thalassemia β patient has same CD39 (C>T) variant as the patient but does not have any additional mutation. The RBCs were then challenged with two different concentrations of Yoda 1 and the change in intracellular free Ca²⁺ was used as a read-out parameter. The results of the flow-cytometry measurements using the Ca²⁺-indicator Fluo-4 are summarized in Figure 3.9.

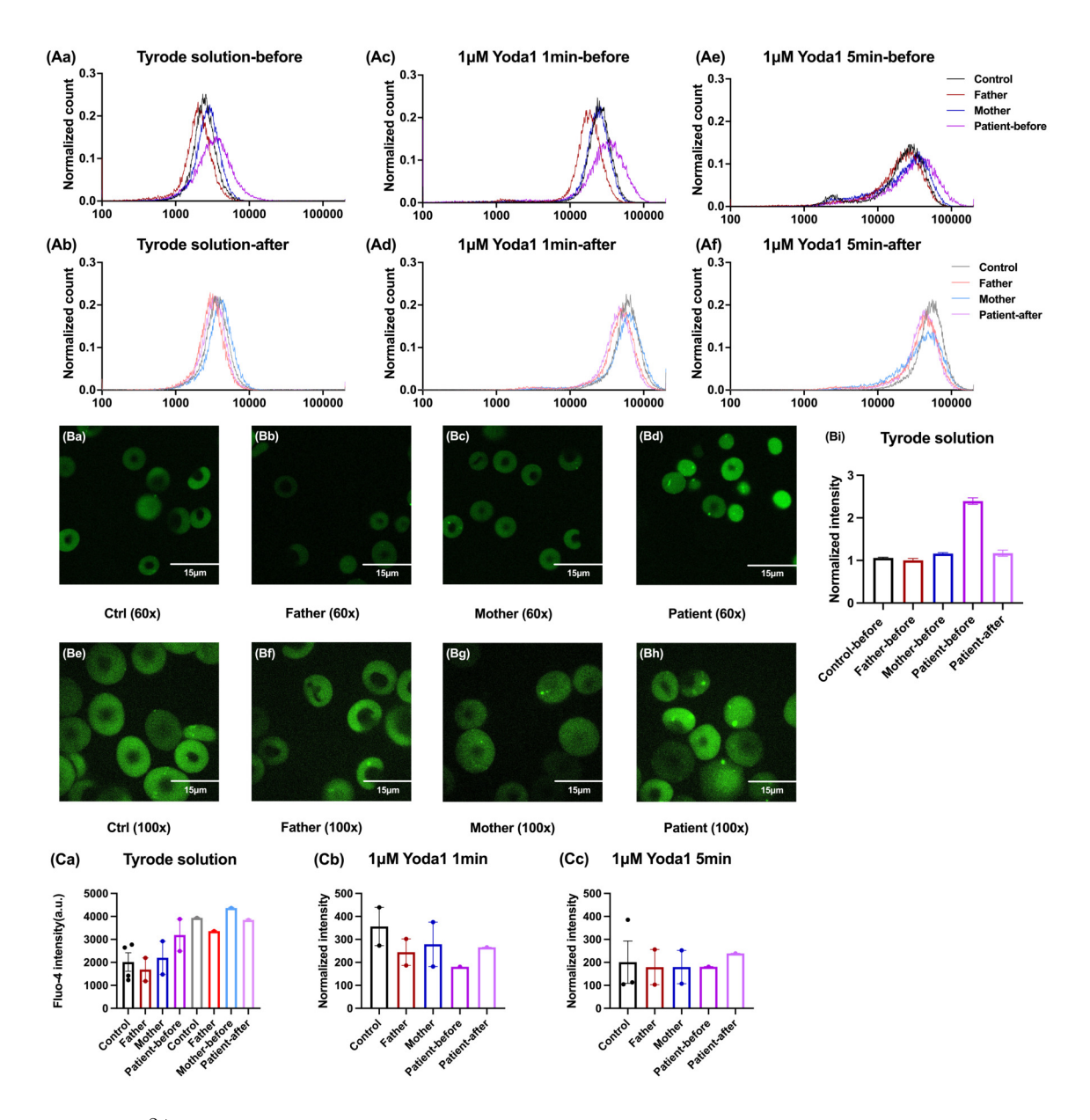


Fig. 3.8: Ca²⁺-signaling in RBCs from a Piezo 1 and spectrin double mutation pediatric patient, family members of the patient and healthy controls under different conditions. (A) Representative normalized histograms of Fluo-4 intensity of controls (black and gray trace), father (dark red or light red trace), mother (dark blue or light blue trace) and the pediatric patient (patient) (dark purple or light purple trace) in different conditions. Darker color for samples taken before the date of splenectomy of the patient and lighter color for samples taken after the date of splenectomy. (Aa)–(Ab) Samples in Tyrode solution. (Ac) – (Ad) Samples after 1 µM Yoda 1 stimulation for 1 minute. (Ae)-(Af) Samples after 1 µM Yoda 1 stimulation for 5 minutes. (B) Example of confocal images for each sample and comparison of Fluo-4 intensity before and after the date of splenectomy. (Ba)-(Bd) displayed in same range with 60x magnification and samples taken before the date of splenectomy: (Ba) Control, (Bb) Father, (Bc) Mother and (Bd) Patient. (Be)-(Bh) displayed in same range with 100x magnification and samples taken after the date of splenectomy: (Be) Control, (Bf) Father, (Bg) Mother and (Bh) Patient. (Bi) Normalized Fluo-4 intensity measured by confocal imaging in Tyrode solution. (C) Statistical analysis of average Fluo-4 intensity measured by flow cytometry in different conditions. (Ca) Fluo-4 intensity measured in Tyrode solution. (Cb)-(Cc) Fluo-4 intensity measured after 1 µM Yoda 1 stimulation $after \ (Cb) 1 \ minute \ and \ (Cc) \ After \ 5 \ minutes. \ (N_{control-donor} = 5, \ N_{father-sampling} = 3, \ N_{mother-sampling} = 3, \ N_{mother-s$ N_{patient-sampling-before}=2, N_{patient-sampling-after}=1, n_{cell-flow cytometry}>30,000, n_{cell-confocal}>50). Data is shown as means ± SEM in (Bi)-(Cd). The sampling number of patient were smaller than 3, thus, the statistical analysis was not applied.

The basal Ca²⁺ level is lowest in the thalassemia patient without Piezo 1 mutation. The control also has low intracellular Ca²⁺ compared to the patient with both thalassemia mutation and Piezo 1 mutation. The thalassemia patient with the Piezo 1 mutation has also greater variation among RBCs (Fig. 3.9 A,B). When RBCs are challenged with Yoda 1, the Piezo 1 activator, both the average Fluo-4 intensity and the high Ca²⁺ population increase in all the samples (Fig. 3.9). The RBCs stimulated with 5 µM Yoda 1 have similar Fluo-4 intensity as 1 µM Yoda 1 application from the same donor but there are higher percentage of high Ca^{2+} population in RBCs with $5\,\mu\mathrm{M}$ Yoda 1 challenging (Fig. 3.9 C-F). The average Fluo-4 intensity decreased over time but the percentage of high Ca²⁺ population maintain the similar level within 5 minutes after Yoda 1 application (Fig. 3.9 E,F). Compared to the healthy control and the thalassemia patient without Piezo 1 mutation, the thalassemia patient with the Piezo 1 mutation has a significant higher average Fluo-4 intensity after Yoda 1 stimulation (Fig. 3.9 C,E). In addition, the thalassemia patient without the Piezo 1 mutation has the lowest average Fluo-4 intensity (Fig. 3.9 C,E). In contrast, the patient with Piezo 1 mutation has the smallest percentage of high Ca²⁺ population. The healthy control has higher percentage of high Ca²⁺ population than that of the thalassemia patient without Piezo 1 mutation. (Fig. 3.9 D,F).

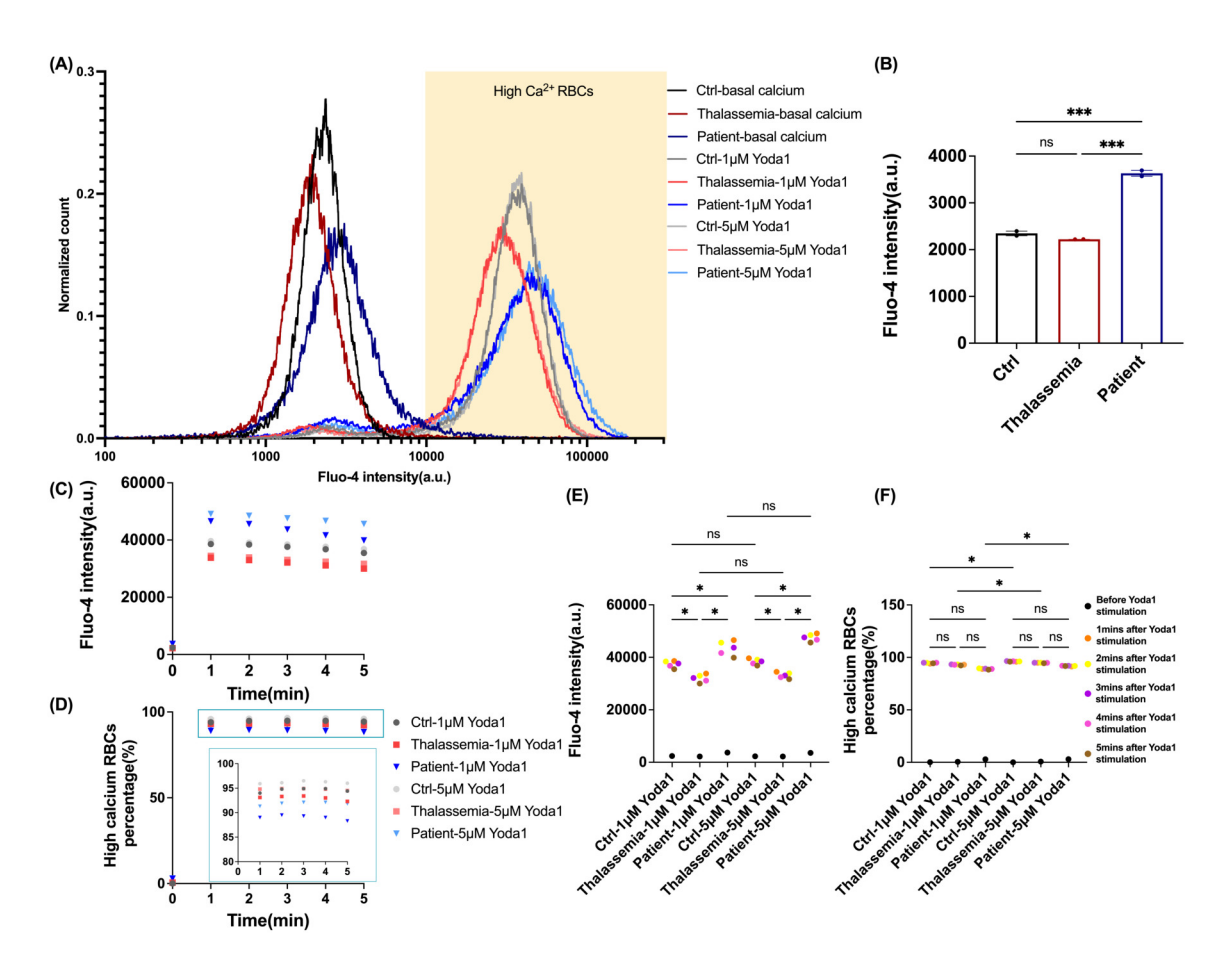


Fig. 3.9: The results of the flow-cytometry measurements of Ca^{2+} -signaling in RBCs from patient and controls. (A) Representative normalized histograms of Fluo-4 intensity of control (black black and gray traces), thalassaemia β only patient (red traces) and the Piezo 1 mutant thalassemia patient (blue traces). in different conditions. (Darkest colors for samples in Tyrode solution without any additional stimulation, darker colors for samples with 1 μ M Yoda 1 stimulation and lightest colors for samples with 5 μ M Yoda 1 stimulation). (B)-(H) Statistical analysis of flow cytometry results. (B) Average Fluo-4 intensity comparison of RBCs in Tyrode solution. (C) Average Fluo-4 intensity change over time. (D) Percentage change of high Ca^{2+} RBCs population over time. (E) Average Fluo-4 intensity change in different conditions; (F) Percentage change of high Ca^{2+} RBCs population in different conditions ($n_{cell} > 30,000$). Data is shown as means \pm SEM in (B) and data is shown as mean in (C)-(H). Statistical differences were evaluated using one-way ANOVA test with Tukey's multiple comparison method. p < 0.05 was deemed significant.

3.2 Gárdos Channel Activation and Intracellular Ca²⁺

Activation of the Gárdos channel causes K^+ loss, followed by Cl^- and water loss, leading to cell shrinkage. Cell shrinkage causes a reduction in cell volume and shape, creating mechanical stress on the cell membrane, which could activate the Piezo 1 channel and increase intracellular Ca^{2+} . In addition, Gárdos channel opening causes a change in membrane potential, which could induce voltage-dependent channel opening, in particular $Ca_v 2.1$, to affect intracellular Ca^{2+} concentration. To investigate the effects of Gárdos channel activation on intracellular Ca^{2+} concentration, the healthy RBCs were challenged with $100\,\mu\mathrm{M}$ NS309 or $10\,\mu\mathrm{M}$ Ionomycin in solution with different Ca^{2+} concentrations.

The change in intracellular free Ca^{2+} as a read-out parameter was measured by flow cytometry. Flow cytometry histogram of Fluo-4 intensity of RBCs with NS309 or without stimulation are taken from Jansen et al [599]. The percentage of high Ca^{2+} RBCs with NS309 stimulation as a function of the external Ca^{2+} concentration is also taken from Jansen et al [599].

When the extracellular free Ca²⁺ concentration is 1 µM, the Ionomycin, the Ca²⁺-ionophore stimulation increases the intracellular Ca²⁺ concentration of almost all RBCs and about 90% RBCs can be considered as responding cells. In contrast, after NS309 stimulation, a small population of RBCs with slightly higher intracellular Ca²⁺ level and a slightly higher percentage of responding RBCs than RBCs without stimulation (Fig. 3.10 A,F). At extracellular Ca^{2+} concentrations of $10\,\mu\mathrm{M}$, $100\,\mu\mathrm{M}$ and $350\,\mu\mathrm{M}$, there is an obvious population of responding cells after application of NS309. The RBCs in solutions containing 10 μM or 100 μM free Ca²⁺ have a similar percentage of responding cells, which is higher than in RBCs in a solution containing 350 µM free Ca²⁺ (Fig. 3.10 B,C,D,F). However, RBCs with NS309 stimulation in a solution containing 1 mM free Ca²⁺ shows a similar percentage of responding cells as RBCs with NS309 treatment in 1 µM free Ca²⁺ solution, which is lower than other conditions with NS309 application (Fig. 3.10 E,F). Ionomycin treatment results in more than 95% responding cells when RBCs are kept in solution with 10 μM, 100 μM, 350 μM or 1 mM free Ca²⁺. The intracellular Ca²⁺ concentration appeared to be higher than RBCs with the NS309 challenge in solution same free Ca²⁺ concentration (Fig. 3.10 B-F). Furthermore, instead of a linear regression, the percentage of high Ca²⁺ RBCs population shows a bell-shaped relationship as a function of external Ca²⁺ concentration after stimulation with 100 µM NS309 (Fig. 3.10 F).

In summary, the data show the Gárdos channel activation can induce the Ca^{2+} entry the RBCs, but the Ca^{2+} influx is dependent on extracellular Ca^{2+} and it can be inhibited by a high Ca^{2+} concentration.

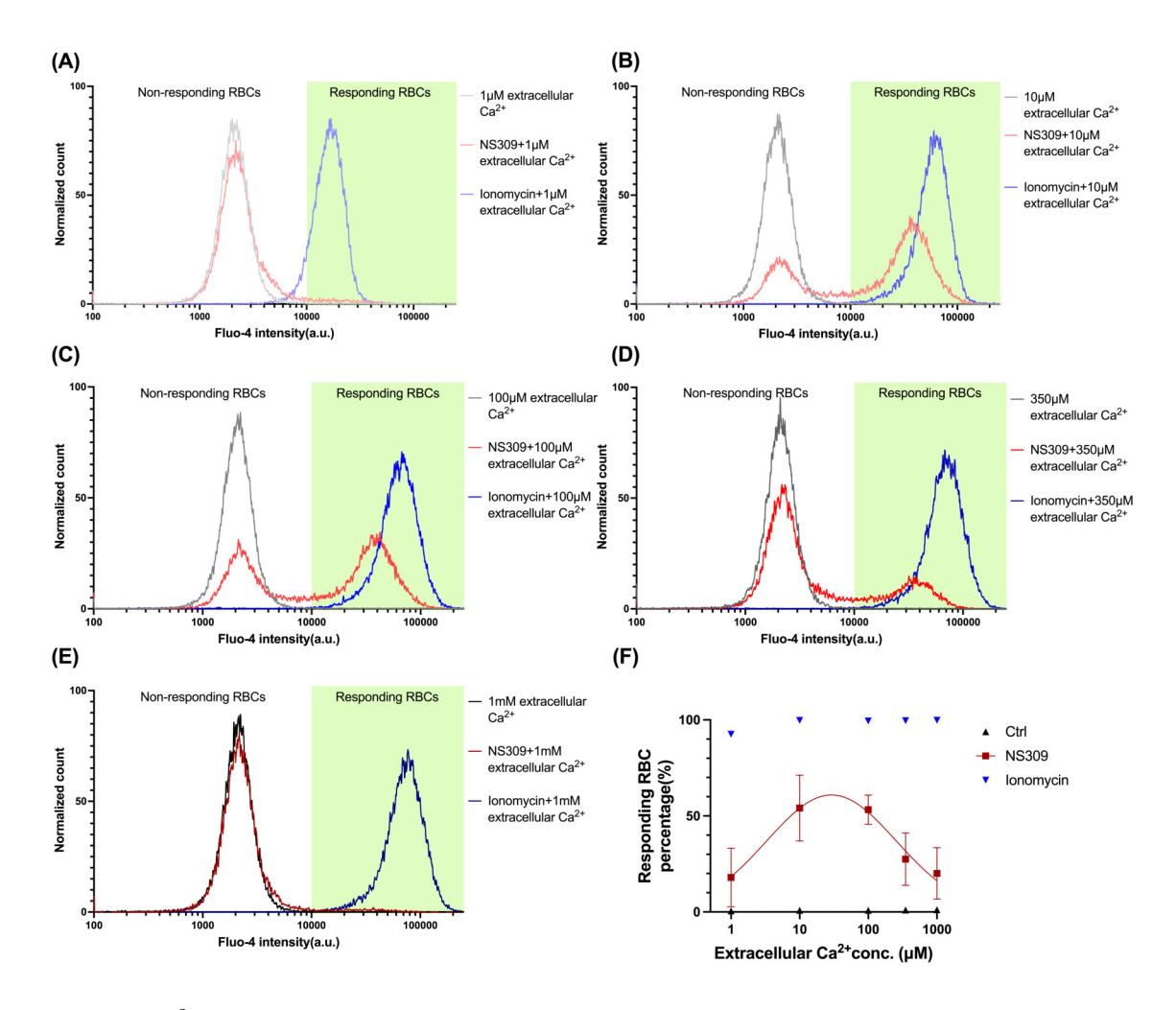


Fig. 3.10: Ca²⁺-dependence of NS309 and Ionomycin stimulation. (A)–(E) Flow-cytometry histogram of Fluo-4 intensity of RBCs in a solution containing different concrntration of free Ca²⁺ with 100 μM NS309 or 10 μM Ionomycin or no stimulation (black trace: no stimulation, red trace: with 100 μM NS309 and blue trace: 10 μM Ionomycin). The white area defines non-responding RBCs and the green area defines responding RBCs: (A) Solution containing 1 μM free Ca²⁺; (B) Solution containing 10 μM free Ca²⁺; (C) Solution containing 100 μM free Ca²⁺; (D) Solution containing 350 μM free Ca²⁺; (E) Solution containing 1 mM free Ca²⁺. (F) Comparison of the percentage of high Ca²⁺ RBCs after 100 μM NS309 or 10 μM Ionomycin or no stimulation as a function of the external Ca²⁺ concentration. Percentage of high Ca²⁺ RBCs after 100 μM NS309 stimulation as a function of the external Ca²⁺ concentration shows a bell-shaped fit. (N_{Ctrl-donor}=3, N_{NS309-donor}=3, N_{Ionomycin-donor}=1, n_{cell}>30,000). Data is shown as means ± SEM in (F).

3.3 Transient Receptor Potential Vanilloid Type 2 (TRPV2) Channel

3.3.1 Influence of Long-term Cannabis Consumption on TRPV2 Channel Function in RBCs

To understand the physiological functions of TRPV2 in RBCs and the effects of long-term marijuana consumption on TRPV2 function, blood was collected from healthy non-smokers

(NS) and regular marijuana smokers (MS). The RBCs were challenged with 30 μ M Δ^9 -THC and the change in intracellular free Ca²⁺ was used as a read-out parameter. The Fluo-4 intensity was measured by confocal imaging and flow cytometry. Representative normalized histograms of Fluo-4 intensity of NS and MS RBCs in Tyrode solution with or without 30 μ M Δ^9 -THC stimulation are taken from Flormann et al, as well as high Ca²⁺ RBCs population percentage comparison of samples in Tyrode solution and right after Δ^9 -THC stimulation [644]. Some representative confocal slices of RBCs treated with Δ^9 -THC and quantification of TRPV2 expression by flow cytometry and Western blots are also taken from Flormann et al [644].

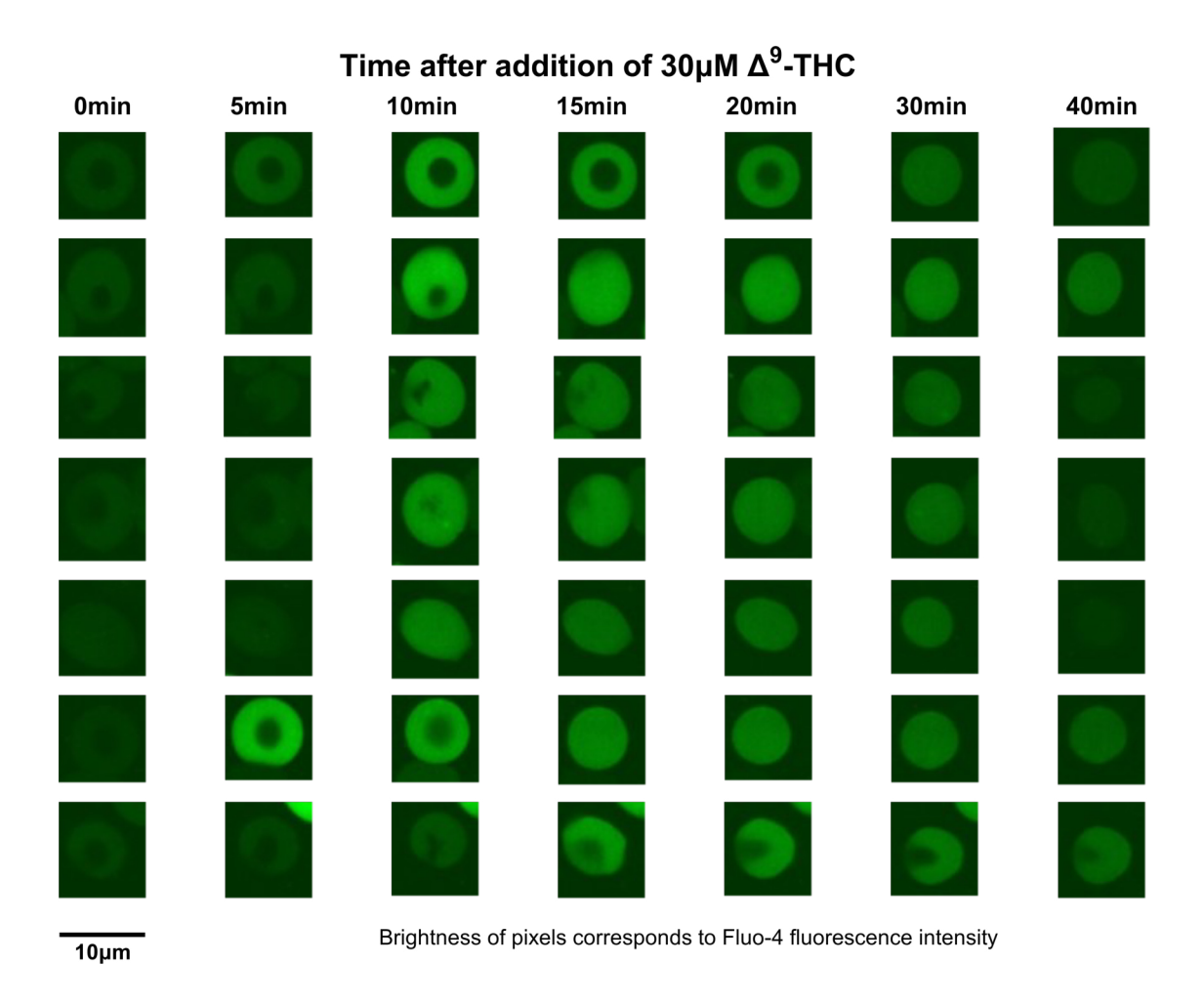


Fig. 3.11: Representative confocal slices of RBCs from a healthy control loaded with the Ca^{2+} -fluorophore Fluo-4. Each row represents the change in the same RBC over time. The time after addition of Δ^9 -THC is indicated above each image column. Both, RBC shape and Ca^{2+} content indicate the transient nature of the Δ^9 -THC stimulation.

As the images show in Figure 3.11, after Δ^9 -THC application, within 10 minutes of application of Δ^9 -THC, RBCs responding to Δ^9 -THC have an increased intracellular Ca²⁺ concentration. The intracellular calcium concentration decreases after reaching its highest level. Meanwhile, the responding discocytes become hyperhydrated and transform into stomatocytes and even spherocytes.

The basal Ca²⁺ concentration in MS RBCs is similar to that in NS RBCs (Fig. 3.12 A, B,C,E). Right after Δ^9 -THC stimulation, the population of high Ca²⁺ RBCs is increased in both NS and MS (Fig. 3.12 A,D) and the average Fluo-4 intensity of RBCs is increased (Fig. 3.12 C). There is a higher percentage of high Ca²⁺ RBCs in MS (20%) than that in NS (16%) right after Δ^9 -THC application (Fig. 3.12 D) and therefore the average Fluo-4 intensity is higher in MS (Fig. 3.12 C). After 10 minutes of Δ^9 -THC stimulation, the high Ca²⁺ population in MS is maintained at the same percentage. However, the high Ca²⁺ population in NS is increased by 25% (Fig. 3.12 D,F). The average Fluo-4 intensity of RBCs from NS is similar to that of MS after 10 minutes of Δ^9 -THC stimulation (Fig. 3.12 E).

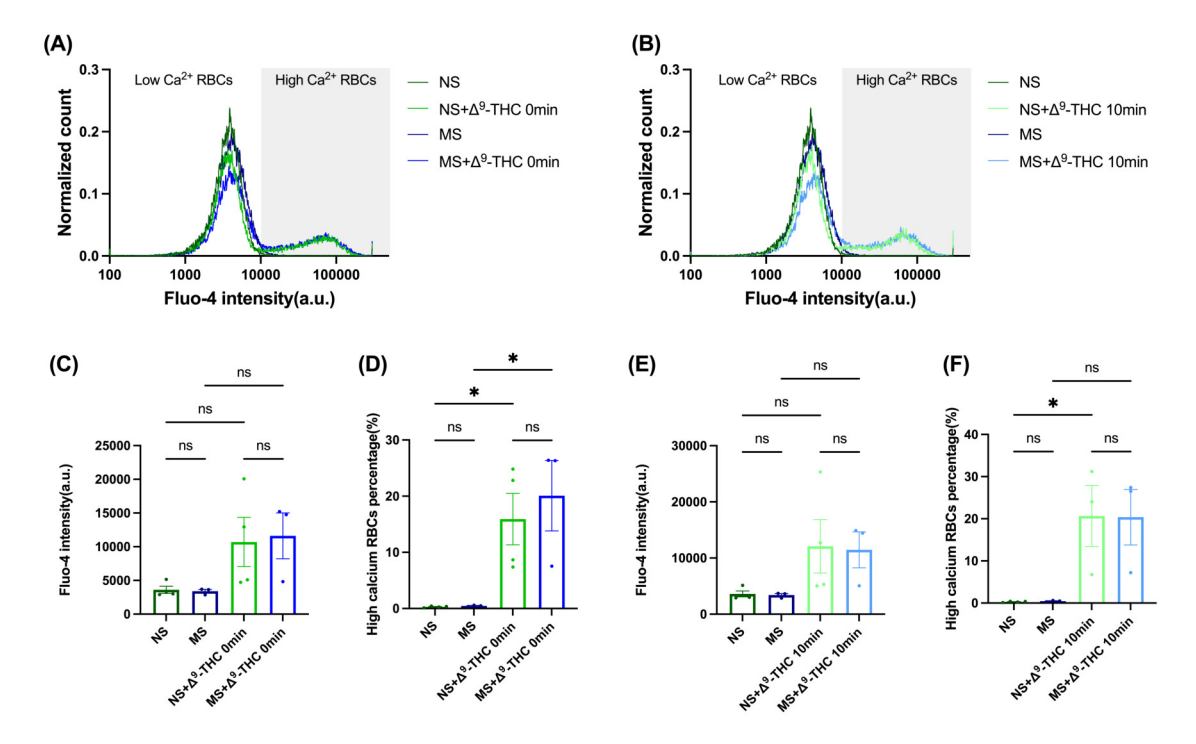


Fig. 3.12: The results of the flow-cytometric measurements of Ca^{2+} -signaling in RBCs from marijuana smokers (MS) and healthy non-smokers (NS) with 30 μ M Δ^9 -THC stimulation. (A) Representative normalized histograms of Fluo-4 intensity of NS (green traces) and MS (blue traces). Darker colors for samples in Tyrode solution without any additional stimulation and lighter colors for samples measured right after Δ^9 -THC stimulation. The color code also applied to panel B. (B) Representative normalized histograms of Fluo-4 intensity of NS and MS in Tyrode solution without any additional stimulation and 10 minutes after Δ^9 -THC stimulation. (C)-(F) Statistical analysis of flow-cytometric results. (C) Average Fluo-4 intensity comparison and (D) High Ca^{2+} RBCs population percentage comparison of samples in Tyrode solution and right after Δ^9 -THC stimulation (N_{MS}=3, N_{NS}=4, n_{cell}>30,000). Data is shown as means \pm SEM in (C)-(F) Statistical differences were evaluated using one-way ANOVA test with Tukey's multiple comparison method. p < 0.05 was deemed significant.

To investigate the difference in intracellular $\mathrm{Ca^{2+}}$ concentration between MS and NS RBCs after Δ^9 -THC stimulation due to the difference in TRPV2 expression under long-term cannabis consumption, TRPV2 antibody and fluorescent secondary antibody against TRPV2 antibody were used for WB and flow cytometry. The secondary antibody used for flow cytometry was conjugated to Alexa-647A dye and the secondary antibody used for WB measurement was conjugated to HRP.

As shown in Figure 3.13 A and B, the expression level of TRPV2 shows no difference between MS and NS. In addition, both antibodies do not show significant differences in the expression level of TRPV2 normalized to the spectrin between MS and NS with WB measurement, the more accurate and sensitive protein quantification method compared to flow cytometry (Fig. 3.13 C-F).

The data shows only a small population of RBCs can respond to Δ^9 -THC and the population is slightly bigger in marijuana smokers than healthy people. RBCs responding to Δ^9 -THC can lead to cell swelling and Ca²⁺ entry. However, the number of TRPV2 copies seem to have no difference between marijuana smokers and non-smokers.

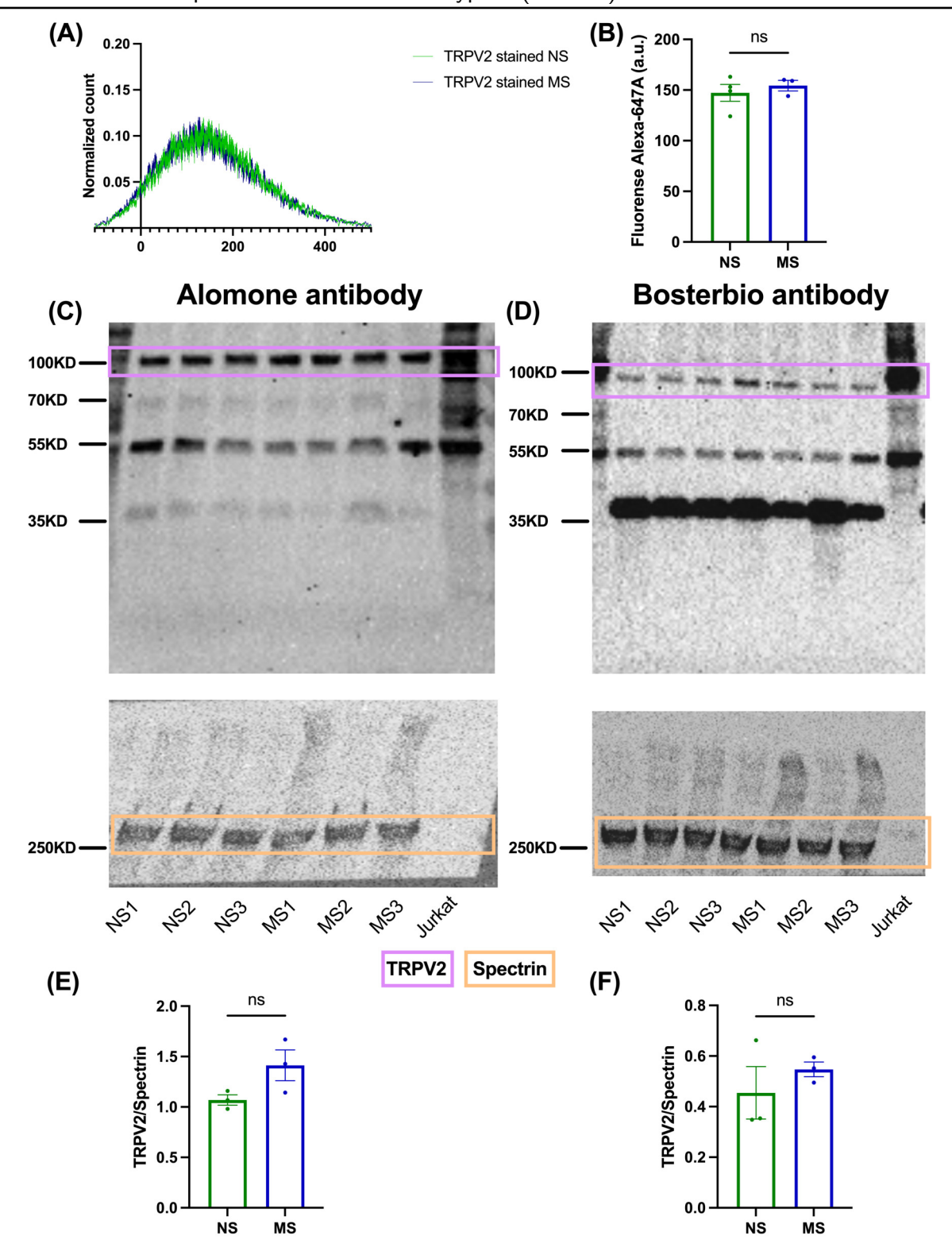


Fig. 3.13: Quantification of TRPV2 expression by flow cytometry and Western blots. (A) and (B) Flow cytometry measurement with TRPV2 antibody (Alomone). (A) Representative normalized histograms of Fluo-4 intensity of NS (green traces) and MS (blue traces). (B) Averaged fluorescence of Alexa-647A of RBCs from MS and NS. (C)-(F) Western blot for TRPV2 with two different antibodies from Alomone (left) and Bosterbio (right). Purple boxed bands are TRPV2 staining and yellow boxed bands are spectrin staining. Unboxed bands indicate non-specific cross reactivity of the antibodies. (C) WB image of TRPV2 antibody (Alomone) staining (upper panel) and spectrin antibody staining (lower panel). (D) WB images of TRPV2 antibody (Bosterbio) staining (upper panel) and spectrin antibody staining (lower panel). (E) Statistical analysis of the normalized expression level of TRPV2 stained with the Alomone antibody, data was normalized to the spectrin. (F) Statistical analysis of the normalized expression level of TRPV2 stained with the Bosterbio antibody, data was normalized to the spectrin. (N_{MS-donor}=3, N_{NS-donor}=4). Data is shown as means \pm SEM in (B), (E) and (F). Statistical differences were evaluated using unpaired T-test. p<0.05 was deemed significant.

3.3.2 Effects of TRPV2 Activation on Sickle Cells

During deoxygenation, increased Ca^{2+} conductance could promote dehydration of sickle cells through activation of the Gárdos channels, leading to RBCs sickling. Activation of the TRPV2 channel, a non-selective cation channel, could increase intracellular Ca^{2+} concentration. To investigate whether TRPV2 channel activation has impacts on sickle cells, RBCs from healthy controls (AA) and sickle cell patients (SS) were challenged with Δ^9 -THC and the Ca^{2+} signaling was detected by flow cytometry. In addition, the MBE method was used to measure the change in membrane potential after Δ^9 -THC stimulation. Dose-response effects of Δ^9 -THC in healthy RBCs, statistical comparison of the normalized Fluo-4 intensity before THC stimulation and normalized Fluo-4 intensity change after Δ^9 -THC application are taken from Hatem et al [645]. Quantitative analysis of normalized Fluo-4 intensity of AA and SS RBCs responding to Δ^9 -THC in different time slots are taken from Hatem et al as well [645]. In addition, resting membrane (E_m) and hyperpolarization magnitudes (Δ (Vm_{Max}- E_m) of RBCs from SS and AA with 80 µM Δ^9 -THC in different conditions are taken from Hatem et al [645].

When the concentration of Δ^9 -THC is less than 1 μ M, there is no obvious increase in the size of the high Ca²⁺ population. When the RBCs are stimulated with more than 1 μ M Δ^9 -THC, the percentage of high Ca²⁺ cells increased with time during the first 50 seconds after Δ^9 -THC stimulation. The high Ca²⁺ population also increases with the Δ^9 -THC concentration (Fig. 3.14 A). The high Ca²⁺ population has no obvious difference between groups receiving 60 μ M, 90 μ M and 120 μ M Δ^9 -THC stimulation for 55 seconds (Fig. 3.14 A,B). The Δ^9 -THC effects are shown in Figure 3.14 B. The curve shows the percentage of responding cells in response to different concentrations of Δ^9 -THC after 1 minute of incubation. The EC₅₀ of Δ^9 -THC in RBCs is about 13.35 μ M (Fig. 3.14 B). According to the dose-response curve, 30 μ M are chosen as the dose close to the EC₅₀ and 80 μ M as the dose of a maximum Δ^9 -THC effect in further experiments.

Intracellular Ca²⁺ is significantly higher in sickle cell patients compared to healthy controls under basal conditions (without stimulation) with 45% higher normalized Fluo-4 intensity (Fig. 3.14 C,D black and red traces respectively). After 30 µM Δ^9 -THC stimulation, an increase in the percentage of high Ca²⁺ RBCs occurs in both AA and SS groups (Fig. 3.14 D-F). The percentage in the SS group is higher than in the AA group and the high Ca²⁺ RBCs from the SS group have slightly higher intracellular Ca²⁺ as well (Fig. 3.14 D-H). When RBCs are stimulated with 30 µM Δ^9 -THC, the percentage of high Ca²⁺ RBCs is increased significantly after stimulation and reaches the maximum plateau after 3 minutes in both SS and AA groups. The SS group maintains a significantly higher percentage of high Ca²⁺ cells than AA (Fig. 3.14 E,F). In addition, both AA RBCs and SS RBCs that respond to Δ^9 -THC reach the highest intracellular Ca²⁺ after 3 minutes of Δ^9 -THC application and the calcium level starts to decrease after 5 minutes. The intracellular Ca²⁺ concentration is higher in SS RBCs than AA RBCs with a 20% higher normalized Fluo-4 intensity (Fig. 3.14 G,H). RBCs treated with 80 µM Δ^9 -THC show a similar trend as that of the RBCs with 30 µM Δ^9 -THC (Fig. A.2).

 $80 \,\mu\text{M}$ Δ^9 -THC can induce, as expected, hyperpolarization of $-16.3 \pm 1.5 \,\text{mV}$ in SS RBCs in oxygenated conditions with an average $-22.4 \pm 1.4 \,\text{mV}$ as the maximum hyperpolarization potential reached (Fig. 3.15 B,C, Fig. 3.16 C,D). Ethanol at an equivalent amount

does not cause any membrane potential change (Fig. 3.15). The significant difference in maximal hyperpolarization and hyperpolarization magnitudes between Δ^9 -THC and ethanol stimulated RBCs indicates the hyperpolarization is induced by Δ^9 -THC. The hyperpolarization is enhanced by 74% and the maximum membrane potential achieved during hyperpolarization in SS RBCs is significantly increased to $28.4 \pm 2.4 \,\mathrm{mV}$ under deoxygenation conditions with oxygen levels reduced to $0.8-1\,\mathrm{mg/L}$ (O₂ partial pressure: 19.6 – 24.5 mmHg). In addition to increased maximal hyperpolarization and hyperpolarization magnitudes, the hyperpolarization rate is 68% faster in the deoxygenation condition (Fig. 3.16 C,D). However, the same amount of Δ^9 -THC induces only a small change in the membrane potential of AA RBCs in both oxygen condition $(-3.8 \pm 0.7 \,\mathrm{mV})$ and deoxygen conditions $(-5.8 \pm 1.3 \,\mathrm{mV})$ (Fig. 3.16 C,D). The hyperpolarization could be prevented by pre-incubation with 100 nM charybdotoxin, the Gárdos channel inhibitor (Fig. 3.16 C-E). In contrast, 30 μ M Δ^9 -THC induces almost no change in membrane except in SS RBCs in deoxygenated condition (Fig. A.4). It is noteworthy that the resting membrane potential of SS RBCs is on average less electronegative $(-6.3 \pm 0.3 \,\mathrm{mV})$ than that of AA cells $(-10.4 \pm 0.5 \,\mathrm{mV})$. SS RBCs also have a less negative resting membrane potential $(-4.1 \pm 0.4 \,\mathrm{mV})$ under deoxygenated condition. In addition, charybdotoxin has no effect on the resting membrane potential (Fig. 3.16 B).

The data show RBCs respond to acute Δ^9 -THC stimulation can lead to a rapid and prolonged increase in intracellular Ca²⁺ and the RBCs from SCD patients are more responsive than the ones of healthy people. The increase of Ca²⁺ in RBCs from SCD patients can active the Gárdos channels and induce hyperpolarization. The hyperpolarization of SS RBCs can be enhanced in deoxygenation condition.

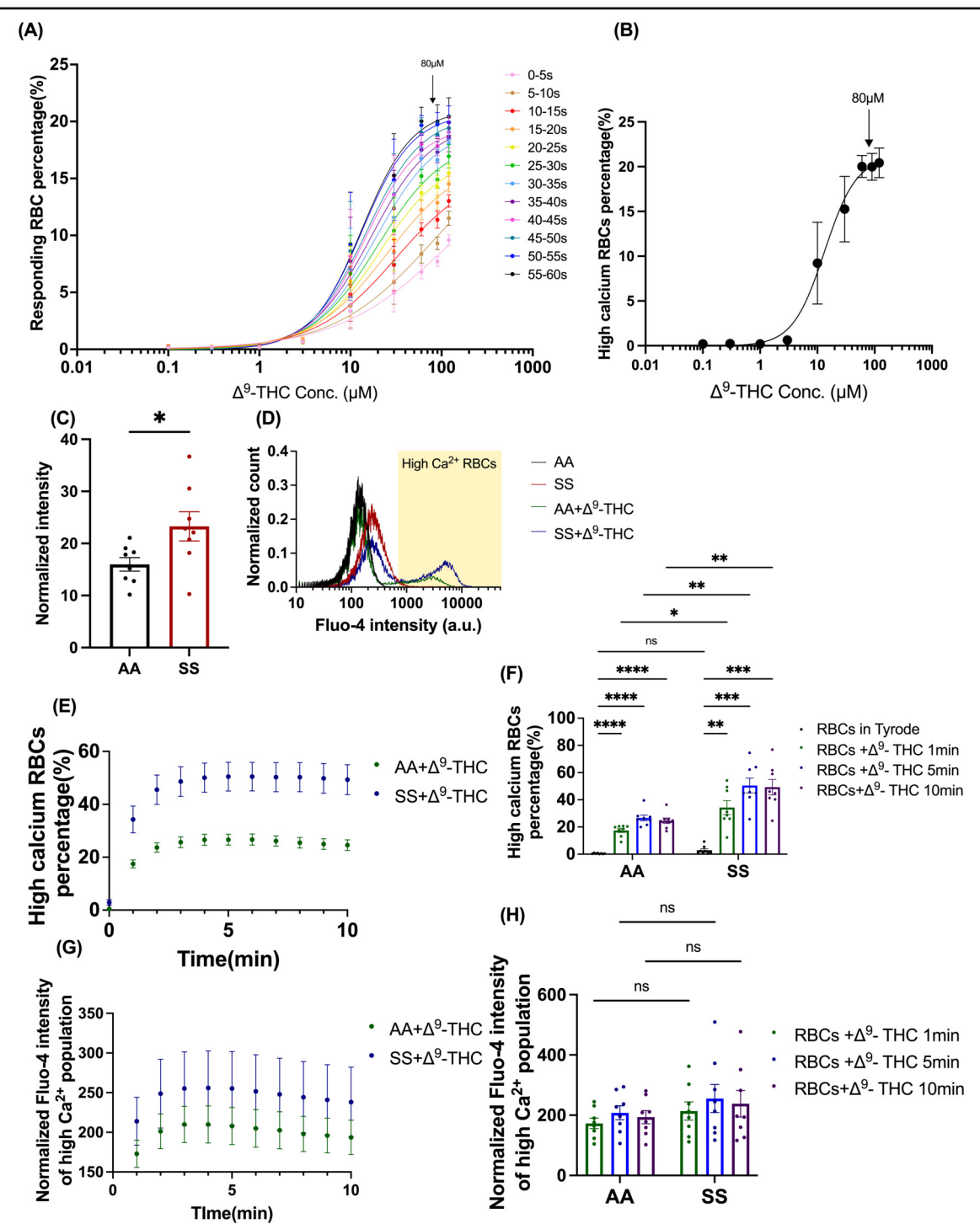


Fig. 3.14: The results of the flow-cytometry measurements of Ca²⁺-signaling in RBCs from healthy controls (AA) and sickle cell patients (SS). (A) Different effect of Δ^9 -THC dose and time change on the population of RBCs with high Ca^{2+} within the first minute after Δ^{9} -THC application. (B) Dose-response effects of Δ^9 -THC in healthy RBCs. The curve shows the percentage of responding cells in response to different concentrations of Δ^9 -THC after 1 minute of incubation. (C) Statistical comparison of the normalized Fluo-4 intensity before THC stimulation between AA and SS cells. (D)-(H) Flow-cytometry data and statistical analysis after $30\,\mu\mathrm{M}$ Δ^9 -THC stimulation: (D) Representative normalized histograms of Fluo-4 intensity in the high Ca^{2+} population of AA cells without Δ^9 -THC (black trace), SS cells without Δ^9 -THC (red trace), AA cells with Δ^9 -THC (green trace), and SS cells with Δ^9 -THC (blue trace); (E) Percentage change in the high Ca^{2+} population over time after Δ^{9} -THC application (green-AA, blue-SS); (F) Quantitative analysis of AA and SS RBCs with high Ca^{2+} in response to Δ^{9} -THC in different time slots; (G) Normalized Fluo-4 intensity change in AA and SS RBCs responding to Δ^9 -THC over time after Δ^9 -THC application (green-AA, blue-SS), (H) Quantitative analysis of normalized Fluo-4 intensity of AA and SS RBCs responding to Δ^9 -THC in different time slots. (In (A) and (B) $N_{donor}=4$, in (C)-(M) $N_{donor}=8$, $n_{cell}>30,000$). Data is shown as means \pm SEM in (B), (C), (E)-(H) and (J)-(M). Statistical differences were evaluated using unparied T-test for (B); two-way ANOVA test with Šídák multiple comparison method in (F) and (H).

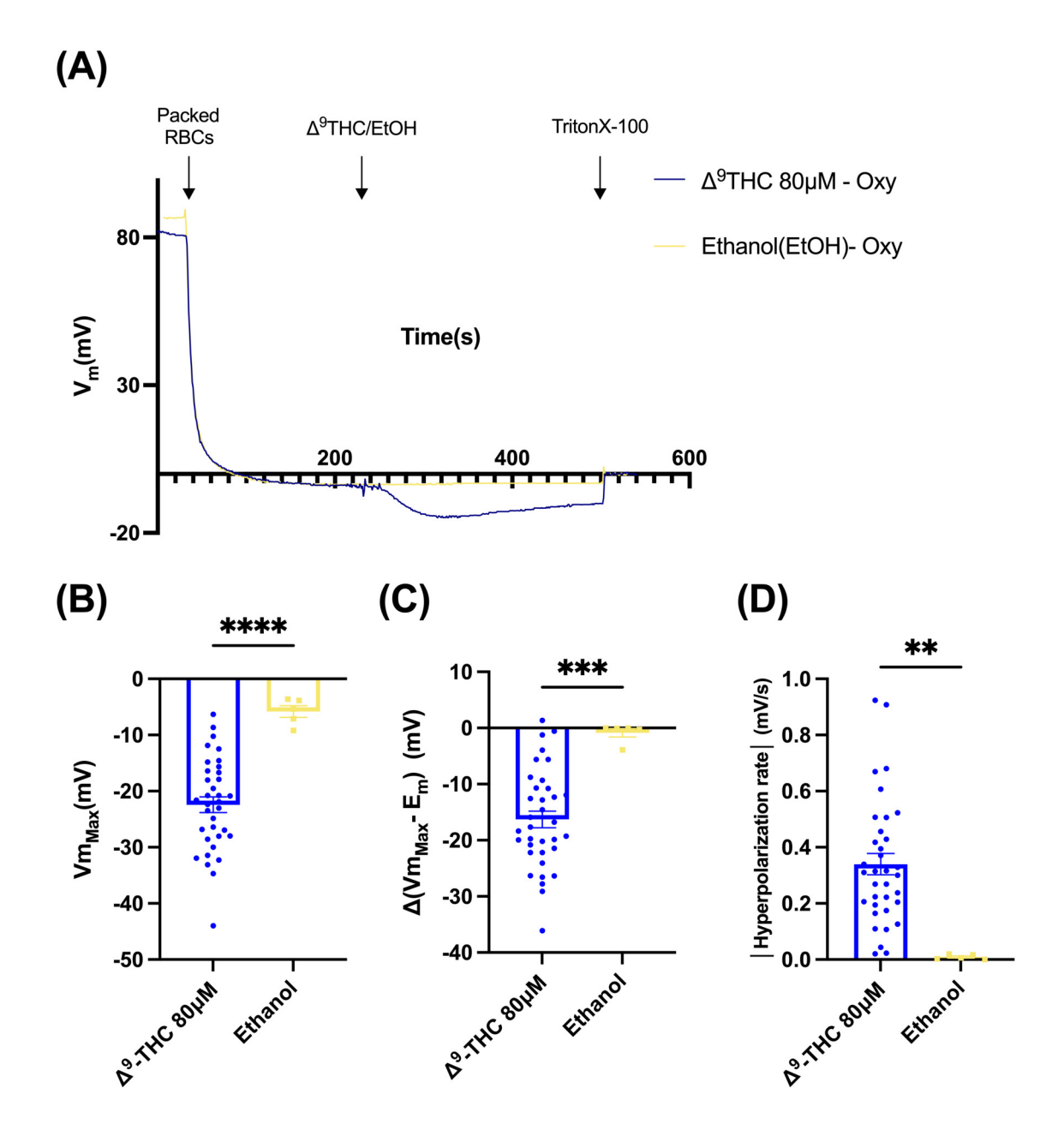


Fig. 3.15: Membrane potential with 80 μ M Δ^9 -THC and corresponding amount of solvent (ethanol) stimulation in SS RBCs. (A) Representative trace with Δ^9 -THC (blue), with EtOH (yellow). Arrows indicate when packed RBCs, stimulation with indicated compound and TritonX-100 were added to the measuring system. (B) Maximal hyperpolarization (Vm_{Max}). (C) Hyperpolarization magnitudes (Δ (Vm_{Max}-E_m)) are obtained after the deduction of resting membrane potential (E_m) from the maximal hyperpolarization (Vm_{Max}) reached at each condition Membrane potential change. (D) Absolute value of hyperpolarization rate (N_{SS+80 μ M-THC-donor=35, N_{SS+EtoH-80-donor}=5). Data is shown as means \pm SEM in (B)-(D). Statistical differences were evaluated using unpaired T-test. p < 0.05 was deemed significant.}

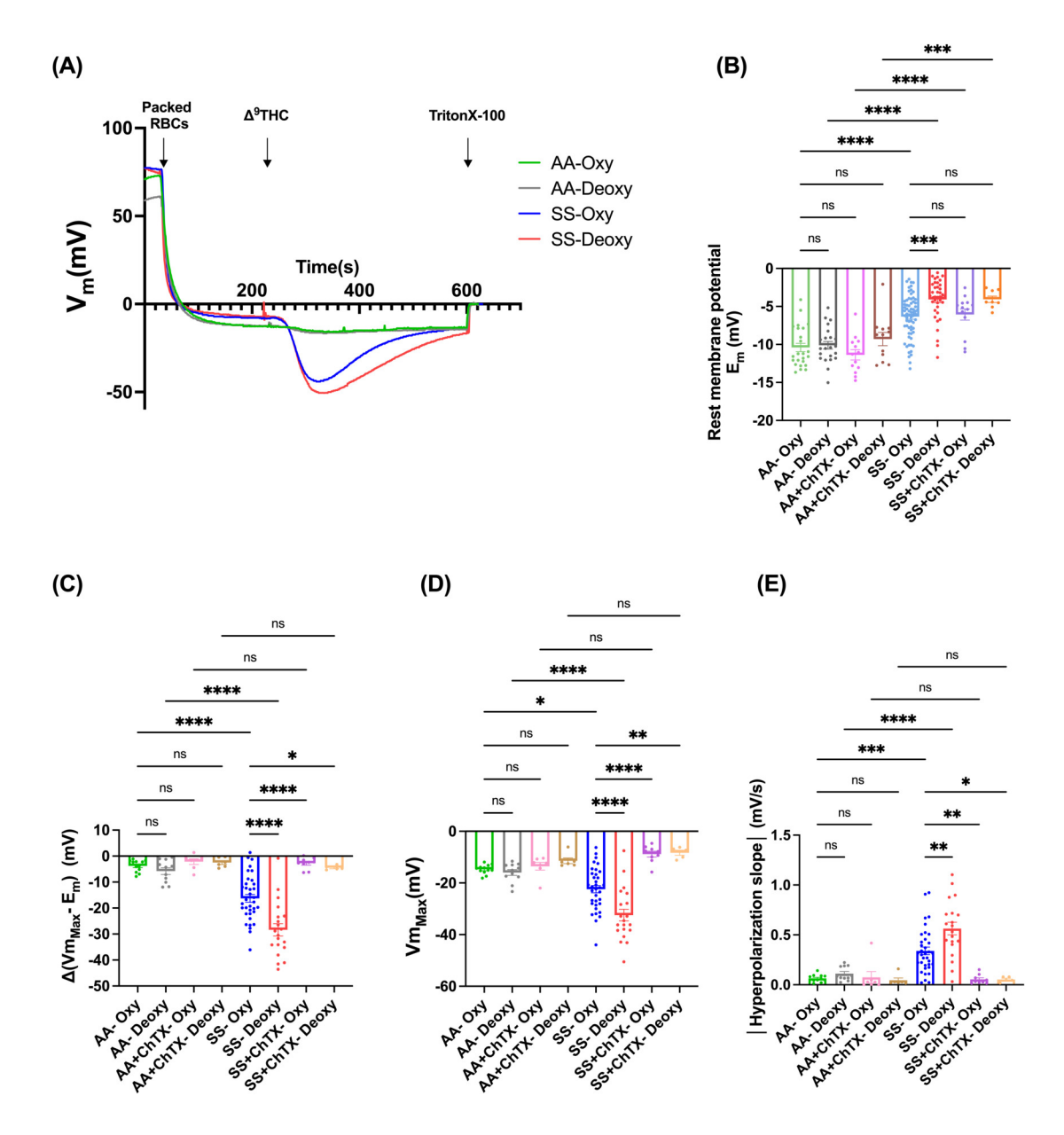


Fig. 3.16: Membrane potential upon Δ^9 -THC stimulation in AA and SS RBCs in different oxygen conditions. (A) Representative traces with 80 μM Δ^9 -THC in different oxygen conditions: AA RBCs in oxygenated condition (green), AA RBCs in deoxygenated condition (black), SS RBCs in oxygenated condition (blue), SS RBCs in deoxygenated condition (red). Arrows indicate when packed RBCs, Δ^9 -THC and TritonX-100 were added to the measuring system. (B) Resting membrane (E_m) of RBCs from AA and SS under different conditions. (C) Hyperpolarization magnitudes ($\Delta(Vm_{Max}^- E_m)$ of RBCs from SS and AA with 80 μM Δ^9 -THC in different conditions. Maximal hyperpolarization (Vm_{Max}). (D) Maximal hyperpolarization (Vm_{Max}) and (E) Absolute value of hyperpolarization rate of RBCs from SS and AA with 80 μM Δ^9 -THC in different conditions. (N_{AA-Oxy-donor}=12, N_{AA-Deoxy-donor}=11, N_{AA+ChTX-Oxy-donor}=7, N_{AA+ChTX-Deoxy-donor}=6, N_{SS-Oxy-donor}=35, N_{SS-Deoxy-donor}=20, N_{SS+ChTX-Oxy}=9, N_{SS+ChTX-Deoxy-donor}=5) Data is shown as means ± SEM in (B) - (E). Statistical differences were evaluated using one-way ANOVA test with Tukey's multiple comparison method. p < 0.05 was deemed significant.

3.4 Calcium Quantification by Fluorescence Lifetime Image Microscopy (FLIM)

3.4.1 Hemoglobin Concentration Influence on Fluorescence Intensity Dependent Semi-quantification of Calcium Concentration

As shown in previous sections 1.3.3 and 2.2.3, the most common measurement of intracellular Ca²⁺ concentration is the measurement of the change in Ca²⁺-indicator intensity by confocal microscopy or flow cytometry. By comparing the measured fluorescence intensity of the indicators with the fluorescence intensity of the indicators in the basal state, a semi-quantification of intracellular Ca²⁺ could be achieved. The absorption of excitation light as well as the absorption of the emission light by RBCs, in particular the hemoglobin, influences the finally recorded fluorescence intensity of the Ca²⁺-indicators during the experiments. In order to study the influence of the hemoglobin, the fluorescence intensity of Fluo-4 was measured in RBCs after they had been challenged with hypoosmotic (130 mOsm/L), isotonic (300 mOsm/L) and hyperosmotic Tyrode solution (800 mOsm/L). The RBCs in 130 mOsm/L Tyrode solution can transform to stomatocytes, and RBCs in 800 mOsm/L Tyrode solution could transform to echinocytes.

In Figure 3.17 A and B show, that when RBCs are challenged with iostonic Tyrode solution and hyperosmotic Tyrode solution, there is only one RBCs population. The averaged Fluo-4 intensity of echinocytes in 800 mOsm/L Tyrode solution is slightly lower than that of discocytes but not significantly (Fig. 3.17 A,B). The Fluo-4 intensity in echinocytes as measured by confocal microscopy is nearly (40% lower compared to discocytes, see Figure 3.17 C. Differently, RBCs in hypoosmotic Tyrode solution show two population with different Fluo-4 intensity. Both groups show a significant higher average Fluo-4 intensity than RBCs in isotonic Tyrode solution and hyperosmotic Tyrode solution (Fig. 3.17 A,B).

The data shows the volume of RBCs changing could lead to fluorescence intensity change. The decreased volume will lead to decreased fluorescence intensity of intracellular dye in RBCs. In contrast, the increased volume can cause the stronger fluorescence intensity of intracellular dye in RBCs.

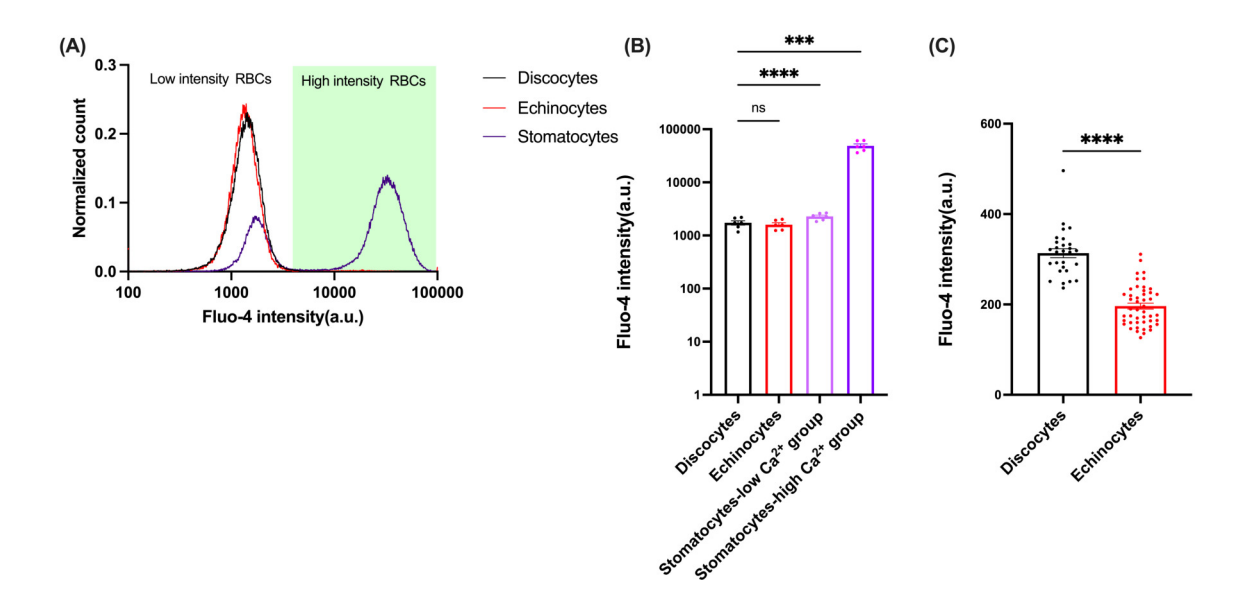


Fig. 3.17: Results of flow cytometry and confocal imaging measurements of Fluo-4 intensity of RBCs challenged with solutions of different osmolarity. (A) Representative normalized histograms of Fluo-4 intensity of discocytes (RBCs in $300\,\mathrm{mOsm/L}$ Tyrode - black trace), echinocytes (RBCs in $800\,\mathrm{mOsm/L}$ Tyrode - red trace) and stomatocytes (RBCs in $130\,\mathrm{mOsm/L}$ Tyrode - purple trace). The white panel indicates RBCs with low fluorescence intensity and green panel indicated the RBCs with high fluorescence intensity. (B) Average Fluo-4 intensity of discocytes, echinocytes and stomatocytes with low Fluo-4 intensity and stomatocytes with high Fluo-4 intensity (Nexperiment=6). (C) Statistical analysis of Fluo-4 intensity measured by confocal imaging of discocytes and echinocytes. For each condition, $n_{\rm cell} > 50$. Data is shown as means \pm SEM in (B) and (C). Statistical differences were evaluated using one-way ANOVA test with Tukey's multiple comparison method. p < 0.05 was deemed significant.

3.4.2 FLIM Measurement of Intracellular Ca²⁺ Concentration

Because the intensity of the Ca²⁺-indicator is influenced by the hemoglobin concentration, the methods based on Ca²⁺-indicators can not be calibrated and hence does not allow exact quantification. The differences we achieve as differences in fluorescence sensor intensity I refer to as semiquantification. In addition, the intensity measurement by confocal microscopy or flow cytometry lacks sensitivity among other limitations. Therefore, a sensitive quantitative method is needed that only depends on the intrinsic characteristics of the indicator. The fluorescence lifetime is a possible parameter with an independent Ca²⁺ response under ideal conditions. The experimental methods and results presented in the following sections aim at studying the potential of the FLIM method in a real laboratory scenario. During experiments, Three FLIM microscopy system were used: a Leica 2-photon excitation (2PE) fluorescence lifetime imaging microscopy system (Leica 2PE FLIM system), a TauMap 2PE fluorescence lifetime imaging microscopy system (TauMap 2PE FLIM system) and customised 1-Photon (1PE) excitation fluorescence lifetime imaging microscope system (1PE FLIM system).

3.4.2.1 Ca²⁺-indicators Selection and Hemoglobin Influence

There are several groups of Ca^{2+} indicators on the market. In the experiments, RBCs were loaded separately with different Ca^{2+} indicators and treated with or without Ca^{2+} -ionophore to obtain RBCs with high intracellular Ca^{2+} or maintain low intracellular Ca^{2+} . FLIM of RBCs with different Ca^{2+} indicators were measured using the Leica 2PE FLIM system.

As shown in Figure 3.18 Aa,Ab,Ba,Bb,Ca,Cb,Da and Db, RBCs with Fluo-4, Fura-2, Oregon Green 488 BAPTA-1 (OGB-1) and Fura-red show similar fast lifetimes in the FLIM images. RBCs containing low and high intracellular Ca²⁺ have similar decay curves when the RBCs are loaded with OGB-1, Fura-2 and Fura-red (Fig. 3.18 Bc,Cc,Dc). However, the statistics shows that there is a significant difference in the amplitude averaged lifetime between high and low Ca²⁺ conditions when RBCs were stained with OGB-1, Fura-2 and Fura-red (Fig. 3.18 Bd,Cd,Dd). In contrast, RBCs stained with Fluo-4 show a faster decay in the high Ca²⁺ condition than in the low Ca²⁺ condition but the amplitude averaged lifetime is not significantly different between these two conditions (Fig. 3.18 Ac,Ad).

Surprisingly, RBCs with X-rhod-1 show a distinctly different fast lifetime in FLIM images and clearly different decay curves between high and low Ca^{2+} conditions (Fig. 3.18 Ea,Eb,Ec). Statistics shows that the amplitude-averaged lifetime is significantly longer in RBCs at high Ca^{2+} than in RBCs at low Ca^{2+} (Fig. 3.18 Ed).

The influence of hemoglobin on lifetime is discussed in the following. Firstly, if there are detectable fluorescent signals from RBCs under imaging conditions was checked by imaging RBCs without any loaded dyes at different excitation wavelengths with three different FLIM systems. Only data recorded by the Leica 2PE FLIM system is shown in this section. Data obtained using another two systems are shown in Appendix A.2.

Using Leica 2PE FLIM system, the excitation and emission spectrum using unstained RBCs was recorded. As shown in Figure 3.19 B, there are three emission peaks detected. The highest emission peak is detected between 620 nm to 680 nm while the second highest emission peak is around 500 nm. The smallest peak is around 440 nm to 460 nm and the intensity is less than half that of the biggest peak (Fig. 3.19 B). The highest excitation peak is detected at 690 nm wavelength, and the detected signal intensity decreases with increasing wavelength (Fig. 3.19 B).

FLIM images of unstained RBCs were obtained with excitation laser wavelength of 700 nm, 800 nm, 900 nm and 915 nm. As shown in Figure 3.19 Aa-Ad, with increasing excitation laser wavelength, fewer photons are recorded in the FLIM images taken by the Leica 2PE FLIM system. FLIM images with 700 nm excitation has the highest average intensity, which is 10.5 times higher than the average intensity of FLIM images with 915 nm excitation, the group with the lowest average intensity (Fig. 3.19 D). The representative decay curves show that the 915 nm excitation of RBCs have the fastest lifetime decay among all conditions (Fig. 3.19 C). And the amplitude averaged lifetime in the 915nm excitation condition is shorter than the 800 nm and 900 nm excitation groups. FLIM images with 700 nm excitation is not able to be analyzed so the data is not included (Fig. 3.19 E).

To investigate the influence of Hb on the excitation and emission spectrum of dyes, the excitation and emission spectrum using unstained RBCs were compared with those of

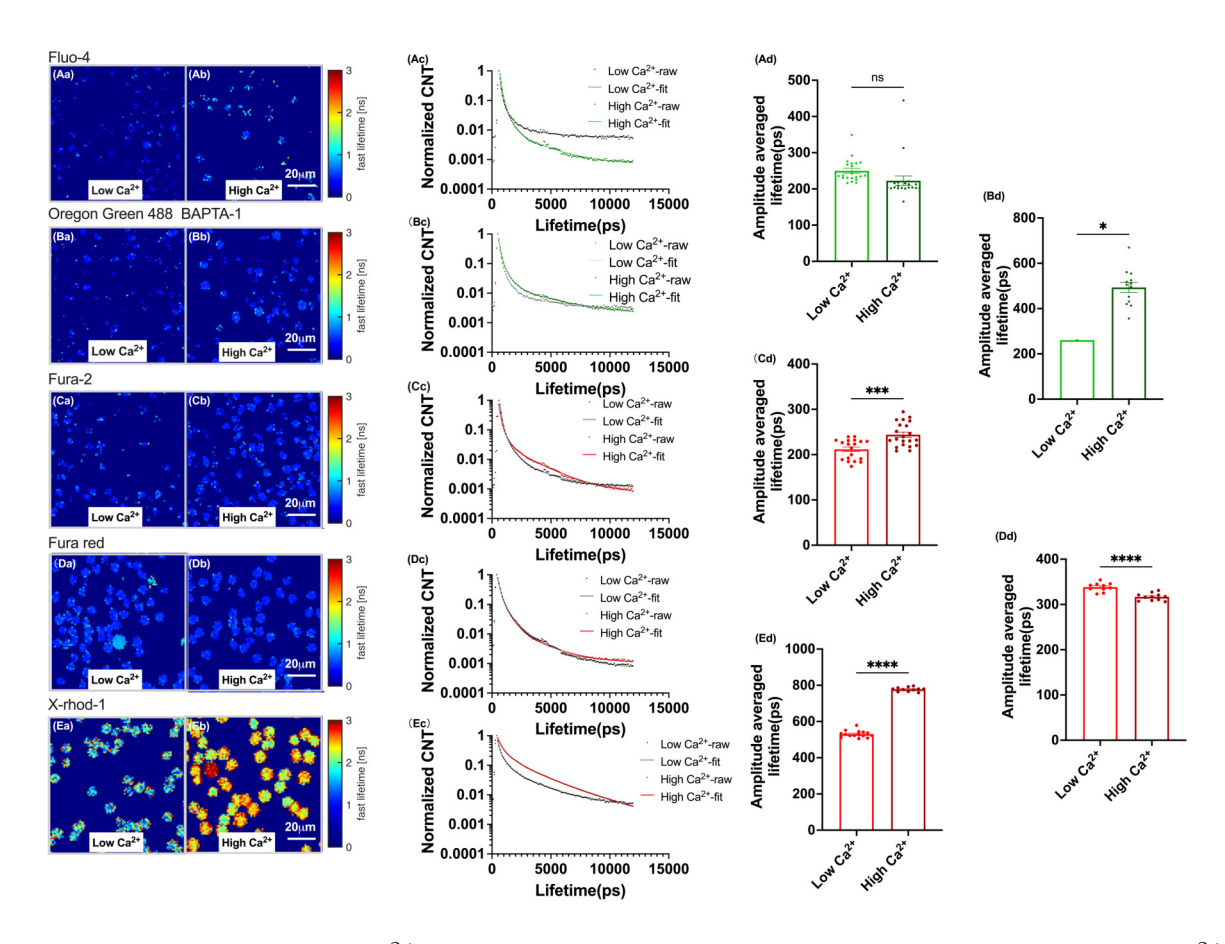


Fig. 3.18: FLIM images of Ca²⁺- indicator loaded RBCs with low and high intracellular Ca²⁺ and statistical analysis. Data obtained by a Leica 2-photon excitation (2PE) fluorescence lifetime imaging microscope (Leica 2PE FLIM system). (Aa)-(Ab) FLIM images of Fluo-4 loaded RBCs with low and high intracellular Ca²⁺. Blue represents shorter lifetime and red represents longer lifetime, which are also applied to panel (Ba), (Bb), (Ca), (Cb), (Da), (Db), (Ea) and (Eb). (Ac) Representative decay curves of Fluo-4 loaded RBCs with low (black) and high (green) intracellular Ca²⁺. Dots show the measured data, and lines indicate the fitted regression, which are also applied to panel (Bc), (Cc), (Dc) and (Ec). (Ad) Amplitude-averaged lifetime of Fluo-4 loaded RBCs with low and high intracellular Ca²⁺. $(n_{low\text{-}Ca} = 21, \ n_{high\text{-}Ca} = 20). \ (Ba)\text{-}(Bb) \ FLIM \ images \ of \ Oregon \ Green \ 488 \ BAPTA-1 \ (OGB-1) \ loaded$ RBCs with low and high intracellular Ca²⁺. (Bc) Representative decay curves of OGB-1 loaded RBCs with low (black) and high (green) intracellular Ca²⁺. (Bd) Amplitude-averaged lifetime of OGB-1 loaded RBCs with low and high intracellular Ca²⁺ (n_{low-Ca}=1, n_{high-Ca}=13). (Ca)-(Cb) FLIM images of Fura-2 loaded RBCs with low and high intracellular Ca²⁺. (Cc) Representative decay curves of Fura-2 loaded RBCs with low (black) and high (red) intracellular Ca²⁺. (Cd) Amplitude-averaged lifetime of Fura-2 loaded RBCs with low and high intracellular Ca²⁺ (n_{low-Ca}=19, n_{high-Ca}=21). (Da)-(Db) FLIM images of Fura red loaded RBCs with low and high intracellular Ca²⁺. (Dc) Representative decay curves of Fura red loaded RBCs with low (black) and high (red) intracellular Ca²⁺. (Dd) Amplitude-averaged lifetime of Fura red loaded RBCs with low and high intracellular Ca²⁺ (n_{low-Ca}=10, n_{high-Ca}=11). (Ea)-(Eb) FLIM images of X-rhod-1 loaded RBCs with low and high intracellular Ca²⁺. (Ec) Representative decay curves of X-rhod-1 loaded RBCs with low (black) and high (red) intracellular Ca²⁺. (Ed) Amplitude-averaged lifetime of X-rhod-1 loaded RBCs with low and high intracellular Ca²⁺ (n_{low-Ca}=15, n_{high-Ca}=11). Data is shown as means ± SEM in (Ac), (Ad) (Bc), (Bd), (Cc), (Cd), (Dc), (Dd), (Ec) and (Ed). Statistical differences were evaluated using unpaired T-test. p < 0.05 was deemed significant.

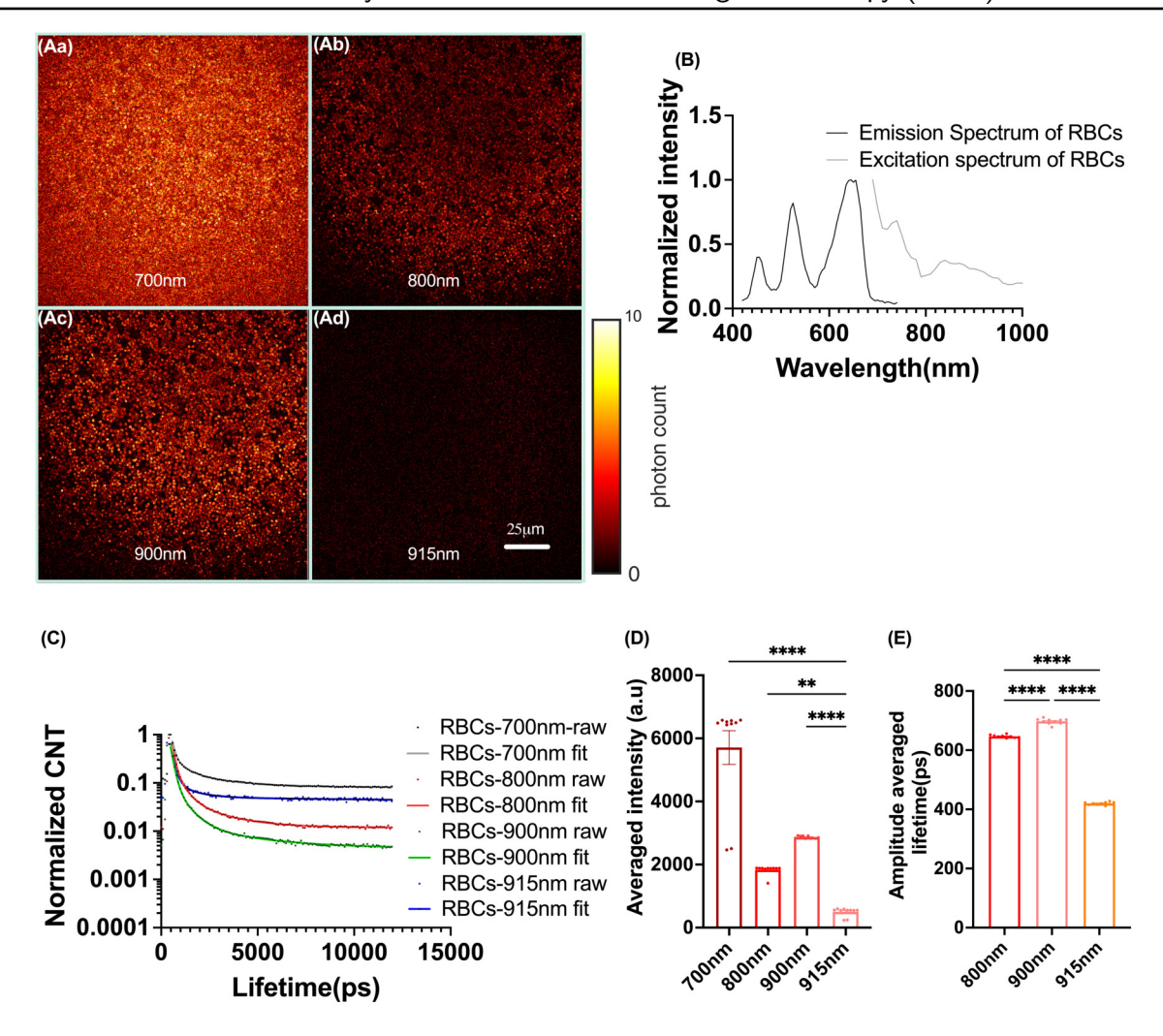


Fig. 3.19: Overview of the signals from pure RBCs after laser excitation. Data were obtained using the Leica 2PE FLIM system. (A) Representative photon-count images of RBCs with (Aa) 700nm 2PE, (Ab) 800nm 2PE, (Ac) 900nm 2PE and (Ad) 915nm 2PE. Each spot represents one RBC. Black represents lower photon counts and white represents higher photon counts. (B) Excitation and emission spectrum of RBCs with 2PE. (C) Representative decay curves of RBCs with 750nm 2PE (black), 800nm 2PE (red), 900nm 2PE (green) and 915nm 2PE (blue). (D) Average intensity of RBCs with 750nm 2PE, 800nm 2PE, 900nm 2PE and 915nm 2PE (n=10). (E) Amplitude averaged lifetime of RBCs with 800nm 2PE, 900nm 2PE and 915nm 2PE (n=10). Data is shown as means \pm SEM in (D) and (E). Statistical differences were evaluated using one-way ANOVA with Tukey's multiple comparison method. p < 0.05 was deemed significant.

different dyes in RBCs or a cell line derived from human embryonic kidney cells (HEK293). As shown in Figure 3.20 Aa and Ba, the peaks of the emission and excitation spectrum of Fluo-4 and OGB-1 in RBCs seem to be red-shifted compared to that in HEK cells. The peaks of the excitation and emission spectrum of Fura red in RBCs are shifted to the left compared to HEK cells (Fig. 3.20 Da). However, the peaks of the excitation and emission spectrum of X-rhod-1 is the same for HEK cells (Fig. 3.20 Ea). The peaks of the excitation and emission spectrum of different dyes in RBCs were also compared with the peaks of pure RBCs (Fig. 3.20 Aa,Ba,Ca,Da,Ea). The emission peak of Fluo-4 overlaps with the second biggest emission peak of RBCs and the peak of the excitation spectrum of Fluo-4 is similar to that of RBCs (Fig. 3.20 Aa). The excitation peak of OGB-1 is

shifted to the right compared to RBCs, but the peak of the emission spectrum overlapped the second biggest emission peak of RBCs (Fig. 3.20 Ba). For Fura-2, the peak of the excitation spectrum is similar to that of RBCs, while the peak of the emission spectrum is slightly right-shifted comparing to the second biggest peak of RBCs (Fig. 3.20 Ca). For Fura red and X-rhod-1, the peak of the excitation spectrum is obviously separated from the peak of RBCs (Fig. 3.20 Da,Ea). However, the peak of the emission spectrum of Fura-red overlapped with the biggest peak of the emission spectrum of RBCs (Fig. 3.20 Da). In contrast, the peak of the emission spectrum of X-rhod-1 in in yellow rnange with the smallest overlap to RBC emission peaks (Fig. 3.20 Ea).

When the decay curves of different dyes in RBCs with high or low calcium are compared with the decay curves of pure RBCs, all five dyes show obviously different lifetime decay compared to RBCs (Fig. 3.20 Ab,Bb,Cb,Db,Eb).

In summary, lifetime of X-rhod-1 is distinguished from the signals originating in RBCs which makes it the best dye for FLIM imaging with least influence of additional signals from RBC and was selected for further studies.

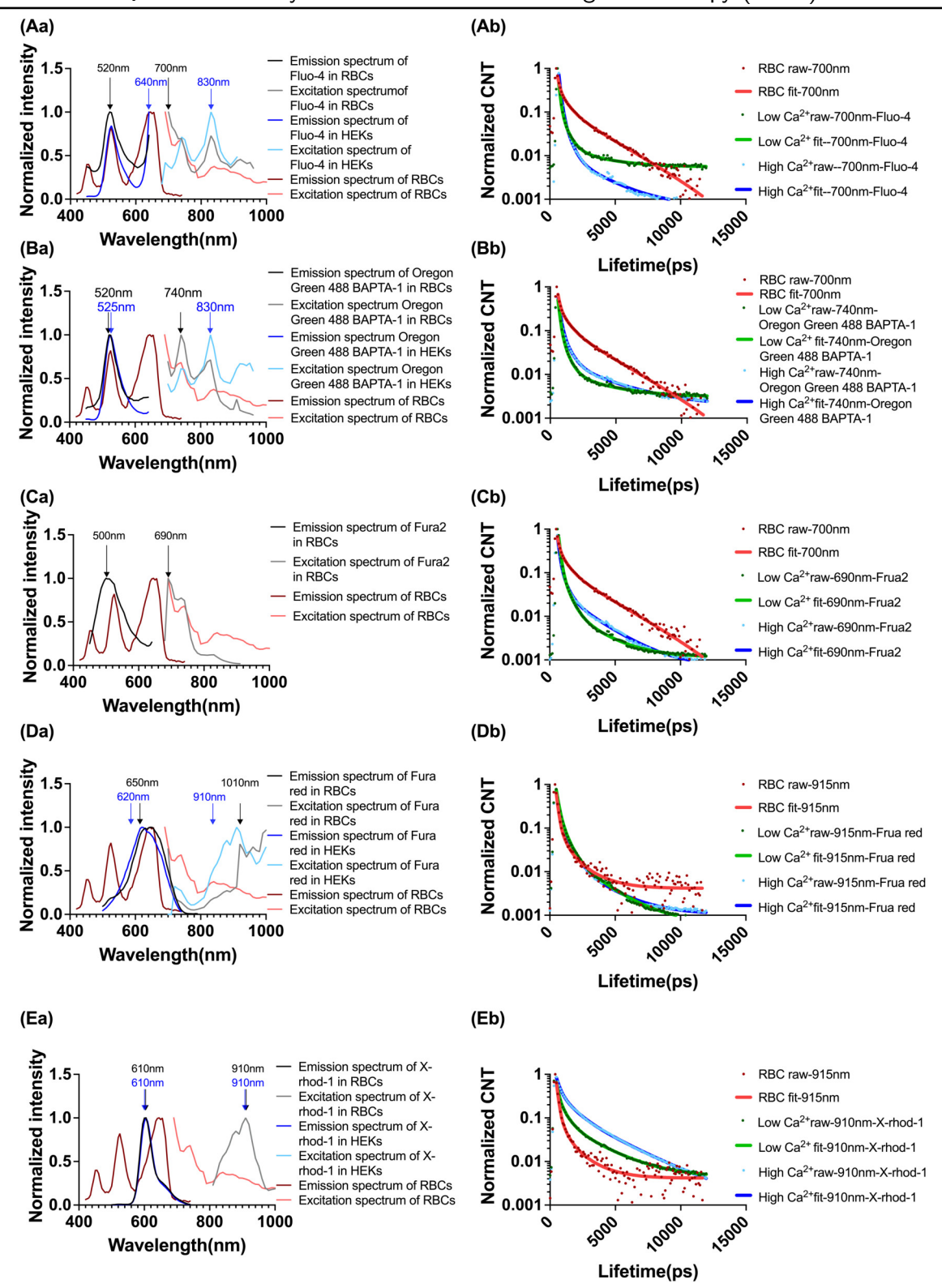


Fig. 3.20: Excitation and emission spectrum of hemoglobin and five different dyes in RBCs and HEK cells and decay curves of RBCs and dyes under high or low Ca²⁺ conditions in RBCs in the Leica 2PE FLIM system. (Aa) Emission spectrum of Fluo-4 in RBCs (black), HEK cells (dark blue) and Hb (dark red) and excitation spectrum of Fluo-4 in RBCs (gray), HEK cells (light blue) and Hb (light red). (Ab) Representative decay curves of Fluo-4 in RBCs with low (green) and high (blue) Ca²⁺ and Hb (red). Dots displayed the measured data and the lines indicated the fitted regression, which are also applied to panel Bb, Cb, Db and Eb. (Ba) Emission spectrum of Oregon Green 488 BAPTA-1 in RBCs (black), HEK cells (dark blue) and Hb (dark red) and excitation spectrum of Oregon Green 488 BAPTA-1 in RBCs (gray), HEK cells (light blue) and Hb (light red). (Bb) Representative decay curves of Oregon Green 488 BAPTA-1 in RBCs with low (green) and high (blue) Ca²⁺ and Hb (red). (Ca) Emission spectrum of Fura-2 in RBCs (black) and Hb (dark red) and excitation spectrum of Fura-2 in RBCs (gray) and Hb (light red). (Cb) Representative decay curves of Fura-2 in RBCs with low (green) and high (blue) Ca²⁺ and Hb (red). (Da) Emission spectrum of Fura red in RBCs (black), HEK cells

Fig. 3.20 (previous page): (dark blue) and Hb (dark red) and excitation spectrum of Fura red in RBCs (gray), HEK cells (light blue) and Hb (light red). (Db) Representative decay curves of Fura red in RBCs with low (green) and high (blue) Ca²⁺ and Hb (red). (Ea) Emission spectrum of X-rhod-1 in RBCs (black), HEK cells (dark blue) and Hb (dark red) and excitation spectrum of X-rhod-1 in RBCs (gray), HEK cells (light blue) and Hb (light red). (Eb) Representative decay curves of X-rhod-1 in RBCs with low (green) and high (blue) Ca²⁺ and Hb (red).

3.4.2.2 FLIM Data Analysis Methods

During the FLIM data analysis, the advanced FLIM fitting method (AFFM) and the maximum entropy method (MELT) were used for data analysis. Compared to AFFM, the MELT method provides the spectrum of the lifetime component distribution of the maximum entropy fitting (Fig. 3.21 A). Comparing the perfection of the fitting, the MELT method has a significantly smaller chi-square than AFFM (Fig. 3.21 B). In addition, AFFM methods with preset number of components could obtain unreasonable lifetime components and amplitudes in some conditions, whereas MELT could directly show the resolvable number of components with a more realistic fitting (Fig. 3.21 C,D).

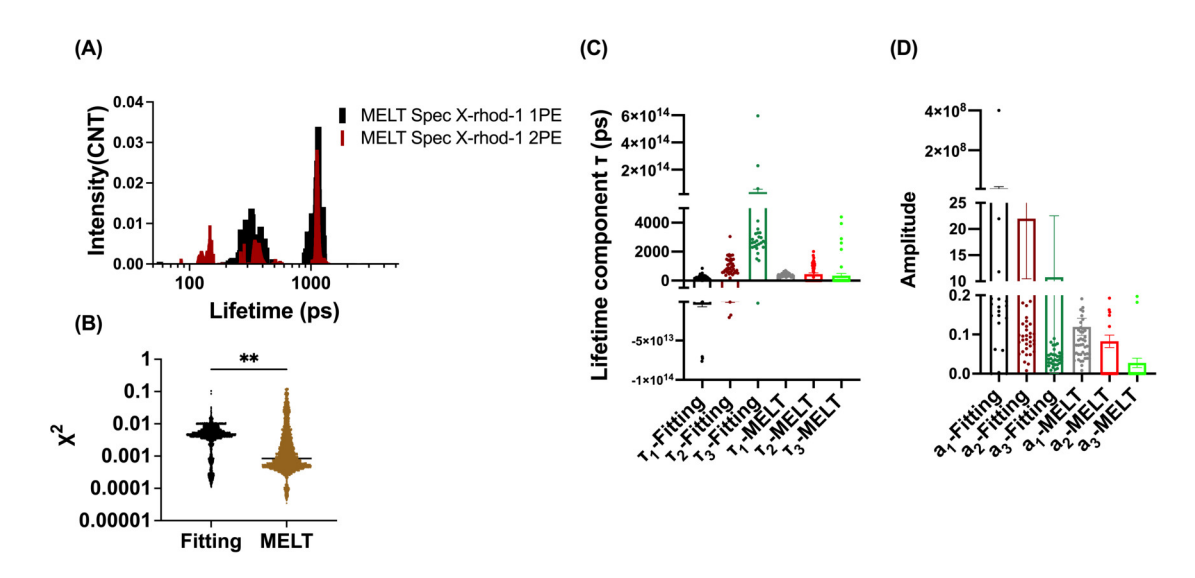


Fig. 3.21: Comparison of two data fitting methods. (A) Lifetime components spectral of X-rhod-1 in RBCs with 1PE (black trace) and 2PE (red trace) detected by the maximum entropy method (MELT). Data is obtained by the Leica 2PE FLIM system and 1PE FLIM system. (B) Statistical comparison of chi-square between the advanced FLIM fitting method (AFFM) and MELT (n=4516). (C) Examples of unreasonable fitted lifetime components from AFFM compared to MELT (n=49). (D) Examples of unreasonable fitted amplitudes between AFFM and MELT (n=49). in (B)-(D), Data is obtained by the Leica 2PE FLIM system and shown as means \pm SEM. Statistical differences were evaluated using paired T-test in (B). p < 0.05 was deemed significant.

3.4.2.3 Influence of 1PE and 2PE on FLIM Parameters of X-rhod-1 Loaded RBCs.

Three FLIM systems were used for experiments presented in this thesis. Two of the systems used 2PE (the Leica 2PE FLIM system and the TauMap 2PE FLIM system) and one of

the systems used 1PE (the 1PE FLIM system). As shown in Figure 3.21 A, with 1PE, the FLIM images of X-rhod-1 loaded RBCs show only two lifetime component peaks in the spectrum. However, with 2PE, the FLIM images of X-rhod-1 loaded RBCs show three lifetime components. The second longest lifetime component τ_2 and the longest lifetime component τ_3 are similar to the two lifetime components τ_1 and τ_2 of the FLIM images taken with the 1PE FLIM system. The shortest lifetime component τ_1 of the FLIM images taken by the Leica 2PE FLIM system is not detected in FLIM images taken by the 1PE FLIM system.

3.4.2.4 Influence of Acquisition Parameters on X-rhod-1 Lifetime in RBCs

To investigate whether the image acquisition parameters could influence the lifetime of X-rhod-1 in RBCs, FLIM images of RBCs loaded with X-rhod-1 were taken using different acquisition parameters, including excitation wavelength, exposure time and temperature. In addition, the reproducibility of the experiment of the lifetime of X-rhod-1 in RBCs on different days of the experiment was tested.

As shown in Figure 3.22 A, in FLIM images taken by the TauMap 2PE FLIM system, the decay curve of X-rhod-1 in 800 nm 2PE, 850 nm 2PE, 900 nm 2PE and 920 nm 2PE are similar to each other. Data analysis resolved three lifetime components (τ_1 , τ_2 and τ_3). τ_1 is the shortest lifetime component. τ_2 is the second longest lifetime component and τ_3 is the longest lifetime component (Fig. 3.22 B,C,D). There is no statistical difference between τ_1 and τ_2 among conditions with different excitation laser wavelengths (Fig. 3.22 B,C). In contrast, the τ_3 from 800 nm 2PE excitation is significantly different from τ_3 of the image taken with 900 nm 2PE and 920 nm 2PE (Fig. 3.22 D). With the 1PE FLIM system, the FLIM images are taken with two different excitation laser wavelengths, 470 nm and 532 nm. The FLIM parameters shows no difference between the two laser wavelength excitations (Fig. A.6).

Next, FLIM images of RBCs loaded with X-rhod-1 are acquired using the same excitation laser wavelength and different exposure times in the TauMap 2PE system. As shown in Figure 3.23 A, the decay curves are similar under different acquisition conditions. τ_1 and τ_2 show no difference among different acquisition conditions (Fig. 3.23 B,C). For τ_3 , there is a significant difference between images taken with 4.4 second exposure time and images taken with 97 second exposure time. The τ_3 of images with another exposure time show no difference to the images with 4.4 second exposure time but a downward trend (Fig. 3.23 D).

The effects of surrounding temperature during FLIM imaging with the Leica 2PE FLIM system is shown in Figure 3.24. As shown in Figure 3.24 A, the lifetime decay curves of X-rhod-1 at different temperature conditions show a slight difference in the tail. Regarding the tail, the decay of X-rhod-1 FLIM images taken at 26 °C is the slowest decay in the tail and the decay of X-rhod-1 FLIM images taken at 37 °C is the fastest decay (Fig. 3.24 A). The τ_1 and τ_2 are significantly shorter with increasing temperature (Fig. 3.24 B,C). Differently, the τ_3 of FLIM images taken in 26 °C and 29 °C show no significant difference (Fig. 3.24 D). However, both of them are significantly longer than τ_3 of FLIM images taken in 37 °C (Fig. 3.24 D). The amplitude-averaged lifetime is also significantly shorter with increasing temperature (Fig. 3.24 E). However, the lifetime-weighted ratio shows no significant difference with changing temperature (Fig. 3.24 G). Furthermore, although there

are significant differences between the amplitude ratio of the three conditions at different extracellular temperatures, there is not enough data to show a clear relationship between temperature and amplitude ratio (Fig. 3.24 F).

In addition, the reproducibility of the lifetime components of FLIM images with the same FLIM system and acquisition parameters was tested. As Figure 3.25 A show, in Leica 2PE FLIM system, the lifetime decay curves of X-rhod-1 in RBCs in the same condition are similar in different experiment days. The lifetime components show variations among different experiment days but there is no significant difference detected (Fig. 3.25 B-D). Data obtained using other FLIM imaging system are shown in Appendix (Fig. A.7).

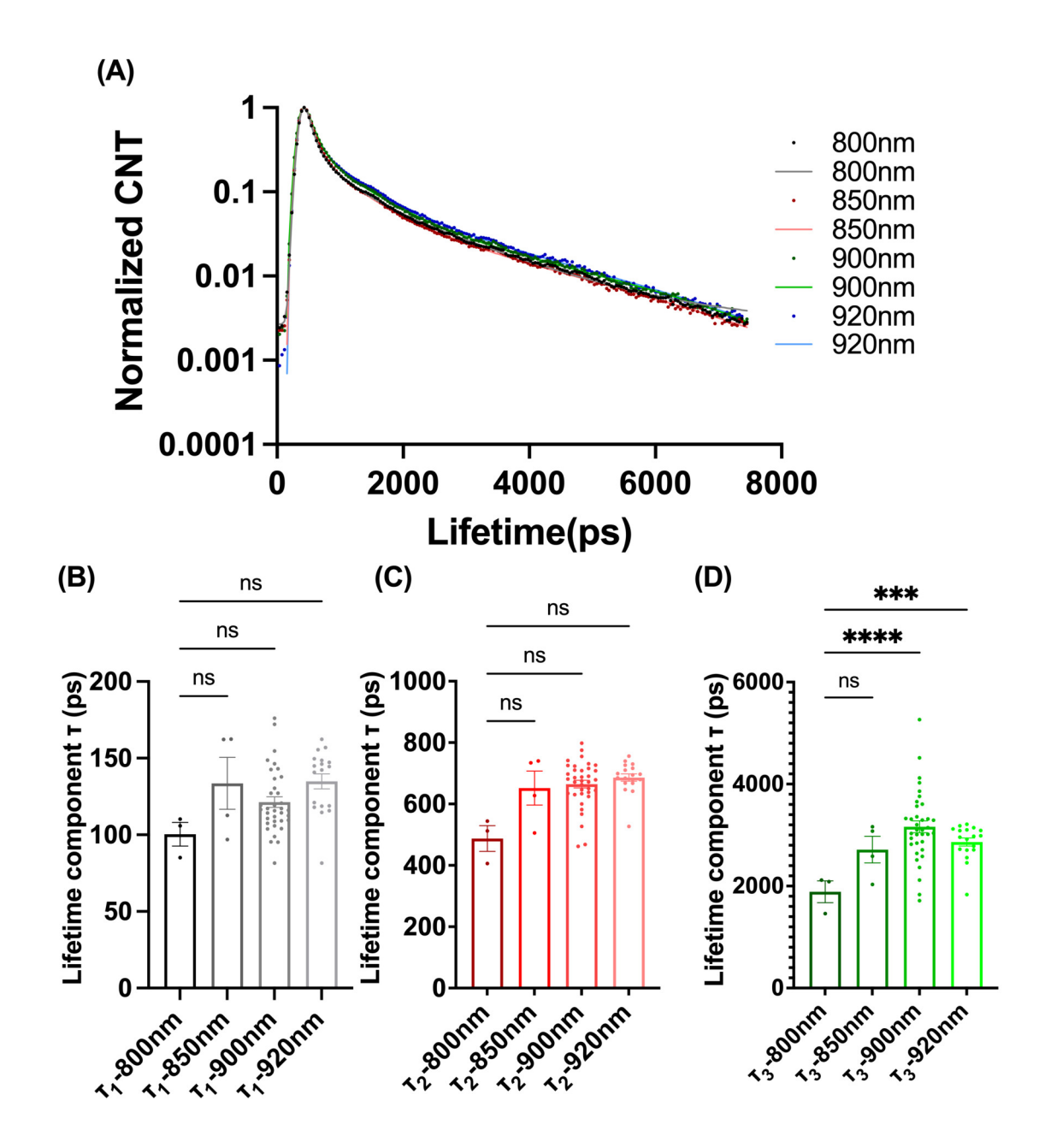


Fig. 3.22: Effect of excitation laser wavelength on lifetime and lifetime components. Data were taken from FLIM images of X-rhod-1-stained RBCs acquired by the TauMap 2PE FLIM system. (A) Representative decay curves of X-rhod-1 in RBCs with 800 nm 2PE (black), 850 nm 2PE (red), 900 nm 2PE (green) and 920 nm 2PE (blue). Dots displayed the measured data and lines indicated the fitted regression. (B)–(D) Statistical comparison of lifetime components of FLIM images with different excitation laser wavelengths: (B) shortest lifetime component (τ_1); (C) second longest lifetime component (τ_2); (D) longest lifetime component (τ_3) ($n_{800 \text{ nm}}$ =6, $n_{850 \text{ nm}}$ =6, $n_{900 \text{ nm}}$ =47, $n_{920 \text{ nm}}$ =18). Data is shown as means \pm SEM in (B)-(D). Statistical differences were evaluated using one-way ANOVA with Tukey's multiple comparison method. p < 0.05 was deemed significant.

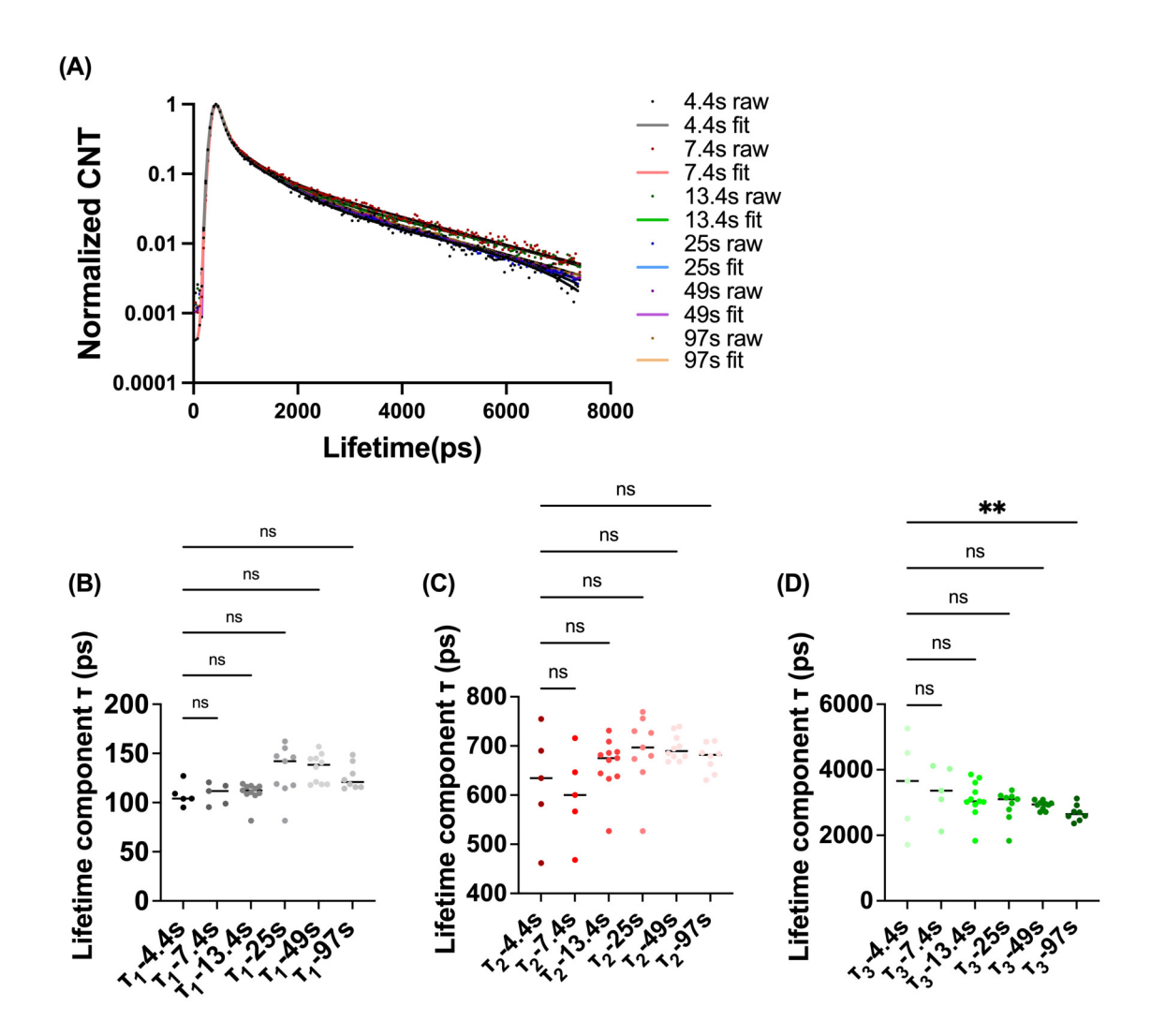


Fig. 3.23: Effect of acquisition time on lifetime and lifetime components. Data were taken from FLIM images of X-rhod-1-stained RBCs acquired by the TauMap 2PE FLIM system. (A) Representative decay curves of FLIM imaged of X-rhod-1 in RBCs with 4.4 seconds acquisition time (black), 7.4 seconds acquisition time (red), 13.4 seconds acquisition time (green), 25 seconds acquisition time (blue), 49 seconds acquisition time (purple) and 97 seconds acquisition time (light brown). (B)-(D) Statistical comparison of lifetime components of FLIM images with different acquisition time: (B) τ_1 , (C) τ_2 and (D) τ_3 . ($n_{4.4}$ s=5, $n_{7.4}$ s=5 $n_{13.4}$ s=11, n_{25} s=9, $n_{4.4}$ s=9, n_{97} s=8). Data is shown as median in (B)-(D). Statistical differences were evaluated using one-way ANOVA with Tukey's multiple comparison method in (B). p < 0.05 was deemed significant.

In summary, with the same system, the lifetime components of X-rhod-1 stained RBCs from the same donor are stable. In the 1PE FLIM system, two different excitation laser wavelengths do not influence the lifetime components of X-rhod-1 stained RBCs as well. In the TauMap 2PE FLIM system, the longest lifetime component τ_3 is only different at 800 nm, the shortest laser wavelength and when the acquisition time is only 4.4 second. The other two lifetime components τ_1 and τ_2 are not influenced by either excitation wavelength or acquisition time. Environment temperature has a significant influence on τ_1 , τ_2 , amplitude averaged lifetime and amplitude ratio. The is τ_3 less sensitive for temperature compared to τ_1 and τ_2 and the lifetime weighted amplitude ratio is not affected by temperature.

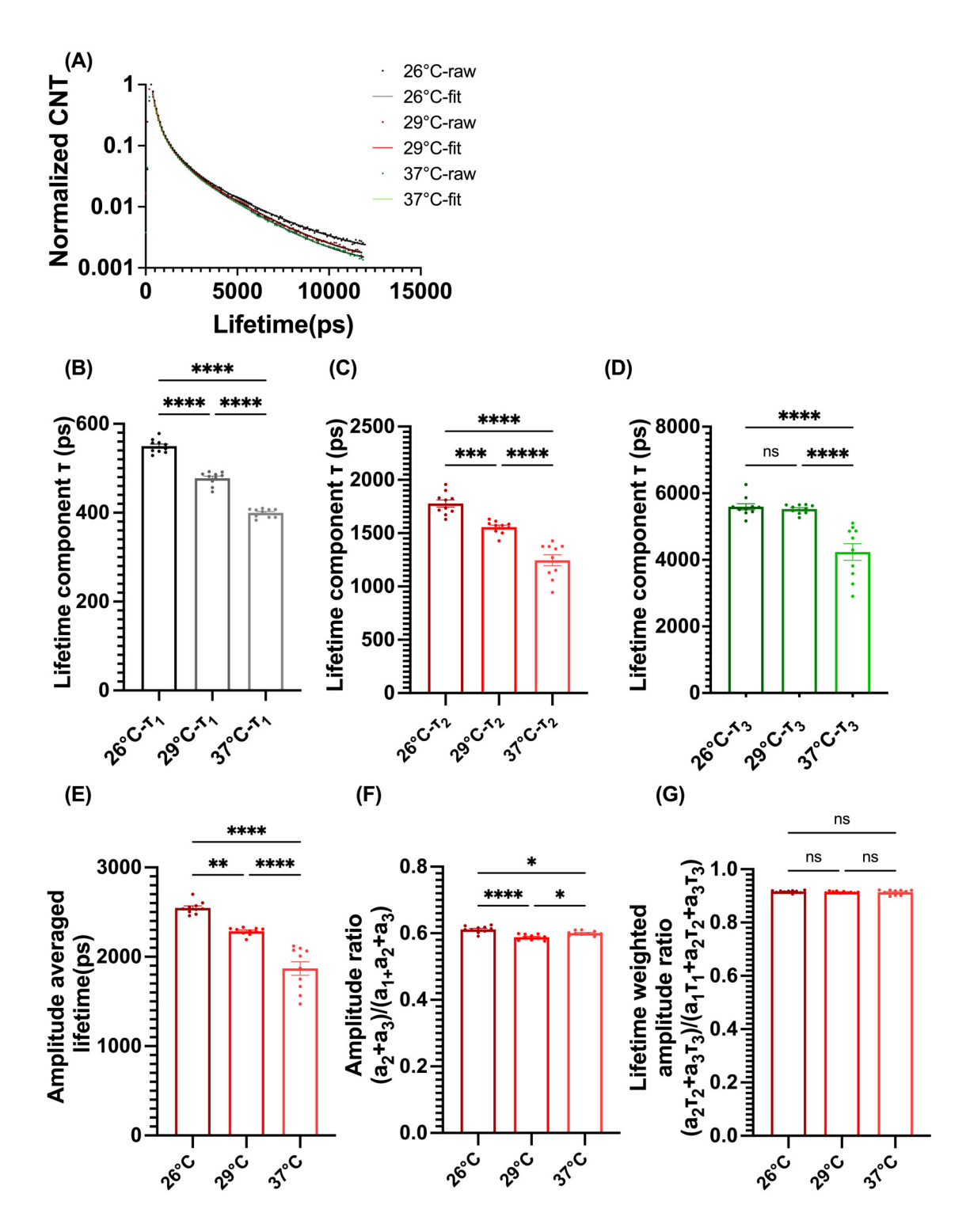


Fig. 3.24: Effect of ambient temperature on FLIM parameters. FLIM images of X-rhod-1 loaded RBCs were acquired with the Leica 2PE FLIM system. (A) Representative decay curves of FLIM images of X-rhod-1 in RBCs at 26 °C (black), 29 °C (red) and 37 °C (green). The dots displayed the measured data and the lines indicated the fitted regression. (B) Statistical comparison of different FLIM images taken at different temperatures: (B) τ_1 , (C) τ_2 , (D) τ_3 , (E) amplitude averaged lifetime, (F) amplitude ratio, and (G) lifetime weighted amplitude ratio (n=10). Data is shown as means \pm SEM in (B)-(D). Statistical differences were evaluated using one-way ANOVA with Tukey's multiple comparison method in (B). p < 0.05 was deemed significant.

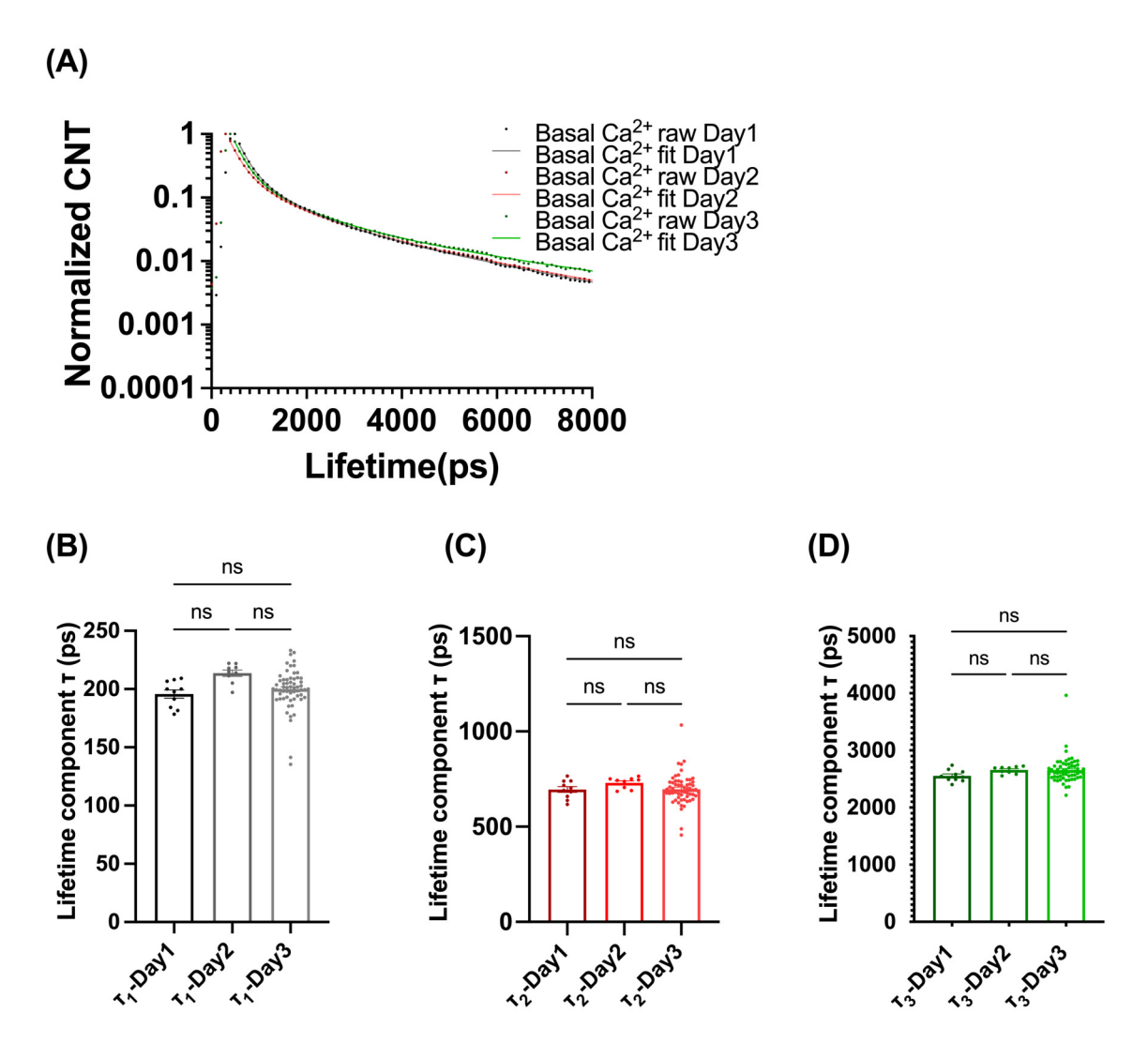


Fig. 3.25: Parameters of FLIM images of X-rhod-1 loaded RBCs from the same donor on different days. Data acquired using the Leica 2PE FLIM system. ($n_{Day1}=10,\,n_{Day2}=9,\,n_{Day3}=60$). (A) Representative decay curves of FLIM images from three different days (day 1-black, day 2-red, day 3-green). (B)–(D) Statistical comparison of lifetime components of FLIM images taken on three different experimental days: (B) τ_1 , (C) τ_2 and (D) τ_3 . Data is shown as means \pm SEM in (B)-(D). Statistical differences were evaluated using one-way ANOVA with Tukey's multiple comparison method. p < 0.05 was deemed significant.

3.4.2.5 Ca²⁺-ionophore Selection

Bromo-A23187 and Ionomycin are two common Ca^{2+} ionophores used in the biological experiments. Their addition potentially equalizes intracellular Ca^{2+} concentration and the extracellular Ca^{2+} concentration. In this way, with the help of the ionophore, the RBCs with a known concentration of Ca^{2+} can be obtained for further experiments.

To find the ionophores that do not contribute to the lifetime components of the decay, FLIM images of unstained RBCs treated with Ionomycin or Bromo-A-23187 were acquired using the Leica 2PE FLIM system.

As shown in Figure 3.26 Aa, in the MELT analysis, both untreated RBCs and Ionomycintreated unstained RBCs show two lifetime components (τ_1 and τ_2). The τ_1 and τ_2 of untreated RBCs are similar to those of Ionomycin treated RBCs and do not show much variation at different excitation laser wavelengths. However, the FLIM images of Bromo-A23187 treated unstained RBCs show only one lifetime component, which is slightly shorter than τ_1 of Ionomycin-treated and untreated RBCs (Fig. 3.26 A). At the same excitation wavelength, Bromo-A23187 treated RBCs show a similar lifetime decay like Ionomycin treated RBCs (Fig. 3.26 B). The average intensity of Bromo-A23187 treated RBCs is significantly less than that of Ionomycin-treated RBCs at 915 nm 2PE (Fig. 3.26 C). In addition, the amplitude-weighted lifetime of Bromo-A23187 treated RBCs is obviously less than that of Ionomycin-treated RBCs at 900 nm 2PE (Fig. 3.26 D). The FLIM images of Bromo-A23187 treated RBCs with 915 nm 2PE could not be resolved due to the low number of photons, so the data are not included in Figure 3.26 D.

In addition, the FLIM images of X-rhod-1 stained RBCs treated with either Ionomycin or Bromo-A23187 were taken in the TauMap 2PE FLIM system and 1PE FLIM system. Data show that there is no significant difference between Ionomycin and Bromo-A23187 treated X-rhod-1 stained RBCs (Fig. A.9).

In summary Ionomycin and Bromo-A23187 do not show significant influence on X-rhod-1 decay in RBCs. Ionomycin shows higher fluorescence intensity than Bromo-A23187 in the same condition and the Bromo-A23187 is only resolved one very short lifetime component. Thus, Bromo-A23187 was selected for further experiments.

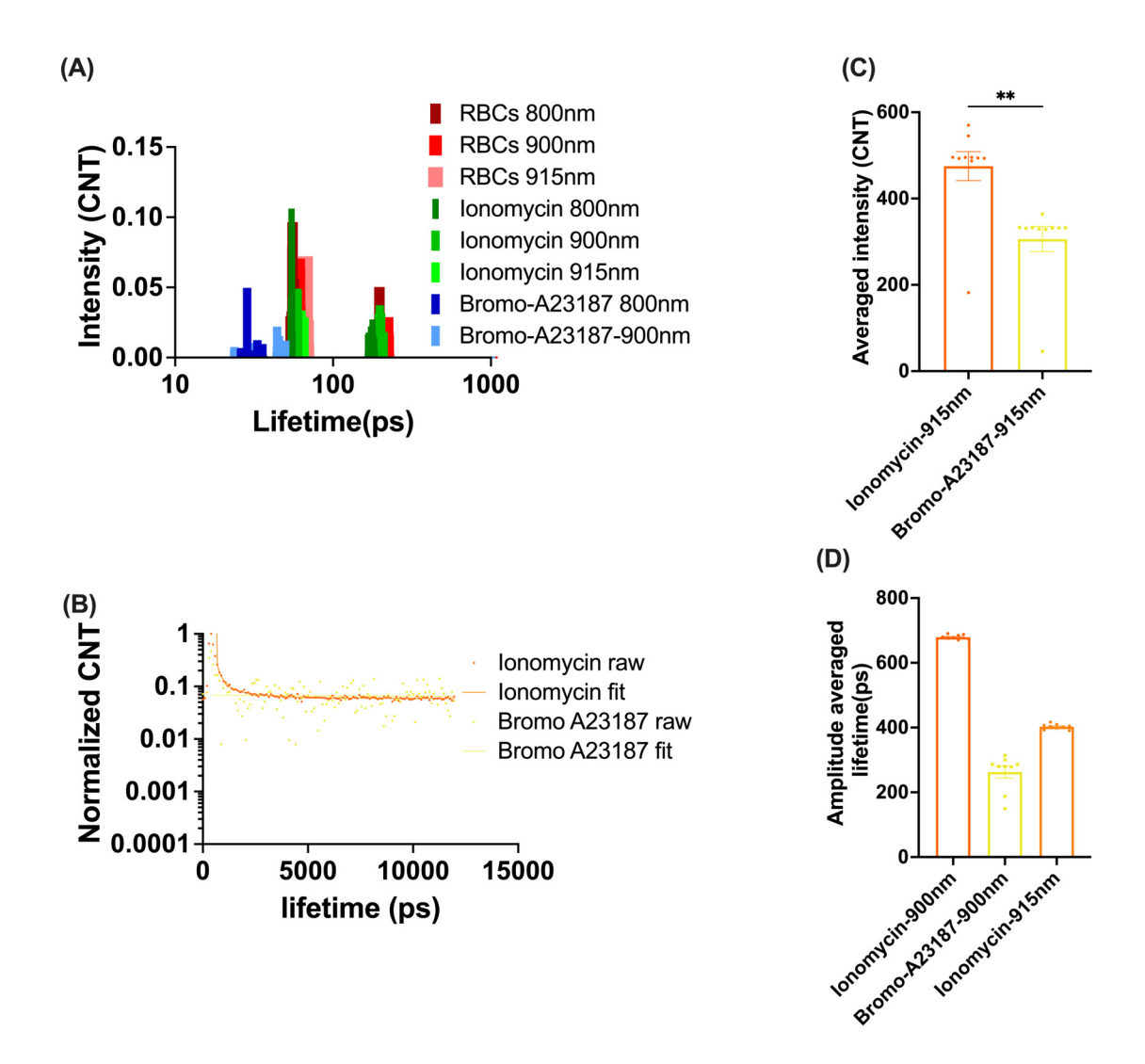


Fig. 3.26: Influence of ionophores on the parameters of FLIM images. Raw data acquired by the Leica 2PE FLIM system (n=10). (A) MELT components spectral of RBCs (red), RBCs with Ionomycin (green) and RBCs with Bromo-A23187 (blue) with different excitation laser wavelengths. The darkest color indicates 800 nm 2PE. The second darkest color indicates 900 nm 2PE and the lightest color indicates 915 nm 2PE. (B) Representative decay curves of FLIM images of RBCs with Ionomycin (orange) and Bromo-A23187 (yellow). The dots displayed the measured data and the lines indicated the fitted regression. (C) –(D) Statistical comparison of FLIM images between Ionomycin-stimulated RBCs and Bromo-A23187-stimulated RBCs: (C) Average intensity with 915 nm 2PE; (D) Amplitude-averaged lifetime with 900 nm and 915 nm 2PE. Data is shown as means \pm SEM in (C) - (D). Statistical differences were evaluated using unpaired T-test. p < 0.05 was deemed significant.

3.4.2.6 Influence of Donor Variation and Ca^{2+} pumps on X-rhod-1 Lifetime in RBCs

When a Ca²⁺-ionophore is applied to living RBCs and the intracellular Ca²⁺ concentration increases, the Ca²⁺ pump of the RBCs is as able to open and reduce the intracellular Ca²⁺ concentration. RBCs in the experiments had been fasted for 72 hours to deplete ATP. The time that ATP-depleted RBCs maintained the same Ca²⁺ concentration was tested. In addition, the effects of donor variation on the lifetime of X-rhod-1 in RBCs were tested.

RBCs from three donors were stained with X-rhod-1 and FLIM images were taken using the Leica 2PE FLIM system. As shown in Figure 3.27 A, the lifetime decay curves of X-rhod-1 loaded RBCs show no obvious difference among the three donors. The three lifetime components τ_1 , τ_2 and τ_3 also show no statistical difference between donors (Fig. 3.27 B,C,D).

The next step was to test how long the designed intracellular $\rm Ca^{2+}$ concentration of ATP-depleted RBCs could be maintained. A time series of FLIM images of X-rhod-1 loaded RBCs with the desired intracellular $\rm Ca^{2+}$ concentration was acquired using the Leica 2PE FLIM system. As shown in Figure 3.28, the amplitude-averaged lifetime of RBCs at basal intracellular $\rm Ca^{2+}$ does not change over time. The amplitude-averaged lifetime of RBCs with $\rm 10\,\mu M$ or $\rm 100\,\mu M$ $\rm Ca^{2+}$ is relatively stable for around 300 seconds then decreases with time. And the RBCs with $\rm 10\,\mu M$ $\rm Ca^{2+}$ show a faster decrease than the RBCs with $\rm 10\,\mu M$ $\rm Ca^{2+}$ (Fig. 3.28).

The time series of FLIM images of X-rhod-1 loaded RBCs were also taken using the 1PE FLIM system (Fig. A.11). The results were similar to the FLIM images from the Leica 2PE FLIM system.

In summary, the RBC variation due to different donors does not affect the lifetime components of X-rhod-1 stained RBCs. The intracellular concentration of $\mathrm{Ca^{2+}}$ in fasted RBCs induced by Bromo-A23187 can only maintain around 5 minutes after FLIM image acquisition starts.

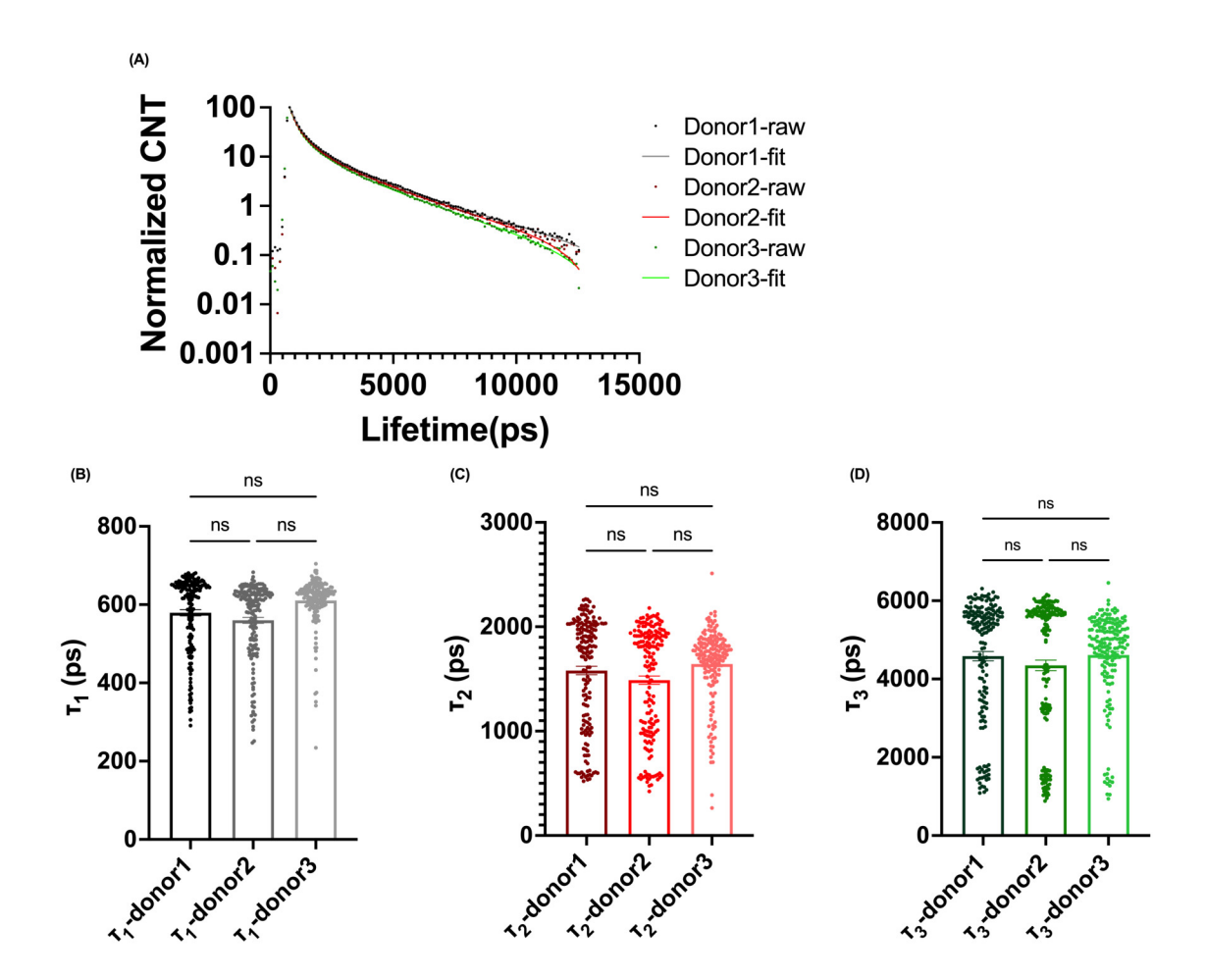


Fig. 3.27: Influence of donor variation on FLIM parameters. Data acquired using the Leica 2PE FLIM system. (A) Representative decay curves of FLIM images of X-rhod-1-stained RBCs from three donors (donor 1: black, donor 2: red, donor 3: green). Dots displayed the measured data, and the lines indicated the fitted regression. (B)-(D) Statistical comparison of FLIM images of X-rhod-1-stained RBCs from three donors: (B) τ_1 ; (C) τ_2 ; (D) τ_3 ($n_{donor1}=122$, $n_{donor2}=131$, $n_{donor3}=171$). Data is shown as means \pm SEM in (B)-(D). Statistical differences were evaluated using ANOVA with Tukey's multiple comparison method. p < 0.05 was deemed significant.

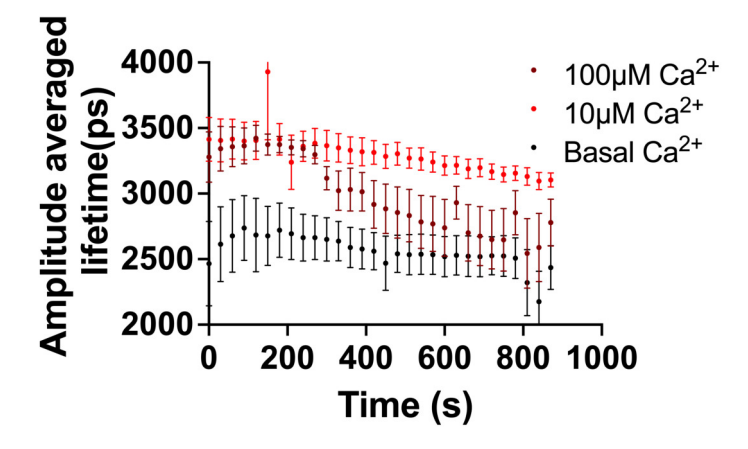


Fig. 3.28: Influence of time after ionophore application on FLIM parameters. Data acquired using the Leica 2PE FLIM system. Amplitude-averaged lifetime of 15 mintue time series of FLIM of X-rhod-1 in RBCs with basal $\mathrm{Ca^{2+}}$ (black) or after application of Bromo-A23187 with additional $\mathrm{Ca^{2+}}$ in the environment (10 μ M $\mathrm{Ca^{2+}}$ -light red, 100 μ M $\mathrm{Ca^{2+}}$ -dark red). ($\mathrm{n_{image/per\ data\ point}=6.}$)

3.4.2.7 The Influence of Hemoglobin (Hb) Concentration on X-rhod-1 Lifetime in RBCs

Physiological or pathophysiological environmental changes could lead to changes in the RBC shape following the SDE sequence. The SDE sequence is often associated with changes in RBC volume and Hb concentration. During experiments, the shape change of RBCs were often observed in the images due to increased intracellular ${\rm Ca^{2+}}$ and the subsequent biological cascade of increased ${\rm Ca^{2+}}$. To test whether a change in Hb concentration could influence the measured X-rhod-1 lifetime in RBCs, X-rhod-1 loaded RBCs were challenged with hypoosmotic PBS solution (about 130 mOsm/L), isotonic PBS solution (approximately 300 mOsm/L) and hyperosmotic PBS solution (around 800 mOsm/L). The different osmolar environments were supposed to create X-rhod-1 loaded stomatocytes, discocytes and echinocytes. Additional ${\rm Ca^{2+}}$ and Bromo-A23187 were applied to the environment to test whether the potential changes in FLIM parameters occurred due to a change in intracellular ${\rm Ca^{2+}}$ concentration. The FLIM images of the challenged RBCs were then acquired and analyzed. In addition, HEK cells were loaded with X-rhod-1 and FLIM images were acquired and compared with FLIM images of RBCs in the same condition.

As expected, the X-rhod-1 loaded stomatocytes without extra Ca²⁺ have a significantly higher intensity than RBCs in isotonic PBS without added Ca²⁺ (Fig. 3.29 A). The X-rhod-1 loaded echinocytes without additional Ca²⁺ have a slightly lower average intensity than RBCs in isotonic PBS, but the difference is not significant (Fig. 3.29 A). The decay curves of X-rhod-1 in RBCs in hypoosmotic solution are slower than the decay curves of X-rhod-1 in RBCs in isotonic and hyperosmotic environments (Fig. 3.29 B). The decay curves of X-rhod-1 in discocytes are slightly slower than the lifetime decay of X-rhod-1 in echinocytes (Fig. 3.29 B). However, the RBCs challenged with the same osmolarity solution with or without additional Ca²⁺ show that no obvious difference in the intensity and lifetime decay curves (Fig. 3.29 A,B).

As shown in Figure 3.29 C,D,E, the measured τ_1 , τ_2 and τ_3 of X-rhod-1 loaded stomatocytes are longer than those of X-rhod-1 loaded discocytes and echinocytes. In addition, the three lifetime components of X-rhod-1 loaded echinocytes in hyperosmotic PBS are shorter than those of X-rhod-1 loaded RBCs in isotonic PBS (Fig. 3.29 C,D,E). Furthermore, τ_1 , τ_2 and τ_3 of X-rhod-1 loaded RBCs in isotonic PBS with added Ca²⁺ are significantly longer than in isotonic PBS but there is no obvious difference in three lifetime components of echinocytes with or without additional Ca²⁺ (Fig. 3.29 C,D,E). Interestingly, τ_1 of X-rhod-1 loaded stomatocytes is significantly shorter than that of stomatocytes with extra Ca²⁺, but the and τ_3 is higher. However, there is no significant difference in τ_2 between stomatocytes with or without additional Ca²⁺ (Fig. 3.29 C,D E).

The stomatocytes loaded with X-rhod-1 have almost twice longer amplitude-averaged lifetime of X-rhod-1 than discocytes, and the variation of stomatocytes is greater (Fig. 3.29 F). The amplitude-averaged lifetime of X-rhod-1 in echinocytes is about 25% shorter than in discocytes, which is significantly different (Fig. 3.29 F). When the Ca^{2+} -ionophore and Ca^{2+} are added to the solution, the averaged lifetime of stomatocytes is 10% shorter than in stomatocytes without Ca^{2+} supplementation (Fig. 3.29 F). Differently, the amplitude-averaged lifetime of X-rhod-1-stained discocytes with extra Ca^{2+} in the environment is

significantly longer than that of X-rhod-1-stained discocytes without additional Ca^{2+} (Fig. 3.29 F). In addition, there is no significant difference between echinocytes with and without increased intracellular Ca^{2+} (Fig. 3.29 F).

The amplitude ratio shows a similar trend to the amplitude-averaged lifetime (Fig. 3.29 F,G). The X-rhod-1 stained stomatocytes have the higher amplitude ratio than discocytes and echinocytes (Fig. 3.29 G). The X-rhod-1 stained RBCs in isotonic solution without additional Ca^{2+} have a significantly lower amplitude ratio than RBCs in isotonic PBS with extra Ca^{2+} (Fig. 3.29 G). Differently, not only the X-rhod-1 loaded echinocytes with or without increased intracellular Ca^{2+} have a similar amplitude ratio, but the amplitude ratio of the stomatocytes with or without increased intracellular Ca^{2+} has no significant difference (Fig. 3.29 G). The lifetime-weighted amplitude ratio shows a similar trend, but differences between groups are smaller compared to the amplitude ratio (Fig. 3.29 G,H).

The FLIM images of X-rhod-1 in HEK cells were also acquired. There are three peaks in the lifetime component spectra of X-rhod-1 in HEK cells, where the peak of the second longest lifetime component is smaller than the other components (Fig. 3.30 A). All peaks of the lifetime component spectra of X-rhod-1 in HEKs are shifted to the right compared to that of X-rhod-1 in RBCs (Fig. 3.30 A). The amplitude-averaged lifetime of X-rhod-1 in HEK cells is much longer than that in RBCs at the same intracellular Ca^{2+} concentration (Fig. 3.30 B). When the lifetime components of the FLIM images of X-rhod-1 in HEK cells are compared with those in RBCs in different osmolar solutions, the X-rhod-1-stained HEK cells have the longest τ_1 , τ_2 and τ_3 (Fig. 3.30 C,D,E). The X-rhod-1-stained RBCs in low osmolarity solution have τ_1 , τ_2 and τ_3 close to those of HEK cells but significantly shorter (Fig. 3.30 C,D,E). The three lifetime components of X-rhod-1-stained RBCs in normal and high osmolarity solution are much shorter than those of X-rhod-1 stained HEK cells (Fig. 3.30 C,D,E). In addition, the amplitude-averaged lifetime, amplitude ratio and lifetime-weighted amplitude ratio of X-rhod-1 in HEK cells are longer than those of X-rhod-1 in RBCs in solution at each osmolarity (Fig. 3.30 F,G,H).

In summary, with increased Hb concentration in RBCs, τ_1 , τ_2 , τ_3 , amplitude-averaged lifetime, amplitude ratio and lifetime weighted amplitude decrease.

3.4.2.8 The Influence of Fluorescence Intensity on Measured X-rhod-1 Lifetime in RBCs

The Fluorescence Intensity Difference between Different FLIM Images

During FLIM data analysis, the lifetime components and the amplitude averaged lifetime appears to be dependent on the fluorescence intensity or photon count of the FLIM images. To understand whether fluorescence intensity had an effect on the measured lifetime parameters of X-rhod-1 in RBCs and what factors might influence fluorescence intensity, FLIM images of X-rhod-1-loaded RBCs were compared under the same physical acquisition conditions.

As shown in Figure 3.31 A, the amplitude-averaged lifetime increases with an increasing average intensity of FLIM images. There seems to follow a logarithmic regression between the amplitude-averaged lifetime and the average intensity with a plateau when average intensity reached around 15 photons per pixel. Similarly, the three lifetime components

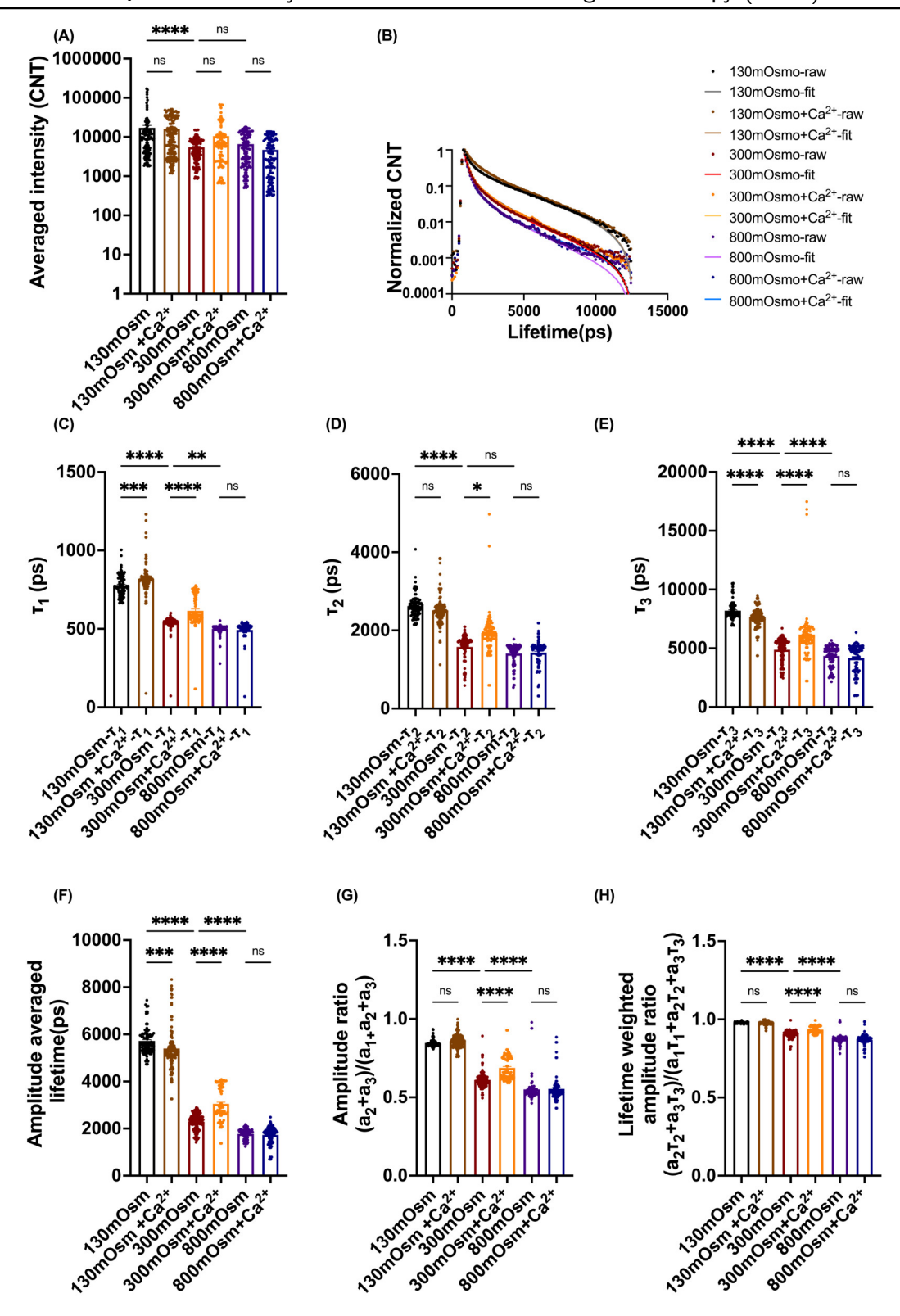


Fig. 3.29: Effect of Hb concentration on FLIM parameters. Data obtained by the Leica 2PE FLIM system. (A) Comparison of the average intensity of X-rhod-1 in RBCs exposed to different osmolar environments, with or without additional Ca^{2+} . (B) Representative decay curves of FLIM images of X-rhod-1-stained RBCs in PBS solution with different osmolarity, with or without additional Ca^{2+} (130 mOsm/L: black, 130 mOsm/L+ Ca^{2+} : brown, 300 mOsm/L: red, 300 mOsm/L+ Ca^{2+} : orange, 800 mOsm/L: purple, 800 mOsm/L+ Ca^{2+} : blue). Dots displayed the measured data, and lines indicated the fitted regression. (C)-(H) Statistical comparison of FLIM images of X-rhod-1-stained RBCs in different osmolarity environments, with or without additional Ca^{2+} : (C) τ_1 ; (D) τ_2 ; (E) τ_3 ; (F) Amplitude-averaged lifetime; (G) Amplitude ratio; (H) Lifetime-weighted ratio ($n_{RBCs-130 \text{ mOsm/L}}=96$, $n_{RBCs-130 \text{ mOsm/L}}+Ca=133$, $n_{RBCs-300 \text{ mOsm/L}}=133$, $n_{RBCs-300 \text{ mOsm/L}}+Ca=89$, $n_{RBCs-800 \text{ mOsm/L}}=94$, $n_{RBCs-800 \text{ mOsm/L}}+Ca=86$). Data is shown as means \pm SEM in (A) and (C)-(H). Statistical differences were evaluated using one-way ANOVA with Tukey's multiple comparison method. p < 0.05 was deemed significant.

98 3 Results

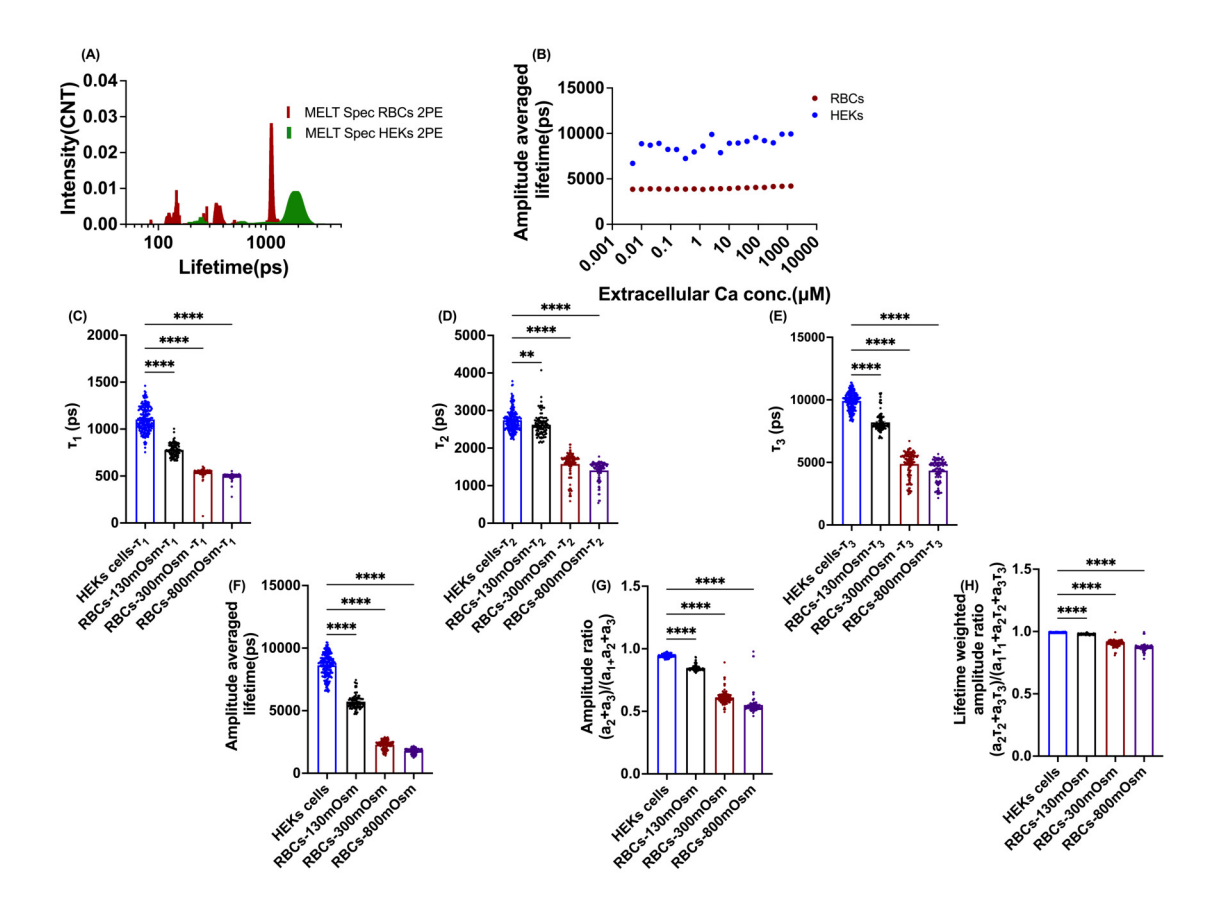


Fig. 3.30: FLIM parameters of X-rhod-1 in RBCs with different Hb concentrations and HEK cells. (A) Lifetime components spectrum of X-rhod-1 in RBCs with 1PE (black), X-rhod-1 in RBCs with 2PE (red) and X-rhod-1 in HEK cells (green). (B) Statistical comparison of the amplitude averaged lifetime of X-rhod-1 in RBCs (red) and HEK cells (blue) with different intracellular Ca^{2+} ($n_{RBCs}=30$ per data point, $n_{HEKs}=10$ per data point) (C)-(H) Statistical comparison of FLIM images of X-rhod-1-stained RBCs in PBS with different osmolarity (130 mOsm/L, 300 mOsm/L and 800 mOsm/L and HEK cells in 300 mOsm/L PBS): (C) τ_1 ; (D) τ_2 ; (E) τ_3 ; (F) Amplitude-averaged lifetime; (G) Amplitude ratio; (H) Lifetime weighted amplitude ratio ($n_{HEKs}=210$, $n_{RBCs-130\,mOsm/L}=96$, $n_{RBCs-300\,mOsm/L}=133$, $n_{RBCs-800\,mOsm/L}=94$). Data is shown as means \pm SEM in (B)-(G). Statistical differences were evaluated using one-way ANOVA with Tukey's multiple comparison method in (C)-(G). p < 0.05 was deemed significant.

 $(\tau_1, \tau_2 \text{ and } \tau_3)$ follow logarithmic regression over the average intensity with a saturation, independent of the intracellular Ca²⁺ concentration (Fig. 3.31 B). In case of saturation, the three components are considered as fully resolvable, a low intensity only allows a coarse resolution. This results in only a single component in the MELT spectrum equal to the average lifetime. The number of resolved components increases with the average intensity. In the intermediate case of two components, the lifetimes are similar to the lowest and highest components in the fully resolved case (Fig. 3.31 B).

To find out whether the intensity difference was caused by the focusing of the image, the sharpness of the image was analyzed. As shown in Figure 3.31 C, there is a good linear relation between sharpness and average intensity with R^2 close to one. Further, τ_1 , τ_2 , τ_3 and the amplitude-averaged lifetime show a similar logarithmic regression to image sharpness like between the lifetime parameters and the average intensity (Fig. 3.31 D). This

indicates that the intensity influences the resolution of the lifetime component detection, which is highly dependent on the focus.

The model clearly shows the saturation behavior between image focus and lifetime components or amplitude-averaged lifetime. The three lifetime components, as fully resolvable conditions, can only be achieve when enough photons are recorded.

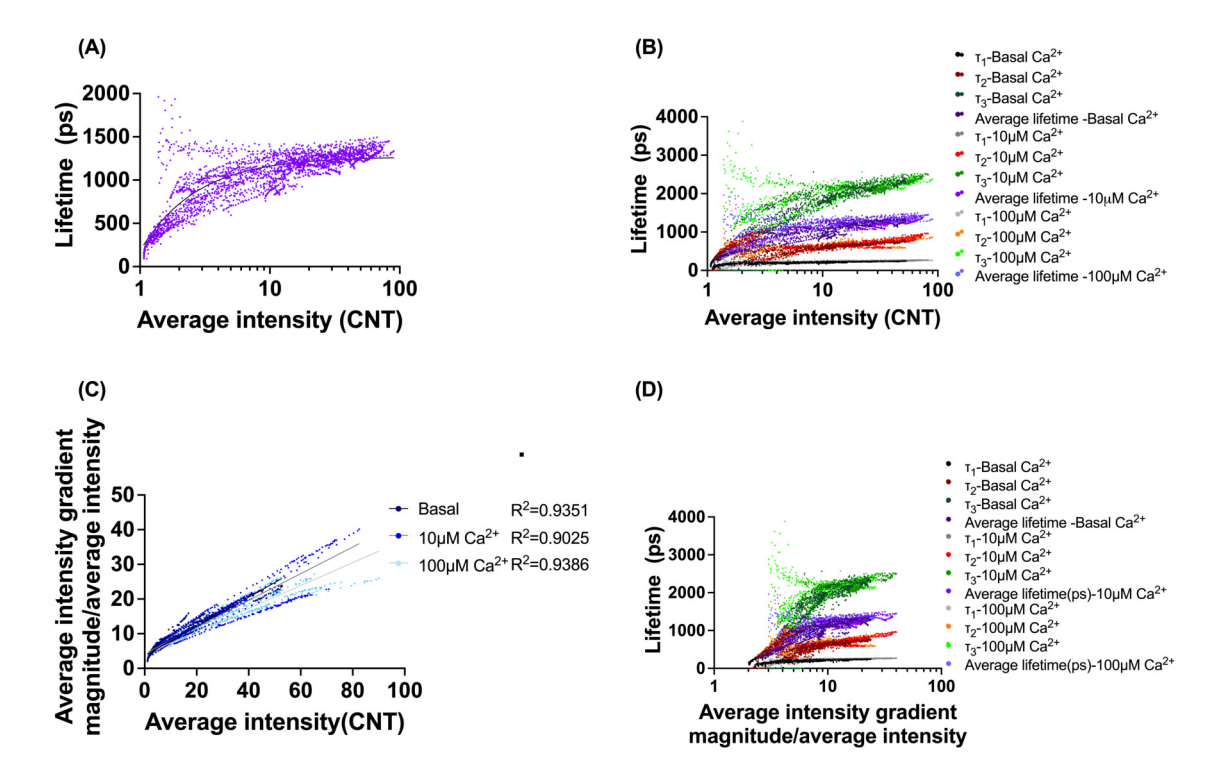


Fig. 3.31: Effects of fluorescence intensity and image sharpness on FLIM parameters. Data acquired by the Leica 2PE FLIM system. (A) Regression between amplitude-averaged lifetime and average intensity (n=2545). (B) Relationship between lifetime parameters and average intensity under different intracellular Ca^{2+} conditions. (C) Regression of average intensity and image sharpness in different intracellular Ca^{2+} conditions. (D) Relationship between lifetime parameters and image sharpness in different intracellular Ca^{2+} conditions. ($n_{basal-Ca}=734$, $n_{10\,\mu\text{M-Ca}}=749$, $n_{100\,\mu\text{M-Ca}}=1061$.)

The Fluorescence Intensity Difference within the Same FLIM Image

An intensity difference was also observed in the same image. To test the influence of the intensity within the same image on lifetime parameters, the FLIM images of X-rhod-1-stained RBCs with the same intracellular Ca^{2+} concentration was analyzed.

From the statistical percentile of the fluorescence intensity distribution, the RBCs from the same image can be divided into 20 groups (Fig. 3.32, Fig. 3.34 A). The average intensity of all the populations above 15 photons per pixel indicating that the resolution of each population is high enough to resolve the three stable lifetime components (Fig. 3.31 B, Fig. 3.34 A). As shown in Figure 3.34 B, The sharpness of each population shows little variation from each other. In addition, the amplitude-averaged lifetime of each population does not vary much from each other (Fig. 3.33 and Fig. 3.34 C). This indicates that the intensity difference between the populations is not due to focus variation and do not

100 3 Results

influence the amplitude averaged lifetime. The first ten populations are considered as low intensity populations, and the last ten populations are grouped as high intensity populations. The intensity between the low and high intensity population is significant, but there is no difference in sharpness between the low and high intensity population, nor in amplitude averaged lifetime (Fig. 3.34 D-F). The variation of sharpness and averaged lifetime is smaller in the high intensity group than in the low intensity group (Fig. 3.34 E,F). However, the τ_1 and τ_2 of the low intensity population are significantly different from the high intensity population, while the τ_3 of the low and high intensity populations are similar (Fig. 3.34 G).

In summary, within same image, the intensity difference is not because of the focus. The amplitude-averaged lifetime is not influenced by the different intensity. The intensity difference shows influence on τ_1 and τ_2 but not τ_3 .

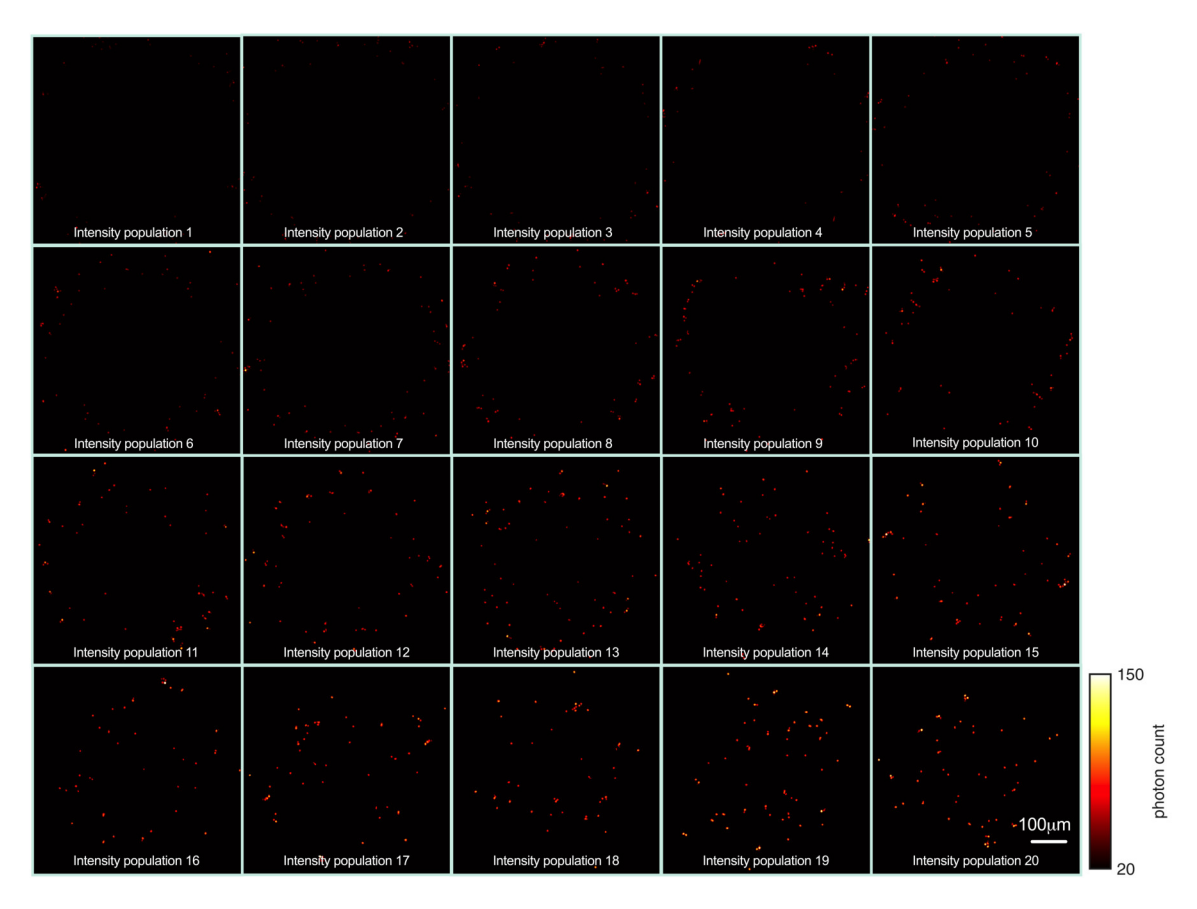


Fig. 3.32: The example photon-count images of X-rhod-1-stained RBCs populations with different intensity from the same image. The intensity populations were divided into 20 populations according to the statistical percentile of the fluorescence intensity distribution. RBCs from opulation 1 had the lowest photon counts and RBCs from population 20 had the highest photon counts. Black represents lower photon counts and white represents higher photon counts. Each spot in image is one RBC.

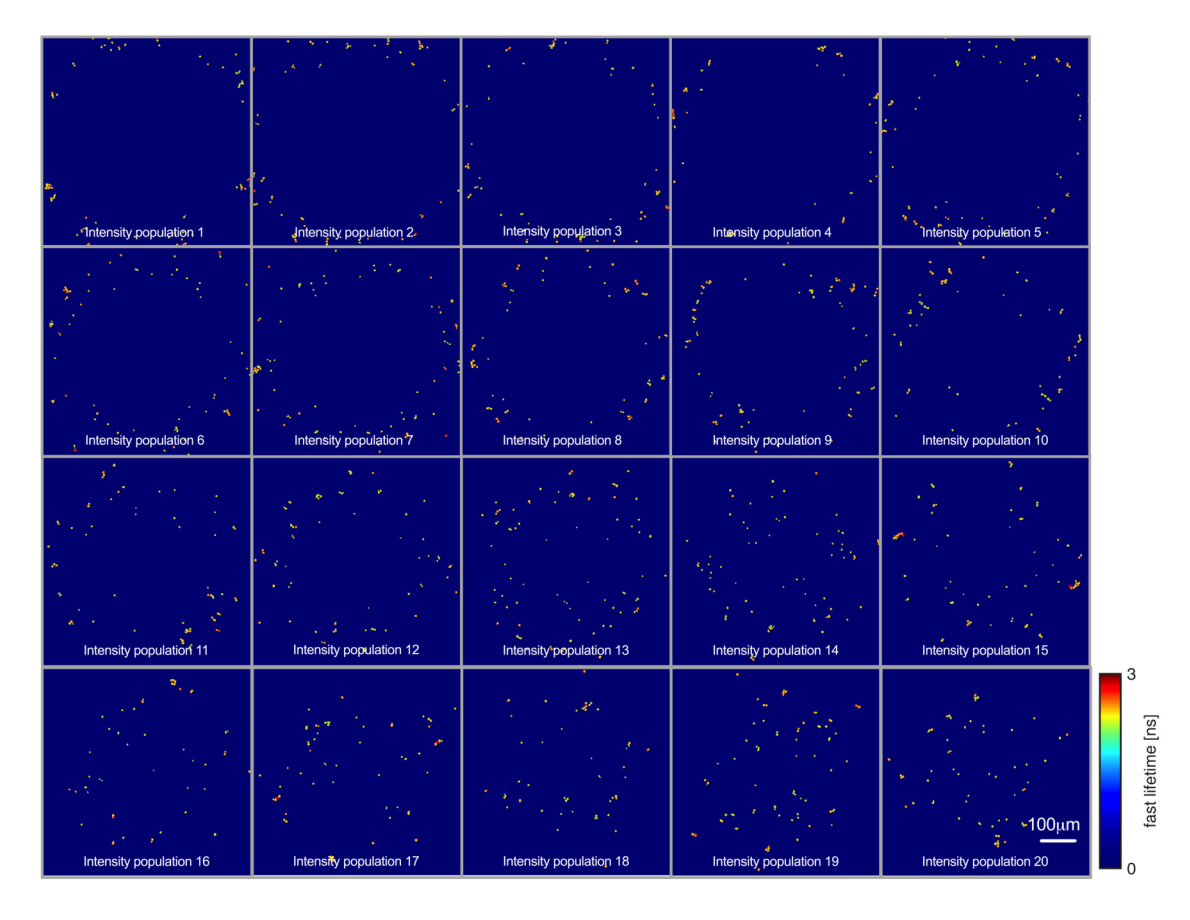


Fig. 3.33: The example FLIM images of X-rhod-1-stained RBC populations with different intensity from the same image as Figure 3.32. Blue represents shorter lifetime and red represents longer lifetime. Each spot in image is one RBC.

3.4.2.9 Theoretical Relation between Intracellular Ca²⁺ Concentration and FLIM Parameters of X-rhod-1 in RBCs

To test whether there was a parameter of FLIM images that could be used to measure the intracellular $\mathrm{Ca^{2+}}$. The X-rhod-1 loaded RBCs were challenged with PBS containing a designed $\mathrm{Ca^{2+}}$ concentration and Bromo-A23187. The FLIM images of the challenged RBCs were acquired using the 1PE FLIM system (Fig. A.12) or the Leica 2PE FLIM system.

With the Leica 2PE FLIM system, FLIM images of the RBCs with 19 different theoretical intracellular Ca²⁺ concentration from three independent experiments were acquired and analyzed (Fig. 3.35). Surprisingly, the amplitude-average lifetime shows a dependence on intracellular Ca²⁺ concentration but neither amplitude ratio nor the lifetime-weight amplitude ratio shows a strong dependence on Ca²⁺ concentration (Fig. 3.36 A-C). The variation between three experiments is obvious (Fig. 3.36 A-C). Taking the average of three experiments, all amplitude-averaged lifetime, amplitude ratio and lifetime-weighted amplitude ratio show a relationship with intracellular Ca²⁺ concentration (Fig. 3.36 D-F). The amplitude ratio and the lifetime-weighted amplitude ratio have larger error bars (Fig. 3.36 E,F).

102 3 Results

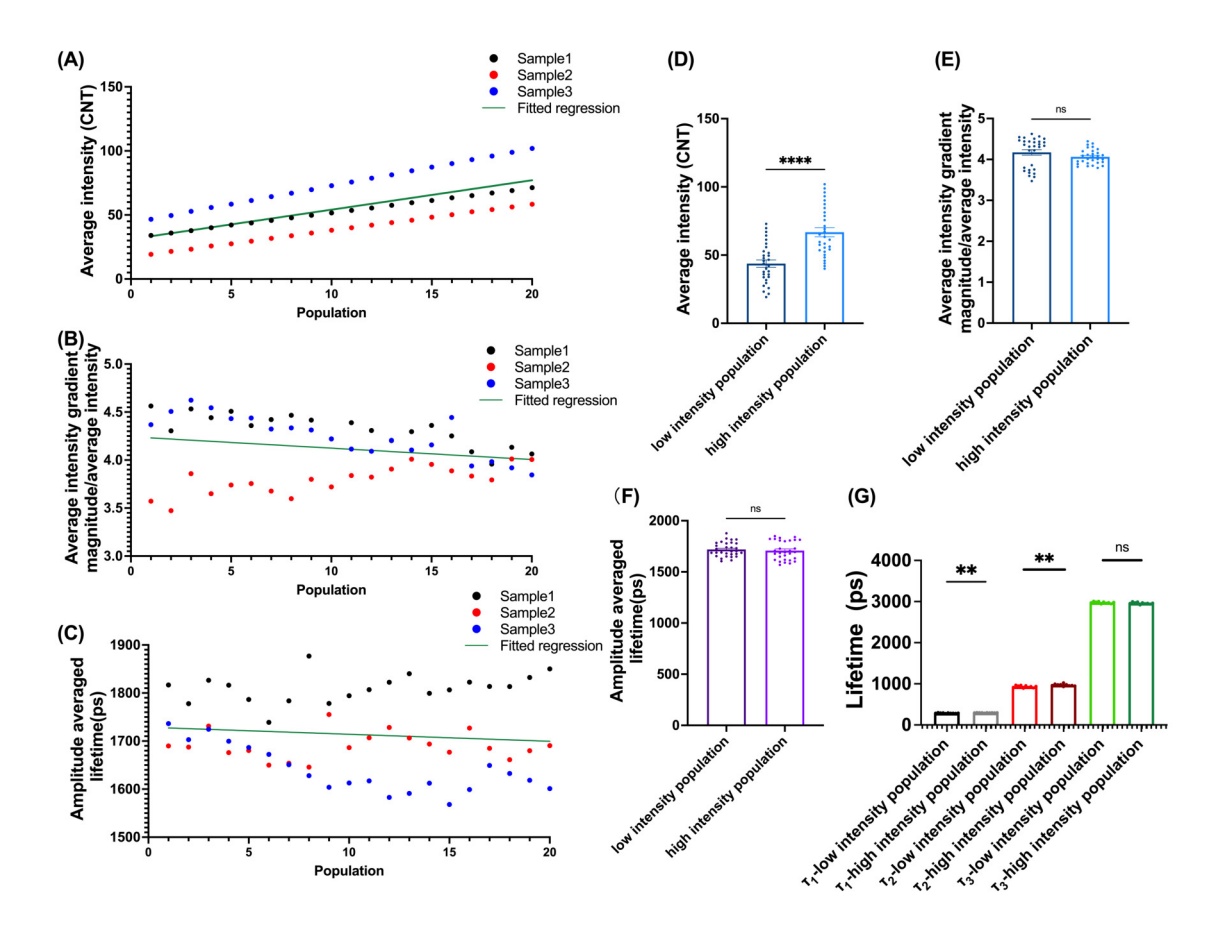


Fig. 3.34: The effects of intensity differences within the same images on the sharpness and parameters of FLIM images. (A) The average intensity of different intensity populations. (B) The sharpness of different intensity populations. (C) The amplitude-averaged lifetime of different intensity populations. (D)-(G) Statistical comparison of parameters between low and high intensity populations. The first ten intensity populations as in (A) were considered as low intensity population and the remaining ten populations were grouped as high intensity population: (D) Average intensity (E) Sharpness; (F) Amplitude-averaged lifetime; (G) τ_1 , τ_2 and τ_3 . (N=3).

Then the normalized amplitude averaged lifetime, normalized amplitude ratio and normalized lifetime-weighted amplitude ratio are used to reduce temperature influence. As shown in Figure 3.37 A, after normalization, the variation of amplitude averaged lifetime among three experiments is smaller and there is a clear the dependence on amplitude averaged lifetime on intracellular $\mathrm{Ca^{2+}}$. However, there is still an obvious variation in amplitude ratio and lifetime-weighted amplitude ratio among three experiments (Fig. 3.37 B,C). The relationship between either amplitude ratio or lifetime-weighted amplitude ratio and intracellular $\mathrm{Ca^{2+}}$ is not strong. Taking the average value of three experiments, amplitude averaged lifetime does not change when the intracellular $\mathrm{Ca^{2+}}$ is lower than 1 $\mu\mathrm{M}$. When the intracellular $\mathrm{Ca^{2+}}$ is higher than 1 $\mu\mathrm{M}$, the amplitude-averaged lifetime increases with increasing $\mathrm{Ca^{2+}}$ concentration (Fig. 3.37 D). The amplitude ratio shows a slightly increase as the $\mathrm{Ca^{2+}}$ concentration increased, but the change is not large and the error bar is still big (Fig. 3.37 E). The averaged lifetime-weighted amplitude ratio shows an increase when intracellular $\mathrm{Ca^{2+}}$ reached 100 $\mu\mathrm{M}$ with a huge error bar in each data point (Fig. 3.37 F).

In summary, the fast FLIM show dependence to the intracellular Ca²⁺ concentration. Amplitude ratio, lifetime-weight amplitude ratio and amplitude averaged lifetime also change with increased Ca²⁺ concentration. Compared to amplitude ratio and lifetime-weight amplitude ratio, amplitude averaged lifetime shows more sensitivity.

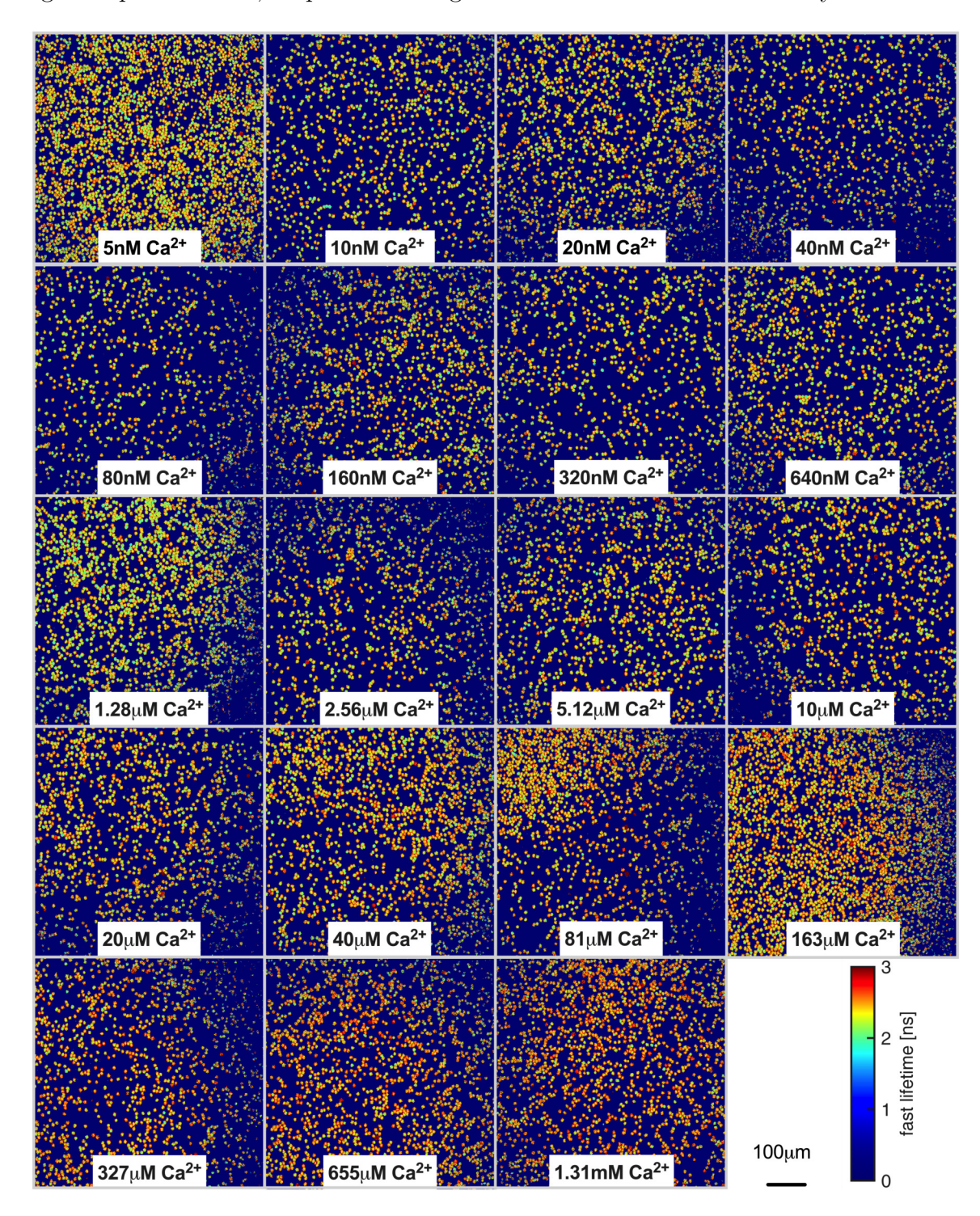


Fig. 3.35: FLIM images of X-rhod-1 in RBCs with defined intracellular Ca^{2+} concentration. The color represents the fast lifetime τ_x . Blue represents shorter lifetime and red represents longer lifetime. Data was acquired with the Leica 2PE FLIM system. Each spot is an individual RBC.

104 3 Results

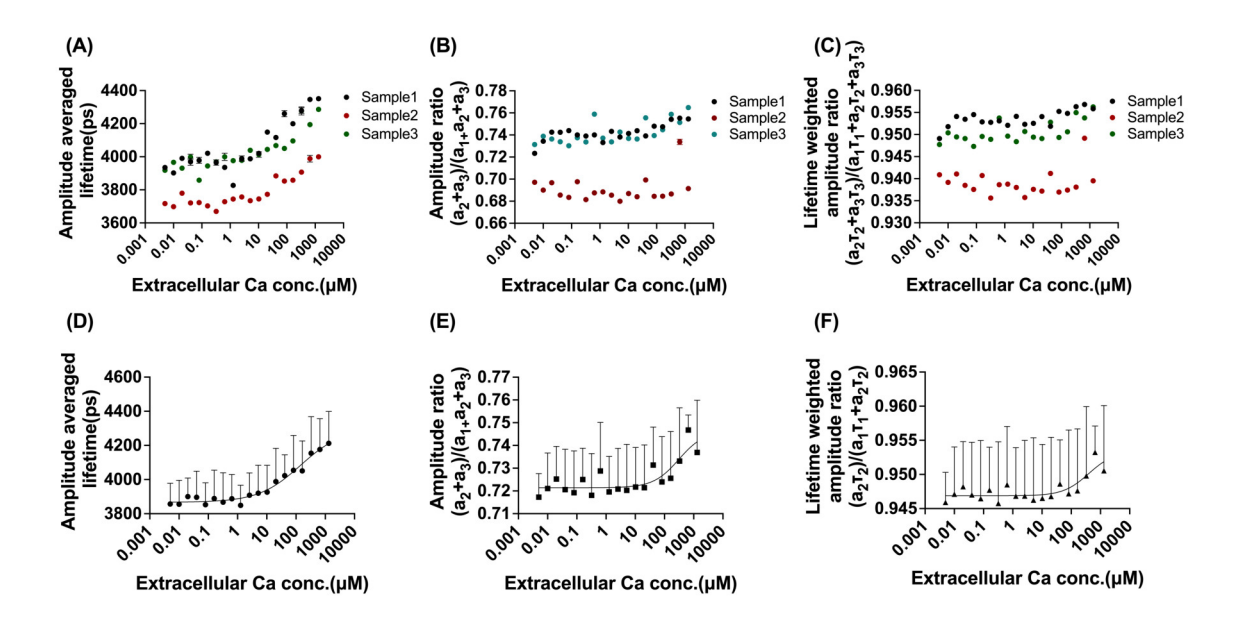


Fig. 3.36: Regression of intracellular Regression of intracellular Ca^{2+} concentration and FLIM parameters concentration and FLIM parameters. Data from FLIM images were taken with the Leica 2PE FLIM system. (A)-(C) FLIM parameters of X-rhod-1 loaded RBCs over 19 defined intracellular Ca^{2+} concentrations from three independent experiments. (A) Amplitude-averaged lifetime; (B) Amplitude ratio; (C) Lifetime-weighted amplitude ratio. (D)-(F) FLIM parameters of X-rhod-1 loaded RBCs over 19 defined intracellular Ca^{2+} concentrations in average of three independent experiments: (D) Amplitude averaged lifetime; (E) Amplitude ratio; (F) Lifetime-weighted amplitude ratio. Data acquired using the Leica 2PE FLIM system (N=3). Data is shown as means \pm SEM.

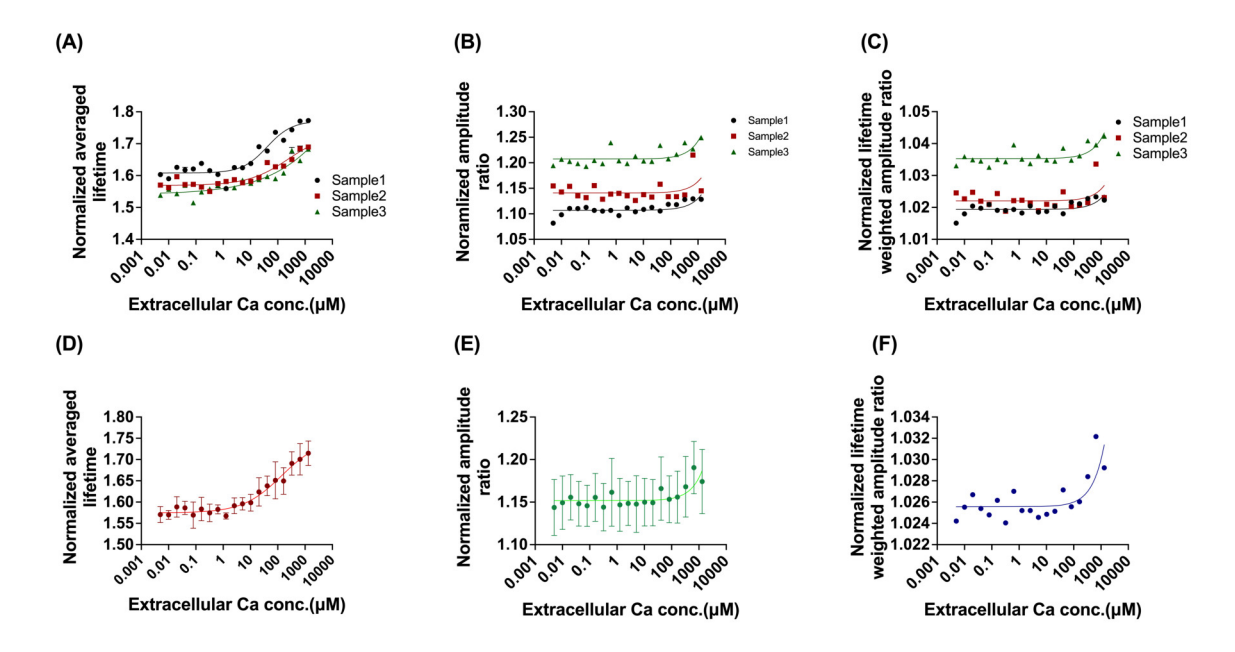


Fig. 3.37: Regression of intracellular Ca^{2+} concentration and normalized FLIM parameters. Data from FLIM images were taken with the Leica 2PE FLIM system. (A)–(C) Normalized FLIM parameters of X-rhod-1 loaded RBCs over 19 defined intracellular Ca^{2+} concentrations from three independent experiments: (A) Amplitude-averaged lifetime; (B) Amplitude ratio; (C) Lifetime-weighted amplitude ratio. (D)-(F) Normalized FLIM parameters of X-rhod-1 loaded RBCs over 19 defined intracellular Ca^{2+} concentrations in average of three independent experiments: (D) Amplitude-averaged lifetime; (E) Amplitude ratio; (I) Lifetime-weighted amplitude ratio (N=3). Data is shown as means \pm SEM.

4 Discussion

4.1 Mechanistic Ion Channel Regulation and Interactions in RBCs

RBCs are one of the elements of blood, the important tissue for transport nutrition and waste, defense of microbios and homeostasis of pH, and ions [1,2]. The special biconcave disc shape, large amount of hemoglobin (Hb) and lack of nuclei and organelles help RBCs to perform physiology functions, including gas transport and maintenance of systematic acid-base balance [7,8,14]. Human RBCs have a lifespan of in average 120 days. During this time, RBCs need to survive and cope with stresses related to their function. However, they lack a nucleus and organelles and lose the capacity for protein renewal [15–17]. Ions play an essential role in RBCs to regulate cellular activities, including maintaining pH and osmotic homeostasis [75–77], maintaining electrical neutrality [74], as well as generating and conducting membrane potentials [78]. Ion also participate in cell volume changes [79], metabolism regulation [80], and signal transduction [81]. In addition, ions alter the affinity of hemoglobin for oxygen and the ability to transport oxygen [82]. Ca^{2+} , as a universal signaling molecule, is involved in various stages of the RBCs life cycle, from precursor cells to apoptosis [107]. Most Ca²⁺ in RBCs is bound and buffered and the free Ca²⁺ concentration in healthy mature RBCs at basal level is estimated to be in the range of 30 – 60 nM [109, 110]. The extremely low basal permeability of the human RBC membrane to Ca²⁺ and a powerful Ca²⁺ pump help RBCs to maintain the low basal free Ca²⁺ concentration [108]. In blood plasma, the Ca²⁺ concentration is about 2.44 mM [87]. Since one open channel can carry up to 100 million (10^7) per second [212], the tremendous gradient across the RBC membrane can lead to more than 10-fold changes in the free Ca²⁺ level in the submembrane space within milliseconds when a few hundred channels open and transport 10^6 ions per second [108]. The huge change in free Ca^{2+} level can cause acute changes in the activity of multiple Ca²⁺-sensitive proteins and regulate multiple activities [108]. Long-term dysregulation of Ca^{2+} leads to the formation of polymeric protein complexes and induces cytoskeletal remodeling and associated changes in cell shape and membrane plasticity [152]. Thus, understanding regulation is important for understanding physiological and pathophysiological conditions of RBCs.

With decades of studies, several channels have been identified as sources of Ca^{2+} entry in RBCs under physiological and pathophysiological conditions, including Piezo 1 [646–648], $Ca_v 2.1$ [128], transient receptor potential canonical 6 (TRPC6) [649], transient receptor potential vanilloid type 2 (TRPV2) [310], N-methyl-D-aspartic acid (NMDA)-receptors [108] and other non-selective voltage-activated cation channels [650]. In addition, the studies of Ca^{2+} -regulated channels in RBCs, namely the Gárdos channel, the Ca^{2+} -dependent K^+ channel, showed strong evidence for interaction properties between Gárdos

106 4 Discussion

channel and Piezo 1 channel in RBCs [378]. It indicates that ion channels can regulate the physiological and pathophysiological function of other channels and the interactions between ion channels are important for RBCs. However, after years of studies, the regulation and interplay characteristics of the Gárdos channel and Piezo 1 channel are still not fully understood because it can be distinctly different from those in other cell types [651]. Studies of the interaction of ion channel in RBCs are just started.

Piezo 1 channel is a non-selective cationic mechanosensitive channel and has been found in human RBCs with a few hundred copies per cell [244, 249, 251, 252]. Piezo 1 can be rapidly activated by mechanical stimulation related to lipid bilayer tension [249] including membrane stretching [244], fluid shear flow [260, 261], osmotic stress [258], substrate stiffness [262], matrix roughness [263] and environmental confinement [264]. Pizeo 1 channel is classified as a non-selective cation channel and it is permeable to monovalent ions (such as alkali ions, K⁺, Na⁺, and Cs⁺), divalent ions (Ba²⁺, Ca²⁺, Mg²⁺, and Mn²⁺), and several organic cations (tetramethyl ammonium, tetraethyl ammonium), with a selectivity sequence of Ca²⁺> K⁺> Na⁺> Mg²⁺ [244,266]. Combined with the enormous gradient across the RBC membrane and its high permeability for Ca²⁺, the activation of Piezo 1 channels will cause Ca²⁺ influx and induce downstream signaling cascade [108,244]. As shown in Figure 3.1, Yoda 1, the Pizeo 1 activator, could significantly increase the intracellular Ca²⁺ concentration in RBCs. The Ca²⁺ increase of shows two phases with different Ca²⁺-entry time constants (Fig. 3.1 E).

As Piezo 1 is a mechanosensitive channel, the lipid bilayer tension could active it [244]. This suggests that changes in the membrane and cytoskeleton structure may influence the function of Piezo 1 channel. The study of a family in which the mother carries the Piezo 1 mutation p.Asp710Asn, the father has the spectrin alpha mutation p.Gln2002Ter and the patient has both mutations provides some evidence of cytoskeletal structure influence on the Piezo 1 channel function. After clinical examination, the Piezo 1 variant was predicted to be benign and the mother has no clinical phenotype. As intracellular Ca²⁺ concentration measurements by flow cytometry of the mother with Piezo 1 mutation p.Asp710Asn shows, a slightly higher basal Ca²⁺ level than healthy controls but the confocal microscopy images show as slightly lower basal Ca²⁺ level than healthy controls. After Yoda 1 application, the average intensity of RBCs from the mother is similar to healthy control or slightly lower (Fig. 3.8 A,C, and Fig. A.1). The additional, automatic patch clamp experiments from Nanion Technologies show no differences in the baseline current, the percentage of Yoda 1 responders and the Yoda 1-induced current between healthy controls and the mother [652]. It supports that the p.Asp710Asn mutation is a benign mutation and has no obvious effect on Pizeo 1 function. Differently, RBCs from the father with the spectrin alpha mutation p.Gln2002Ter showed lower basal Ca²⁺ level in flow cytometry measurements and confocal microscopy imaging. After stimulation with Yoda 1, the father's RBCs also have lower Ca²⁺ level than healthy controls (Fig. 3.8, Fig. A.1). The additional patch clamp shows the reduced baseline current [652]. It hints the spectrin alpha p.Gln2002Ter mutation has a negative influence on normal Piezo 1 channel activation. In contrast, the patient, who has both Piezo 1 and spectrin alpha mutations, shows a different phenotype. Before the splenectomy, the patient' RBCs shows huge size variations and a much higher basal Ca²⁺ and a higher maximum Ca²⁺ level after Yoda 1 stimulation measured by flow cytometry measurement (Fig. 3.8 A,C and Fig. A.1). The patch clamp measurements show that the

patient's RBCs have a significantly higher basal current. The Yoda 1 induced absolute current of the patient's RBCs at 80 mV, which is higher than others, but not significant. All data show that the combination of the spectrin mutation alpha p.Gln2002Ter and, the p.Asp710Asn mutated Piezo 1 channel results in a higher open probability and higher sensitivity of the RBCs to Yoda 1. It supports the theory that changes in cytoskeletal structure can affect the function of the Piezo 1 channel.

In addition, the study of thalassemia patients shows altered Piezo 1 channel function in thalassemic RBCs. In the experiments, RBCs from a thalassemia β patient (HBB CD39 variant) with a Piezo 1 mutation (p.Arg1940Gln) and a thalassemia β patient (same HBB CD39 variant) without any additional mutation were studied. The RBCs of the patient with only thalassemia β have lower basal Ca²⁺ and lower Yoda 1-induced Ca²⁺ entry than the healthy control. The number of responding cells is also lower than that of the healthy control (Fig. 3.9). It shows that the thalassemia β mutation has a negative effect on wild type Piezo 1 channel function. In contrast, combined thalassemia β mutant and the Piezo 1 variant p.Arg1940Gln, the RBCs show a significantly higher basal Ca²⁺ and Yoda 1-induced Ca^{2+} entry than the healthy control. The percentage of Yoda 1 responding RBCs is slightly less than the healthy control (Fig. 3.9). This indicates the combination of thalassemia β mutation and Piezo 1 variant has a positive influence on Piezo 1 function. According to several studies, the β-thalassemic RBCs have irregular tetramers. These irregular tetramers have irregular oxygen affinity and can precipitate to RBCs membrane surface, causing oxidative deformability [497, 499, 500]. The altered deformability can influence the membrane lipid tension and it may influence the activation of Piezo 1 channels. In addition, the Piezo 1 mutation p.Arg1940Gln can be expected to be a gain-of-function mutation and its effect on Piezo 1 function is greater than that of the thalassemia mutation. Then the RBCs from the patient with both thalassemia β and Piezo 1 mutation shown an increased Ca²⁺ uptake. But these interpretations still need further investigation to be confirmed.

As mentioned before, the Gárdos channel can be activated by Ca²⁺ influx and lead to K⁺ loss [122, 315, 316]. When healthy RBCs are incubated in solution with external Ca²⁺ and treated with 100 μM NS309, the Gárdos channel activator, there is a group of RBCs showing increased intracellular Ca²⁺, considered as high Ca²⁺ RBCs (Fig. 3.10). The number of RBCs with increasing internal Ca²⁺ shows a bell-shape relationship with external Ca²⁺ concentration and the maximum high Ca²⁺ RBC number at around 20 µM external Ca²⁺ (Fig. 3.10 G). The healthy RBCs treated with Ionomycin, a Ca²⁺ ionophore, in the same solution as NS309 treated RBCs show an almost 100% RBCs with increased internal Ca²⁺ and the intracellular Ca²⁺ concentration is higher than NS309-treated RBCs (Fig. 3.10). In previous studies, the NS309-induced Gárdos channel activation depends on external Ca²⁺ concentration and the relationship between the NS309 induced membrane potential change and external Ca²⁺ concentration is linear rather than bellshaped [599,653]. Considering that the Gárdos channel is a K⁺ channel and not permeable to Ca²⁺, the mechanism of Ca²⁺ increase triggered by the Gárdos channel is completely elusive. In addition, the studies of NS309 shows NS309 acts as a Gárdos channel activator and increase the channel sensitivity towards Ca²⁺, but NS309 cannot cause an increase of Ca²⁺ influx into RBCs [330,653]. Thus, the increased intracellular free Ca²⁺ in RBCs depends on other Ca²⁺ transporters related to Gárdos channel activity. In a study by

108 4 Discussion

Jensen et al, the NS309 induced Ca²⁺ entry can be partially blocked by Gárdos channel inhibitors and a Ca_v2.1 channel blocker. However, the Piezo 1 inhibitors can increase the number of high Ca²⁺ RBCs [599]. The activation of Gárdos channel can lead to the increase in K⁺ permeabilization. When the membrane permeability to a specific ion gets higher, the membrane potential shifts more toward equilibrium potential of that ion. Thus, the increase of permeablizeation of K⁺ can cause more negative of membrane potential, leading to hyperpolarizarzation [212]. In addition, in RBCs, intracellular K⁺ is approximately 30 times higher than in the extracellular part in RBCs (Table 1.1). The activation of Gárdos channel cause huge amount K⁺ loss, which reduce positive charges in RBCs, resulting in hyperpolarization. Hyperpolarization induced by Gárdos channel activation can be altered by the addition of Yoda 1, the Piezo 1 channel activator, resulting in depolarization induced by the open state of the Piezo 1 channel [599]. According to previous studies, the number of Gárdos channels in RBCs is very low and the behavior of channel openings is stochastic [335, 339]. It is assumed that the activation of Gárdos channels leads to membrane potential flickers and the membrane potential flickering can activate Ca_v2.1 [654]. When the external Ca²⁺ concentration is below 20 µM, i.e. below the estimated concentration of maximum response in the presence of NS309, the number of responding RBCs increases with the Ca²⁺ concentration. Simultaneously, the opening probability of the Gárdos channels increases. This induces flickering in the RBC membrane potential, leading to activation of Ca_v2.1. There are two mechanisms which can lead to a predominant opening of the Gárdos channel. First, when the external Ca²⁺ concentration is above 20 µM in presence of NS309, second if there is an acute increase in Ca²⁺ concentration caused by Piezo 1 channel activation. This in turn results in less flicker and decreased Ca_v2.1 activity. The flickering of the membrane potential is more sensitive to lower Ca²⁺ concentration in the presence of NS309.

When RBCs are only stimulated with the Yoda 1, the Ca²⁺ influx caused by Piezo 1 channel openings can activate the Gárdos channel, leading to K⁺ loss and resulting in immediate hyperpolarization (Fig. 3.5). The use of the Gárdos channel inhibitor, Tram-34, leads to a significant decrease of the hyperpolarization parameters shows Gárdos channel activation causes hyperpolarization after Yoda 1 application (Fig. 3.5 C,D,E). No difference in resting membrane potential between RBCs with and without Tram-34 shows that Gárdos channel does not affect resting membrane potential and the Tram-34 either (Fig. 3.5 B). As Figure 3.4 E shows, when Yoda 1 stimulation time is shorter 150 seconds, the increase of Ca²⁺ concentration is characterized by two different slopes, a slower increase during phase 1 followed by a faster increase during phase 2. Interestingly, the inhibition of the Gárdos channel can further slow down the increase speed of Ca²⁺ in phase 1. This indicates that the hyperpolarization induced by the Gárdos channel is important for the first phase of Ca²⁺ influx, and the second phase of Ca²⁺ influx is slightly inhibited by the hyperpolarization. Moreover, instead of maintaining the maximum Ca²⁺ concentration for a few minutes, with Gárdos channel inhibition, the Ca²⁺ concentration decrease faster (Fig. 3.4 E). It indicates that the membrane potential change is important for maintaining the Ca²⁺ at high levels in RBCs. At the beginning of Yoda 1-induced Piezo 1 activation, the intracellular Ca²⁺ concentration is below the threshold for a permanent open state of the Gárdos channel. The increased Ca²⁺ leads to an increased open probability of the Gárdos channel and the induction of more membrane flickering. The Ca_v2.1 channels are activated and lead to additional Ca²⁺ influx. During this period, the inhibition of Gárdos channel

does not result in membrane flickering. Then the $\rm Ca_v 2.1$ is inactivated and there is no extra $\rm Ca^{2+}$ influx from $\rm Ca_v 2.1$ in RBCs, the rate of $\rm Ca^{2+}$ increase is reduced. After some time of Yoda 1 stimulation, the intracellular $\rm Ca^{2+}$ concentration reaches the level where the Gárdos channel is predominantly open. The membrane potential is no longer flickering and the $\rm Ca_v 2.1$ channel is not activated, the $\rm Ca^{2+}$ influx through $\rm Ca_v 2.1$ disappears and the rate of $\rm Ca^{2+}$ influx is also reduced. However, the maximum $\rm Ca^{2+}$ concentration in RBCs treated with Yoda 1 and Tram-34 indicated other sources of $\rm Ca^{2+}$ -entry. The fast drop in $\rm Ca^{2+}$ concentration in RBCs treated with Yoda 1 and Tram-34 after reaching the maximum also indicates fast $\rm Ca^{2+}$ efflux pathways in RBCs, which are highly dependent on the membrane potential depolarization.

The Cl⁻ conductance is the main factor to determine resting membrane [78, 196]. In addition, Cl⁻ is also involved in regulating cell volume [655] and intracellular pH [197, 198]. After inhibition of Cl⁻ conductance by NS3623, the two phases of Ca²⁺ increase induced by Yoda 1 in normal RBCs is replaced by a single delayed phase of Ca²⁺ increase. With NS3623 and Yoda 1-stimulated normal RBCs, the rate of the Ca²⁺ increase is slower than either phase of Ca²⁺ increase in normal RBCs with only Yoda 1 stimulation (Fig. 3.6). In addition, the maximum Ca²⁺ concentration is smaller, indicating that the Cl⁻ conductance is also one of the positive factors, likely a key factor, of the first phase of Ca²⁺ increase. Cl⁻ conductance is also a positive factor in the second phase of Ca²⁺ increase. As for the membrane potential changing, the application of NS3623 causes a slightly reduced resting membrane potential and significantly increased hyperpolarization magnitude (Fig. 3.7 B,D). Previous experiments show that the hyperpolarization induced by Yoda 1 is highly dependent on the activation of Gárdos channels. As described above, the Gárdos channel activation subsequently increases K⁺ permeability, followed massive K⁺ efflux, which shifts the membrane potential of RBCs towards the equilibrium of K⁺ and creates a favorable electrochemical gradient for anion release, including Cl⁻ [212,656]. The release of Cl⁻ also moves out the negative charges and makes the membrane potential less negative. The inhibition of Cl⁻ conductance can reduce the loss of negative charge from Cl⁻ during Gárdos channel activation and the hyperpolarization magnitude is higher. In addition, the reduced Ca²⁺ entry rate of NS3623 treated normal RBCs shows that the hyperpolarization is not in favor of the Ca^{2+} influx caused by Yoda 1 stimulation, which is contrary to the Gárdos channel inhibition experiments. It suggests too high hyperpolarization works as inhibition of Ca²⁺ influx, which might relate to the Ca_v2.1 channel. As mentioned above, the Ca_v2.1 is likely activated by membrane potential flickering. The inhibition of Cl⁻ conductance leads to higher hyperpolarization and might reduce the membrane potential flickering. Thus, the contribution of Ca_v2.1 activation in Ca²⁺ increase is inhibited. The data also indicate there are likely other unknown pathways regulated by Cl⁻ conductance involved in Ca²⁺ influx. In addition, there is the possibility that NS3623 can in addition of being a Cl⁻ conductance inhibitor induce additional effects. The report by Mondero Alonso et al. shows that NS3623 can enhances the activity of nonselective cation channels (NSC) in hyperpolarizing conditions [656]. According to the data from Mondero Alonso et al., 100 uM NS3623 could increase intracellular Na⁺ concentration in a short time and prevent RBCs from reaching their maximum hyperpolarization [656]. The only known conducting pathways capable of transporting large amounts of Na⁺ in short time are NSCs [657–659]. Interestingly, NS3623 induced the Na⁺ uptake induced by NS3623 is voltage- and Ca^{2+} -dependent. However, the ability of NS3623 to enhance NSC

4 Discussion

is only evident at high concentrations ($100\,\mu\mathrm{M}$) but not at low concentrations ($10\,\mu\mathrm{M}$ or less) [656]. In Yoda 1-related experiments, only $10\,\mu\mathrm{M}$ NS3623 was used. In addition, the application of $10\,\mu\mathrm{M}$ NS3623 results in a rapid development of hyperpolarization instead of preventing RBCs from reaching maximum hyperpolarization (Fig. 3.7 A,C,D), which is consistent with the data reported by Mondero Alonso et al. [656]. Even if $10\,\mu\mathrm{M}$ NS3623 actually activates NSC, due to the Ca²⁺ gradient across the membrane, there should be an additional Ca²⁺ influx, resulting in a faster Ca²⁺ increase and a higher maximum Ca²⁺ level. However, Figure 3.6 I and J show opposite results. Thus, it is less possible to regulate Ca²⁺ influx because of the improved NSC function due to NS3623 in the Yoda 1 stimulation experiments.

After ATP depletion, the 5 µM Yoda 1 can increase the intracellular Ca²⁺ with two phases but the first phase has a faster increase speed and higher Ca²⁺ maximum concentration compared to the non-ATP-depleted RBCs with Yoda 1 stimulation, (Fig. 3.2 E). The rate of decrease of Ca²⁺ after the Ca²⁺ concentration reaches the maximum Ca²⁺ in ATP-depleted RBCs is slower than in non-ATP-depleted RBCs (Fig. 3.2 E). This can be explained by the fact that the function of the plasma membrane Ca²⁺ ATPase (PMCA) function is not functional due to the missing ATP. Without enough ATP, the PMCAs do not have enough energy to transport Ca²⁺ against the gradient across RBC membrane and reduce the intracellular Ca²⁺ concentration. The Ca²⁺ concentration in ATP-depleted RBCs without Yoda 1 stimulation increases slightly during experiments (Fig. 3.2 E). One possible reason is that the shear stress causes a small Ca²⁺ influx through a few copies of Piezo 1 or other mechanical-sensitive channels. The small Ca²⁺ increase can be balanced by PMCAs activities. When PMCAs activities are inhibited, a small amount of Ca²⁺ accumulates and leads to increased intracellular Ca²⁺. The resting membrane potential between normal RBCs and ATP-depleted RBCs is the same (Fig. 3.3). In addition, compared to normal RBCs and ATP-depleted RBCs after Yoda 1 stimulation, only the maximum hyperpolarization and depolarization time are significantly different (Fig. 3.3 C,H). The hyperpolarization magnitude is not significantly different statistically, but the p value is 0.15 (Fig. 3.3 D). The ATP-depleted RBCs can also reach higher membrane potential at the end of depolarization (Fig. 3.3 A). It suggests that ATP-regulated pumps are not involved in the regulation of resting membrane potential, hyperpolarization and depolarization. However, reduced pumped-out Ca²⁺ can cause increased cation concentration in RBCs and can result in a higher membrane potential during depolarization. The Ca²⁺ pump can slow the first phase of Ca influx caused by Yoda 1 induced Piezo 1 channel activation. It also shows that the 5 µM Yoda 1 activated Piezo 1 channels and generated fluxes that are above the pumping capacity of the PMCA, hence the intracellular Ca²⁺ concentration increases.

When RBCs are ATP-depleted and treated with both Tram-34 and Yoda 1, the speed of the first phase of Ca²⁺ increase is much faster than that of normal RBCs treated with Tram-34 and Yoda 1, followed by the second phase of Ca²⁺ increase at the same speed and higher Ca²⁺ maximum (Fig. 3.4 I,J). In addition, the ATP-depleted RBCs with Tram-34 and Yoda 1 stimulation can maintain the high Ca²⁺ concentration longer than normal RBCs with Tram-34 and Yoda 1 stimulation (Fig. 3.4 I). When Cl⁻ conductance has been inhibited and ATP has been depleted, the RBCs after Yoda 1 stimulation had a higher maximum Ca²⁺ than normal cells stimulated with NS3623 and Yoda 1 (Fig. 3.6). It not only supports that the ATP-regulated Ca²⁺-pumps are among the factors rather

suppressing the first phase of Ca²⁺ increase, but also shows that the Gárdos channel activation and Cl⁻ conductance are positive factors for the first phase of Ca²⁺ increase. However, the membrane potential change after Yoda 1 stimulation has no difference between ATP-depleted RBCs with Tram-34 and normal RBCs with Tram-34 (Fig. 3.5). No differences in membrane potential change after Yoda 1 stimulation between ATP-depleted RBCs and normal RBCs with NS3623 stimulation (Fig. 3.7) occurd, supporting that PMCAs do not contribute much to membrane potential regulation.

Transient receptor potential vanilloid type 2 (TRPV2) channel, another non-selective cation channel, has been reported to be present in RBCs [310]. TRPV2 is known as a thermosensitive cation channel and can be activated at temperatures above 52 °C [297, 298]. TRPV2 is also reported to be a mechanosensitive channel [299]. Belkacemi et al. conclude that activation of TRPV2 may mediate Ca²⁺ entry and subsequent activation of the Gárdos channel [310]. Data from our experiment are consistent with the conclusion of study from Belkacemi et al. When healthy RBCs are stimulated with Δ^9 -THC, a TRPV2 agonist, a Ca²⁺ increase has been observed in a group of RBCs (Fig. 3.12, Fig. 3.14, and Fig. A.2) and hyperpolarization has been recorded by the MBE method (Fig. 3.16 A,C,D). An initial study shows that the RBCs from a healthy donor have a significantly milder response to Δ^9 -THC than RBCs from a regular marijuana smoker [644], suggesting that long-term cannabis use may be able to upregulate RBCs responding to Δ^9 -THC. In experiments, RBCs from three marijuana consumers (MS) and four matched healthy donors (NS) are tested. As shown in Figure 3.12, both MS and NS RBCs show heterogeneous responses to Δ^9 -THC. MS show a slightly higher number of cells responding to Δ^9 -THC immediately after stimulation (Fig. 3.12). Interestingly, the Western blot (WB) results show no significant differences in TRPV2 expression levels between MS and NS (Fig. 3.13). The additional patch clamp experiments performed at Nanion Technologies show no difference in cellular conductance between NS and MS RBCs [644]. All these data suggest that the hypersensitivity of TRPV2 in MS RBCs is not due to increased expression levels, but rather to altered sensitivity or gating behavior of TRPV2.

Similarly, heterogeneity of Δ^9 -THC response has also been observed in sickle cells (SS) (Fig. 3.14 D,E,F and Fig. A.2 A,B,C). Compared to healthy controls (AA), the percentage of responding cells in the SS group is much higher, as well as the average Fluo-4 intensity (Fig. 3.14 and Fig. A.2). Additional patch clamp experiments showing higher average conductance and higher number of responding cells in SS groups also provide evidence for the heterogeneity of Δ^9 -THC response [645]. Monitoring by the MBE method, 80 μ M Δ^9 -THC can cause only a very small change in membrane potential in AA RBCs, whereas the same concentration can induce a larger hyperpolarization in SS RBCs (Fig. 3.16 A,C,D). It seems that SS RBCs are also more responsive to Δ^9 -THC stimulation. However, no difference of TRPV2 expression level can be found between SS and AA groups by westernblot detection [645]. It may suggest that the observed hypersensitivity to Δ^9 -THC of SS RBCs is also because of altered sensitivity or gating behavior. However, the influence of the large difference in the number of RBCs with high sensitivity to Δ^9 -THC on the observed parameters should be considered. Interestingly, the hyperpolarization induced by Δ^9 -THC is more dependent on the oxygenation level. Under deoxygenated condition with an oxygen partial pressure only about 19.6 – 24.5 mmHg, the hyperpolarization is enhanced (Fig. 3.16 C,D, and Fig. A.4 B,C). It appears that deoxygenation enhances Gárdos channel activation, as hyperpolarization can be prevented by Gárdos channel inhibitors

4 Discussion

(Fig. 3.16 C,D, and Fig. A.4 B,C), suggesting that oxidative stress may influence ion channel activation.

In addition, activation of the Gárdos channel can lead to K⁺ efflux and subsequent water loss, which should result in RBC dehydration/shrinkage. Thus, cell dehydration should be observed after RBCs stimulated with Δ^9 -THC and TRPV2 channels are activated. However, in our experiments, RBCs stimulated with Δ^9 -THC showed swelling instead of shrinkage (Fig. 3.11), which is in agreement with previous studies [310, 312]. In addition, Na⁺/K⁺-ATPase always works in RBCs, with ratio of 3 Na⁺ moving outward for 2 K⁺ transported inward. The observed RBCs swelling effects could likely be explained by Na⁺ entry through TRPV2 channels exceeding the K⁺ efflux via the Gárdos channel [645,660]. The increased swelling in MS RBCs is possibly due to the impaired counter-regulation by the ion pumps but not involving cannabinoid G-protein coupled receptors [310]. Variability in the relative abundance of TRPV2 and Gárdos channels in individual RBCs could explain the differences in RBC hydration state after Δ^9 -THC stimulation. The response of Δ^9 -THC induced overhydration in healthy RBCs seems to be transit, within less than 1 hour after stimulation. It is likely due to counter-regulation via Na⁺/K⁺-ATPase and the Ca²⁺-ATPase, the pumps important for maintaining ion homeostasis and membrane potential, in addition to a time-dependent decrease in swollen cell volume via Gárdos channel [644].

In contrast, the immediate consequence of Δ^9 -THC exposure of SS RBCs is a rapid and prolonged increase in intracellular Ca²⁺ concentration via TRPV2, which reaches and exceeds the threshold for activation of the Gárdos channel. In this case, the Gárdos channel remains open long enough to cause significant K⁺ loss, offsetting the Na⁺ influx through TRPV2, ultimately increasing intracellular Hb concentration and promoting sickling due to cell volume reduction. In addition, the increased basal Ca²⁺ level in SS RBCs (Fig. 3.14 C) makes it easier to reach the threshold for Gárdos channel activation, which can accelerate sickling. The lower activity of PMCA in SS RBCs may also provoke delayed Ca²⁺ effects [661].

All experiments with patient's samples and the heterogeneity of Δ^9 -THC responses raise the question of the relationship between ion channel responses and the age of RBCs in circulation. According to the studies of SCD, the HbS in sickle cells can distort and damage RBCs resulting in an overall shorter lifespan than healthy RBCs [18,662,663]. The age of RBCs from patient with Piezo 1 and spectrin mutation and the patient with thalassemia β and Piezo 1 mutation may also be younger than healthy controls. The spleen is the largest filter of RBCs and can remove RBCs from circulation because of either physiological senescence or pathological alterations [664]. The high basal level of Ca²⁺ in RBCs from these patients may influence the multiple cell activities, including cell clearance. Ca²⁺ can regulate the cytoskeletal stability by activating Calcium-calmodulin complex (Ca-CaM) and regulating Ca²⁺-dependent phosphorylation on cytoskeletal proteins, inducing remodeling of the cytoskeletal structure and associated changes in cell shape and membrane plasticity [108]. These changes in high Ca²⁺ RBCs lead to RBC clearance in the spleen. In addition, the studies show that some diseases, including thalassemia, SCD or severe hematological diseases can induce spleen enlargement with a subsequent propensity to filter not only abnormal cells but also healthy RBCs [665,666]. Patients may have increased RBC clearance, resulting in shorter RBC lifespan, anemia and hypoxia, which induces

RBC hematopoiesis and leads to an increased proportion of young RBCs in circulation. Ion channel sensitivity may decrease over time and thus young RBCs have higher responses to ion channel activators stimulation. Data from patients with both spectrin and Piezo 1 mutation may show evidence of a relationship between ion channel activity and cell age. Before splenectomy, the patient's RBCs have different phenotypes compared to healthy controls, including higher basal Ca²⁺, higher response to Yoda 1, higher baseline current and higher Yoda 1 induced current. However, after splenectomy, all of the above parameters are at the same level as healthy controls (Fig. 3.8 and Fig. A.1) [652]. It is possible that after splenectomy, the rate of RBCs clearance is reduced and the average age of RBCs in the patient is increased, which is getting closer to healthy controls. The reduced RBCs clearance also means the RBCs can remain longer in the circulation with less aneamia. which require less stress erythropoiesis and RBCs have better quality with longer lifespan until new equilibrium is reached. The reduced proportion of young RBCs and the increased average age of the RBCs lead to reduced ion channel sensitivity in the patient. This means that the overall behavior of the patient's RBCs is closer to that of healthy controls. However, further experiments are needed to prove this.

In addition, the physiological environment of sickle RBCs and thalassemic RBCs may be disturbed by increased oxidative stress, associated with nitric oxide and altered ion balance [667, 668]. This could also change the activity of various channels. The upregulated ion channel activities shown in MS and sickle cell patients rising the concerns of risk of cannabinoid use. In long-term cannabinoid users, cannabinoid-induced RBCs have overhydration (Fig. 3.11) [310, 312] and reduced filterability [644], in combination with vasoconstriction also associated with cannabis use [669], it may increase the risk of thrombotic complications. In SCD patients, TRPV2 activation leads to cell shrinkage and increased likelihood of sickling, which may explain why daily cannabis users with SCD have worse pain episode severity scores in recent reports [670]. But the SCD patients with daily cannabis treatment also show lower rate of hospital admissions and emergency room visits [670]. The regular levels found in the blood of daily smokers are lower than the Δ^9 -THC concentration used in the experiment [671]. Maybe RBCs can encounter an acutely high Δ^9 -THC concentration peak in the lungs after puffing on a cannabis cigarette. Longitudinal clinical studies on cannabis use are still needed.

Although the experimental data show the activities of several ion channels and their interactions in Ca²⁺ regulation in RBCs. There are still weaknesses in the studies.

Firstly, comparing the effects of $5\,\mu\mathrm{M}$ Yoda 1 in healthy RBCs in different experiments, the data clearly shows that the maximum $\mathrm{Ca^{2+}}$ concentration can be reached after Yoda 1 stimulation decreased over the experimental time of one and half years. This is because repeated freezing and thawing leads to degradation of Yoda 1, which can reduce the effective concentration of Yoda 1 in the experimental solution. This may affect the outcome of the experiments.

Secondly, the RBCs were loaded with Fluo-4 before being fasted to deplete ATP. During the 16-hour incubation, the Fluo-4 in the RBCs could degrade over time, resulting in low fluorescence intensity in the experiments.

Thirdly, Tram-34, the used Gárdos channel inhibitor, cannot completely eliminate the Yoda 1 induced hyperpolarization. There is always a small and rapid hyperpolarization

4 Discussion

in the beginning followed by a slightly more pronounced hyperpolarization. A second type of Gárdos channel inhibitor should be used in future experiments to investigate if Tram-34 completely inhibit Gárdos channel activity and there is another type of K^+ channel involved in the progression of Yoda 1-induced hyperpolarization. Or Tram-34 has other effects on RBCs which could lead to hyperpolarization in combination with Yoda 1.

Fourthly, due to the limited number of available blood donors, there are only three donors in some of the experiments, which is the least number to perform statistics. Some of the statistics might become significant when the number of donors is increased.

Fifthly, the MBE method is reflecting membrane potential change in a RBC population rather than in individual cells. Thus, it is difficult to represent channel activation and membrane potential change in single cell, which makes it difficult to study membrane potential flickering by MBE methods. To investigate the regulatory factors of $\rm Ca_{\rm V}2.1$ channel activation, further experiments are needed.

In conclusion, Piezo 1 channel function may be affected by membrane composition and cytoskeletal structure. Piezo 1 and TRPV2 channel activation can lead to $\rm Ca^{2+}$ increase and activation of the Gárdos channel. Gárdos channel open may lead to membrane potential flickering and $\rm Ca_v 2.1$ channel activation. Gárdos channel, $\rm Ca_v 2.1$ channel and $\rm Cl^-$ conductance have a positive contribution to Piezo 1 induced intracellular $\rm Ca^{2+}$ concentration. Finally, PMCAs activity counteracts the $\rm Ca^{2+}$ increase. The data further supports the concept of ion channel interaction, such as linkage between Piezo 1 channel, Gárdos channel and $\rm Ca_v 2.1$ channel. In addition, the data provide the evidence that the oxygenation state of the RBCs can alter ion channel activities.

4.2 FLIM Measurement to Quantify Intracellular Ca²⁺ Concentration

As mentioned in the previous chapter 1.2.2.2, concentration of Ca²⁺, the important cellular massager, is tightly regulated inside cells. Changes in Ca²⁺ concentration can trigger different downstream pathways to regulate cellular activities [108]. Therefore, the quantification of Ca²⁺ concentration is one of the most important challenges in RBC biology or cell biology. The most common method is to measure the change of Ca²⁺indicator intensity in cell imaging. By comparing the measured fluorescence intensity of the indicators with the fluorescence intensity of the indicators in the basal state, in theory a semi-quantification of the intracellular Ca²⁺ concentration could be achieved. However, when measuring the intensity of Ca²⁺-indicators in RBCs, the absorption of excitation and emission light by Hb can influence the detected fluorescence intensity of the Ca²⁺-indicators. During experiments, in hypoosmotic solutions we observe two populations of RBCs, a high intensity and a low intensity group respectively. An elevated fluorescence intensity can be induced by the membrane stretching as a consequence of the volume increase. Such a mechanical stress might trigger a Piezo 1 channel activation and significantly increase the level of Ca²⁺. In the group of RBCs with low intensity the Piezo 1 channel might not have been active. In this case, the concentration of Ca²⁺-indicator in swollen RBCs should be diluted due to the increased volume, and the Ca²⁺ concentration

should decrease as well. The fluorescence intensity of this group is expected to be lower compared to RBCs in isotonic solution. However, as shown in Figure 3.17 A and B, the intensity was higher instead of lower. For echinocytes, the decrease in volume will cause both Ca²⁺ and Ca²⁺-indicator concentrations to increase, which should result in an increase in fluorescence intensity. However, the fluorescence intensity was lower compared to RBCs in isotonic solution (Fig. 3.17). This inverse behavior could be explained by a change in Hb concentration and consequently the absorption of the excitation and emission light by Hb has greater effects on the detected fluorescence intensity than Ca^{2+} and Ca^{2+} indicator concentrations. In swollen RBCs, the Hb concentration is decreased, hence the absorption of the excitation light reduced, leaving more light for absorption by fluorescent indicators and causing more emission light. Moreover, the decreased Hb concentration will also decrease the absorption of emission light, which means more emission light can be detected. In the opposite way, in echinocytes, the increase in Hb concentration causes an increased absorption of excitation and emission light. Both factors will reduce the detected emission light respectively. The influence of Hb is likely to have an exponential relationship with the final detected fluorescence intensity. Compared to the linear relationship between Ca²⁺ and Ca²⁺-indicator concentration and fluorescence intensity, it therefore has a greater influence with respect to the same concentration change.

Fluorescence lifetime, the time that a fluorophore remains in an excited state before emitting a photon, is one of the most important intrinsic properties of a fluorophore [526]. Fluorescence lifetime is independent on fluorophore concentration, initial perturbation conditions and fluorescence intensity. On the other hand it is highly dependent on internal factors such as fluorophore structure, polarity, viscosity and microenvironmental factors including temperature, and the presence of fluorescence quenchers [525, 526]. FLIM can exploit the lifetime decay properties of fluorescence to provide high-resolution images and is distinct from other imaging techniques. Driven by advanced instrumentation and laser technology, FLIM is not only used for obtaining high-resolution images, but also for the visual observation of molecule interactions as well as drug delivery and release when combined with FRET technology [672–675]. Recently, FLIM has also been used to monitor the concentration of macromolecules [611,676]. In theory, when Ca²⁺-indicators bind Ca²⁺, their structure undergoes small changes, which likely influence the fluorescence lifetime. Because the lifetime is not affected by the initial perturbation conditions, FLIM has the potential of being a reliable quantification method to detect intracellular ion concentrations.

The FLIM technique involves scanning a sample area and obtaining spatially resolved photon statistics (Time-Correlated Single Photon Counting - TCSPC). Several methods are used to analyze FLIM data. The advanced FLIM fitting method (AFFM) and the maximum entropy lifetime method (MELT) were used in the data analysis. As shown in Figure 3.21 A, the MELT method could provide the maximum entropy lifetime component spectrum, which helps to visualize the number and variation of present lifetime components. Compared to AFFM, MELT results in a smaller chi-square value, which means that MELT can provide a better fit than AFFM (Fig. 3.21 B). In addition, AFFM with a preset number of components sometimes leads to fitting with inappropriate lifetime components and amplitudes (Fig. 3.21 C,D). In conclusion, the MELT method could more easily find the number of components for best fitting and provide reliable fitting parameters. However,

4 Discussion

for some experiments with small sample sizes, which were only aimed at assessing whether there is a difference between conditions with different experimental parameters, the data was analyzed only by AFFM to reach a quick and preliminary conclusion. Thus, in the data analysis, only data acquired by the 1PE FLIM system and Leica 2PE FLIM system were analyzed using the MELT method. Data acquired by the TauMap 2PE FLIM system was analyzed using AFFM.

Not all Ca²⁺-indicators are lifetime sensitive to Ca²⁺ concentrations. Fluo-4, one of the most common Ca²⁺-indictors for RBCs, has a stable lifetime (Fig. 3.18 A). Fura-2, Fura red, Oregon Green 488 BAPTA-1 (OGB-1) and X-rhod-1 have Ca²⁺ concentration dependent lifetimes (Fig. 3.18 B-E). However, emission and lifetime decay can also be detected from unstained laser-excitated RBCs (Fig. 3.19, and Fig. A.5), whether RBCs receive 1PE or 2PE. The emission and excitation spectrum of RBCs was obtained with 2PE (Fig. 3.19B). In addition, most of the excitation and emission spectra of the tested indicators are different in RBCs compared to HEK cells, except for the excitation spectrum of X-rhod-1. Some of the excitation and emission spectra of Ca²⁺-indicators have similar maximum intensity peaks to unstained RBCs under equal excitation (Fig. 3.20 Aa, Ba, Ca, Da and Ea). The lifetime decays of Fluo-4, OGB-1, Fura2 and X-rhod-1 are significantly different from those of RBCs (Fig. 3.20 Ab, Bb, Cb, Eb). Photon emission and lifetimes detected from unstained RBCs (Fig. 3.19 and Fig. A.5) seem to suggest that Hb generate autofluorescence like some other studies suggest [565–568, 570]. However, the excitation spectrum of pure RBCs recorded in experiments (Fig. 3.19B) is different from the absorption spectrum of Hb [677]. This indicates that the signal detected by pure RBCs in the experiment may not be the autofluorescence of Hb, but a photoconversion-based fluorescence. There are also studies suggesting that the fluorescence detected from RBCs with UV light excitation is not from Hb but from bilirubin isomers, since the detected spectral response is similar to bilirubin. The high energy of laser excitation, especially 2PE, potentially breaks down Hb to bilirubin isomers and generate fluorescence [573–575]. Thus, the fluorescence signal from RBCs after laser excitation is most likely photoconversion-based fluorescence, but further investigation is needed. Nevertheless, RBC signals could affect the spectrum of Ca²⁺-indicators and their lifetime. The Ca²⁺- indicator with the least influence of RBC signals and the most pronounced lifetime decay is X-rhod-1. Therefore, X-rhod-1 was selected for further experiments.

Theoretically, the fluorescence lifetime is independent of the excited emission intensity, photobleaching, excitation laser wavelength and intensity as well as fluorophore concentration [676,678]. However, in real experiments the fluorescence is not an isolated mechanism but the entirety of emitted light is influenced by energy conversions and light scattering in the complex environment of biological samples. During the experiments, the FLIM images of X-rhod-1 loaded RBCs with 2PE show three lifetime components but the FLIM images with 1PE show only two lifetime components (Fig. 3.21 A). The smallest lifetime component τ_1 is an additional one in the 2PE. Since the other lifetime components τ_2 and τ_3 in 2PE are similar to the two lifetime components in 1PE, the τ_1 in 2PE most likely originates in RBCs. Because 2PE requires cooperating two low-energy photons to cause a higher-energy electron transition in the fluorophore, and it is a nonlinear process in that the absorption rate depends on the second power of the light intensity, the total energy absorbed by the fluorophore is higher compared to 1PE [679, 680]. The high energy of

the excitation may break down Hb to bilirubin and generate the photoconversion based fluorescence (Fig. 3.19 and Fig. A.5). However, the shortest lifetime components $\tau 1$ were also detected in X-rhod-1 loaded HEK cells with 2PE. It lies between τ_1 and τ_2 in X-rhod-1 loaded RBCs. The spectrum of τ_1 in HEK cells shows a small overlap with τ_2 in X-rhod-1 loaded RBCs (Fig. 3.30 A). The data suggest that the shortest lifetime components are from the Ca²⁺-indicator or the microenvironment around the indictor in cytosol.

The experiments also show that for the same type of laser excitation (1PE or 2PE), neither the excitation laser wavelength nor the acquisition time influence the lifetime decay or the fitted lifetime components (Fig. 3.22, Fig. 3.23 and Fig. A.6). However, there are significant differences between τ_3 -800 nm and τ_3 -900 nm or τ_3 -920 nm and a significant difference between FLIM images with 4.4 seconds and 97 seconds acquisition time (Fig. 3.22 D, Fig. 3.23 D), which can be explained by a significant statistical error due to low photon counts. The laser with a wavelength of 800 nm cannot induce the high intensity in emission light of X-rhod-1 compared to the 900 nm and 920 nm lasers, resulting in low photon counts (Fig. 3.20 Ea). The total photon counts for an acquisition time of 4.4 seconds were smaller compared to 97 seconds. The large variation within the data set obtained by 4.4 seconds acquisition time also supports the low photon counts theory mentioned above (Fig. 3.23 D). To avoid additional signals from RBCs while obtaining maximum excitation, the 532 nm laser wavelength is ideal for the 1PE FLIM system and the 915 nm laser wavelength is ideal for the Leica 2PE FLIM system.

Further experiments with 2PE also prove that the number of photons (intensity) and the focus of the FLIM image can influence the measured lifetime components and the amplitude-averaged lifetime (Fig. 3.31). As shown in Figure 3.31 A, the amplitude-averaged lifetimes increase with the average intensity of the FLIM images in a logarithmic way. The amplitude-averaged lifetime may reach a plateau when the average intensity reaches about 15 photons per pixel. The similar trends also apply to the three separate lifetime components (Fig. 3.31 B). The intensity change is highly dependent on the focus during imaging with a linear relationship. The trend between focus and average lifetime or three components is similar to the trend between average intensity and lifetime parameters (Fig. 3.31 C,D). The MELT method is theoretically able to resolve all lifetime components present in a multi-component decay, and better statistics lead to finer resolution of the decay structure, ultimately allowing resolution of all lifetime components. The MELT components show saturation with increasing FLIM intensity, i.e. photon count. In the saturated case there are three components and these are assumed to be all resolvable components. The histogram resolution depends on the photon count according to the law of large numbers. At low intensities, the spectrum shows only a single lifetime component equal to the average lifetime. As the intensity increases, two components are resolved with lifetimes similar to the lowest and highest components in the fully resolved case. This suggests that for the same sample, as long as the focus setting or other acquisition parameters allow the FLIM system to collect enough photons, the number of lifetime components and the lifetime parameters are stable. It also strongly supports that the significant difference between 800 nm 2PE FLIM images and 900 nm or 920 nm 2PE FLIM images, as well as between 4.4 seconds and 97 seconds acquisition time FLIM images, is due to low photon counts.

However, in the same image, the average intensity of the cells is not homogeneous. As Figure 3.32 shows, each RBC has an individual average intensity. The amplitude-averaged

4 Discussion

lifetime seems not homogeneous either (Fig. 3.33). To simplify the analysis, the recorded RBC population is divided into 20 groups according to the percentiles of the average intensity distribution, and all the groups have enough photon counts that exceed the temporal resolution limit of the FLIM system. The average intensity has obvious differences between these groups but the focus parameter and amplitude average lifetime seem similar to each other (Fig. 3.34 A-C). If the first ten populations are considered as low-intensity populations, and the last ten populations are grouped as high-intensity populations. Apart from the significant differences in average intensity, τ_1 and τ_2 between low and high intensity populations have small but significant difference (Fig. 3.34 D,G), indicating that other factors could influence the lifetime components.

The lifetime can be influenced by internal factors. In experiments, those potential factors might include temperature, Hb concentration, and biological variation of RBCs from different donors. Theoretically, lower temperatures lead to longer fluorescence lifetimes [525, 681]. As Figure 3.24 A shows, the decay curves of X-rhod-1 loaded RBCs are slightly different. The lifetime components τ_1 , τ_2 and the amplitude-averaged lifetime have an obvious dependency on temperature (Fig. 3.24 B,C,E). Component τ_3 shows no significant difference between 26 °C and 29 °C but at 37 °C it is significantly shorter (Fig. 3.24 D). That shows that the two shorter lifetime components are more sensitive to temperature changes than τ_3 . The combined average lifetime is strongly dependent on temperature as found in previous studies. The higher the temperature, the shorter the average lifetime. However, the amplitude ratio and the lifetime-weighted amplitude ratio do not show a significant relationship with temperature (Fig. 3.24 F,G).

Hb has higher concentration in mature RBCs [54], indicating a possible small distance between Hb and X-rhod-1 molecule. In Hb molecule, Hb can act as a good internal quenching molecule and cause FRET between X-rhod-1 and Hb [562–564]. FRET could influence the lifetime of the donor, in this case, the lifetime of X-rhod-1. When RBCs are in hypotonic solutions and swell to stomatocytes, cell volume increases and Hb concentration decreases [463,464,480,481]. In contrast, when RBCs are placed in hypertonic solution, RBCs will shrink to echinocytes with decreased cell volume and increased Hb concentration [463,464]. As expected, stomatocytes in hypotonic solution emit a higher intensity than RBCs in isotonic solution and echinocytes in hypertonic solution (Fig. 3.29 A). The significant differences of decay curves, τ_1 , τ_3 amplitude-averaged lifetime, amplitude ratio and lifetime-weighted amplitude ratio between stomatocytes, normal RBCs and echinocytes shows that when Hb concentration increases, the parameters become shorter or smaller (Fig. 3.29 B,C,E-H). Although the difference of τ₂ between normal RBCs and echinocytes is not significant, it shows that τ_2 decreases with increasing Hb concentration (Fig. 3.29 D). Comparing the lifetime parameters of HEK cells, which can be considered as cells with the lowest possible Hb concentration (0 mM), to three RBCs groups, all lifetime parameters of X-rhod-1 loaded HEK cells are bigger or longer than those of RBCs in all osmolar conditions (Fig. 3.30 B-H). However, HEK cells have organelles which can store Ca²⁺, such as the endoplasmic reticulum (ER), mitochondria and Golgi apparatus [248]. In HEK cells, Ca²⁺ can be released from ER in some conditions, for example, via inositol 1,4,5-trisphosphate (IP₃) receptor, an intracellular Ca²⁺ channel. IP₃ can be activated by increasd Ca^{2+} in nanomolar range and lead to Ca^{2+} release from ER [682–686]. The application of Ca²⁺-ionophores can unselectively releases Ca²⁺ from ER, mitochondria, and other cell compartments and provide an extra source of Ca²⁺ into cytosol [687]. In addition, HEK cells were not incubated in glucose-free solution to deplete their ATP stores in the experiments. All these factors together make the free Ca²⁺ levels in HEK cells and RBCs not exactly comparable. Therefore, only the lifetime components could be compared. All data support that Hb concentration has an influence on these lifetime parameters and possibly because of FRET. But the small Hb concentration differences due to donor differences result in similar decays and lifetime components (Fig. 3.27), indicating that the variations in the Hb amount in RBCs due to donor differences seem not strong enough to change the lifetime parameters.

In addition, it is common for chemicals and biochemicals commonly used for solution preparation, even distilled water, to have trace amounts of Ca²⁺ contamination in the range of 1 – 10 µM [688]. Thus, the commercial Ca²⁺-free PBS may also contain traces of Ca²⁺. Contamination in the micromolar range is a significant problem in the preparation of solutions containing Ca²⁺ in the nano- to micromolar range. The Ca²⁺ contamination is higher than the basal Ca²⁺-level in RBCs. When RBCs are placed in hypo- or hyperosmotic solutions, the changes in cell shape due to osmolarity can cause mechanical stress on the cell membrane, which can activate Piezo 1 channels and possibly resulting in an increased intracellular Ca²⁺. This explains the associated changes in lifetime parameters, especially the amplitude-average lifetime, amplitude ratio and lifetime-weighted amplitude ratio in RBCs. RBCs are placed in low or high osmotic solution with an additional amount of 1 mM Ca²⁺. The data show no differences in all lifetime parameters of X-rhod-1 in echinocytes with or without extracellular Ca^{2+} (Fig. 3.29 C-H). For stomatocytes, τ_1 , τ₃, and the amplitude-average lifetime of X-rhod-1 have around 5% difference between conditions with or without extracellular Ca²⁺, which is significant. There is no difference in τ₂, amplitude ratio and lifetime-weighted amplitude ratio of X-rhod-1 in stomatocytes (Fig. 3.29 C-H). The very small difference in τ_1 and τ_3 of X-rhod-1 in stomatocytes and no differences in τ_2 of X-rhod-1 in stomatocytes and τ_1 to τ_3 of X-rhod-1 in echinocytes shows that the differences in lifetime components observed between stomatocytes, echinocytes and discocytes are highly dependent on Hb concentration. The difference in amplitudeaveraged lifetime in stomatocytes in solution with or without extracellular Ca^{2+} could be due to the difference of τ_1 and τ_3 (Fig. 3.29 C,E,F).

Additional chemicals such as Cell-tak (to 'glue' cells to the substrate for optical investigations), Pluronic-127 (as an additive to enhance dye uptake by the cells) and Ca²⁺ ionophores were used for experiments. In Figure A.8 and Figure A.10, the data suggest that the Pluronic F-127 and Cell-tak do not affect the intensity or lifetime. For the Ca²⁺ ionophore, the Ionomycin-treated unstained RBCs have a similar spectrum with two peaks as unstained RBCs but the Bromo-A23187-treated unstained RBCs have a spectrum with only one peak, which is smaller than the shortest peak of unstained RBCs (Fig. 3.26 A). It suggests the possibility that Bromo-A23187 reduces emitted photons from RBCs. The average intensity and amplitude averaged lifetime of Bromo-A23187 in unstained RBCs is smaller than that of Ionomycin in RBCs (Fig. 3.26 C,D). Additionally, both Bromo-A23187 and Ionomycin do not contribute to the intensity, lifetime and lifetime components of X-rhod-1 in RBCs (Fig. A.9). Bromo-A23187 is slightly more suitable due to the lower average intensity and lifetime in untreated RBCs and the spectrum with only one and the smallest component.

120 4 Discussion

The use of Ca²⁺ ionophore and increase the Ca²⁺ concentration may lead to Ca²⁺ ATPases (PMCA) to work and reduce the Ca²⁺ concentration to basal condition. Although the RBCs were incubated in glucose-free solution for 72 hours. According to the literature, RBCs incubated in glucose-free solution for 24 hours already can be considered as ATP depleted [576, 577, 642, 643]. In addition, residual ATP in RBCs after incubation was tested once by ATP detection assay, and the amount of residual ATP is below the sensitivity of the ATP detection assay (data not show). The amplitude averaged lifetime starts to decrease after 5 minutes in the Leica FLIM system with precise time sequence (Fig. 3.28). The amplitude-averaged lifetime, amplitude ratio and lifetime-weighted amplitude ratio start to decrease after 2 images in the 1PE FLIM system with roughly 5 minutes per image (Fig. A.11). The high Ca²⁺ concentration in RBCs induced by Bromo-A23187 is not maintained for more than 10 minutes. One of the potential reasons for this is that complete ATP depletion is impossible. Hence, the remaining ATP can still support PMCA function and reduce the concentration. Or there are other Ca²⁺ transporters that can reduce Ca²⁺ concentration in RBCs. Another possible reason is because of increased intracellular Ca²⁺, the Gárdos channels are activated and RBCs start to dehydrate and shrink. The shrinkage could reduce or shorten the lifetime parameters. The changes in amplitude-averaged lifetime, amplitude ratio and lifetime-weighted amplitude ratio over the Bromo-A23187 stimulation time indicated these three parameters can be used for further Ca^{2+} quantification.

In addition, experiments conducted on different days may have variations due to handling and changes in the lab environment. The decay and lifetime components of experiments on different experimental days with RBCs from the same donor and treated in the same condition are similar (Fig. 3.25 and Fig. A.7). This indicates that FLIM measurements with the same FLIM microscopy system are stable and the data are repeatable. Once all the experiment parameters have been set, series of FLIM images of X-rhod-1 loaded RBCs with different intracellular Ca²⁺ concentration were acquired and analyzed. There is a clear fast lifetime change between different Ca²⁺ concentrations (Fig. 3.35). The three ideal parameters, amplitude-averaged lifetime, amplitude ratio and lifetime-weighted amplitude ratio, changes with increased Ca²⁺ concentration (Fig. 3.36 and Fig. A.12). However, the variation of each parameter between samples is up to 5% (Fig. 3.36 A-C). After normalizing the data to the basal Ca²⁺ condition to remove the influence of temperature, the variation of the amplitude-averaged lifetime between samples is smaller but the amplitude ratio or lifetime-weighted amplitude ratio are not (Fig. 3.37 A-C). Normalized amplitude-averaged lifetime and Ca²⁺ concentration show an obvious non-linear relation (Fig. 3.37 A.D). The normalized amplitude ratio and the normalized lifetime-weighted amplitude ratio seem to have a nonlinear relation with the Ca²⁺ concentration. However, compared to normalized amplitude-averaged lifetime, normalized amplitude ratio and normalized lifetime-weighted amplitude ratio are not sensitive to changes in Ca²⁺ concentration (Fig. 3.37).

It seems promising that FLIM images of X-rhod-1 loaded RBCs can be used to quantify Ca^{2+} concentration and normalized amplitude-averaged lifetime can be used as a read-out parameter. However, there are still some questions and technical problems need to be answered and solved in further experiments.

Firstly, are signals from unstained RBCs detected Hb based on photoconversion fluorescence? Understanding this question may help to reduce the influence of signals from RBCs on the measured decay. However, there is not enough evidence to make a conclusion here and this needs to be investigated in the future. In addition, the influence of Hb concentration on the lifetime components of X-rhod-1 needs to be reduced. The application of third harmonic generation microscopy may allow to measure local Hb concentration label-free [689]. The determined Hb concentration can be included in the data analysis and reduce the influence of FRET from the Hb around indicator.

Secondly, what do these lifetime components represent? Theoretically, there should be two lifetimes, one representing the Ca²⁺ bound X-rhod-1 and one representing the Ca²⁺ unbound X-rhod-1. But there is lack of explanation of the third lifetime component. Which lifetime component represents which states of X-rhod-1 also needs further investigation.

Thirdly, the heterogeneous intensity and lifetime of RBCs in the same images. It might indicate the heterogeneous response of RBCs to ionophores which leads to different actual Ca^{2+} concentration in RBCs from the ideal concentration, leading errors in the determination of the amplitude-averaged lifetime of a given Ca^{2+} concentration.

Fourthly, the measurement of extracellular Ca^{2+} concentration is difficult. The available Ca^{2+} -electrode is supposed to be able to measure Ca^{2+} -concentration between $10\,\mu\mathrm{M}$ to $10\,\mathrm{mM}$. However, during experiments, there are defined conditions with Ca^{2+} concentration lower than $10\,\mu\mathrm{M}$. Additionally, although it is claimed that the sensitivity of the sensor is lower to $10\,\mu\mathrm{M}$, during the real measurement, the reading of low Ca^{2+} -concentration solution is unstable with huge errors. During the imaging, the RBCs need to stay in PBS, a buffered solution. The buffered solution can influence the read-out of the Ca^{2+} -electrode. Troubleshooting is still in progress at the time of this writing. Therefore, all Ca^{2+} concentrations for the experiments conducted with the Leica FLIM system are still theoretical. Further determination of extracellular Ca^{2+} concentration should be done.

In conclusion, FLIM is a technique with great potential to quantify intracellular Ca²⁺ concentration. However, whether the FLIM could be used for quantify Ca²⁺ concentration in single RBCs need to be further tested.

A.1 Detailed Protocols of Experiments

RBCs Collection and Washing

The protocol for washing the RBCs is outlined in the following steps:

- I. A defined volume of blood was mixed with Tyrode solution, saline or Ringer solution and centrifuged to remove plasma and buffy coat (at 500 rcf for 5 minutes or 5500 rcf for 3 minutes).
- II. The sedimented RBCs were resuspended in Tyrode solution, saline or Ringer solution and centrifuged (at 500 rcf for 5 minutes or 5500 rcf for 3 minutes). This is called the washing step. The washing step was repeated in three times.
- III. After the last washing step, the sedimented RBCs were ready for further experiments.

ATP-depleted RBCs Preparation

The protocol to prepare the ATP-depleted RBCs suspension is outlined in the following steps:

- I. A defined volume of blood or washed cells was mixed with 1 ml of glucose-free Tyrode solution or phosphate-buffered saline (PBS) and centrifuged at 500 rcf for 5 minutes to remove plasma and buffy coat or supernatant.
- II. Sedimented RBCs were washed three times with 1 ml of glucose-free Tyrode solution or PBS.
- III. After the last washing step, sedimented RBCs were incubated in 1 ml glucose-free Tyrode solution or PBS for 16 hours at at 4 °C or 72 hours in RT.

Calcium Indicators Loaded RBCs

The protocol to prepare the Ca^{2+} indicator loaded RBCs is outlined in the following steps:

- I. Washed RBCs were mixed with 1 ml of experimental medium containing $5\,\mu\mathrm{M}$ of the Ca²⁺ indicators required for the experiment. These RBCs were incubated in a thermomixer (Thermomixer comfort or ThermoMixer C) at $37\,^{\circ}\mathrm{C}$ with $400\,\mathrm{rpm}$ shaking speed for 1 hour in the dark.
- II. After incubation, the RBCs were centrifuged at 500 rcf for 5 minutes to remove the probe solution.
- III. Sedimented RBCs were washed three times with 1 ml of experimental medium to remove probe in the extracellular environment.

124 Appendix

IV. After the final washing step, sedimented RBCs were resuspended with experimental medium for subsequent fluorescence detection.

Fluorescent-dye-conjugated Antibody bound RBCs Preparation

The protocol to prepare fluorescence-labeled RBCs is described in the following steps:

- I. Washed RBCs were mixed with 100 µl of the label buffer containing primary antibodies at the designed concentration, followed by incubation in thermomixer at RT with 400 rpm shaking speed for 1 hour.
- II. After incubation, the RBCs were centrifuged at 500 rcf for 5 minutes to remove supernatant.
- III. Sedimented RBCs were washed three times with 1 ml of label buffer to remove unbound primary antibodies.
- IV. After the third wash, the sedimented RBCs were resuspended with 100 µl of label buffer containing secondary antibodies, followed by incubation in thermomixer at RT with 400 rpm shaking speed for 1 hour in the dark.
- V. After incubation, the RBCs were centrifuged at 500 rcf for 5 minutes to remove the supernatant.
- VI. Sedimented RBCs were washed three times with 1 ml of the label buffer to remove unbound secondary antibodies.
- VII. After the final wash, the sedimented RBCs were resuspended with 1 ml of the label buffer for further experiments.

Cell Lysis preparation

The detailed protocol of lysing cells by NP-40 is described in the following steps:

- I. Washed cells with PBS, followed by centrifugation at 1500 rcf for 5 minutes. Repeated washing step 4 times.
- II. Added $300\,\mu l$ of lysis buffer for other cells to the sedimented cells and lysed cells for $10\,minutes$ on ice.
- III. Centrifuge cell lysis at 4°C, 14000 rcf for 10 minutes. Collect supernatant.

Ghost RBCs Preparation

The detailed protocol of harvesting ghost cells is described in the following steps:

- I. 200 μl of blood was mixed with 300 μl of 0.1 M phosphate buffer to wash RBCs. Centrifuged at 14000 rcf for 30 seconds, removed supernatant.
- II. Added 300 µl of lysis buffer for ghost preparation to the sedimented RBCs and lysed RBCs for 10 minutes on ice.
- III. Centrifuged cell lysis at 4°C, 14000 rcf for 20 minutes, removed supernatant.
- IV. Added 150 μl of the same lysis buffer and centrifuged at 14000 rcf for 20 minutes at 4°C to wash ghost cells. Repeated washing steps twice.

- V. Added 150 µl of the same lysis buffer to the ghost cells and centrifuged at 14000 rcf for 45 minutes at 4 °C to wash and pack ghost cells.
- VI. Resuspended the ghost cells with 100 μl of the same lysis buffer.

Membrane Potential Measurements According to MBE method

The detailed protocol of the MBE method is described in the following steps:

- I. The RBCs prepared as described in previous section 2.2.1 must be packed by centrifugation at 13000 rcf for 2 minutes to obtain 99.99% of the hematocrit value.
- II. 100 μl or 150 μl of packed RBCs was loaded into a beaker or 2 ml Eppendorf tube containing Ringer solution with calcium, pretreated with 20 μM CCCP.
- III. The tested chemical was added to the measuring system
- IV. If necessary, a second tested chemical was added to the measuring system
- V. Triton X-100 detergent (1% in 3 M NaCl) was added to the measuring system as a cell lysis solution.

Bradford assay

The measurement steps of the Bradford assay are described below:

- I. Added 5 μl of the BSA standard or 2 μl of sample to a 96-well plate.
- II. Prepared a substrate mixture with Reagent A and Reagent S (A:S 1:50). Added 25 µl of the substrate mixture to each well
- III. Added 200 µl of Reagent B to each well
- IV. Incubated the mixture in the dark at RT for 15 20 minutes
- V. Measured the total protein in the spectrophotometer and recorded data by BIoTek's Gen5 PC

NanoDrop measurement

The detailed NanoDrop measurement steps are described below:

- I. Blanked Nanodrop by adding 10 µl same lysis buffer as cell lysis to the bottom pedestal, lowered the arm and obtained blank data file.
- II. Cleaned the lower and upper pedestals
- III. Mixed the sample by vortex.
- IV. Added 10 µl of the sample to the bottom pedestal. Lowered the arm and read the absorbance at 280 nm.
- V. Removed the sample and cleaned the pedestals.

SDS-PAGE experiment

The detailed SDS-PAGE experiment protocol is described below:

I. Mixed 5 μl sample buffer with sample solution containing 30 μg protein. The sample was boiled at 95 °C for 5 minutes.

II. Placed pre-cast gel in running box and filled SDS running buffer to the running box. Removed comb from gel.

- III. Loaded samples and protein ladder to designed wells. Added sample buffer to rest empty wells.
- IV. Electrophoresis was conducted at $100\,\mathrm{V}$ for $30\,\mathrm{minutes}$ followed by $45\,\mathrm{minutes}$ at $120\,\mathrm{V}$.

Western Blot experiment

The detailed protocol of western blot is described below:

- I. Pre-run gel was transferred to the electroblotting stack, on the blotting nitrocellulose membrane and under cathode stack, when the anode stack was under the blotting membrane.
- II. Placed the transferred stacks into the transfer device and performed electroblotting for 5.5 minutes at 20 V.
- III. The membrane was blocked with blocking buffer for 2 hours, at RT.
- IV. The blocked membrane was incubated with the primary antibody in blocking buffer overnight at 4°C with gentle agitation.
- V. The blot was washed with Tris-buffered saline with tween-20 (TBST) solution for 15 minutes at RT. The blot needed to be washed three times.
- VI. The blot was incubated with the secondary antibody in blocking buffer for 1 hour at Rt with gentle agitation.
- VII. The blot was washed with TBST solution for 10 minutes at RT. The blot needed to be washed three times.
- VIII. The blot was incubated in ECL Western Blotting Substrate for 1 minute at RT.

A.2 Supplementary Figures

The Combination of Mutations of Piezo 1 and Spectrin

Before the pediatric patient (with both Piezo 1 mutation and spectrin mutation as previous section 3.1.2.1 mentioned) underwent splenectomy, the pediatric patient's RBCs have the highest average intracellular Ca^{2+} concentration while the father's (with spectrin mutation) RBCs have the lowest Ca^{2+} after 1 minute of 5 μ M Yoda 1 stimulation (Fig. A.1 Aa,Ba). However, after 5 minutes, the intracellular Ca^{2+} concentration in the different samples is similar (Fig. A.1 Ac,Bb). In contrast to the pre-surgery conditions, the pedriatric patient's RBCs do not show much difference in intracellular Ca^{2+} concentration compared to the others after 5 μ M Yoda 1 stimulation after the splenectomy (Fig. A.1 Ab,Ad,Ba,Bb).

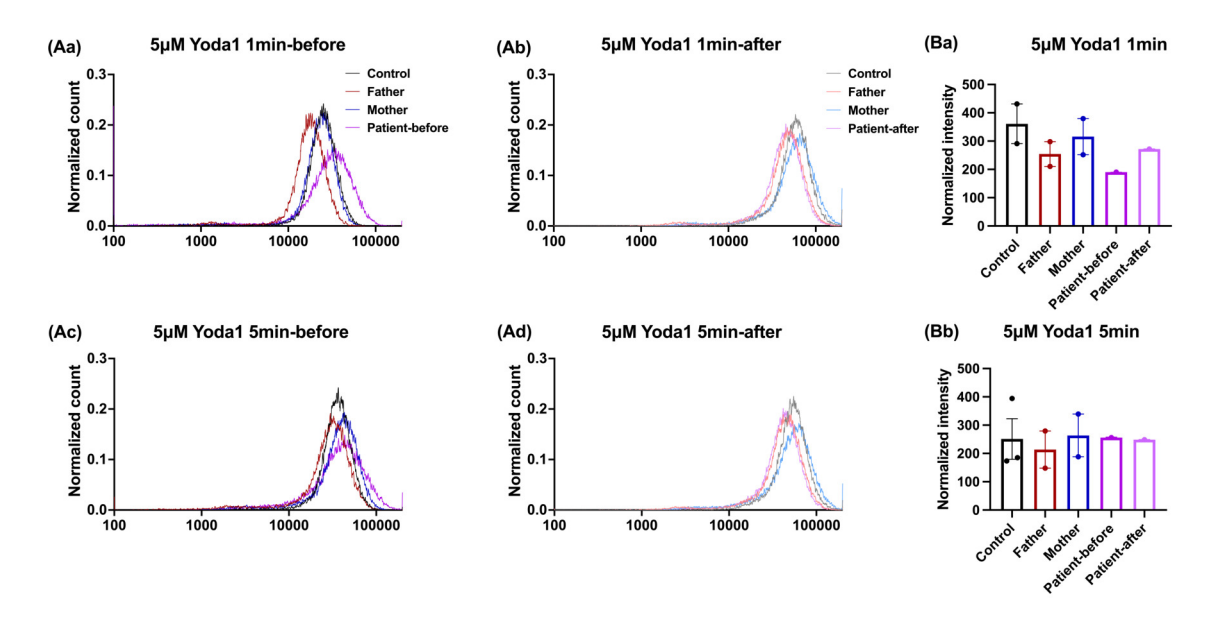


Fig. A.1: Ca²⁺-signaling in RBCs from a Piezo 1 and spectrin double mutation pediatric patient, family members of the patient and healthy controls after 5 μM Yoda 1 conditions. (A) Representative normalized histograms of Fluo-4 intensity of controls (black and gray trace), father (dark red or light red trace), mother (dark blue or light blue trace) and the pediatric patient (patient) (dark purple or light purple trace) in different conditions. Darker color for samples taken before the date of splenectomy of the patient and lighter color for samples taken after the date of splenectomy. (Aa)–(Ab) Samples after 5 μM Yoda 1 stimulation for 1 minute. (Ac)–(Ad) Samples after 5 μM Yoda 1 stimulation for 5 minutes. (B) Statistical analysis of average Fluo-4 intensity in different conditions. Fluo-4 intensity measured (Ba) after 1 minute and (Bb) after 5 minutes. (N_{control-donor}=5, N_{father-sampling}=3, N_{mother-sampling}=3, N_{patient-sampling-before}=2, N_{patient-sampling-after}=1, n_{cell}>30,000). Data is shown as means ± SEM in (Ba) and (Bb). The sampling number of patient were smaller than 3, thus, the statistical analysis was not applied.

Effects of TRPV2 Activation on Sickle Cells

After 80 μ M Δ^9 -THC stimulation, an increase in the percentage of high Ca²⁺ RBCs occurs in both AA and SS groups. (Fig. A.2 B,C). The percentage of high Ca²⁺ RBCs is increased significantly after stimulation and reaches the maximum plateau after 3 minutes in both

SS and AA groups. The SS group maintains a significantly higher percentage of high Ca^{2+} cells than AA (Fig. A.2 B,C). In addition, both AA RBCs and SS RBCs that respond to Δ^9 -THC reach the highest intracellular Ca^{2+} after 3 minutes of Δ^9 -THC application and the calcium level starts to decrease since 5 minutes. The intracellular Ca^{2+} concentration is slightly higher in SS RBCs than AA RBCs with a (20% higher normalized Fluo-4 intensity (Fig. A.2 D,E). However the difference is not significant (Fig. A.2 D,E).

In contrast to $80\,\mu\text{M}$ Δ^9 -THC mentioned in previous section 3.3.2, $30\,\mu\text{M}$ Δ^9 -THC induces almost no change in membrane potential in either AA RBCs ($-2.5\pm0.7\,\text{mV}$) or SS RBCs ($-5.0\pm1.1\,\text{mV}$) in oxygenated condition (Fig. A.4). In addition, the ethanol as equivalent amount of $30\,\mu\text{M}$ Δ^9 -THC could not induce membrane potential change in SS RBCs in oxygen condition (Fig. A.4 A-C). However, $30\,\mu\text{M}$ Δ^9 -THC could induce significant hyperpolarization of $-11.6\pm1.8\,\text{mV}$ in SS RBCs in deoxygenated condition (Fig. A.4). Ethanol at an equivalent amount does not cause any significant membrane potential change (Fig. A.3 A-D).

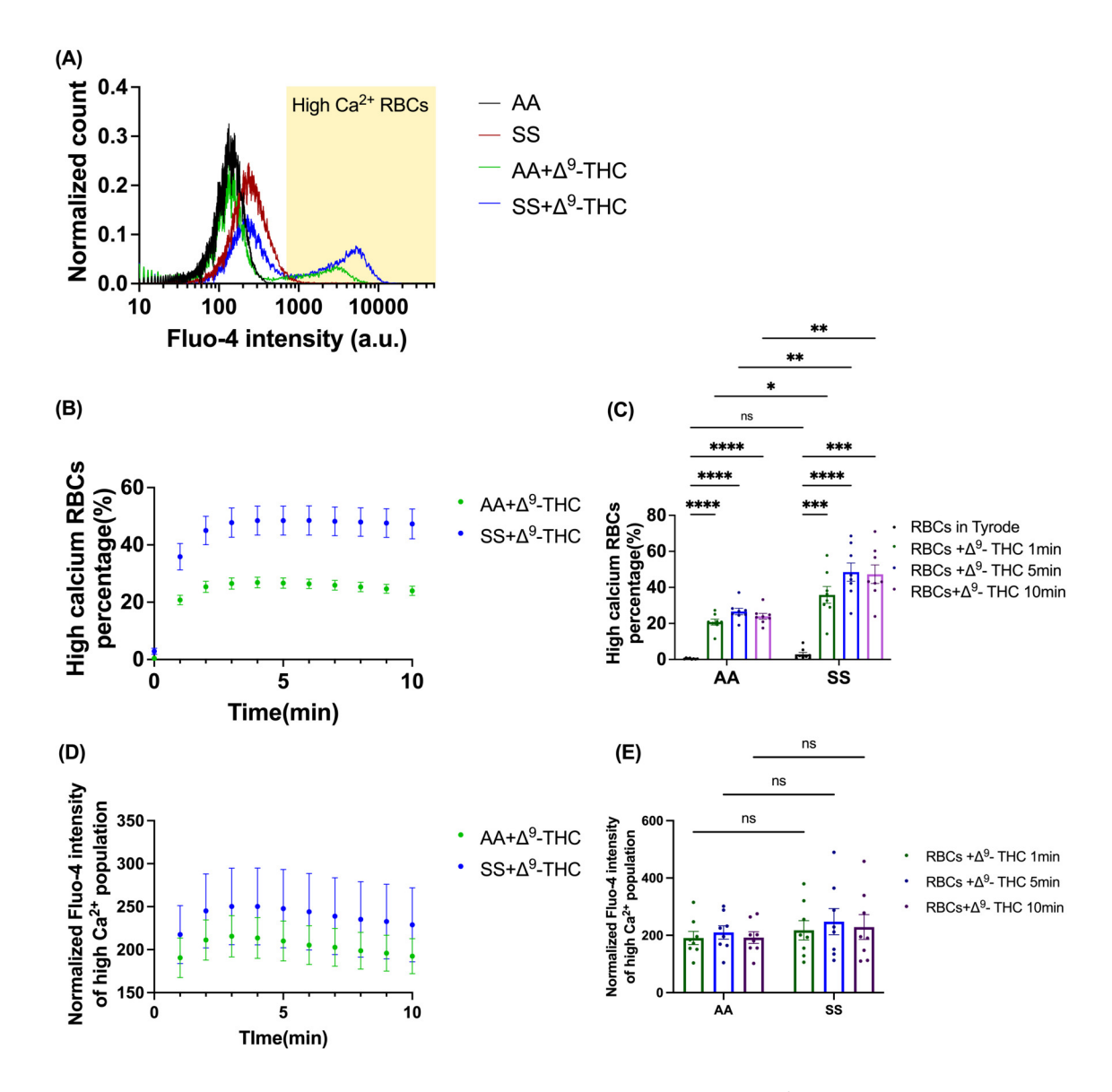


Fig. A.2: The results of the flow cytometry measurements of Ca^{2+} -signaling in RBCs from healthy controls (AA) and sickle cell patients (SS) after 80 µM Δ^9 -THC stimulation. (A) Representative normalized histograms of Fluo-4 intensity in the high Ca^{2+} population of AA cells without Δ^9 -THC (black trace), SS cells without Δ^9 -THC (red trace), AA cells with Δ^9 -THC (green trace), and SS cells with Δ^9 -THC (blue trace); (B) Percentage change of the high Ca^{2+} population over time after Δ^9 -THC application (green-AA, blue-SS); (C) Quantitative analysis of AA and SS RBCs with high Ca^{2+} in response to Δ^9 -THC in different conditions; (D) Normalized Fluo-4 intensity change in AA and SS RBCs responding to Δ^9 -THC over time after Δ^9 -THC application (green-AA, blue-SS); (E) Quantitative analysis of normalized Fluo-4 intensity of AA and SS RBCs that responding to Δ^9 -THC in different time points. (donor=8, n_{cell}>30,000.) Data is shown as means \pm SEM in (B)- (E). Statistical differences were evaluated by two-way ANOVA test with Tukey's multiple comparison method. p < 0.05 was deemed significant.

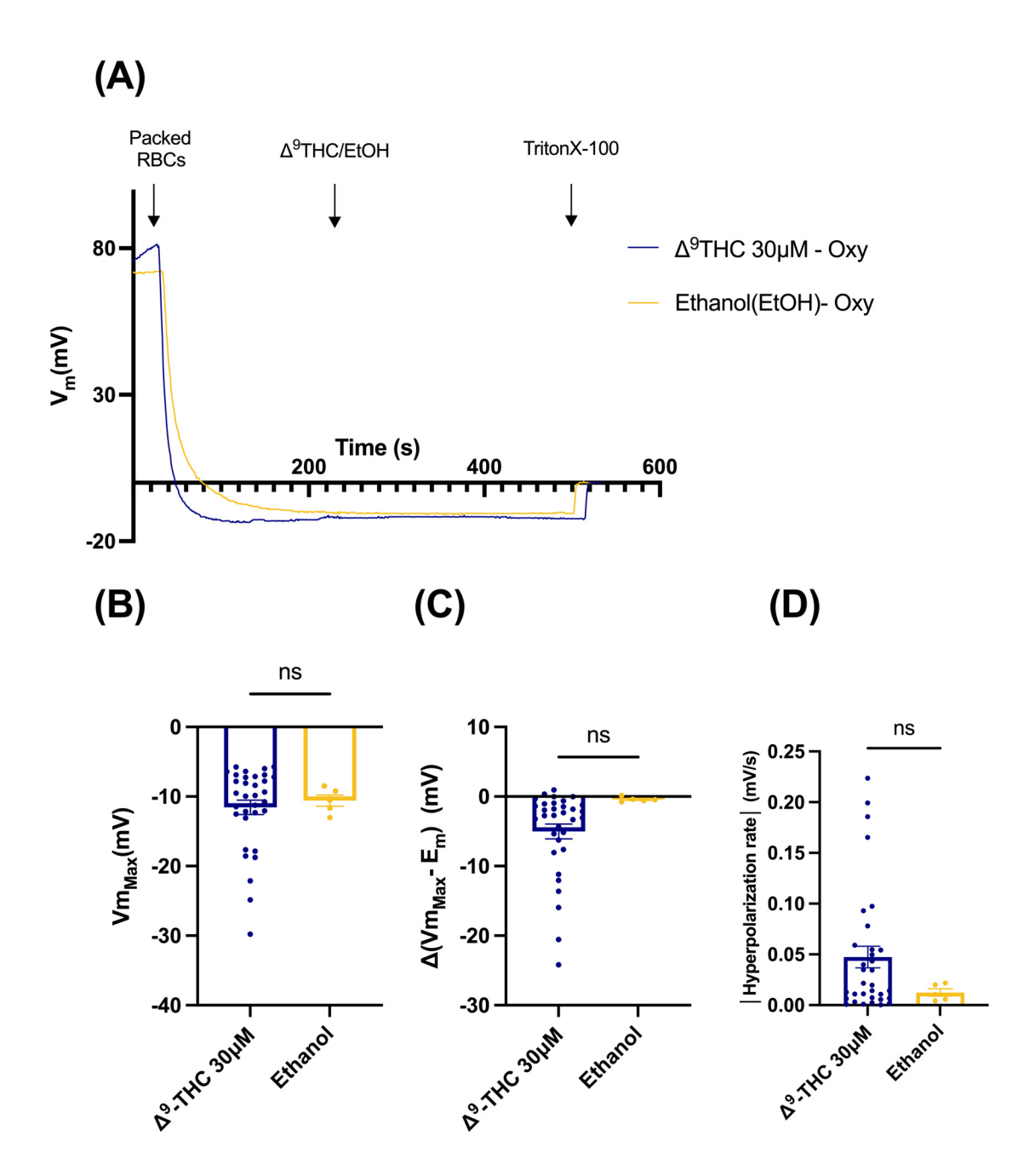


Fig. A.3: Membrane potential with 30 μ M Δ^9 -THC and corresponding amount of solvent (ethanol) stimulation in SS RBCs. (A) Representative trace with Δ^9 -THC (blue), with ethanol (EtOH) (yellow). Arrows indicate when packed RBCs, stimulation and TritonX-100 were added to the measuring system. (B) Maximal hyperpolarization (Vm_{Max}). (C) Hyperpolarization magnitudes (Δ (Vm_{Max}-E_m)) are obtained after the deduction of resting membrane potential (E_m) from the maximal hyperpolarization (Vm_{Max}) reached at each condition Membrane potential change. (D) Absolute value of hyperpolarization rate. (N_{SS+30 μ M-THC-donor=33, N_{SS+EtoH-30-donor}=5.) Data is shown as means \pm SEM in (B)-(D). Statistical differences were evaluated using unpaired T-test. p < 0.05 was deemed significant.}

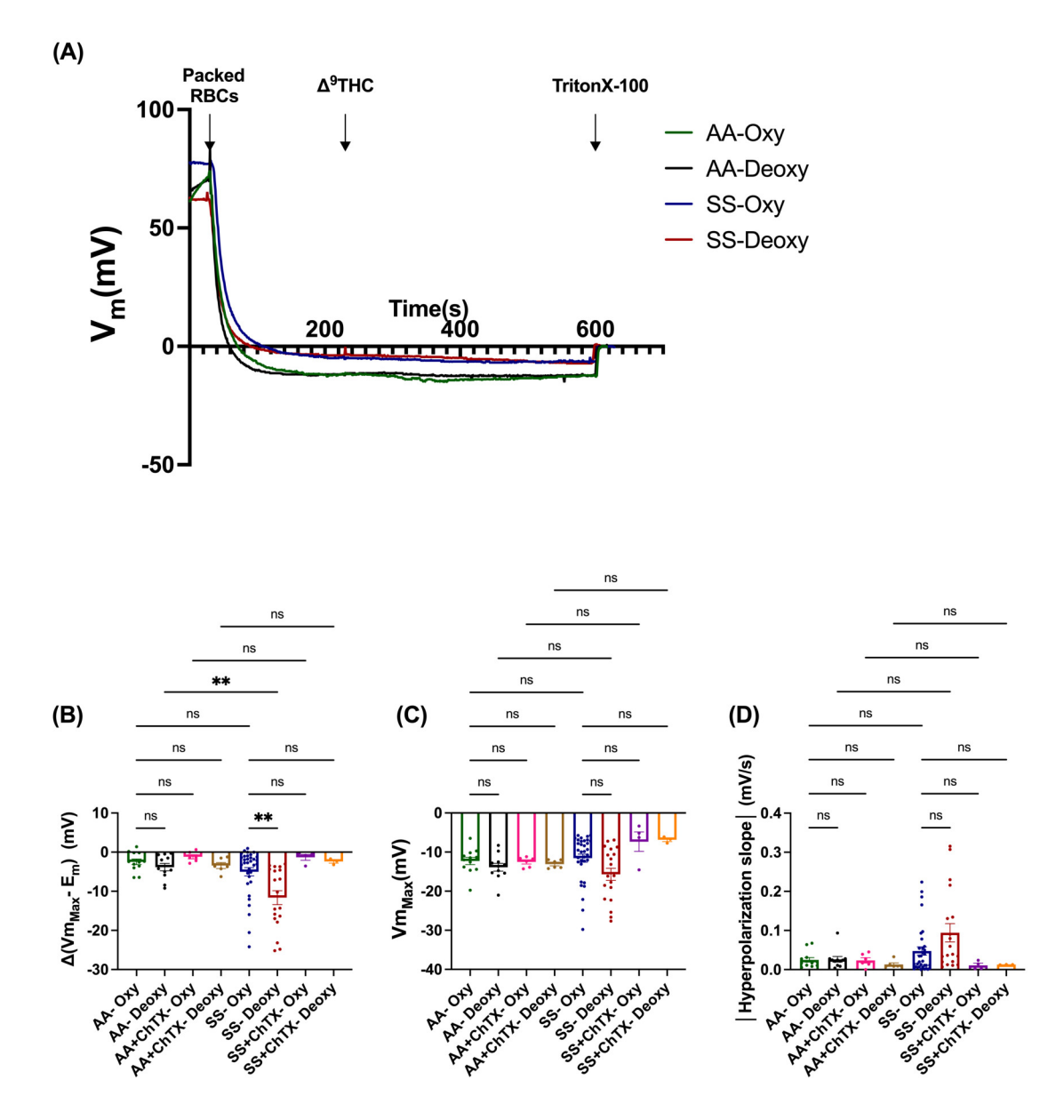


Fig. A.4: Membrane potential upon 30 μM Δ^9 -THC stimulation in AA and SS RBCs in different oxygen conditions. (A) Representative traces with 30 μM Δ^9 -THC in different oxygen conditions: AA RBCs in oxygenated condition (green), AA RBCs in deoxygenated condition (black), SS RBCs in oxygenated condition (blue), SS RBCs in deoxygenated condition (red). Arrows indicate when packed RBCs, Δ^9 -THC and TritonX-100 were added to the measuring system. (B) Hyperpolarization magnitudes ($\Delta(Vm_{Max}$ - $E_m)$ of RBCs from SS and AA with 30 μM Δ^9 -THC in different conditions. (C) Maximal hyperpolarization (Vm_{Max}) of RBCs from SS and AA with 30 μM Δ^9 -THC in different conditions. (D)Absolute value of hyperpolarization rate of RBCs from SS and AA with 30 μM Δ^9 -THC in different conditions. ($N_{AA-Oxy-donor}=12$, $N_{AA-Deoxy-donor}=11$, $N_{AA+ChTX-Oxy-donor}=6$, $N_{AA+ChTX-Deoxy-donor}=6$, $N_{SS-Oxy-donor}=33$, $N_{SS-Deoxy-donor}=19$, $N_{SS+ChTX-Oxy}=4$, $N_{SS+ChTX-Deoxy-donor}=3$.) Data is shown as means ± SEM in (B)-(D). Statistical differences were evaluated using one-way ANOVA test with Tukey's multiple comparison method. p < 0.05 was deemed significant.

Detected Signal from Pure RBCs in FLIM Image

As shown in Figure A.5 Aa, in customised 1-Photon (1PE) excitation fluorescence lifetime imaging microscope system (1PE FLIM system), clear RBC shapes could be detected at 470 nm wavelength, indicating originate in RBCs at 470 nm 1PE. However, no clear RBCs are seen in images with 532 nm wavelength 1PE (Fig. A.5 Ab). The representative decay curves show the RBCs with 532 nm excitation has more noise, indicating low photon counts under this imaging condition (Fig. A.5 Ac). The average intensity of the image with 532 nm wavelength excitation is significant lower than in the 470 nm excitation condition, while the amplitude-averaged lifetime of the RBCs under 532 nm wavelength excitation is significantly lower than the RBCs with 470 nm wavelength excitation as well (Fig. A.5 Ad, Ae).

FLIM images of unstained RBCs were obtained using a TauMap 2PE fluorescence lifetime imaging microscope (TauMap 2PE FLIM system) with excitation laser wavelength of 750 nm, 800 nm, 900 nm and 920 nm. As shown in Figure A.5 Ba, the representative decay curves in the FLIM images taken by TauMap 2PE FLIM system show similar lifetime decays. In the TauMap 2PE FLIM system, with increasing excitation wavelength, the average intensity of images decreases (Fig. A.5 Bb). The 920 nm excitation condition has the lowest average intensity, which is only 14% of the 750 nm excitation condition. In contrast, the amplitude averaged lifetime of the 750 nm condition is lower than the other conditions. The 920 nm condition has similar amplitude averaged lifetime to the 900 nm condition which is lower than the 800 nm condition (Fig. A.5 Bc).

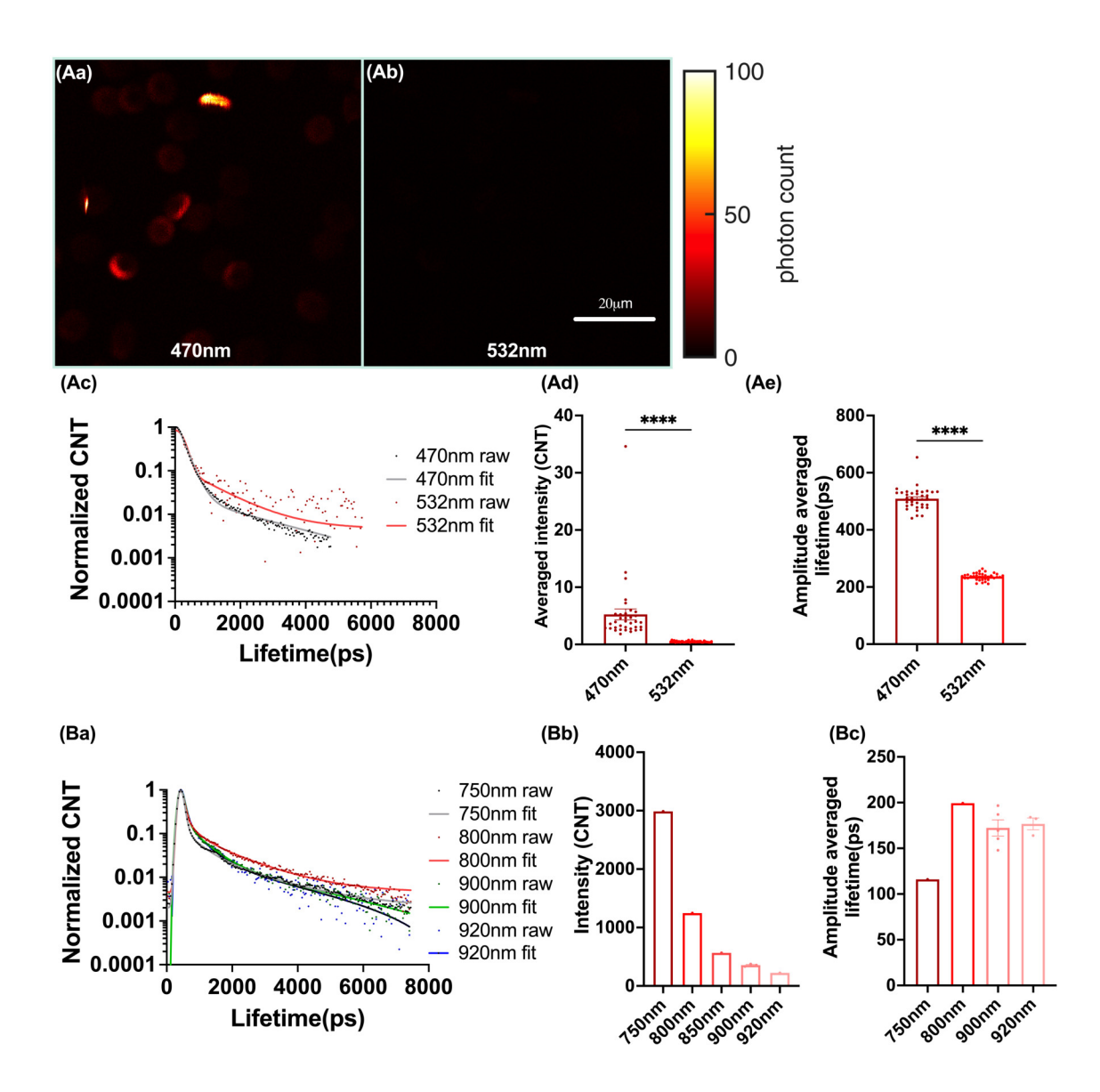


Fig. A.5: Overview of the signals from pure RBCs after laser excitation. (Aa)-(Ae) Data obtained with a customized 1-Photon (1PE) excitation fluorescence lifetime imaging microscope system (1PE FLIM system). (Ba)-(Bc) were obtained with the TauMap 2PE fluorescence lifetime imaging microscopy system (TauMap 2PE FLIM system). (Aa)-(Ab) Representative photon-count image of RBCs with (Aa) 470 nm 1PE and (Ab) 532 nm 1PE. Black represents lower photon counts and white represents higher photon counts. (Ac) Representative decay curves of RBCs with 470 nm 1PE (black) and 532 nm 1PE (red). The points displayed the measured data and the lines indicated the fitted regression, which are also applied to panel (Ba). (Ad) Average intensity and (Ae) Amplitude-averaged lifetime of RBCs with 470 nm 1PE and 532 nm 1PE. ($n_{470 \text{ nm}} = 2 n_{532 \text{ nm}} = 2$). (Ba) Representative decay curves of RBCs with 750nm 2PE (black), 800nm 2PE (red), 900nm 2PE (green) and 920nm 2PE (blue). (Bb) Average intensity and (Bc) Amplitude averaged lifetime of RBCs with 750nm 2PE, 800nm 2PE, 900nm 2PE and 920nm 2PE ($n_{750 \text{nm}} = 1$, $n_{800 \text{nm}} = 1$, $n_{900 \text{nm}} = 5$, $n_{920 \text{nm}} = 3$.) Data is shown as means \pm SEM in (Ad), (Ae), (Bb) and (Bc). Statistical differences were evaluated using one-way ANOVA with Tukey's multiple comparison method. p < 0.05 was deemed significant.

Influence of Excitation Laser wavelength on X-rhod-1 Lifetime in RBCs

With the 1PE FLIM system, the FLIM images are taken with two different excitation laser wavelengths, 470 nm and 532 nm. The lifetime decay curves of X-rhod-1 in RBCs in the two conditions are similar to each other (Fig. A.6 A). Unlike the 2PE system, the decay in the 1PE FLIM system only shows two components. The two lifetime components (τ_1 and τ_2) have no significant difference between the two laser wavelength excitation (Fig. A.6 B,C).

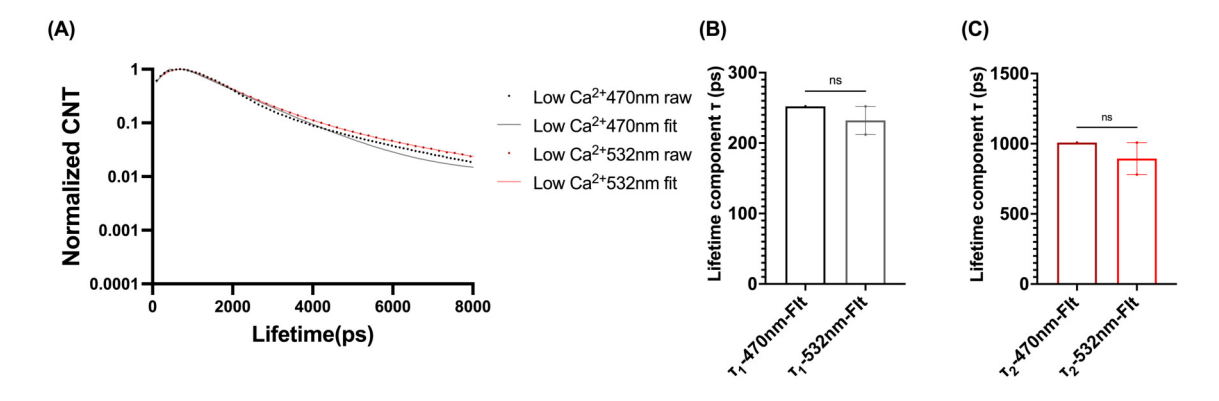


Fig. A.6: Effect of excitation laser wavelength time on lifetime and lifetime components. Data were obtained from FLIM images of X-rhod-1-stained RBCs taken with the 1PE FLIM system. (A) Representative decay curves of X-rhod-1 in RBCs with 470 nm 1PE (black) and 532 nm 1PE (red). (B)-(C) Statistical comparison of lifetime components of FLIM images with two different excitation laser wavelengths: (B) The shortest lifetime component (τ_1) ; (C) longest lifetime component (τ_2) (n=2). Data is shown as means \pm SEM in (B) and (C). Statistical differences were evaluated using one-way ANOVA with Tukey's multiple comparison method in (B). p < 0.05 was deemed significant.

The Reproducibility of the Lifetime Components of FLIM Images

As Figure A.7 Aa and Ba show, in 1PE FLIM system and TauMap 2PE FLIM system, the lifetime decay curves of X-rhod-1 in RBCs in the same condition are similar in different experiment days. The lifetime components show variations among different experiment days but there is no significant difference detected (Fig. A.7 Ab-Ad,Bb,Bc).

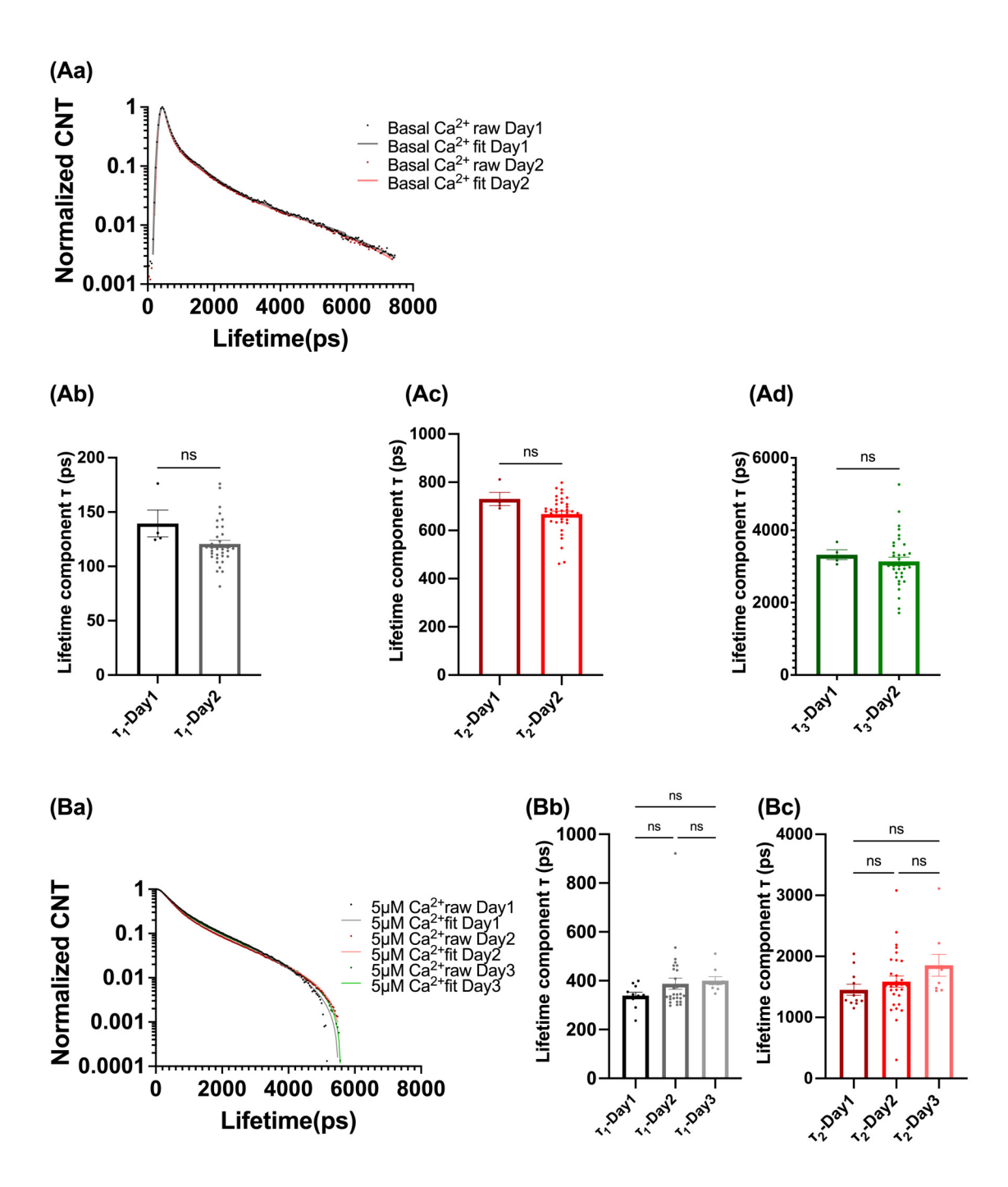


Fig. A.7: Parameters of FLIM images of X-rhod-1 loaded RBCs from the same donor on different days. (Aa)-(Ad) Data acquired using the TauMap 2PE FLIM system. ($n_{Day1}=4$, $n_{Day2}=35$). (Ba)-(Bc) Data acquired using the 1PE FLIM system. ($n_{Day1}=11$, $n_{Day2}=30$, $n_{Day3}=9$). (Aa) Representative decay curves of FLIM images from two different days (day 1-black, day 2-red). Dots displayed the measured data and lines indicated the fitted regression, which are also applied to panel Ba. (Ab)-(Ad) Statistical comparison of lifetime components of FLIM images taken on two different experimental days: (Ab) τ_1 , (Ac) τ_2 and (Ad) τ_3 . (Ba) Representative decay curves of FLIM images from three different days (day 1-black, day 2-red, day 3-green). (Bb)-(Bc) Statistical comparison of lifetime components of FLIM images taken on three different experimental days: (Bb) τ_1 and (Bc) τ_2 . Statistical differences were evaluated using one-way ANOVA with Tukey's multiple comparison method. p < 0.05 was deemed significant.

Pluronic-F127 Influence on X-rhod-1 Lifetime in RBCs

According to the chemical supplier's instructions, the X-rhod-1 AM dye must be dissolved in DMSO or 20% Pluronic-F127 in DMSO solution before use. To understand the influence of the solvent (20% Pluronic-F127 in DMSO) on the lifetime of X-rhod-1 in RBCs, the lifetime images of RBCs which were treated with Pluronic-F127 only were acquired using the TauMap 2PE FLIM system and the Leica 2PE FLIM system. The lifetime decay curves of Pluronic-F127 in RBCs were compared with the lifetime decay curves of RBCs alone and X-rhod-1 stained RBCs under the same acquisition conditions. In addition, the averaged intensity and amplitude-averaged lifetime were compared.

For the FLIM images taken with the TauMap 2PE FLIM system, the decay curves of Pluronic F-127 treated RBCs show similar decay curves to untreated RBCs (Fig. A.8 Aa). The decay of X-rhod-1 loaded RBCs is obviously different compared to Pluronic F127 treated RBCs and untreated RBCs (Fig. A.8 Aa). Surprisingly, FLIM images of Pluronic F-127 treated RBCs show similar average intensity and only half of the amplitude-averaged lifetime as FLIM images of untreated RBCs. However, neither the averaged intensity nor the amplitude averaged lifetime shows significant differences (Fig. A.8 Ab,Ac). As expected, the FLIM images of X-rhod-1 loaded RBCs show significantly higher amplitude averaged lifetime and averaged intensity than the other two conditions (Fig. A.8 Ab,Ac). Similarly, the FLIM images acquired using the Leica system show that the lifetime decay of Pluronic F-127 treated RBCs is slightly slower compared to untreated RBCs under the same acquisition conditions (Fig. A.8 Ba). Pluronic F-127 treated RBCs show significantly lower average intensity compared to Untreated RBCs under using 800nm 2PE (Fig. A.8 Bb). In summary, the Pluronic F-127 is not florescent and do not contribute to the lifetime decay of X-rhod-1 in RBCs.

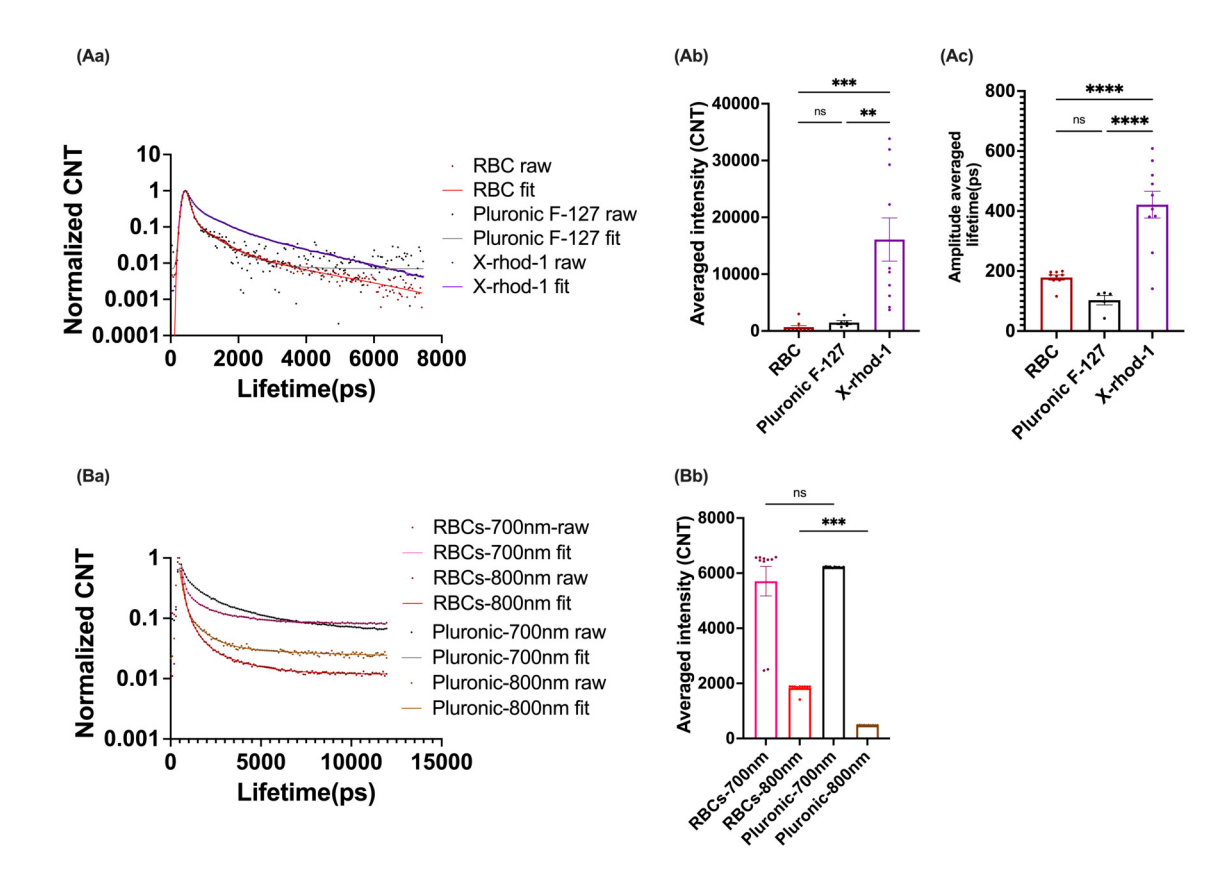


Fig. A.8: Comparison of FLIM parameters among RBCs, Pluronic-127 treated RBCs and X-rhod-1 stained RBCs. (Aa)-(Ac) Data acquired using the TauMap 2PE FLIM system with 900nm laser wavelength (n_{RBCs}=11, n_{Pluronic}=4, n_{X-rhod-1}=29). (Ba) and (Bb) Data acquired by Leica 2PE FLIM system (n=10). (Aa) Representative decay curves of FLIM images of RBCs (red), Pluronic-127 treated RBCs (black) and X-rhod-1 stained RBCs (purple). The dots displayed the measured data and the lines indicated the fitted regression, which are also applied to panel Ba. (Ab) –(Ac) Statistical comparison of FLIM images of RBCs, Pluronic-127 treated RBCs and X-rhod-1 stained RBCs: (Ab) Averaged intensity, (Ac) Amplitude-averaged lifetime. (Ba) Representative decay curves of FLIM images of RBCs with 700 nm 2PE (pink), RBCs with 800 nm 2PE (red), Pluronic-127 treated RBCs with 700 nm 2PE (black) and Pluronic-127 treated RBCs with 800 nm 2PE (brown). (Bb) Statistical comparison of the averaged intensity of FLIM images of RBCs and Pluronic-127 treated RBCs. Data is shown as means ± SEM in (Ab), (Ac) and (Bb). Statistical differences were evaluated using one-way ANOVA with Tukey's multiple comparison method in (B). p < 0.05 was deemed significant.

Ca²⁺-ionophore Selection

The FLIM images of Ionomycin treated and Bromo-A23187 treated X-rhod-1 stained RBCs were taken via TauMap 2PE FLIM system and 1PE FLIM system. The lifetime decay curves of Ionomycin treated RBCs are not significantly different to that of Bromo-A23187 treated RBCs (Fig. 3.26 Aa,Ba). The average intensity, and amplitude-averaged lifetime are not significantly different between Ionomycin-treated RBCs and Bromo-A23187-treated RBCs (Fig. 3.26 Ab,Ac,Bb,Bc). In addition, the lifetime components show no statistical difference between Ionomycin-treated RBCs and Bromo-A23187 treated RBCs (Fig. 3.26 Ad,Bd).

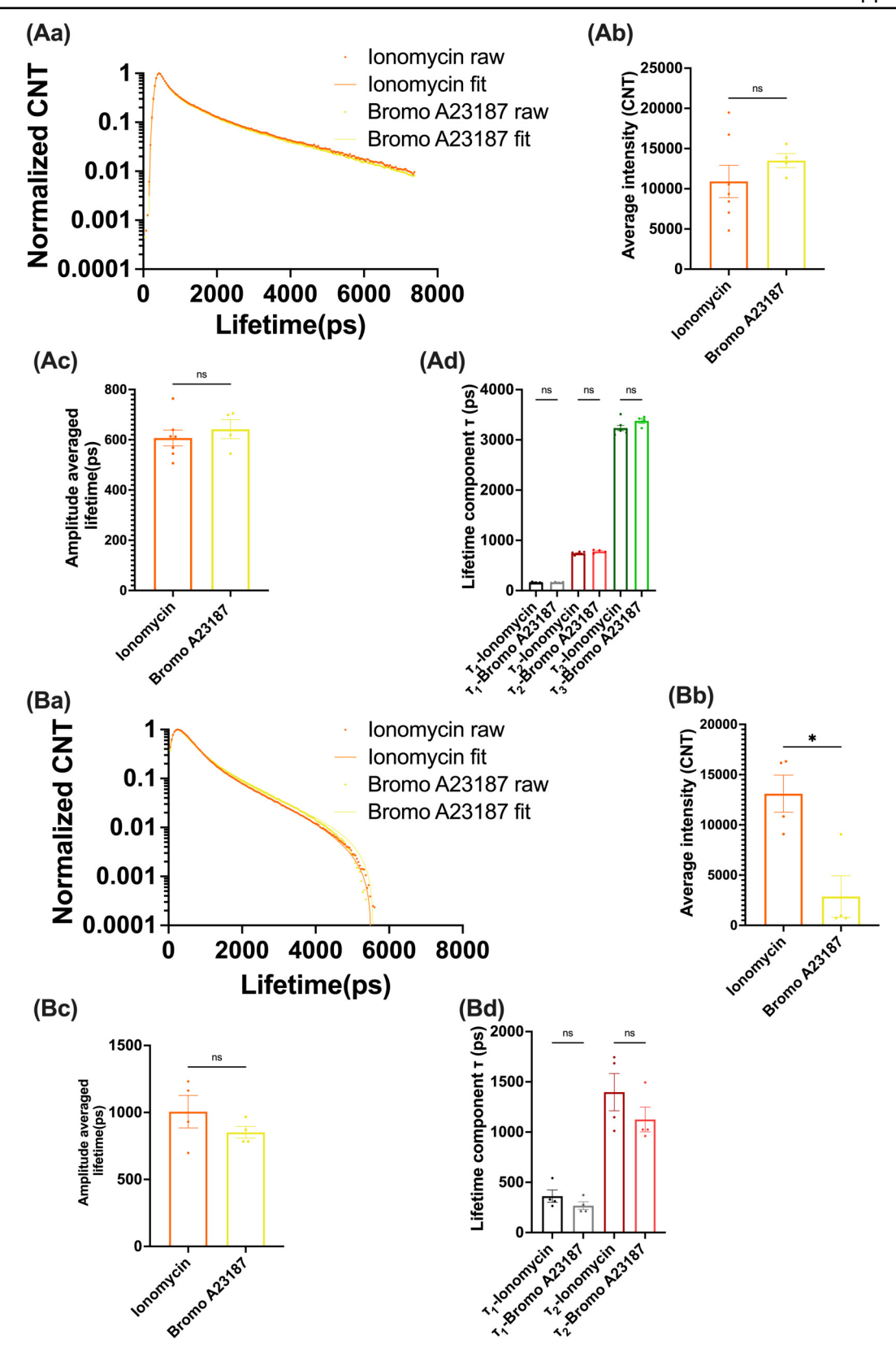


Fig. A.9: Influence of ionophores on the parameters of FLIM images. (Aa)-(Ad) Data acquired by TauMap 2PE FLIM system ($n_{Ionomycin}=25$, $n_{BromoA23187}=12$). (Ba)-(Bd) Data acquired by 1PE FLIM system ($n_{Ionomycin}=4$, $n_{BromoA23187}=4$). (Aa) Representative decay curves of FLIM images of X-rhod-1 loaded RBCs with Ionomycin (orange) and Bromo-A23187 (yellow). The dots displayed the measured data and the lines indicated the fitted regression, which is also applied to (Ba). (Ab)-(Ad) Statistical comparison of FLIM images between Ionomycin-treated and Bromo-A23187-treated RBCs with X-rhod-1: (Ab) Average intensity; (Ac) Amplitude averaged lifetime. (Ad) Lifetime components τ_1 , τ_2

Fig. A.9 (previous page): and τ_3 . (Ba) Representative decay curves of FLIM images of X-rhod-1 loaded RBCs with Ionomycin (orange) and Bromo-A23187 (yellow). (Bb)-(Bd) Statistical comparison of FLIM images between Ionomycin-stimulated RBCs and Bromo-A23187-stimulated RBCs with X-rhod-1. (Bb) Average intensity; (Bc) Amplitude averaged lifetime; (Bd) Lifetime components τ_1 and τ_2 . Data is shown as means \pm SEM in (Ab) - (Ad) and (Bb) - (Bd). Statistical differences were evaluated using unpaired T-test. p < 0.05 was deemed significant.

The Influence of Cell-tak on the X-rhod-1 Fluorescence Lifetime in RBCs

For FLIM images, the time between focus finding and image acquisition was usually a few minutes. During this time, free sedimented RBCs could influence the best focus finding, which could lead to blurred images in the last few images of a long-term recording. In addition, the free sedimented RBCs could fall on top of other RBCs and affected the single cell analysis. To solve the problems, cell-tak, a type of biological glue, was used to fix the position of RBCs on the imaging slides or dishes. To determine whether cell-tak could influence the lifetime of X-rhod-1 in RBCs, the parameters of FLIM images of X-rhod-1 in RBCs with and without fixation by cell-tak via the 1PE FLIM system was compared. As shown in Figure A.10 A, the lifetime decay curves of free sedimented X-rhod-1 stained RBCs and position-fixed RBCs show a slightly difference. However, the amplitude-average lifetime and both two lifetime components show no significant difference between free sedimented RBCs and position fixed RBCs (Fig. A.10 B,C). In summary, cell tak does not affect the lifetime of X-rhod-1 stained RBCs.

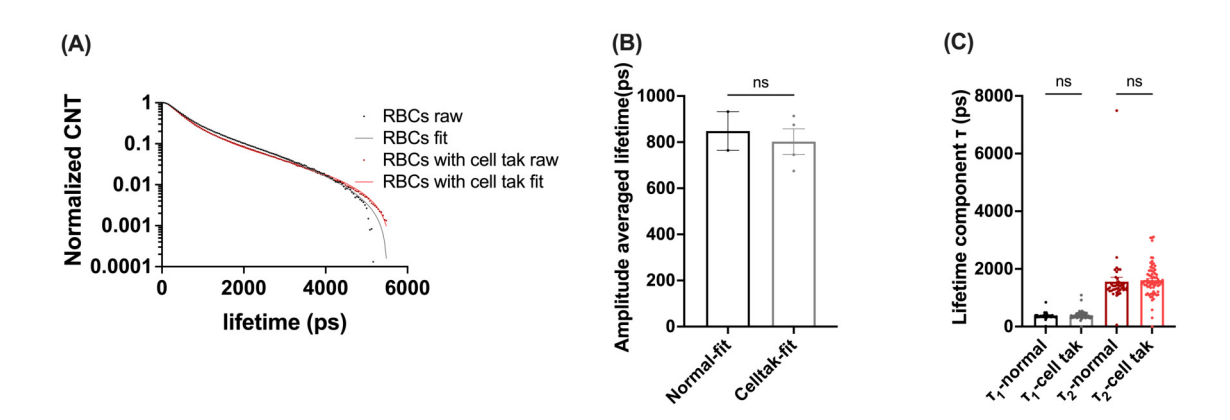


Fig. A.10: Comparison of FLIM parameters of X-rhod-1 with and without cell-tak. Data obtained by the 1PE FLIM system. (A) Representative decay curves of FLIM images of RBCs with and without cell-tak in the environment. (without cell-tak: black, with cell-tak: red). The dots displayed the measured data and the lines indicated the fitted regression. (B) Comparison of the amplitude-averaged lifetime between FLIM images of X-rhod-1-loaded RBCs with or without cell-tak in the environment. ($N_{normal}=2, N_{cell-tak}=5.$) (C) Comparison of the lifetime components τ_1 and τ_2 between FLIM images of X-rhod-1-loaded RBCs with and without cell-tak in the environment ($n_{normal}=43, n_{cell-tak}=77$). Data is shown as means \pm SEM in (B) and (C). Statistical differences were evaluated using one-way ANOVA with Tukey's multiple comparison method. p < 0.05 was deemed significant.

Influence of Ca²⁺ pumps on X-rhod-1 Lifetime in RBCs

The time series of FLIM images of X-rhod-1 loaded RBCs were taken using the 1PE FLIM system. The amplitude-averaged lifetime of RBCs in PBS solution is stable over time (Fig. A.11 A). The amplitude-averaged lifetime of RBCs with $5\,\mu\text{M}$ and $30\,\mu\text{M}$ Ca²⁺ decrease over time (Fig. A.11 A). In addition, similar to the amplitude-averaged lifetime, the amplitude ratio and lifetime-weighted amplitude ratio of RBCs with $5\,\mu\text{M}$ or $30\,\mu\text{M}$ Ca²⁺ show a decrease over time but that of basal Ca²⁺ is stable (Fig. A.11 B,C).

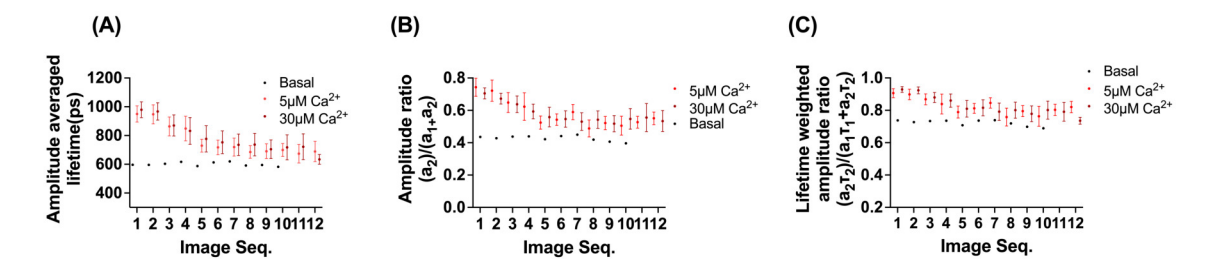


Fig. A.11: Influence of time after ionophore challenge on FLIM parameters. Data acquired with the 1PE FLIM system. (A) Amplitude-averaged lifetime, (B) Amplitude ratio and (C) Lifetime-weighted amplitude-ratio of 12-time-series FLIM images of X-rhod-1 in RBCs with basal Ca^{2+} (black) or after application of Bromo-A23187 with additional Ca^{2+} in the environment (5 μM Ca^{2+} -light red, 30 μM Ca^{2+} -dark red). ($N_{basal-Ca}=1$, $N_{5\,uM-Ca}=6$, $N_{30\,uM-Ca}=4$.) Data is shown as means ± SEM.

Theoretical Relation between Intracellular Ca^{2+} Concentration and FLIM Parameters of X-rhod-1 in RBCs

With the 1PE FLIM system, FLIM images of the RBCs with 8 different theoretical intracellular Ca²⁺ concentration from three independent experiments were acquired and analyzed (Fig. A.12).

As shown in Figure A.12 A, the shortest FLIM lifetime of RBCs increases with increasing theoretical intracellular Ca^{2+} . The amplitude-averaged lifetime, amplitude ratio and lifetime-weighted amplitude ratio show dependence on intracellular Ca^{2+} concentration (Fig. A.12 A-C). However, there is a huge variation within groups and the plateau is reached around $40\,\mu\mathrm{M}$ (Fig. A.12 A-C).

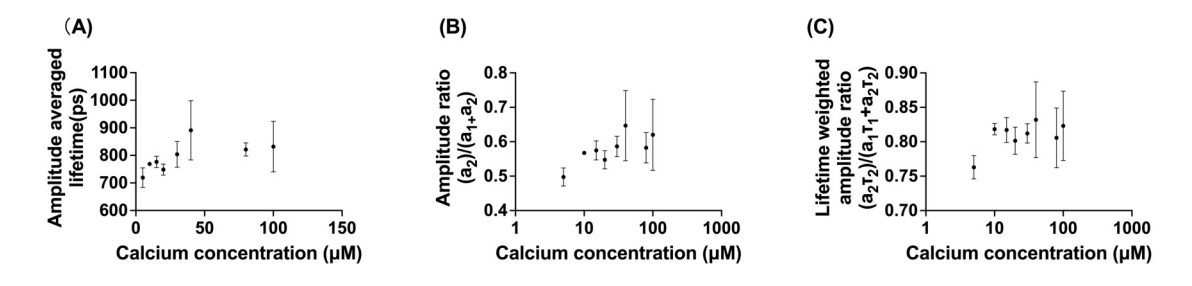


Fig. A.12: Regression of intracellular Regression of intracellular Ca^{2+} concentration and FLIM parameters concentration and FLIM parameters. (A)-(C) FLIM parameters of X-rhod-1 loaded RBCs over 8 defined intracellular Ca^{2+} concentrations: (A) Amplitude-averaged lifetime; (B) Amplitude ratio; (C) Lifetime-weighted amplitude ratio. Data acquired using the 1PE FLIM system (N=1). Data is shown as means \pm SEM.

A.3 Information of Used Chemicals

Name	Information	Cat. No.
Anti-spectrin antibody	Monoclonal Anti-Spectrin (α and β) antibody produced in mouse (1:3000): ThermoFisher, Waltham, MA, USA	S3396
Anti-TRPV2 antibody	Anti-Human TRPV2 (VRL1) (extracellular) Antibody (1:500): Alomone, Jerusalem, Israel	ACC-139
	Anti-VRL1/TRPV2 Antibody Picoband TM (1:1000): Bosterbio, Pleasanton, CA, USA	A02786-3
ATPlite luminescence ATP detection assay system (300 assay kit)	PerkinElmer, Shelton, CT, USA	6016943
Benzonase [®] β-mercaptoethanol	Sigma-Aldrich, St. Louis, MO, USA	M7154
Bromo-A23187	Cayman, Ann Arbor, Mi, USA	Cay20438-5
Bovine serum albumin (BSA)	Sigma-Aldrich, St. Louis, MO, USA	A4503/A7030
$CaCl_2 \cdot 2H_2O$	VWR, Radnor, PA, USA	22317.297
Carbonyl cyanide m-chlorophenyl hydrazine (CCCP) ionophore	Sigma-Aldrich, St. Louis, MO, USA	215911
Cell tak	Corning, Corning, NY, USA	354240
Charybdotoxin	Alomone Labs, Jerusalem, Israel	
DMSO	Carl-Roth- GmbH, Karlsruhe, Germany	67-68-5
DMSO	Sigma-Aldrich, St. Louis, MO, USA	D8418
Ethylenediaminetetra- aceticacid (EDTA) 0.5M pH 8.0	Invitrogen, Waltham, MA, USA	15575
EDTA · 2Na	Sigma-Aldrich, St. Louis, MO, USA	E5134
Ethyleneglycoltetraaceticacid (EGTA)	Sigma-Aldrich, St. Louis, MO, USA	03777
Fluo-4, AM	Molecular Probes, Eugene, OR, USA	F14201
Fura-2, AM	Invitrogen, Waltham, MA, USA	M1292
Fura-red, AM	Invitrogen, Waltham, MA, USA	F3021
Glucose	Sigma-Aldrich, St. Louis, MO, USA	G5146
Glycerol	Sigma-Aldrich, St. Louis, MO, USA	G6279
Glycine	MerckMillipore, Burlington, MA, USA	1.00590
HCl (37%)	Merck, Darmstadt, Germany	1.00317
	Bernd Kraft, Oberhausen, Germany	05430.4700
HEPES	Carl-Roth-GmbH, Karlsruhe, Germany	9105.4

	Polyclonal Goat Anti-Rabbit Immunoglobu-	
HRP conjugated	lins/HRP (affinity isolated) (1:3000): Dako,	P0448
antibody	Santa Clara, CA, USA)	
	Polyclonal Goat Anti-Mouse Immunoglobu-	
	lins/HRP (affinity isolated) (1:4000): Dako,	P0447
	Santa Clara, CA, USA)	10111
	Stemcells, Vancouver, British Columbia,	
Ionomycin	Canada	73724
KCl	Carl-Roth- GmbH, Karlsruhe, Germany	6781.1
$MgCl_2 \cdot 6H_2O$	Sigma-Aldrich, St. Louis, MO, USA	M-2670
MgCl2 0H2O		
Na ₂ HPO ₄	Grüssing, Filsum, Germany	12147
- 1	Merck, Darmstadt, Germany	1.06580
NaCl	VWR, Radnor, PA, USA	27810.295
	Merck, Darmstadt, Germany	1.06404
NaF	Sigma-Aldrich, St. Louis, MO, USA	S7920
1101	Merck, Darmstadt, Germany	1.06449
NaH ₂ PO ₄	Fisher Scientific, Nidderau, Germany	389870005
Na1121 O4	Merck, Darmstadt, Germany	1.06346
NaHCO ₃	Grüssing, Filsum, Germany	12143
NaN ₃	Sigma-Aldrich, St. Louis, MO, USA	S2002
NaOH	Grüssing, Filsum, Germany	12155
Nonidet TM P 40	0, , ,	
	Sigma-Aldrich, St. Louis, MO, USA	74385
Substitute (NP-40) NS309	Ciarra Aldriah Ct I arria MO IICA	N8161
	Sigma-Aldrich, St. Louis, MO, USA	
NS3623	Sigma-Aldrich, St. Louis, MO, USA	SML2843
Ocadaic acid (OA)	Sigma-Aldrich, St. Louis, MO, USA	459620
Oregon Green 488 BAPTA-1, AM	Molecular Probes, Eugene, Oregon, USA	O-6807
Orthevanadate (OV)	Bioke, Leiden, The Netherlands	NEB P0758L
PageRuler TM Plus		
Prestained Protein		20010
Ladder (10 to 250	ThermoFisher, Waltham, MA, USA	26619
kDa)		
Phenylmethylsulfonyl-	Sigma-Aldrich, St. Louis, MO, USA	PMSF-RO
fluride (PMSF)	Roche, Mannheim, Germany	10837091001
Pluronic F127, 20%	Toolie, Maninelli, Germany	10001031001
solution in	ThermoFisher, Waltham, MA, USA	P3000MP
Protease Inhibitor		
Cocktail Set V,	Sigma-Aldrich, St. Louis, MO, USA	539137
EDTA-Free		
Sodium dodecyl	Cirros Aldrich Ct I MO IICA	05020
sulfate (SDS)	Sigma-Aldrich, St. Louis, MO, USA	05030
Tram34	Tocris Bioscience, Bristol, UK	2946
Tris base	Merck, Darmstadt, Germany	10708976001

TWEEN® 20	Sigma-Aldrich, St. Louis, MO, USA	P7949
X-rhod-1, AM	Molecular Probes, Eugene, OR, USA	X14210
Yoda1	Sigma Aldrich, Saint Louis, MO, USA	SML1558
Δ^9 -Tetrahydro- cannabinol (Δ^9 -THC) -ethanol solution	Sigma Aldrich, Saint Louis, MO, USA	T-005
Δ^9 - Tetrahydrocannabinol (Δ^9 -THC) -methanol solution	LGC GmbH, Wiesel, Germany	LGCAMO- 1088.00-05

144 Appendix

A.4 Information of Used Solutions

Name of solutions	Composition
0.1 M phosphate buffer	$0.1\mathrm{M}$ Na ₂ HPO ₄ , use $0.1\mathrm{M}$ NaH ₂ PO ₄ adjust pH to 7.2
1 M Tris-HCl	1 M Tris base, adjust pH to 8.0 by HCl
1. Dheamhata huffanad	Thermo Fisher, Waltham, MA, USA
1× Phosphate-buffered	Fresenius-kabi, St. Wendel, Germany
saline (PBS)	Orphi Farma B.V. Dordrecht, Netherlands
5 mM phosphate buffer	1:20 dilution of 0.1 M phosphate buffer with MilliQ water
Canin buffer	20 mM Tris-HCl, 137 mM NaCl, 10 mM EDTA, 100 mM
Carin buffer	NaF, 10% Glycerol, 1% NP-40
Cell Tak coating solution	95 mM NaHCO ₃ , 16.7 mM NaOH, 3.3% CellTak
ECL Western Blotting	Thomas Figher Welthern MA IICA
Substrate	ThermoFisher, Waltham, MA, USA
Cluege from Tyrodo	130 mM NaCl, 5 mM KCl, 10 mM HEPES, 1 mM MgCl ₂ ,
Glucose-free Tyrode solution	1.5 mM CaCl ₂ , pH 7.39, osmolarity between 280 mOsm to
Solution	$300\mathrm{mOsm}$
High osmolarity PBS	Use 5 M NaCl adjust osmolarity of 1× PBS to 800 mOsm
ISE standard Ca	Mottler Tolodo CmbH Croifenges Switzerland
$10\mathrm{mg/L}$	Mettler-Toledo GmbH, Greifensee, Switzerland
ISE standard Ca	Mottler Tolodo CmbH Croifenges Switzerland
$100\mathrm{mg/L}$	Mettler-Toledo GmbH, Greifensee, Switzerland
ISE standard Ca	Mottler Telede Crobil Cheifengee Creitzenland
$1000\mathrm{mg/L}$	Mettler-Toledo GmbH, Greifensee, Switzerland
Label buffer	2% BSA, 0.05% NaN ₃ in $1\times$ PBS
Low osmolarity PBS	1× PBS 2:5 dilution with MilliQ water
Lysis buffer for MBE	6% Triton-X 100 in 3 M NaCl
Lysis buffer for other	Carin buffer, proteolysis inhibitor (1:100), PMSF (1:100),
cells	OV (1:100), OA (1:1000), benzonase (1:1000)
Lysis buffer for RBCs	5 mM phosphate buffer, proteolysis inhibitor (1:100), PMSF
ghost harvest	(1:100), OV (1:100), OA (1:1000)
perfectION calcium ISA	Mettler-Toledo GmbH, Greifensee, Switzerland
perfectION ion	Mottley Tolede Crobil Cheifengee Creitzenland
electrolyte A	Mettler-Toledo GmbH, Greifensee, Switzerland
Protein Assay Reagent A	BIO-RAD, Hercules, CA, USA
Protein Assay Reagent B	BIO-RAD, Hercules, CA, USA
Protein Assay Reagent S	BIO-RAD, Hercules, CA, USA
Ringer solution	153 mM NaCl, 2 mM KCl
Ringer solution with	153 mM NaCl, 2 mM KCl, 4 mM CaCl ₂ Saline 0.9% NaCl
Ca^{2+}	in H ₂ O (w/w)
SDS running buffer	200 mM glycine, 25 mM Tris base and 0.1% SDS
	130 mM NaCl, 5 mM KCl, 5 mM glucose, 10 mM HEPES,
Standard Tyrode	1 mM MgCl ₂ and 1.5 mM CaCl ₂ , pH 7.39, osmolarity be-
solution	tween 280 mOsm to 300 mOsm

Tris-Buffered Saline with	150 mM NaCl, 10 mM Tris, 0.1% Tween-20 and HCl. 5%
Tween-20 (TBST)	BSA
Tyrode solution with $1 \mu\mathrm{M}$ free Ca^{2+}	112 mM NaCl, 5 mM KCl, 10 mM HEPES, 1 mM MgCl ₂ ,
	$9.32\mathrm{mM}$ CaCl ₂ and $10\mathrm{mM}$ EGTA, pH 7.39, osmolarity
	between 280 mOsm to 300 mOsm
Tyrode solution with 10 μM free Ca ²⁺	$112\mathrm{mM}$ NaCl, $5\mathrm{mM}$ KCl, $10\mathrm{mM}$ HEPES, $1\mathrm{mM}$ MgCl ₂ ,
	$9.94\mathrm{mM}$ CaCl ₂ and $10\mathrm{mM}$ EGTA, pH 7.39, osmolarity
	between 280 mOsm to 300 mOsm
Tyrode solution with $100\mu\mathrm{M}$ free Ca^{2+}	$112\mathrm{mM}$ NaCl, $5\mathrm{mM}$ KCl, $10\mathrm{mM}$ HEPES, $1\mathrm{mM}$ MgCl ₂ ,
	$10.093\mathrm{mM}$ CaCl ₂ and $10\mathrm{mM}$ EGTA, pH 7.39, osmolarity
	between 280 mOsm to 300 mOsm
Tyrode solution with 1 mM free Ca ²⁺	$112\mathrm{mM}$ NaCl, $5\mathrm{mM}$ KCl, $10\mathrm{mM}$ HEPES, $1\mathrm{mM}$ MgCl ₂ ,
	$10.999\mathrm{mM}$ CaCl ₂ and $10\mathrm{mM}$ EGTA, pH 7.39, osmolarity
	between 280 mOsm to 300 mOsm
Tyrode solution with $350\mu\mathrm{M}$ free Ca^{2+}	112 mM NaCl, 5 mM KCl, 10 mM HEPES, 1 mM MgCl ₂ ,
	$10.348\mathrm{mM}$ CaCl ₂ and $10\mathrm{mM}$ EGTA, pH 7.39, osmolarity
	between 280 mOsm to 300 mOsm

A.5 Information of Used Equipment

c Name of Equipment	Information
μ-Dishes	ibidi, Munich, Germany
5 ml round bottom	Corning Inc., Corning, NY, USA
polystyrene test tubes	Corning Inc., Corning, NT, USA
BD FACS Diva TM Soft-	Becton Dickinson, San Jose, CA, USA
ware	Decton Dickinson, San Jose, CA, USA
BioTek's Gen5 PC	BioTek Instruments, Inc, Winooski, Vermont, U.S
Ca-buf software	Guy Droogmans, KU Leuven, Belgium
ChemiDoc MP	BIO-RAD, Hercules, CA, USA
Criterion Cell	BIO-RAD, Hercules, CA, USA
Criterion TGX Precast Midi Protein 18-well Gel	BIO-RAD, Hercules, CA, USA
Criterion TGX Precast Midi Protein 26-well Gel	BIO-RAD, Hercules, CA, USA
Eclipse Ti Fluorescence Microscope	Nikon, Tokyo, Japan
EDTA tube	EDTA K Monovette: SARSTEDT, Nümbrecht, Germany EDTA tube: BD Switzerland Sarl, Vaud. Switzerland
Excel	Microsoft, Redmond, Washington, U.S
Fiji	ImageJ
	BD FACSCantoTM II: BD Biosciences, Erembodegem, Bel-
Flow cytometers	gium
	BD LSRFortessa: Becton Dickinson, San Jose, CA, USA
	Axiovert 200M Fluorescence DIC Phase Contrast Inverted
	Microscope: Carl Zeiss Microscopy Deutschland GmbH,
	Oberkochen, Germany
	FemtoFiber pro TVIS laser: TOPTICA Photonics AG, Mu-
Fluorescence Lifetime	nich, Germany
Imaging Microscope-	PicoHarp 300 TCSPC system: PicoQuant, Berlin, Germany
customized fluorescence	Picosecond delayer: Micro Photon devices, Bolzano, Italy
lifetime image micro-	Nanosecond delay box NS-DELAY 7800-7: FAST ComTech,
scope	Oberhaching, Germany
	LCI Plan-NEOFLUAR 63× DIC objective: Carl Zeiss Mi-
	croscopy Deutschland GmbH, Oberkochen, Germany
	Photon counting module SPCM AQR-14: PerkinElmer Op-
	toelectronics, Rodgau, Germany

Fluorescence Lifetime Imaging Microscopy- TauMap	Fluorescence lifetime imaging microscopy TauMap: JenLab GmbH, Berlin, Germany High-NA objective (Zeiss neonplanar 1.3 NA, 40×): Carl Zeiss Microscopy Deutschland GmbH, Oberkochen, Germany Time correlated single photon counting (TCSPC) card SPC-150: Becker&Hickl, Berlin, Germany PMT detector (PMH-100-0): Becker&Hickl, Berlin, Germany Tuneable titanium sapphire laser MaiTAi XF-1: Newport
	Spectra Physics, Darmstadt, Germany
GraphPad Prism version	GraphPad Software,
10	San Diego, California USA
Heparin tube	Lithium-Heparin Monovette: SARSTEDT, Nümbrecht, Germany Na-Heparin tube: BD Switzerland Sarl, Vaud. Switzerland
iBlot [™] 2 Gel Transfer Device	ThermoFisher, Waltham, MA, USA
iBlot [™] 2 Transfer Stacks	ThermoFisher, Waltham, MA, USA
Ion/pH meter and electrode	SevenCompact pH meter S220 coupled with perfectION comb CA, Combined Ion-selective electrode: Mettler-Toledo GmbH, Greifensee, Switzerland
Leica Fluorescence Lifetime Imaging Microscope	Upright TCS SP8 TPE DIVE microscope with FALCON (FAst Lifetime CONtrast): Leica Mikrosysteme Vertrieb GmbH, Wetzlar, Germany HC PL IRAPO 25× dipping objective: Leica Mikrosysteme Vertrieb GmbH, Wetzlar, Germany Leica Application Suite LAS x FLIM/FCS (v. 3.5.6): Leica Mikrosysteme Vertrieb GmbH, Wetzlar, Germany
Matlab [®] 2022	The MathWorks, Inc, Portola Valley, CA, USA
NanoDrop TM 2000/2000c Spectrophotometers	ThermoFisher, Waltham, MA, USA
NanoDrop 2000 software	ThermoFisher, Waltham, MA, USA
ORCA-Flash4.0 4.2MP Monochrome sCMOS	Hamamatsu Photonics, Hamamatsu City, Japan
Osmometer	Automaticsemi-micro osmometer A0300: KNAUER, Berlin, Germany Gonotec® Osmomat 3000 Basic: Ganotec Inc, Montréal, Canada

pH meter and electrodes for MBE method	SevenCompact pH meter S210 coupled with InLab Solids Pro-ISM pH electrode: Mettler-Toledo GmbH, Greifensee, Switzerland PHM210 pH-meter coupled with a G200 pH electrode and a red Rod 200 reference electrode: Radiometer, Copenhagen, Denmark
pH meter and electrodes for pH measurement	SevenEasy SevenEasy S20 pH Meter coupled with InLab Expert Pro pH electrode: Mettler-Toledo GmbH, Greifensee, Switzerland
pH meter recording software	Logger Lite: Vernier; Millikan Way, Beaverton, OR France Internal program from group
Plan Apo TIRF 100× oil objective	Nikon, Tokyo, Japan
Plan Apo TIRF 40× oil objective	Nikon, Tokyo, Japan
Plan Apo TIRF 60× oil objective	Nikon, Tokyo, Japan
$\begin{array}{ c c c } \hline PowerPac^{^{TM}} HC \\ \hline 100 \ \ 120 \ \ \ \ \ \ \ \ \ \ \ \ \ \ \ \ \ \ \$	BIO-RAD, Hercules, CA, USA
Synergy TM 2 Spectrophotometer	BioTek Instruments, Inc, Winooski, Vermont, U.S
Spinning disk confocal microscope	Yokogawa, Tokyo, Japan
Thermomixer	Thermomixer comfort: Eppendorf, Hamburg, Germany ThermoMixer C: Eppendorf, Hamburg, Germany

List of Publications

Min Qiao - ORCiD-ID: 0000-0002-2734-6824

- 1. Julia Jansen, **Min Qiao**, Laura Hertz, Xijia Wang, Elisa Fermo, Anna Zaninoni, Raffaella Colombatti, Ingolf Bernhardt, Paola Bianchi, and Lars Kaestner, "Mechanistic ion channel interactions in red cells of patients with Gárdos channelopathy", Blood Advances 5(17): 3303–3308, (2021)
 - https://doi.org/10.1182/bloodadvances.2020003823
- 2. Prause, Michala, Signe Schultz Pedersen, Violeta Tsonkova, **Min Qiao**, and Nils Billestrup. "Butyrate Protects Pancreatic Beta Cells from Cytokine-Induced Dysfunction" *International Journal of Molecular Sciences* 22(19):10427. (2021) https://doi.org/10.3390/ijms221910427
- 3. Daniel Flormann, Min Qiao, Nicoletta Murciano, Giulia Iacono, Alexis Darras, Sebastian Hof, Steffen M. Recktenwald, Maria Giustina Rotordam, Nadine Becker, Jürgen Geisel, Christian Wagner, Marieke von Lindern, Emile van den Akker, and Lars Kaestner "Transient receptor potential channel vanilloid type 2 in red cells of cannabis consumer", American Journal of Hematology 97: E180-E183, (2022) https://doi.org/10.1002/ajh.26509
- 4. Aline Hatem, Sofia Esperti, Nicoletta Murciano, **Min Qiao**, Maria Giustina Rotordam, Nadine Becker, Elie Nader, Felix Maurer, Laurent Pérès, Guillaume Bouyer, Lars Kaestner, Philippe Connes, and Stéphane Egée "Adverse effects of delta-9-tetrahydrocannabinol on sickle red blood cells", *American Journal of Hematology* 98: E383-E386, (2023)
 - https://doi.org/10.1002/ajh.26509
- 5. Myrthe J. van Dijk, Brigitte A. van Oirschot, Alexander N. Harrison, Steffen M. Recktenwald, **Min Qiao**, Amaury Stommen, Anne-Sophie Cloos, Juliette Vanderroost, Romano Terrasi, Kuntal Dey, Jennifer Bos, Minke A. E. Rab, Anna Bogdanova, Giampaolo Minetti, Giulio G. Muccioli, Donatienne Tyteca, Stéphane Egée, Lars Kaestner, Robert S. Molday, Eduard J. van Beers, Richard van Wijk "A novel missense variant in ATP11C is associated with reduced red blood cell phosphatidylserine flippase activity and mild hereditary hemolytic anemia", *American Journal of Hematology* 98(12): 1877-1887, (2023)
 - https://doi.org/10.1002/ajh.27088
- 6. Polina Petkova-Kirova, Nicoletta Murciano, Julia Jansen, Greta Simionato, Giulia Iacono, Maria Giustina Rotordam, Thomas John, Min Qiao, Laura Hertz, Arjan J. Hoogendijk, Nadine Becker, Christian Wagner, Marieke von Lindern, Stephane Egee, Emile Van den Akker, and Lars Kaestner "The Gárdos Channel and Piezo1 Revisited: Comparison between Reticulocytes and Mature Red Blood Cells", International Journal of Molecular Sciences 25(3), 1416, (2024)
 - https://doi.org/10.3390/ijms25031416

Eidesstattliche Erklärung

Erklärung gemäß § 7 Abs. 1 Nr. 2

Ich erkläre hiermit an Eides statt, dass ich die vorliegende Artreit ohne unzulässige Hilfe Dritter und ohne Benutzung anderer als der angegebenen Hilfsmittel angefertigt habe. Die aus anderen Quellen direkt oder indirekt übemommenen Daten und Konzepte sind unter Angabe der Quelle gekennzeichnet. Bei der Auswertung zum Membranpotenzial nach der Methode von Macey, Bennekou und Egee und der FLIM Daten hat Felix Milan Maurer mir Hilfestellung gegeben.

Weitere Personen waren an der inhaltlich-materiellen Erstellung der vorliegenden Arbeit nicht beteiligt. Insbesondere habe ich nicht die entgeltliche Hilfe von Vermittlungs- bzw. Beratungsdiensten (Promotionsberaterinnen/Promotionsberater oder anderer Personen) in Anspruch genommen. Außer den Angegebenen hat niemand von mir unmittelbar oder mittelbar geldwerte Leistungen für Arbeiten erhalten, die im Zusammenhang mit dem Inhalt der vorgelegten Dissertation stehen.

Die Arbeit wurde bisher weder im Inland noch im Ausland in gleicher oder in ähnlicher Form in einem anderen Verfahren zur Erlangung des Doktorgrades einer anderen Prüfungsbehörde vorgelegt.

Ich versichere an Eides statt, dass ich nach bestem Wissen die Wahrheit gesagt und nichts verschwiegen habe.

Die Bedeutung der eidesstattlichen Erklärung und die strafrechtlichen Folgen einer unrichtigen oder unvollständigen eidesstattlichen Erklärung sind mir bekannt.

Saarbrücken, den 4. März 2025 Min Qiao

Die/der Kandidatin/Kandidat: Min Qiao

geboren am: 22.03.1994 in Shanxi, China

Matrikelnummer: 7013589

versichert hiermit, dass die gedruckte und die elektronische Version der schriftlichen Ausarbeitung der Arbeit inhaltlich übereinstimmen.

Saarbrücken, den 4. März 2025 Min Qiao

Acknowledgements

As I approach this chapter of my thesis, I find myself at the moment, reaching the end of my PhD journey. The exciting and challenging journey began in the august of 2020 and ends in winter of 2024. There are too many beautiful moments in through this journey but as the moment arrives, I found myself at loss of words to express my grateful.

First and foremost, I would like to express my deepest gratitude to my supervisor, Lars Kastner, for his unwavering guidance, constructive feedback, and encouragement throughout my Ph.D. journey. His extensive expertise has been instrumental in shaping the direction and depth of my work. I am deeply grateful to Christian Wagner, who graciously employed me for months at the end of my first programme contract and provided insightful advice on my work during group meetings. I am deeply grateful to the members of my AG Wagner group for their cooperation and camaraderie throughout this process. I would like to thank Thomas for his patient help with IT problems, equipment issues and all programming and statistical questions, Felix for programming MatLab algorithms and all scientific and non-scientific discussions, Karin for experiment preparation, Sara, Nina, Elke for all administrative questions, Julia, Greta, Steffen, Alexander and Alexis for all experimental knowledge and all others for creating such a nice, dedicated and supportive environment with lots of encouragement.

I would like to extend my sincere thanks to everyone in the EVDIENCE network, whose support and collaborative environment were instrumental in completing this thesis. The resources, workshops and discussions provided a strong foundation for my research. The collective knowledge shared by this network has enriched my understanding and inspired me to push the boundaries of my abilities. I would like to thank Yazdan and Marcelle, who share the same base with me, for all the information and help in academic area and personal life, Giulia for nice host in Amsterdam, Aline for nice host in Roscoff, Sofia and Nicoletta for great secondment experiments, Miriam, Silvia, Catarina, Mariam, Robert, Amira, Aishwarya and Carolina for nice memories in the annual meeting and all the collaboration. Of course, I would also like to extend my thanks to the PIs. Marieke for being a wonderful host in Amsterdam, Emile and Staphane for welcoming me to their lab, Phillippe and Richard for arranging samples, Marina for organizing the program events and all the PIs for kindly sharing their experience and knowledge. It was an amazing time with the whole EVDIENCE family.

I would also like to thank our collaborators, Kevin, Isabel and Paola for arranging samples, Giampaolo for experiment methods, Andre, Karsten, Gregor, Georg, Sasha, and Mara for FLIM measurement, Britta for flowcytometry measurement and of course all the patients and healthy donors who generously donate their blood for research.

My last tribute is to those who know I am not perfect but still love me. My family, for their the unwavering support and encouragement. Your belief in my abilities has been my greatest source of strength, especially during difficult times. Your love and reassurance have been a constant motivation throughout this journey. My friends for being a constant source of positivity and encouragement. Thank you for celebrating every milestone, no matter how small. Your support has been a reminder that I am never alone on this journey.

To all of the above, thank you for your invaluable contributions to the completion of this project. May our lives set sail, heading towards great ideals.

- [1] D. Basu and R. Kulkarni, "Overview of blood components and their preparation," *Indian Journal of Anaesthesia*, vol. 58, no. 5, p. 529, 2014 [DOI-CrossRef].
- [2] J. Mathew, P. Sankar, and M. Varacallo, "Physiology, Blood Plasma," in *StatPearls [Internet]*, StatPearls Publishing, 2023.
- [3] V. Acharya, K. Prakasha, and 2Department of I&CT, Manipal Institute of Technology, MAHE, Manipal-576104, "Computer Aided Technique to Separate the Red Blood Cells, Categorize them and Diagnose Sickle Cell Anemia," *Journal of Engineering Science and Technology Review*, vol. 12, pp. 67–80, 2019 [DOI-CrossRef].
- [4] H. Mondal and S. Lotfollahzadeh, "Hematocrit," in *StatPearls*, Treasure Island (FL): StatPearls Publishing, 2024.
- [5] T. Burnouf, "An overview of plasma fractionation," *Annals of Blood*, vol. 3, pp. 33–33, 2018 [DOI-CrossRef].
- [6] J. Schaller, S. Gerber, U. Kämpfer, S. Lejon, and C. Trachsel, *Human Blood Plasma Proteins:* Structure and Function. Wiley, 1 ed., 2008.
- [7] L. Barbalato and L. S. Pillarisetty, "Histology, Red Blood Cell," in *StatPearls [Internet]*, StatPearls Publishing, 2022.
- [8] E. Humphry and C. E. Armstrong, "Physiology of red and white blood cells," *Anaesthesia & Intensive Care Medicine*, vol. 23, pp. 118–122, 2022 [DOI-CrossRef].
- [9] J. H. Fountain and S. L. Lappin, "Physiology, Platelet," in *StatPearls [Internet]*, StatPearls Publishing, 2023.
- [10] T. Gremmel, A. Frelinger, and A. Michelson, "Platelet Physiology," Seminars in Thrombosis and Hemostasis, vol. 42, pp. 191–204, 2016 [DOI-CrossRef].
- [11] K. Jurk and B. E. Kehrel, "Platelets: Physiology and Biochemistry," Seminars in Thrombosis and Hemostasis, vol. 31, pp. 381–392, 2005 [DOI-CrossRef].
- [12] J. Swammerdam, H. Boerhaave, H. D. Gaubius, Aa, Boudewijn Janssoon van der (II, Leiden), Aa, Pieter van der, and Severinus, Isaac (Leiden), Bybel Der Natuure. Te Leyden :: by Isaak Severinus, Boudewyn van der Aa, Pieter van der Aa, 1737.
- [13] G. Minetti, S. Egée, D. Mörsdorf, P. Steffen, A. Makhro, C. Achilli, A. Ciana, J. Wang, G. Bouyer, I. Bernhardt, C. Wagner, S. Thomas, A. Bogdanova, and L. Kaestner, "Red cell investigations: Art and artefacts," *Blood Reviews*, vol. 27, pp. 91–101, 2013 [DOI-CrossRef].
- [14] V. Kuhn, L. Diederich, T. S. Keller, C. M. Kramer, W. Lückstädt, C. Panknin, T. Suvorava, B. E. Isakson, M. Kelm, and M. M. Cortese-Krott, "Red Blood Cell Function and Dysfunction: Redox Regulation, Nitric Oxide Metabolism, Anemia," *Antioxidants & Redox Signaling*, vol. 26, pp. 718–742, 2017 [DOI-CrossRef].
- [15] M. H. Antonelou, A. G. Kriebardi, and I. S. Papassideri, "Aging and death signalling in mature red cells: From basic science to transfusion practice," *Blood Transfusion*, 2010 [DOI-CrossRef].
- [16] R. M. Cohen, R. S. Franco, P. K. Khera, E. P. Smith, C. J. Lindsell, P. J. Ciraolo, M. B. Palascak, and C. H. Joiner, "Red cell life span heterogeneity in hematologically normal people is sufficient to alter HbA1c," *Blood*, vol. 112, pp. 4284–4291, 2008 [DOI-CrossRef].
- [17] R. S. Franco, "Measurement of Red Cell Lifespan and Aging," *Transfusion Medicine and Hemother-apy*, vol. 39, no. 5, pp. 302–307, 2012 [DOI-CrossRef].

[18] D. M. Mock, N. I. Matthews, S. Zhu, R. G. Strauss, R. L. Schmidt, D. Nalbant, G. A. Cress, and J. A. Widness, "Red blood cell (RBC) survival determined in humans using RBCs labeled at multiple biotin densities," *Transfusion*, vol. 51, pp. 1047–1057, 2011 [DOI-CrossRef].

- [19] D. Sonker, Photoacoustic Signal Computation from Different Erythrocytes. PhD thesis, 2018.
- [20] S. E. Lux, "Anatomy of the red cell membrane skeleton: Unanswered questions," *Blood*, vol. 127, pp. 187–199, 2016 [DOI-CrossRef].
- [21] J. E. Smith, "Erythrocyte Membrane: Structure, Function, and Pathophysiology," *Veterinary Pathology*, vol. 24, pp. 471–476, 1987 [DOI-CrossRef].
- [22] SE. Lux, "Disorders of the red cell membrane.," Blood: Principles and Practice of Hematology, vol. 1701, 1995.
- [23] A. J. Verkleij, R. F. A. Zwaal, B. Roelofsen, P. Comfurius, and D. Kastelijn, "The Asymmetric Distribution of Phospholipids in the Human Red Cell Membrane,".
- [24] R. F. Zwaal and A. J. Schroit, "Pathophysiologic Implications of Membrane Phospholipid Asymmetry in Blood Cells," Blood, vol. 89, pp. 1121–1132, 1997 [DOI-CrossRef].
- [25] T. Harrison, B. U. Samuel, T. Akompong, H. Hamm, N. Mohandas, J. W. Lomasney, and K. Haldar, "Erythrocyte G Protein-Coupled Receptor Signaling in Malarial Infection," *Science*, vol. 301, pp. 1734–1736, 2003 [DOI-CrossRef].
- [26] V. Bennett, "The spectrin-actin junction of erythrocyte membrane skeletons," *Biochimica et Biophysica Acta (BBA) Reviews on Biomembranes*, vol. 988, pp. 107–121, 1989 [DOI-CrossRef].
- [27] N. Mohandas and P. G. Gallagher, "Red cell membrane: Past, present, and future," Blood, vol. 112, pp. 3939–3948, 2008 [DOI-CrossRef].
- [28] X. An, X. Guo, H. Sum, J. Morrow, W. Gratzer, and N. Mohandas, "Phosphatidylserine Binding Sites in Erythroid Spectrin: Location and Implications for Membrane Stability," *Biochemistry*, vol. 43, pp. 310–315, 2004 [DOI-CrossRef].
- [29] X. An, G. Debnath, X. Guo, S. Liu, S. E. Lux, A. Baines, W. Gratzer, and N. Mohandas, "Identification and Functional Characterization of Protein 4.1R and Actin-Binding Sites in Erythrocyte β Spectrin: Regulation of the Interactions by Phosphatidylinositol-4,5-bisphosphate," Biochemistry, vol. 44, pp. 10681–10688, 2005 [DOI-CrossRef].
- [30] X. An, X. Zhang, G. Debnath, A. J. Baines, and N. Mohandas, "Phosphatidylinositol-4,5-Biphosphate (PIP 2) Differentially Regulates the Interaction of Human Erythrocyte Protein 4.1 (4.1R) with Membrane Proteins," *Biochemistry*, vol. 45, pp. 5725–5732, 2006 [DOI-CrossRef].
- [31] S. Manno, Y. Takakuwa, and N. Mohandas, "Identification of a functional role for lipid asymmetry in biological membranes: Phosphatidylserine-skeletal protein interactions modulate membrane stability," *Proceedings of the National Academy of Sciences*, vol. 99, pp. 1943–1948, 2002 [DOI-CrossRef].
- [32] J. Cartron and Y. Colin, "Structural and functional diversity of blood group antigens," *Transfusion Clinique et Biologique*, vol. 8, pp. 163–199, 2001 [DOI-CrossRef].
- [33] M. E. Reid and N. Mohandas, "Red blood cell blood group antigens: Structure and function," Seminars in Hematology, vol. 41, pp. 93–117, 2004 [DOI-CrossRef].
- [34] M. Telen, "Erythrocyte blood group antigens: Not so simple after all [editorial; comment]," *Blood*, vol. 85, pp. 299–306, 1995 [DOI-CrossRef].
- [35] G. Garratty, "Blood Group Antigens as Tumor Markers, Parasitic/Bacterial/Viral Receptors, and Their Association with Immunologically Important Proteins," *Immunological Investigations*, vol. 24, pp. 213–232, 1995 [DOI-CrossRef].
- [36] G. Minetti and P. S. Low, "Erythrocyte signal transduction pathways and their possible functions:," Current Opinion in Hematology, vol. 4, no. 2, pp. 116–121, 1997 [DOI-CrossRef].
- [37] A.-M. Marini, G. Matassi, V. Raynal, B. André, J.-P. Cartron, and B. Chérif-Zahar, "The human Rhesus-associated RhAG protein and a kidney homologue promote ammonium transport in yeast," nature genetics, vol. 26, 2000.

[38] A.-M. Marini, A. Urrestarazu, R. Beauwens, and B. André, "The Rh (Rhesus) blood group polypeptides are related to NH4+ transporters," *Trends in Biochemical Sciences*, vol. 22, pp. 460–461, 1997 [DOI-CrossRef].

- [39] B. L. Smith, G. M. Preston, F. A. Spring, D. J. Anstee, and P. Agre, "Human red cell aquaporin CHIP. I. Molecular characterization of ABH and Colton blood group antigens.," *Journal of Clinical Investigation*, vol. 94, pp. 1043–1049, 1994 [DOI-CrossRef].
- [40] M. J. A. Tanner, "Band 3 anion exchanger and its involvement in erythrocyte and kidney disorders:," Current Opinion in Hematology, vol. 9, pp. 133–139, 2002 [DOI-CrossRef].
- [41] A. S. Verkman, "More than just water channels: Unexpected cellular roles of aquaporins," *Journal of Cell Science*, vol. 118, pp. 3225–3232, 2005 [DOI-CrossRef].
- [42] G. Daniels, "Functions of red cell surface proteins," Vox Sanguinis, vol. 93, pp. 331–340, 2007 [DOI-CrossRef].
- [43] A. J. Turner and K. Tanzawa, "Mammalian membrane metallopeptidases: NEP, ECE, KELL, and PEX," *The FASEB Journal*, vol. 11, pp. 355–364, 1997 [DOI-CrossRef].
- [44] S. Lee, M. Lin, A. Mele, Y. Cao, J. Farmar, D. Russo, and C. Redman, "Proteolytic processing of big endothelin-3 by the kell blood group protein," *Blood*, vol. 94, pp. 1440–1450, 1999.
- [45] F. A. Spring and S. F. Parsons, "Erythroid cell adhesion molecules," *Transfusion Medicine Reviews*, vol. 14, pp. 351–363, 2000 [DOI-CrossRef].
- [46] M. J. Telen, "Red blood cell surface adhesion molecules: Their possible roles in normal human physiology and disease," *Seminars in Hematology*, vol. 37, pp. 130–142, 2000 [DOI-CrossRef].
- [47] D. R. Ewald and S. C. Sumner, "Blood type biochemistry and human disease," WIREs Systems Biology and Medicine, vol. 8, pp. 517–535, 2016 [DOI-CrossRef].
- [48] L. Lögdberg, M. E. Reid, and T. Zelinski, "Human Blood Group Genes 2010: Chromosomal Locations and Cloning Strategies Revisited," *Transfusion Medicine Reviews*, vol. 25, pp. 36–46, 2011 [DOI-CrossRef].
- [49] R. Mitra, N. Mishra, and G. Rath, "Blood groups systems," Indian Journal of Anaesthesia, vol. 58, no. 5, p. 524, 2014 [DOI-CrossRef].
- [50] J. A. Chasis and N. Mohandas, "Erythrocyte membrane deformability and stability: Two distinct membrane properties that are independently regulated by skeletal protein associations.," *The Journal of cell biology*, vol. 103, pp. 343–350, 1986 [DOI-CrossRef].
- [51] S.-C. Liu and J. Palek, "Spectrin tetramer-dimer equilibrium and the stability of erythrocyte membrane skeletons," *Nature*, vol. 285, pp. 586–588, 1980 [DOI-CrossRef].
- [52] S. E. Lux, T. P. Stossel, and R. I. Handin, *Blood: Principles & Practice of Hematology*. Lippincott, 1995.
- [53] W. T. Tse and S. E. Lux, "Red blood cell membrane disorders," *British Journal of Haematology*, vol. 104, pp. 2–13, 1999 [DOI-CrossRef].
- [54] J. Dybas, M. J. Bokamper, K. M. Marzec, and P. J. Mak, "Probing the structure-function relationship of hemoglobin in living human red blood cells," *Spectrochimica Acta Part A: Molecular and Biomolecular Spectroscopy*, vol. 239, p. 118530, 2020 [DOI-CrossRef].
- [55] M. F. Perutz, M. G. Rossmann, A. F. Cullis, H. Muirhead, G. Will, and A. C. T. North, "Structure of Hæmoglobin: A Three-Dimensional Fourier Synthesis at 5.5-Å. Resolution, Obtained by X-Ray Analysis," Nature, vol. 185, pp. 416–422, 1960 [DOI-CrossRef].
- [56] M. H. Ahmed, M. S. Ghatge, and M. K. Safo, "Hemoglobin: Structure, Function and Allostery," in Vertebrate and Invertebrate Respiratory Proteins, Lipoproteins and Other Body Fluid Proteins (U. Hoeger and J. R. Harris, eds.), vol. 94, pp. 345–382, Cham: Springer International Publishing, 2020.
- [57] D. A. Gell, "Structure and function of haemoglobins," Blood Cells, Molecules, and Diseases, vol. 70, pp. 13–42, 2018 [DOI-CrossRef].

- [58] F. L. Hünefeld, Der Chemismus in Der Thierischen Organisation. Brockhaus, 1840.
- [59] C. C. Hsia, "Respiratory Function of Hemoglobin," New England Journal of Medicine, vol. 338, pp. 239–248, 1998 [DOI-CrossRef].
- [60] D. P. Kaufman, P. F. Kandle, I. V. Murray, and A. S. Dhamoon, "Physiology, Oxyhemoglobin Dissociation Curve," in *StatPearls [Internet]*, StatPearls Publishing, 2023.
- [61] C. Thomas and A. B. Lumb, "Physiology of haemoglobin," Continuing Education in Anaesthesia Critical Care & Pain, vol. 12, pp. 251–256, 2012 [DOI-CrossRef].
- [62] Chr. Bohr, K. Hasselbalch, and A. Krogh, "Ueber einen in biologischer Beziehung wichtigen Einfluss, den die Kohlensäurespannung des Blutes auf dessen Sauerstoffbindung übt ¹," Skandinavisches Archiv Für Physiologie, vol. 16, pp. 402–412, 1904 [DOI-CrossRef].
- [63] D. Gajecki, J. Gawryś, E. Szahidewicz-Krupska, and A. Doroszko, "Role of Erythrocytes in Nitric Oxide Metabolism and Paracrine Regulation of Endothelial Function," *Antioxidants (Basel, Switzerland)*, vol. 11, p. 943, 2022 [DOI-CrossRef].
- [64] E. Antonini, "Hemoglobin and Myoglobin in Their Reactions with Ligands," Frontiers of Biology, vol. 21, pp. 27–31, 1971.
- [65] G. Antonini, A. Bellelli, M. Brunori, and G. Falcioni, "Kinetic and spectroscopic properties of the cyanide complexes of ferrous haemoglobins I and IV from trout blood," *Biochemical Journal*, vol. 314, pp. 533–540, 1996 [DOI-CrossRef].
- [66] C. M. Park and R. L. Nagel, "Sulfhemoglobinemia: Clinical and Molecular Aspects," New England Journal of Medicine, vol. 310, pp. 1579–1584, 1984 [DOI-CrossRef].
- [67] J. M. Salhany, C. L. Castillo, and S. Ogawa, "Carbon monoxide binding properties of hemoglobin M Iwate," *Biochemistry*, vol. 15, pp. 5344–5349, 1976 [DOI-CrossRef].
- [68] J. Yi, M. K. Safo, and G. B. Richter-Addo, "The Nitrite Anion Binds to Human Hemoglobin via the Uncommon O-Nitrito Mode," *Biochemistry*, vol. 47, pp. 8247–8249, 2008 [DOI-CrossRef].
- [69] T. Yonetani, "Nitric oxide and hemoglobin.," Folia Pharmacologica Japonica, vol. 112, no. 3, pp. 155–160, 1998 [DOI-CrossRef].
- [70] Y. Farid, N. S. Bowman, and P. Lecat, "Biochemistry, Hemoglobin Synthesis," in *StatPearls [Internet]*, StatPearls Publishing, 2023.
- [71] M. Faraday, "V. Experimental researches in electricity," *Philosophical Transactions of the Royal Society of London*, vol. 122, pp. 125–162, 1832 [DOI-CrossRef].
- [72] J. Terry, "The major electrolytes: Sodium, potassium, and chloride," Journal of Intravenous Nursing: The Official Publication of the Intravenous Nurses Society, vol. 17, no. 5, pp. 240–247, 1994.
- [73] K. Funke, "Solid State Ionics: From Michael Faraday to green energy-the European dimension," Science and Technology of Advanced Materials, vol. 14, p. 043502, 2013 [DOI-CrossRef].
- [74] I. Shrimanker and S. Bhattarai, "Electrolytes," in *StatPearls*, Treasure Island (FL): StatPearls Publishing, 2023.
- [75] P. Bie, "Mechanisms of sodium balance: Total body sodium, surrogate variables, and renal sodium excretion," American Journal of Physiology. Regulatory, Integrative and Comparative Physiology, vol. 315, pp. R945–R962, 2018 [DOI-CrossRef].
- [76] V. A. Ruffin, A. I. Salameh, W. F. Boron, and M. D. Parker, "Intracellular pH regulation by acid-base transporters in mammalian neurons," *Frontiers in Physiology*, vol. 5, p. 43, 2014 [DOI-CrossRef].
- [77] P. Strazzullo and C. Leclercq, "Sodium," Advances in Nutrition (Bethesda, Md.), vol. 5, pp. 188–190, 2014 [DOI-CrossRef].
- [78] A. L. Hodgkin, "The Ionic Basis of Electrical Activity in Nerve and Muscle," *Biological Reviews*, vol. 26, pp. 339–409, 1951 [DOI-CrossRef].
- [79] L. J. Bergeron, A. J. Stever, and D. B. Light, "Potassium conductance activated during regulatory volume decrease by mudpuppy red blood cells," *The American Journal of Physiology*, vol. 270, pp. R801–810, 1996 [DOI-CrossRef].

[80] I. Pilchova, K. Klacanova, Z. Tatarkova, P. Kaplan, and P. Racay, "The Involvement of Mg2+ in Regulation of Cellular and Mitochondrial Functions," *Oxidative Medicine and Cellular Longevity*, vol. 2017, p. 6797460, 2017 [DOI-CrossRef].

- [81] M. S. Islam, "Calcium Signaling: From Basic to Bedside," Advances in Experimental Medicine and Biology, vol. 1131, pp. 1–6, 2020 [DOI-CrossRef].
- [82] J. D. Burke, "The effects of different salt concentrations on the affinity of hemoglobin for oxygen," Journal of Cellular and Comparative Physiology, vol. 54, pp. 126–128, 1959 [DOI-CrossRef].
- [83] E. K. Smith, "Observations on the measurement and regulation of the sodium content of human erythrocytes," *Clinical Science*, vol. 42, pp. 447–453, 1972 [DOI-CrossRef].
- [84] J. Izquierdo, J. Ferrero, D. Romeo, J. Badía, and E. Vigil, "Capillary blood potassium, chloride, sodium, calcium, phosphorus and alkaline phosphatase in the newborn," *Clinica Chimica Acta*, vol. 30, pp. 343–346, 1970 [DOI-CrossRef].
- [85] S. Hellerstein, W. Spees, and L. O. Surapathana, "Hemoglobin concentration and erythrocyte cation content," *The Journal of Laboratory and Clinical Medicine*, vol. 76, pp. 10–24, 1970.
- [86] J. Palek, M. Thomae, and D. Ozog, "Red cell calcium content and transmembrane calcium movements in sickle cell anemia," The Journal of Laboratory and Clinical Medicine, vol. 89, pp. 1365–1374, 1977.
- [87] C. Fuchs, K. Paschen, P. G. Spieckermann, and C. Westberg, "Bestimmung des ionisierten Calciums im Serum mit einer ionenselektiven Durchflusselektrode," *Klinische Wochenschrift*, vol. 50, pp. 824–832, 1972 [DOI-CrossRef].
- [88] A. C. Alfrey, N. L. Miller, and D. Butkus, "Evaluation of body magnesium stores," The Journal of Laboratory and Clinical Medicine, vol. 84, pp. 153–162, 1974.
- [89] F. Marongiu, H. J. Holtmeier, and A. von Klein-Wisenberg, "Zur Bestimmung des Mineralgehaltes in Erythrocyten," *Journal of Molecular Medicine*, vol. 44, no. 24, pp. 1405–1412, 1966.
- [90] E. Cotlove, P. Hald, and I. I. Simon, "Chloride," in *Standard Methods of Clinical Chemistry*, vol. 3, pp. 81–92, Elsevier, 1961.
- [91] M. Trevisan, V. Krogh, M. Cirillo, M. Laurenzi, A. Dyer, and J. Stamler, "Red blood cell sodium and potassium concentration and blood pressure," *Annals of Epidemiology*, vol. 5, pp. 44–51, 1995 [DOI-CrossRef].
- [92] S. Kirischuk, V. Parpura, and A. Verkhratsky, "Sodium dynamics: Another key to astroglial excitability?," *Trends in Neurosciences*, vol. 35, pp. 497–506, 2012 [DOI-CrossRef].
- [93] A. Verkhratsky, M. Trebak, F. Perocchi, D. Khananshvili, and I. Sekler, "Crosslink between calcium and sodium signalling," *Experimental Physiology*, vol. 103, pp. 157–169, 2018 [DOI-CrossRef].
- [94] X.-M. Yu, B. R. Groveman, X.-Q. Fang, and S.-X. Lin, "The role of intracellular sodium (Na+) in the regulation of calcium (Ca2+)-mediated signaling and toxicity," *Health*, vol. 2, no. 1, pp. 8–15, 2010 [DOI-CrossRef].
- [95] M. P. Hughes, C. H. Fry, and F. H. Labeed, "Cytoplasmic anion/cation imbalances applied across the membrane capacitance may form a significant component of the resting membrane potential of red blood cells," *Scientific Reports*, vol. 12, p. 15005, 2022 [DOI-CrossRef].
- [96] S. Singh, N. Ponnappan, A. Verma, and A. Mittal, "Osmotic tolerance of avian erythrocytes to complete hemolysis in solute free water," *Scientific Reports*, vol. 9, p. 7976, 2019 [DOI-CrossRef].
- [97] A. Sidwell, R. Munch, E. S. G. Barron, and T. Hogness, "The Salt Effect on the Hemoglobin-oxygen Equilibrium," *Journal of Biological Chemistry*, vol. 123, pp. 335–350, 1938 [DOI-CrossRef].
- [98] B. J. Davis and A. F. Riggs, "Effects of sodium chloride and carbon dioxide on oxygen binding by Artemia hemoglobin," *Journal of Comparative Physiology B*, vol. 156, pp. 355–361, 1986 [DOI-CrossRef].
- [99] I. Vig and I. Aviram, "The effects of salts on the oxygen affinity of hemoglobin," *FEBS Letters*, vol. 90, pp. 247–249, 1978 [DOI-CrossRef].

[100] L. R. Berkowitz and E. P. Orringer, "Passive sodium and potassium movements in sickle erythrocytes," The American Journal of Physiology, vol. 249, pp. C208–214, 1985 [DOI-CrossRef].

- [101] R. M. McLean and N. X. Wang, "Potassium," in Advances in Food and Nutrition Research, vol. 96, pp. 89–121, Elsevier, 2021.
- [102] S. Deshpande, S. Durdagi, and S. Y. Noskov, "Potassium in Biological Systems," in *Encyclopedia of Metalloproteins* (R. H. Kretsinger, V. N. Uversky, and E. A. Permyakov, eds.), pp. 1799–1804, New York, NY: Springer New York, 2013.
- [103] P. J. Stambrook, H. G. Sach, and J. D. Ebert, "The effect of potassium on the cell membrane potential and the passage of synchronized cells through the cell cycle," *Journal of Cellular Physiology*, vol. 85, pp. 283–291, 1975 [DOI-CrossRef].
- [104] M. von Lindern, S. Egée, P. Bianchi, and L. Kaestner, "The Function of Ion Channels and Membrane Potential in Red Blood Cells: Toward a Systematic Analysis of the Erythroid Channelome," Frontiers in Physiology, vol. 13, p. 824478, 2022 [DOI-CrossRef].
- [105] P. J. Garrahan, M. I. Pouchan, and A. F. Rega, "Potassium activated phosphatase from human red blood cells. The mechanism of potassium activation," *The Journal of Physiology*, vol. 202, pp. 305–327, 1969 [DOI-CrossRef].
- [106] B. E. Glader and D. W. Sullivan, "Erythrocyte disorders leading to potassium loss and cellular dehydration," Progress in Clinical and Biological Research, vol. 30, pp. 503–513, 1979.
- [107] L. Repsold and A. M. Joubert, "Eryptosis: An Erythrocyte's Suicidal Type of Cell Death," *BioMed Research International*, vol. 2018, p. 9405617, 2018 [DOI-CrossRef].
- [108] A. Bogdanova, A. Makhro, J. Wang, P. Lipp, and L. Kaestner, "Calcium in Red Blood Cells—A Perilous Balance," *International Journal of Molecular Sciences*, vol. 14, pp. 9848–9872, 2013 [DOI-CrossRef].
- [109] R. M. Bookchin and V. L. Lew, "Progressive inhibition of the Ca pump and Ca:Ca exchange in sickle red cells," *Nature*, vol. 284, pp. 561–563, 1980 [DOI-CrossRef].
- [110] T. Tiffert, R. M. Bookchin, and V. L. Lew, "Calcium Homeostasis in Normal and Abnormal Human Red Cells," in *Red Cell Membrane Transport in Health and Disease* (I. Bernhardt and J. C. Ellory, eds.), pp. 373–405, Berlin, Heidelberg: Springer Berlin Heidelberg, 2003.
- [111] R. B. Govekar and S. M. Zingde, "Protein kinase C isoforms in human erythrocytes," *Annals of Hematology*, vol. 80, pp. 531–534, 2001 [DOI-CrossRef].
- [112] C. M. Cohen and P. Gascard, "Regulation and post-translational modification of erythrocyte membrane and membrane-skeletal proteins," *Seminars in Hematology*, vol. 29, pp. 244–292, 1992.
- [113] S. de Oliveira, A. S. Silva-Herdade, and C. Saldanha, "Modulation of erythrocyte deformability by PKC activity," *Clinical Hemorheology and Microcirculation*, vol. 39, no. 1-4, pp. 363–373, 2008.
- [114] K. P. Hoeflich and M. Ikura, "Calmodulin in action: Diversity in target recognition and activation mechanisms," *Cell*, vol. 108, pp. 739–742, 2002 [DOI-CrossRef].
- [115] H. W. Jarrett and J. Kyte, "Human erythrocyte calmodulin. Further chemical characterization and the site of its interaction with the membrane," *The Journal of Biological Chemistry*, vol. 254, pp. 8237–8244, 1979.
- [116] F. Bassé, J. G. Stout, P. J. Sims, and T. Wiedmer, "Isolation of an erythrocyte membrane protein that mediates Ca2+-dependent transbilayer movement of phospholipid," *The Journal of Biological Chemistry*, vol. 271, pp. 17205–17210, 1996 [DOI-CrossRef].
- [117] J. G. Stout, Q. Zhou, T. Wiedmer, and P. J. Sims, "Change in conformation of plasma membrane phospholipid scramblase induced by occupancy of its Ca2+ binding site," *Biochemistry*, vol. 37, pp. 14860–14866, 1998 [DOI-CrossRef].
- [118] L. A. Woon, J. W. Holland, E. P. Kable, and B. D. Roufogalis, "Ca2+ sensitivity of phospholipid scrambling in human red cell ghosts," *Cell Calcium*, vol. 25, pp. 313–320, 1999 [DOI-CrossRef].
- [119] M. Bitbol, P. Fellmann, A. Zachowski, and P. F. Devaux, "Ion regulation of phosphatidylserine

- and phosphatidylethanolamine outside-inside translocation in human erythrocytes," *Biochimica Et Biophysica Acta*, vol. 904, pp. 268–282, 1987 [DOI-CrossRef].
- [120] G. Morrot, P. Hervé, A. Zachowski, P. Fellmann, and P. F. Devaux, "Aminophospholipid translocase of human erythrocytes: Phospholipid substrate specificity and effect of cholesterol," *Biochemistry*, vol. 28, pp. 3456–3462, 1989 [DOI-CrossRef].
- [121] A. Wieschhaus, A. Khan, A. Zaidi, H. Rogalin, T. Hanada, F. Liu, L. De Franceschi, C. Brugnara, A. Rivera, and A. H. Chishti, "Calpain-1 knockout reveals broad effects on erythrocyte deformability and physiology," *The Biochemical Journal*, vol. 448, pp. 141–152, 2012 [DOI-CrossRef].
- [122] G. Gárdos, "The function of calcium in the potassium permeability of human erythrocytes," *Biochimica et Biophysica Acta*, vol. 30, pp. 653–654, 1958 [DOI-CrossRef].
- [123] J. F. Hoffman, W. Joiner, K. Nehrke, O. Potapova, K. Foye, and A. Wickrema, "The hSK4 (KCNN4) isoform is the Ca ²⁺ -activated K ⁺ channel (Gardos channel) in human red blood cells," *Proceedings of the National Academy of Sciences*, vol. 100, pp. 7366–7371, 2003 [DOI-CrossRef].
- [124] W. J. Joiner, L. Y. Wang, M. D. Tang, and L. K. Kaczmarek, "hSK4, a member of a novel subfamily of calcium-activated potassium channels," *Proceedings of the National Academy of Sciences of the United States of America*, vol. 94, pp. 11013–11018, 1997 [DOI-CrossRef].
- [125] L. Kaestner, W. Tabellion, P. Lipp, and I. Bernhardt, "Prostaglandin E2 activates channel-mediated calcium entry in human erythrocytes: An indication for a blood clot formation supporting process," *Thrombosis and Haemostasis*, vol. 92, pp. 1269–1272, 2004 [DOI-CrossRef].
- [126] L. Kaestner and I. Bernhardt, "Ion channels in the human red blood cell membrane: Their further investigation and physiological relevance," *Bioelectrochemistry (Amsterdam, Netherlands)*, vol. 55, pp. 71–74, 2002 [DOI-CrossRef].
- [127] A. George, S. Pushkaran, D. G. Konstantinidis, S. Koochaki, P. Malik, N. Mohandas, Y. Zheng, C. H. Joiner, and T. A. Kalfa, "Erythrocyte NADPH oxidase activity modulated by Rac GTPases, PKC, and plasma cytokines contributes to oxidative stress in sickle cell disease," *Blood*, vol. 121, pp. 2099–2107, 2013 [DOI-CrossRef].
- [128] D. A. Andrews, L. Yang, and P. S. Low, "Phorbol ester stimulates a protein kinase C-mediated agatoxin-TK-sensitive calcium permeability pathway in human red blood cells," *Blood*, vol. 100, pp. 3392–3399, 2002 [DOI-CrossRef].
- [129] G. Ceolotto, P. Conlin, G. Clari, A. Semplicini, and M. Canessa, "Protein kinase C and insulin regulation of red blood cell Na+/H+ exchange," *The American Journal of Physiology*, vol. 272, pp. C818–826, 1997 [DOI-CrossRef].
- [130] L. Wagner-Britz, J. Wang, L. Kaestner, and I. Bernhardt, "Protein kinase C\$\alpha\$ and P-type Ca channel CaV2.1 in red blood cell calcium signalling," *Cellular Physiology and Biochemistry: International Journal of Experimental Cellular Physiology, Biochemistry, and Pharmacology*, vol. 31, no. 6, pp. 883–891, 2013 [DOI-CrossRef].
- [131] L. C. Wright, S. Chen, and B. D. Roufogalis, "Regulation of the activity and phosphorylation of the plasma membrane Ca(2+)-ATPase by protein kinase C in intact human erythrocytes," *Archives of Biochemistry and Biophysics*, vol. 306, pp. 277–284, 1993 [DOI-CrossRef].
- [132] R. Beitner, "Control of glycolytic enzymes through binding to cell structures and by glucose-1,6-bisphosphate under different conditions. The role of Ca2+ and calmodulin," *The International Journal of Biochemistry*, vol. 25, pp. 297–305, 1993 [DOI-CrossRef].
- [133] K. Nakashima, S. Fujii, K. Kaku, and T. Kaneko, "Calcium-calmodulin dependent phosphorylation of erythrocyte pyruvate kinase," *Biochemical and Biophysical Research Communications*, vol. 104, pp. 285–289, 1982 [DOI-CrossRef].
- [134] A. Dyrda, U. Cytlak, A. Ciuraszkiewicz, A. Lipinska, A. Cueff, G. Bouyer, S. Egée, P. Bennekou, V. L. Lew, and S. L. Y. Thomas, "Local membrane deformations activate Ca2+-dependent K+ and anionic currents in intact human red blood cells," *PloS One*, vol. 5, p. e9447, 2010 [DOI-CrossRef].
- [135] P. Kleinbongard, R. Schulz, T. Rassaf, T. Lauer, A. Dejam, T. Jax, I. Kumara, P. Gharini,

S. Kabanova, B. Ozüyaman, H.-G. Schnürch, A. Gödecke, A.-A. Weber, M. Robenek, H. Robenek, W. Bloch, P. Rösen, and M. Kelm, "Red blood cells express a functional endothelial nitric oxide synthase," *Blood*, vol. 107, pp. 2943–2951, 2006 [DOI-CrossRef].

- [136] B. Ozüyaman, M. Grau, M. Kelm, M. W. Merx, and P. Kleinbongard, "RBC NOS: Regulatory mechanisms and therapeutic aspects," *Trends in Molecular Medicine*, vol. 14, pp. 314–322, 2008 [DOI-CrossRef].
- [137] P. Ulker, N. Yaras, O. Yalcin, C. Celik-Ozenci, P. C. Johnson, H. J. Meiselman, and O. K. Baskurt, "Shear stress activation of nitric oxide synthase and increased nitric oxide levels in human red blood cells," *Nitric Oxide: Biology and Chemistry*, vol. 24, pp. 184–191, 2011 [DOI-CrossRef].
- [138] A. Makhro, P. Hänggi, J. S. Goede, J. Wang, A. Brüggemann, M. Gassmann, M. Schmugge, L. Kaestner, O. Speer, and A. Bogdanova, "N-methyl-D-aspartate receptors in human erythroid precursor cells and in circulating red blood cells contribute to the intracellular calcium regulation," *American Journal of Physiology. Cell Physiology*, vol. 305, pp. C1123–1138, 2013 [DOI-CrossRef].
- [139] S. Palta, R. Saroa, and A. Palta, "Overview of the coagulation system," *Indian Journal of Anaesthesia*, vol. 58, pp. 515–523, 2014 [DOI-CrossRef].
- [140] S.-M. Chung, O.-N. Bae, K.-M. Lim, J.-Y. Noh, M.-Y. Lee, Y.-S. Jung, and J.-H. Chung, "Lysophos-phatidic acid induces thrombogenic activity through phosphatidylserine exposure and procoagulant microvesicle generation in human erythrocytes," *Arteriosclerosis, Thrombosis, and Vascular Biology*, vol. 27, pp. 414–421, 2007 [DOI-CrossRef].
- [141] L. Kaestner, P. Steffen, D. B. Nguyen, J. Wang, L. Wagner-Britz, A. Jung, C. Wagner, and I. Bernhardt, "Lysophosphatidic acid induced red blood cell aggregation in vitro," *Bioelectrochemistry* (Amsterdam, Netherlands), vol. 87, pp. 89–95, 2012 [DOI-CrossRef].
- [142] J.-Y. Noh, K.-M. Lim, O.-N. Bae, S.-M. Chung, S.-W. Lee, K.-M. Joo, S.-D. Lee, and J.-H. Chung, "Procoagulant and prothrombotic activation of human erythrocytes by phosphatidic acid," *American Journal of Physiology*. Heart and Circulatory Physiology, vol. 299, pp. H347–355, 2010 [DOI-CrossRef].
- [143] P. Steffen, A. Jung, D. B. Nguyen, T. Müller, I. Bernhardt, L. Kaestner, and C. Wagner, "Stimulation of human red blood cells leads to Ca2+-mediated intercellular adhesion," *Cell Calcium*, vol. 50, pp. 54–61, 2011 [DOI-CrossRef].
- [144] M.-P. Wautier, W. El Nemer, P. Gane, J.-D. Rain, J.-P. Cartron, Y. Colin, C. Le Van Kim, and J.-L. Wautier, "Increased adhesion to endothelial cells of erythrocytes from patients with polycythemia vera is mediated by laminin alpha5 chain and Lu/BCAM," *Blood*, vol. 110, pp. 894–901, 2007 [DOI-CrossRef].
- [145] M.-P. Wautier, E. Héron, J. Picot, Y. Colin, O. Hermine, and J.-L. Wautier, "Red blood cell phosphatidylserine exposure is responsible for increased erythrocyte adhesion to endothelium in central retinal vein occlusion," *Journal of thrombosis and haemostasis: JTH*, vol. 9, pp. 1049–1055, 2011 [DOI-CrossRef].
- [146] S. Yedgar, D. K. Kaul, and G. Barshtein, "RBC adhesion to vascular endothelial cells: More potent than RBC aggregation in inducing circulatory disorders," *Microcirculation (New York, N.Y.: 1994)*, vol. 15, pp. 581–583, 2008 [DOI-CrossRef].
- [147] B. A. Miller and J. Y. Cheung, "Mechanisms of erythropoietin signal transduction: Involvement of calcium channels," *Proceedings of the Society for Experimental Biology and Medicine. Society for Experimental Biology and Medicine (New York, N.Y.)*, vol. 206, pp. 263–267, 1994 [DOI-CrossRef].
- [148] A. Schaefer, M. Magócsi, and H. Marquardt, "Signalling mechanisms in erythropoiesis: The enigmatic role of calcium," *Cellular Signalling*, vol. 9, pp. 483–495, 1997 [DOI-CrossRef].
- [149] G. J. C. G. M. Bosman, F. L. A. Willekens, and J. M. Werre, "Erythrocyte aging: A more than superficial resemblance to apoptosis?," *Cellular Physiology and Biochemistry: International Journal of Experimental Cellular Physiology, Biochemistry, and Pharmacology*, vol. 16, no. 1-3, pp. 1–8, 2005 [DOI-CrossRef].
- [150] H. U. Lutz, "Innate immune and non-immune mediators of erythrocyte clearance," Cellular and Molecular Biology (Noisy-Le-Grand, France), vol. 50, pp. 107–116, 2004.

[151] N. Mohandas and W. Groner, "Cell membrane and volume changes during red cell development and aging," *Annals of the New York Academy of Sciences*, vol. 554, pp. 217–224, 1989 [DOI-CrossRef].

- [152] L. Lorand, S. N. P. Murthy, A. A. Khan, W. Xue, O. Lockridge, and A. H. Chishti, "Transglutaminase-mediated remodeling of the human erythrocyte membrane skeleton: Relevance for erythrocyte diseases with shortened cell lifespan," Advances in Enzymology and Related Areas of Molecular Biology, vol. 78, pp. 385–414, 2011 [DOI-CrossRef].
- [153] J. W. Eaton, T. D. Skelton, H. S. Swofford, C. E. Kolpin, and H. S. Jacob, "Elevated erythrocyte calcium in sickle cell disease," *Nature*, vol. 246, pp. 105–106, 1973 [DOI-CrossRef].
- [154] J. S. Wiley, "Increased erythrocyte cation permeability in thalassemia and conditions of marrow stress," *The Journal of Clinical Investigation*, vol. 67, pp. 917–922, 1981 [DOI-CrossRef].
- [155] P. J. Henderson, J. D. McGivan, and J. B. Chappell, "The action of certain antibiotics on mitochondrial, erythrocyte and artificial phospholipid membranes. The role of induced proton permeability," *The Biochemical Journal*, vol. 111, pp. 521–535, 1969 [DOI-CrossRef].
- [156] H. A. Lardy, S. N. Graven, and S. Estrada, "Specific induction and inhibition of cation and anion transport in mitochondria," *Federation Proceedings*, vol. 26, pp. 1355–1360, 1967.
- [157] B. Pressman, "Mechanism of action of transport-mediating antibiotics," *Annals of the New York Academy of Sciences*, vol. 147, pp. 829–841, 1969 [DOI-CrossRef].
- [158] B. C. Pressman, "Induced active transport of ions in mitochondria," *Proceedings of the National Academy of Sciences of the United States of America*, vol. 53, pp. 1076–1083, 1965 [DOI-CrossRef].
- [159] B. C. Pressman, E. J. Harris, W. S. Jagger, and J. H. Johnson, "Antibiotic-mediated transport of alkali ions across lipid barriers," *Proceedings of the National Academy of Sciences of the United States of America*, vol. 58, pp. 1949–1956, 1967 [DOI-CrossRef].
- [160] C. Liu and T. E. Hermann, "Characterization of ionomycin as a calcium ionophore," *The Journal of Biological Chemistry*, vol. 253, pp. 5892–5894, 1978.
- [161] M. O. Chaney, P. V. Demarco, N. D. Jones, and J. L. Occolowitz, "Structure of A23187, a divalent cation ionophore," *Journal of the American Chemical Society*, vol. 96, pp. 1932–1933, 1974 [DOI-CrossRef].
- [162] P. W. Reed and H. A. Lardy, "A23187: A divalent cation ionophore," *The Journal of Biological Chemistry*, vol. 247, pp. 6970–6977, 1972.
- [163] C. M. Deber, J. Tom-Kun, E. Mack, and S. Grinstein, "Bromo-A23187: A nonfluorescent calcium ionophore for use with fluorescent probes," *Analytical Biochemistry*, vol. 146, pp. 349–352, 1985 [DOI-CrossRef].
- [164] W.-Z. Zeng and T.-L. Xu, "Proton production, regulation and pathophysiological roles in the mammalian brain," *Neuroscience Bulletin*, vol. 28, pp. 1–13, 2012 [DOI-CrossRef].
- [165] P. Swietach, T. Tiffert, J. M. A. Mauritz, R. Seear, A. Esposito, C. F. Kaminski, V. L. Lew, and R. D. Vaughan-Jones, "Hydrogen ion dynamics in human red blood cells," *The Journal of Physiology*, vol. 588, pp. 4995–5014, 2010 [DOI-CrossRef].
- [166] T. H. Maren, "Carbonic anhydrase: Chemistry, physiology, and inhibition," Physiological Reviews, vol. 47, pp. 595–781, 1967 [DOI-CrossRef].
- [167] N. U. Meldrum and F. J. Roughton, "Carbonic anhydrase. Its preparation and properties," *The Journal of Physiology*, vol. 80, pp. 113–142, 1933 [DOI-CrossRef].
- [168] A. Cass and M. Dalmark, "Equilibrium dialysis of ions in nystatin-treated red cells," *Nature: New Biology*, vol. 244, pp. 47–49, 1973 [DOI-CrossRef].
- [169] J. Funder and J. O. Wieth, "Chloride and Hydrogen Ion Distribution between Human Red Cells and Plasma," *Acta Physiologica Scandinavica*, vol. 68, pp. 234–245, 1966 [DOI-CrossRef].
- [170] D. D. Van Slyke, H. Wu, and F. C. McLean, "Studies of Gas and Electrolyte Equilibria in the Blood," *Journal of Biological Chemistry*, vol. 56, pp. 765–849, 1923 [DOI-CrossRef].
- [171] S. Sörensen, Enzymstudien II: Über Die Messung Und Die Bedeutung Der Wasserstoffionenkonzen-

- tration Bei Enzymatischen Prozessen. Biochemische Zeitschrift, Springer-Verlag, 1909.
- [172] M. Dalmark, "Chloride and water distribution in human red cells," *The Journal of Physiology*, vol. 250, pp. 65–84, 1975 [DOI-CrossRef].
- [173] M. H. Jacobs and D. R. Stewart, "Osmotic properties of the erythrocyte; ionic and osmotic equilibria with a complex external solution," *Journal of Cellular and Comparative Physiology*, vol. 30, pp. 79–103, 1947 [DOI-CrossRef].
- [174] P. Salenius, "A study of the pH and buffer capacity of blood, plasma and red blood cells," *Scandina-vian Journal of Clinical and Laboratory Investigation*, vol. 9, no. 2, pp. 160–167, 1957 [DOI-CrossRef].
- [175] S. Salminen and V. Manninen, "Ion and water shifts produced by ammonium chloride in high K and low K red cells," *Journal of Cellular Physiology*, vol. 68, pp. 19–24, 1966 [DOI-CrossRef].
- [176] V. L. Lew, C. J. Freeman, O. E. Ortiz, and R. M. Bookchin, "A mathematical model of the volume, pH, and ion content regulation in reticulocytes. Application to the pathophysiology of sickle cell dehydration," The Journal of Clinical Investigation, vol. 87, pp. 100–112, 1991 [DOI-CrossRef].
- [177] J. W. Severinghaus and P. B. Astrup, "History of blood gas analysis. II. pH and acid-base balance measurements," *Journal of Clinical Monitoring*, vol. 1, pp. 259–277, 1985 [DOI-CrossRef].
- [178] J. R. Casey, S. Grinstein, and J. Orlowski, "Sensors and regulators of intracellular pH," *Nature Reviews Molecular Cell Biology*, vol. 11, pp. 50–61, 2010 [DOI-CrossRef].
- [179] R. W. Putnam, "Intracellular pH Regulation," in *Cell Physiology Source Book*, pp. 303–321, Elsevier, 2012.
- [180] J. R. Schelling and B. G. Abu Jawdeh, "Regulation of cell survival by Na ⁺ /H ⁺ exchanger-1," *American Journal of Physiology-Renal Physiology*, vol. 295, pp. F625–F632, 2008 [DOI-CrossRef].
- [181] J. Srivastava, D. L. Barber, and M. P. Jacobson, "Intracellular pH Sensors: Design Principles and Functional Significance," *Physiology*, vol. 22, pp. 30–39, 2007 [DOI-CrossRef].
- [182] E. A. Kotova and Y. N. Antonenko, "Fifty Years of Research on Protonophores: Mitochondrial Uncoupling As a Basis for Therapeutic Action," *Acta Naturae*, vol. 14, no. 1, pp. 4–13, 2022 [DOI-CrossRef].
- [183] P. G. Heytler, "Uncoupling of Oxidative Phosphorylation by Carbonyl Cyanide Phenylhydrazones. I. Some Characteristics of m-CI-CCP Action on Mitochondria and Chloroplasts," *Biochemistry*, vol. 2, pp. 357–361, 1963 [DOI-CrossRef].
- [184] W. F. Loomis and F. Lipmann, "Reversible inhibition of the coupling between phosphorylation and oxidation," *The Journal of Biological Chemistry*, vol. 173, p. 807, 1948.
- [185] S. M. Koch and R. W. Taylor, "Chloride ion in intensive care medicine," Critical Care Medicine, vol. 20, pp. 227–240, 1992 [DOI-CrossRef].
- [186] T. J. Jentsch, T. Maritzen, and A. A. Zdebik, "Chloride channel diseases resulting from impaired transepithelial transport or vesicular function," *The Journal of Clinical Investigation*, vol. 115, pp. 2039–2046, 2005 [DOI-CrossRef].
- [187] B. A. Houssay, Human Physiology. McGraw-Hill Book, 1951.
- [188] K. Berend, L. H. van Hulsteijn, and R. O. B. Gans, "Chloride: The queen of electrolytes?," *European Journal of Internal Medicine*, vol. 23, pp. 203–211, 2012 [DOI-CrossRef].
- [189] Y. Marunaka, N. Niisato, A. Taruno, M. Ohta, H. Miyazaki, S. Hosogi, K.-i. Nakajima, K. Kusuzaki, E. Ashihara, K. Nishio, Y. Iwasaki, T. Nakahari, and T. Kubota, "Regulation of Epithelial Sodium Transport via Epithelial Na ⁺ Channel," *Journal of Biomedicine and Biotechnology*, vol. 2011, pp. 1–8, 2011 [DOI-CrossRef].
- [190] H. C. Chan and D. J. Nelson, "Chloride-dependent cation conductance activated during cellular shrinkage," *Science (New York, N.Y.)*, vol. 257, pp. 669–671, 1992 [DOI-CrossRef].
- [191] K. J. Treharne, R. M. Crawford, and A. Mehta, "CFTR, chloride concentration and cell volume: Could mammalian protein histidine phosphorylation play a latent role?," *Experimental Physiology*, vol. 91, pp. 131–139, 2006 [DOI-CrossRef].

[192] J. M. Paredes, A. I. Idilli, L. Mariotti, G. Losi, L. R. Arslanbaeva, S. S. Sato, P. Artoni, J. Szczurkowska, L. Cancedda, G. M. Ratto, G. Carmignoto, and D. Arosio, "Synchronous Bioimaging of Intracellular pH and Chloride Based on LSS Fluorescent Protein," ACS Chemical Biology, vol. 11, pp. 1652–1660, 2016 [DOI-CrossRef].

- [193] L. K. Bekar and W. Walz, "Evidence for chloride ions as intracellular messenger substances in astrocytes," *Journal of Neurophysiology*, vol. 82, pp. 248–254, 1999 [DOI-CrossRef].
- [194] A. T. Piala, T. M. Moon, R. Akella, H. He, M. H. Cobb, and E. J. Goldsmith, "Chloride sensing by WNK1 involves inhibition of autophosphorylation," *Science Signaling*, vol. 7, p. ra41, 2014 [DOI-CrossRef].
- [195] K. Funabashi, M. Fujii, H. Yamamura, S. Ohya, and Y. Imaizumi, "Contribution of chloride channel conductance to the regulation of resting membrane potential in chondrocytes," *Journal of Pharmacological Sciences*, vol. 113, no. 1, pp. 94–99, 2010 [DOI-CrossRef].
- [196] M. M. Balach, C. H. Casale, and A. N. Campetelli, "Erythrocyte plasma membrane potential: Past and current methods for its measurement," *Biophysical Reviews*, vol. 11, pp. 995–1005, 2019 [DOI-CrossRef].
- [197] E. D. Crandall, S. J. Mathew, R. S. Fleischer, H. I. Winter, and A. Bidani, "Effects of inhibition of RBC HCO3-/Cl- exchange on CO2 excretion and downstream pH disequilibrium in isolated rat lungs.," *Journal of Clinical Investigation*, vol. 68, pp. 853–862, 1981 [DOI-CrossRef].
- [198] E. A. Westen and H. D. Prange, "A reexamination of the mechanisms underlying the arteriovenous chloride shift," *Physiological and biochemical zoology: PBZ*, vol. 76, no. 5, pp. 603–614, 2003 [DOI-CrossRef].
- [199] F. B. Jensen, "Red blood cell pH, the Bohr effect, and other oxygenation-linked phenomena in blood O 2 and CO 2 transport," *Acta Physiologica Scandinavica*, vol. 182, pp. 215–227, 2004 [DOI-CrossRef].
- [200] A. Nigen, J. Manning, and J. Alben, "Oxygen-linked binding sites for inorganic anions to hemoglobin.," *Journal of Biological Chemistry*, vol. 255, pp. 5525–5529, 1980 [DOI-CrossRef].
- [201] P. Bennekou, O. Pedersen, A. Møller, and P. Christophersen, "Volume control in sickle cells is facilitated by the novel anion conductance inhibitor NS1652," *Blood*, vol. 95, pp. 1842–1848, 2000 [DOI-CrossRef].
- [202] P. Bennekou, L. De Franceschi, O. Pedersen, L. Lian, T. Asakura, G. Evans, C. Brugnara, and P. Christophersen, "Treatment with NS3623, a novel Cl-conductance blocker, ameliorates erythrocyte dehydration in transgenic SAD mice: A possible new therapeutic approach for sickle cell disease," Blood, vol. 97, pp. 1451–1457, 2001 [DOI-CrossRef].
- [203] A. Gürber, "Die Salze des Blutes," Jahresbericht über die fortschritte der tierchemie oder der physiologischen und pathologischen chemie, vol. 24, pp. 172–175, 1895.
- [204] W. E. Cohn and E. T. Cohn, "Permeability of Red Corpuscles of the Dog to Sodium Ion.," Experimental Biology and Medicine, vol. 41, pp. 445–449, 1939 [DOI-CrossRef].
- [205] A. J. Eisenman, L. Ott, P. K. Smith, and A. W. Winkler, "A Study of the Permeability of Human Erythrocytes to Potassium, Sodium, and Inorganic Phosphate by the Use of Radioactive Isotopes," *Journal of Biological Chemistry*, vol. 135, pp. 165–173, 1940 [DOI-CrossRef].
- [206] B. Alberts, A. Johnson, J. Lewis, D. Morgan, M. Raff, K. Roberts, and P. Walter, Membrane Transport of Small Molecules and the Electrical Properties of Membranes, pp. 597–640. W.W. Norton & Company, 6 ed., 2017.
- [207] H. L. Tepper and G. A. Voth, "Mechanisms of passive ion permeation through lipid bilayers: Insights from simulations," *The Journal of Physical Chemistry*. B, vol. 110, pp. 21327–21337, 2006 [DOI-CrossRef].
- [208] M. Kansy, F. Senner, and K. Gubernator, "Physicochemical High Throughput Screening: Parallel Artificial Membrane Permeation Assay in the Description of Passive Absorption Processes," *Journal of Medicinal Chemistry*, vol. 41, pp. 1007–1010, 1998 [DOI-CrossRef].
- [209] A. Krogh, "The active and passive exchanges of inorganic ions through the surfaces of living cells

- and through living membranes generally," *Proceedings of the Royal Society of Medicine*, vol. 133, pp. 140–200, 1946 [DOI-CrossRef].
- [210] I. M. Glynn, "Sodium and potassium movements in human red cells," The Journal of Physiology, vol. 134, pp. 278–310, 1956 [DOI-CrossRef].
- [211] A. K. Solomon, "The permeability of the human erythrocyte to sodium and potassium," *The Journal of General Physiology*, vol. 36, pp. 57–110, 1952 [DOI-CrossRef].
- [212] B. Alberts, ed., Molecular Biology of the Cell. Haupthd. New York: Garland, 4. ed ed., 2002.
- [213] C. F. Code, "Handbook of physiology. A critical, comprehensive presentation of physiological knowledge and concepts. Section 6. Alimentary canal. Volume 4. Motility.," 1968.
- [214] J. Kulbacka, A. Choromańska, J. Rossowska, J. Weżgowiec, J. Saczko, and M.-P. Rols, "Cell Membrane Transport Mechanisms: Ion Channels and Electrical Properties of Cell Membranes," in Transport Across Natural and Modified Biological Membranes and Its Implications in Physiology and Therapy (J. Kulbacka and S. Satkauskas, eds.), vol. 227, pp. 39–58, Cham: Springer International Publishing, 2017.
- [215] I. Chen and F. Lui, "Physiology, Active Transport," in *StatPearls*, Treasure Island (FL): StatPearls Publishing, 2023.
- [216] M. G. Wolfersberger, "Uniporters, Symporters and Antiporters," *Journal of Experimental Biology*, vol. 196, pp. 5–6, 1994 [DOI-CrossRef].
- [217] P. Labarca, R. Coronado, and C. Miller, "Thermodynamic and kinetic studies of the gating behavior of a K+-selective channel from the sarcoplasmic reticulum membrane," *The Journal of General Physiology*, vol. 76, pp. 397–324, 1980 [DOI-CrossRef].
- [218] K. Peper, R. J. Bradley, and F. Dreyer, "The acetylcholine receptor at the neuromuscular junction," Physiological Reviews, vol. 62, pp. 1271–1340, 1982 [DOI-CrossRef].
- [219] W. Schwarz and H. Passow, "Ca2+-activated K+ channels in erythrocytes and excitable cells," *Annual Review of Physiology*, vol. 45, pp. 359–374, 1983 [DOI-CrossRef].
- [220] J. A. Lamas, L. Rueda-Ruzafa, and S. Herrera-Pérez, "Ion Channels and Thermosensitivity: TRP, TREK, or Both?," *International Journal of Molecular Sciences*, vol. 20, p. 2371, 2019 [DOI-CrossRef].
- [221] R. J. French and R. Horn, "Sodium channel gating: Models, mimics, and modifiers," *Annual Review of Biophysics and Bioengineering*, vol. 12, pp. 319–356, 1983 [DOI-CrossRef].
- [222] A. L. Hodgkin and A. F. Huxley, "A quantitative description of membrane current and its application to conduction and excitation in nerve," *The Journal of Physiology*, vol. 117, pp. 500–544, 1952 [DOI-CrossRef].
- [223] R. W. Tsien, "Calcium channels in excitable cell membranes," Annual Review of Physiology, vol. 45, pp. 341–358, 1983 [DOI-CrossRef].
- [224] B. Martinac, "Mechanosensitive ion channels: An evolutionary and scientific tour de force in mechanobiology," *Channels (Austin, Tex.)*, vol. 6, no. 4, pp. 211–213, 2012 [DOI-CrossRef].
- [225] H. T. Kratochvil, J. K. Carr, K. Matulef, A. W. Annen, H. Li, M. Maj, J. Ostmeyer, A. L. Serrano, H. Raghuraman, S. D. Moran, J. L. Skinner, E. Perozo, B. Roux, F. I. Valiyaveetil, and M. T. Zanni, "Instantaneous ion configurations in the K+ ion channel selectivity filter revealed by 2D IR spectroscopy," Science (New York, N.Y.), vol. 353, pp. 1040–1044, 2016 [DOI-CrossRef].
- [226] S. Y. Noskov, S. Bernèche, and B. Roux, "Control of ion selectivity in potassium channels by electrostatic and dynamic properties of carbonyl ligands," *Nature*, vol. 431, pp. 830–834, 2004 [DOI-CrossRef].
- [227] H. Yu, S. Y. Noskov, and B. Roux, "Two mechanisms of ion selectivity in protein binding sites," Proceedings of the National Academy of Sciences of the United States of America, vol. 107, pp. 20329–20334, 2010 [DOI-CrossRef].
- [228] D. Medovoy, E. Perozo, and B. Roux, "Multi-ion free energy landscapes underscore the microscopic mechanism of ion selectivity in the KcsA channel," *Biochimica et Biophysica Acta (BBA)* -

- Biomembranes, vol. 1858, pp. 1722–1732, 2016 [DOI-CrossRef].
- [229] B. Roux, S. Bernèche, B. Egwolf, B. Lev, S. Y. Noskov, C. N. Rowley, and H. Yu, "Ion selectivity in channels and transporters," *The Journal of General Physiology*, vol. 137, pp. 415–426, 2011 [DOI-CrossRef].
- [230] W. D. Stein and W. R. Lieb, Transport and Diffusion across Cell Membranes. Orlando: Academic Press, 1986.
- [231] M. Canessa, I. Bize, H. Solomon, N. Adragna, D. C. Tosteson, G. Dagher, R. Garay, and P. Meyer, "Na Countertransport and Cotransport in Human Red Cells: Function, Dysfunction, and Genes in Essential Hypertension," *Clinical and Experimental Hypertension*, vol. 3, pp. 783–795, 1981 [DOI-CrossRef].
- [232] L. R. Forrest, R. Krämer, and C. Ziegler, "The structural basis of secondary active transport mechanisms," *Biochimica et Biophysica Acta (BBA) Bioenergetics*, vol. 1807, pp. 167–188, 2011 [DOI-CrossRef].
- [233] R. M. Krupka, "Coupling mechanisms in active transport," *Biochimica Et Biophysica Acta*, vol. 1183, pp. 105–113, 1993 [DOI-CrossRef].
- [234] R. Blostein, "Ion pumps," Current Opinion in Cell Biology, vol. 1, pp. 746-752, 1989 [DOI-CrossRef].
- [235] G. A. Kimmich, "Intestinal absorption of sugar," *Physiology of the gastrointestinal tract*, vol. 2, pp. 1035–1061, 1981.
- [236] G. A. Kimmich, "Intestinal absorption of sugar," *Physiology of the gastrointestinal tract*, vol. 2, pp. 1035–1061, 1981.
- [237] R. K. Crane, "The gradient hypothesis and other models of carrier-mediated active transport," Reviews of Physiology, Biochemistry and Pharmacology, vol. 78, pp. 99–159, 1977 [DOI-CrossRef].
- [238] M. Alfonzo and E. Racker, "Components and mechanism of action of ATP-driven proton pumps," Canadian Journal of Biochemistry, vol. 57, pp. 1351–1358, 1979 [DOI-CrossRef].
- [239] H. E. Kato, K. Inoue, H. Kandori, and O. Nureki, "The light-driven sodium ion pump: A new player in rhodopsin research," *BioEssays: News and Reviews in Molecular, Cellular and Developmental Biology*, vol. 38, pp. 1274–1282, 2016 [DOI-CrossRef].
- [240] L. Reuss, "Mechanisms of Ion Transport Across Cell Membranes and Epithelia," in *Seldin and Giebisch's The Kidney*, pp. 35–56, Elsevier, 2008.
- [241] D. A. Eisner and S. C. Wray, "Ion pumping in biological membranes," *Contemporary Physics*, vol. 26, pp. 3–21, 1985 [DOI-CrossRef].
- [242] J. F. Giudicelli and C. Richer, "[Potassium channel activators: from pharmacology to therapeutics]," *Therapie*, vol. 44, no. 6, pp. 419–430, 1989.
- [243] S. P. Gupta, ed., Ion Channels and Their Inhibitors. Berlin, Heidelberg: Springer Berlin Heidelberg, 2011.
- [244] B. Coste, J. Mathur, M. Schmidt, T. J. Earley, S. Ranade, M. J. Petrus, A. E. Dubin, and A. Patapoutian, "Piezo1 and Piezo2 are essential components of distinct mechanically activated cation channels," *Science (New York, N.Y.)*, vol. 330, pp. 55–60, 2010 [DOI-CrossRef].
- [245] J. Ge, W. Li, Q. Zhao, N. Li, M. Chen, P. Zhi, R. Li, N. Gao, B. Xiao, and M. Yang, "Architecture of the mammalian mechanosensitive Piezo1 channel," *Nature*, vol. 527, pp. 64–69, 2015 [DOI-CrossRef].
- [246] Y. R. Guo and R. MacKinnon, "Structure-based membrane dome mechanism for Piezo mechanosensitivity," *eLife*, vol. 6, p. e33660, 2017 [DOI-CrossRef].
- [247] K. Saotome, S. E. Murthy, J. M. Kefauver, T. Whitwam, A. Patapoutian, and A. B. Ward, "Structure of the mechanically activated ion channel Piezol," *Nature*, vol. 554, pp. 481–486, 2018 [DOI-CrossRef].
- [248] L. Wang, H. Zhou, M. Zhang, W. Liu, T. Deng, Q. Zhao, Y. Li, J. Lei, X. Li, and B. Xiao, "Structure and mechanogating of the mammalian tactile channel PIEZO2," *Nature*, vol. 573, pp. 225–229, 2019 [DOI-CrossRef].
- [249] Q. Zhao, H. Zhou, S. Chi, Y. Wang, J. Wang, J. Geng, K. Wu, W. Liu, T. Zhang, M.-Q. Dong,

- J. Wang, X. Li, and B. Xiao, "Structure and mechanogating mechanism of the Piezo1 channel," *Nature*, vol. 554, pp. 487–492, 2018 [DOI-CrossRef].
- [250] M. Szczot, A. R. Nickolls, R. M. Lam, and A. T. Chesler, "The Form and Function of PIEZO2," *Annual Review of Biochemistry*, vol. 90, pp. 507–534, 2021 [DOI-CrossRef].
- [251] E.-F. Gautier, M. Leduc, S. Cochet, K. Bailly, C. Lacombe, N. Mohandas, F. Guillonneau, W. El Nemer, and P. Mayeux, "Absolute proteome quantification of highly purified populations of circulating reticulocytes and mature erythrocytes," *Blood Advances*, vol. 2, pp. 2646–2657, 2018 [DOI-CrossRef].
- [252] G. Vaisey, P. Banerjee, A. J. North, C. A. Haselwandter, and R. MacKinnon, "Piezo1 as a force-through-membrane sensor in red blood cells," *eLife*, vol. 11, p. e82621, 2022 [DOI-CrossRef].
- [253] X.-Z. Fang, T. Zhou, J.-Q. Xu, Y.-X. Wang, M.-M. Sun, Y.-J. He, S.-W. Pan, W. Xiong, Z.-K. Peng, X.-H. Gao, and Y. Shang, "Structure, kinetic properties and biological function of mechanosensitive Piezo channels," Cell & Bioscience, vol. 11, p. 13, 2021 [DOI-CrossRef].
- [254] Y. Wang, S. Chi, H. Guo, G. Li, L. Wang, Q. Zhao, Y. Rao, L. Zu, W. He, and B. Xiao, "A lever-like transduction pathway for long-distance chemical- and mechano-gating of the mechanosensitive Piezo1 channel," *Nature Communications*, vol. 9, p. 1300, 2018 [DOI-CrossRef].
- [255] C. Bae, F. Sachs, and P. A. Gottlieb, "Protonation of the human PIEZO1 ion channel stabilizes inactivation," *The Journal of Biological Chemistry*, vol. 290, pp. 5167–5173, 2015 [DOI-CrossRef].
- [256] C. D. Cox, C. Bae, L. Ziegler, S. Hartley, V. Nikolova-Krstevski, P. R. Rohde, C.-A. Ng, F. Sachs, P. A. Gottlieb, and B. Martinac, "Removal of the mechanoprotective influence of the cytoskeleton reveals PIEZO1 is gated by bilayer tension," *Nature Communications*, vol. 7, p. 10366, 2016 [DOI-CrossRef].
- [257] A. H. Lewis and J. Grandl, "Mechanical sensitivity of Piezo1 ion channels can be tuned by cellular membrane tension," *eLife*, vol. 4, p. e12088, 2015 [DOI-CrossRef].
- [258] R. Syeda, M. N. Florendo, C. D. Cox, J. M. Kefauver, J. S. Santos, B. Martinac, and A. Patapoutian, "Piezo1 Channels Are Inherently Mechanosensitive," *Cell Reports*, vol. 17, pp. 1739–1746, 2016 [DOI-CrossRef].
- [259] J. L. Nourse and M. M. Pathak, "How cells channel their stress: Interplay between Piezo1 and the cytoskeleton," *Seminars in Cell & Developmental Biology*, vol. 71, pp. 3–12, 2017 [DOI-CrossRef].
- [260] J. Li, B. Hou, S. Tumova, K. Muraki, A. Bruns, M. J. Ludlow, A. Sedo, A. J. Hyman, L. McKeown, R. S. Young, N. Y. Yuldasheva, Y. Majeed, L. A. Wilson, B. Rode, M. A. Bailey, H. R. Kim, Z. Fu, D. A. Carter, J. Bilton, H. Imrie, P. Ajuh, T. N. Dear, R. M. Cubbon, M. T. Kearney, R. K. Prasad, P. C. Evans, J. F. Ainscough, and D. J. Beech, "Piezo1 integration of vascular architecture with physiological force," *Nature*, vol. 515, pp. 279–282, 2014 [DOI-CrossRef].
- [261] S. S. Ranade, Z. Qiu, S.-H. Woo, S. S. Hur, S. E. Murthy, S. M. Cahalan, J. Xu, J. Mathur, M. Bandell, B. Coste, Y.-S. J. Li, S. Chien, and A. Patapoutian, "Piezo1, a mechanically activated ion channel, is required for vascular development in mice," *Proceedings of the National Academy of Sciences of the United States of America*, vol. 111, pp. 10347–10352, 2014 [DOI-CrossRef].
- [262] M. M. Pathak, J. L. Nourse, T. Tran, J. Hwe, J. Arulmoli, D. T. T. Le, E. Bernardis, L. A. Flanagan, and F. Tombola, "Stretch-activated ion channel Piezo1 directs lineage choice in human neural stem cells," Proceedings of the National Academy of Sciences of the United States of America, vol. 111, pp. 16148–16153, 2014 [DOI-CrossRef].
- [263] N. R. Blumenthal, O. Hermanson, B. Heimrich, and V. P. Shastri, "Stochastic nanoroughness modulates neuron-astrocyte interactions and function via mechanosensing cation channels," *Proceedings of the National Academy of Sciences of the United States of America*, vol. 111, pp. 16124–16129, 2014 [DOI-CrossRef].
- [264] W.-C. Hung, J. R. Yang, C. L. Yankaskas, B. S. Wong, P.-H. Wu, C. Pardo-Pastor, S. A. Serra, M.-J. Chiang, Z. Gu, D. Wirtz, M. A. Valverde, J. T. Yang, J. Zhang, and K. Konstantopoulos, "Confinement Sensing and Signal Optimization via Piezo1/PKA and Myosin II Pathways," Cell Reports, vol. 15, pp. 1430–1441, 2016 [DOI-CrossRef].

[265] R. Gnanasambandam, C. Ghatak, A. Yasmann, K. Nishizawa, F. Sachs, A. S. Ladokhin, S. I. Sukharev, and T. M. Suchyna, "GsMTx4: Mechanism of Inhibiting Mechanosensitive Ion Channels," *Biophysical Journal*, vol. 112, pp. 31–45, 2017 [DOI-CrossRef].

- [266] R. Gnanasambandam, C. Bae, P. A. Gottlieb, and F. Sachs, "Ionic Selectivity and Permeation Properties of Human PIEZO1 Channels," *PloS One*, vol. 10, no. 5, p. e0125503, 2015 [DOI-CrossRef].
- [267] T. Zhang, S. Chi, F. Jiang, Q. Zhao, and B. Xiao, "A protein interaction mechanism for suppressing the mechanosensitive Piezo channels," *Nature Communications*, vol. 8, p. 1797, 2017 [DOI-CrossRef].
- [268] R. Peyronnet, J. R. Martins, F. Duprat, S. Demolombe, M. Arhatte, M. Jodar, M. Tauc, C. Duranton, M. Paulais, J. Teulon, E. Honoré, and A. Patel, "Piezo1-dependent stretch-activated channels are inhibited by Polycystin-2 in renal tubular epithelial cells," *EMBO reports*, vol. 14, pp. 1143–1148, 2013 [DOI-CrossRef].
- [269] C. Wetzel, S. Pifferi, C. Picci, C. Gök, D. Hoffmann, K. K. Bali, A. Lampe, L. Lapatsina, R. Fleischer, E. S. J. Smith, V. Bégay, M. Moroni, L. Estebanez, J. Kühnemund, J. Walcher, E. Specker, M. Neuenschwander, J. P. von Kries, V. Haucke, R. Kuner, J. F. A. Poulet, J. Schmoranzer, K. Poole, and G. R. Lewin, "Small-molecule inhibition of STOML3 oligomerization reverses pathological mechanical hypersensitivity," *Nature Neuroscience*, vol. 20, pp. 209–218, 2017 [DOI-CrossRef].
- [270] X.-N. Yang, Y.-P. Lu, J.-J. Liu, J.-K. Huang, Y.-P. Liu, C.-X. Xiao, A. Jazag, J.-L. Ren, and B. Guleng, "Piezo1 is as a novel trefoil factor family 1 binding protein that promotes gastric cancer cell mobility in vitro," *Digestive Diseases and Sciences*, vol. 59, pp. 1428–1435, 2014 [DOI-CrossRef].
- [271] J. Wang, J. Jiang, X. Yang, L. Wang, and B. Xiao, "Tethering Piezo channels to the actin cytoskeleton for mechanogating via the E-cadherin-\$\beta\$-catenin mechanotransduction complex," preprint, Neuroscience, 2020.
- [272] S. N. Bagriantsev, E. O. Gracheva, and P. G. Gallagher, "Piezo proteins: Regulators of mechanosensation and other cellular processes," *The Journal of Biological Chemistry*, vol. 289, pp. 31673–31681, 2014 [DOI-CrossRef].
- [273] R. Syeda, J. Xu, A. E. Dubin, B. Coste, J. Mathur, T. Huynh, J. Matzen, J. Lao, D. C. Tully, I. H. Engels, H. M. Petrassi, A. M. Schumacher, M. Montal, M. Bandell, and A. Patapoutian, "Chemical activation of the mechanotransduction channel Piezo1," eLife, vol. 4, p. e07369, 2015 [DOI-CrossRef].
- [274] G. Parsonage, K. Cuthbertson, N. Endesh, N. Murciano, A. J. Hyman, C. H. Revill, O. V. Povstyan, E. Chuntharpursat-Bon, M. Debant, M. J. Ludlow, T. S. Futers, L. Lichtenstein, J. A. Kinsella, F. Bartoli, M. G. Rotordam, N. Becker, A. Brüggemann, R. Foster, and D. J. Beech, "Improved PIEZO1 agonism through 4-benzoic acid modification of Yoda1," *British Journal of Pharmacology*, vol. 180, pp. 2039–2063, 2023 [DOI-CrossRef].
- [275] C. Bae, F. Sachs, and P. A. Gottlieb, "The mechanosensitive ion channel Piezo1 is inhibited by the peptide GsMTx4," *Biochemistry*, vol. 50, pp. 6295–6300, 2011 [DOI-CrossRef].
- [276] T. M. Suchyna, "Piezo channels and GsMTx4: Two milestones in our understanding of excitatory mechanosensitive channels and their role in pathology," *Progress in Biophysics and Molecular Biology*, vol. 130, pp. 244–253, 2017 [DOI-CrossRef].
- [277] A. Faucherre, K. Kissa, J. Nargeot, M. E. Mangoni, and C. Jopling, "Piezo1 plays a role in erythrocyte volume homeostasis," *Haematologica*, vol. 99, pp. 70–75, 2014 [DOI-CrossRef].
- [278] S. M. Cahalan, V. Lukacs, S. S. Ranade, S. Chien, M. Bandell, and A. Patapoutian, "Piezo1 links mechanical forces to red blood cell volume," *eLife*, vol. 4, p. e07370, 2015 [DOI-CrossRef].
- [279] E. Cinar, S. Zhou, J. DeCourcey, Y. Wang, R. E. Waugh, and J. Wan, "Piezo1 regulates mechanotransductive release of ATP from human RBCs," *Proceedings of the National Academy of Sciences of the United States of America*, vol. 112, pp. 11783–11788, 2015 [DOI-CrossRef].
- [280] L. Kuck, J. N. Peart, and M. J. Simmonds, "Piezo1 regulates shear-dependent nitric oxide production in human erythrocytes," American Journal of Physiology-Heart and Circulatory Physiology, vol. 323, pp. H24–H37, 2022 [DOI-CrossRef].
- [281] A. Caulier and L. Garçon, "PIEZO1, sensing the touch during erythropoiesis," Current Opinion in

- Hematology, vol. 29, pp. 112–118, 2022 [DOI-CrossRef].
- [282] I. Andolfo, B. E. Rosato, F. Manna, G. De Rosa, R. Marra, A. Gambale, D. Girelli, R. Russo, and A. Iolascon, "Gain-of-function mutations in PIEZO1 directly impair hepatic iron metabolism via the inhibition of the BMP/SMADs pathway," *American Journal of Hematology*, vol. 95, pp. 188–197, 2020 [DOI-CrossRef].
- [283] S. Ma, A. E. Dubin, Y. Zhang, S. A. R. Mousavi, Y. Wang, A. M. Coombs, M. Loud, I. Andolfo, and A. Patapoutian, "A role of PIEZO1 in iron metabolism in mice and humans," *Cell*, vol. 184, pp. 969–982.e13, 2021 [DOI-CrossRef].
- [284] S. Martin-Almedina, S. Mansour, and P. Ostergaard, "Human phenotypes caused by PIEZO1 mutations; one gene, two overlapping phenotypes?," The Journal of Physiology, vol. 596, pp. 985–992, 2018 [DOI-CrossRef].
- [285] H. Zhu, W. He, P. Ye, J. Chen, X. Wu, X. Mu, Y. Wu, H. Pang, F. Han, and X. Nie, "Piezo1 in skin wound healing and related diseases: Mechanotransduction and therapeutic implications," *International Immunopharmacology*, vol. 123, p. 110779, 2023 [DOI-CrossRef].
- [286] C. Montell and G. M. Rubin, "Molecular characterization of the Drosophila trp locus: A putative integral membrane protein required for phototransduction," *Neuron*, vol. 2, pp. 1313–1323, 1989 [DOI-CrossRef].
- [287] P. D. Wes, J. Chevesich, A. Jeromin, C. Rosenberg, G. Stetten, and C. Montell, "TRPC1, a human homolog of a Drosophila store-operated channel," *Proceedings of the National Academy of Sciences* of the United States of America, vol. 92, pp. 9652–9656, 1995 [DOI-CrossRef].
- [288] X. Zhu, P. B. Chu, M. Peyton, and L. Birnbaumer, "Molecular cloning of a widely expressed human homologue for the Drosophila trp gene," *FEBS letters*, vol. 373, pp. 193–198, 1995 [DOI-CrossRef].
- [289] M. Gees, B. Colsoul, and B. Nilius, "The role of transient receptor potential cation channels in Ca2+ signaling," *Cold Spring Harbor Perspectives in Biology*, vol. 2, p. a003962, 2010 [DOI-CrossRef].
- [290] M. Gees, G. Owsianik, B. Nilius, and T. Voets, "TRP channels," Comprehensive Physiology, vol. 2, pp. 563–608, 2012 [DOI-CrossRef].
- [291] B. Nilius and G. Owsianik, "The transient receptor potential family of ion channels," *Genome Biology*, vol. 12, no. 3, p. 218, 2011 [DOI-CrossRef].
- [292] L.-J. Wu, T.-B. Sweet, and D. E. Clapham, "International Union of Basic and Clinical Pharmacology. LXXVI. Current progress in the mammalian TRP ion channel family," *Pharmacological Reviews*, vol. 62, pp. 381–404, 2010 [DOI-CrossRef].
- [293] H. Li, "TRP Channel Classification," Advances in Experimental Medicine and Biology, vol. 976, pp. 1–8, 2017 [DOI-CrossRef].
- [294] A. Samanta, T. E. T. Hughes, and V. Y. Moiseenkova-Bell, "Transient Receptor Potential (TRP) Channels," Sub-Cellular Biochemistry, vol. 87, pp. 141–165, 2018 [DOI-CrossRef].
- [295] M. J. Caterina, T. A. Rosen, M. Tominaga, A. J. Brake, and D. Julius, "A capsaicin-receptor homologue with a high threshold for noxious heat," *Nature*, vol. 398, pp. 436–441, 1999 [DOI-CrossRef].
- [296] K. Venkatachalam and C. Montell, "TRP channels," Annual Review of Biochemistry, vol. 76, pp. 387–417, 2007 [DOI-CrossRef].
- [297] C. D. Benham, M. J. Gunthorpe, and J. B. Davis, "TRPV channels as temperature sensors," *Cell Calcium*, vol. 33, no. 5-6, pp. 479–487, 2003 [DOI-CrossRef].
- [298] M. Tominaga and M. J. Caterina, "Thermosensation and pain," Journal of Neurobiology, vol. 61, pp. 3–12, 2004 [DOI-CrossRef].
- [299] K. Muraki, Y. Iwata, Y. Katanosaka, T. Ito, S. Ohya, M. Shigekawa, and Y. Imaizumi, "TRPV2 is a component of osmotically sensitive cation channels in murine aortic myocytes," *Circulation Research*, vol. 93, pp. 829–838, 2003 [DOI-CrossRef].
- [300] L. Zubcevic, M. A. Herzik, B. C. Chung, Z. Liu, G. C. Lander, and S.-Y. Lee, "Cryo-electron microscopy structure of the TRPV2 ion channel," *Nature Structural & Molecular Biology*, vol. 23,

- pp. 180–186, 2016 [DOI-CrossRef].
- [301] N. Qin, M. P. Neeper, Y. Liu, T. L. Hutchinson, M. L. Lubin, and C. M. Flores, "TRPV2 is activated by cannabidiol and mediates CGRP release in cultured rat dorsal root ganglion neurons," The Journal of Neuroscience: The Official Journal of the Society for Neuroscience, vol. 28, pp. 6231–6238, 2008 [DOI-CrossRef].
- [302] L. De Petrocellis, A. Ligresti, A. S. Moriello, M. Allarà, T. Bisogno, S. Petrosino, C. G. Stott, and V. Di Marzo, "Effects of cannabinoids and cannabinoid-enriched Cannabis extracts on TRP channels and endocannabinoid metabolic enzymes," *British Journal of Pharmacology*, vol. 163, pp. 1479–1494, 2011 [DOI-CrossRef].
- [303] H.-Z. Hu, Q. Gu, C. Wang, C. K. Colton, J. Tang, M. Kinoshita-Kawada, L.-Y. Lee, J. D. Wood, and M. X. Zhu, "2-aminoethoxydiphenyl borate is a common activator of TRPV1, TRPV2, and TRPV3," The Journal of Biological Chemistry, vol. 279, pp. 35741–35748, 2004 [DOI-CrossRef].
- [304] V. Juvin, A. Penna, J. Chemin, Y.-L. Lin, and F.-A. Rassendren, "Pharmacological characterization and molecular determinants of the activation of transient receptor potential V2 channel orthologs by 2-aminoethoxydiphenyl borate," *Molecular Pharmacology*, vol. 72, pp. 1258–1268, 2007 [DOI-CrossRef].
- [305] S. Bang, K. Y. Kim, S. Yoo, S.-H. Lee, and S. W. Hwang, "Transient receptor potential V2 expressed in sensory neurons is activated by probenecid," *Neuroscience Letters*, vol. 425, pp. 120–125, 2007 [DOI-CrossRef].
- [306] Y. Iwata, S. Ito, S. Wakabayashi, and M. Kitakaze, "TRPV2 channel as a possible drug target for the treatment of heart failure," *Laboratory Investigation*, vol. 100, pp. 207–217, 2020 [DOI-CrossRef].
- [307] M. P. Neeper, Y. Liu, T. L. Hutchinson, Y. Wang, C. M. Flores, and N. Qin, "Activation properties of heterologously expressed mammalian TRPV2: Evidence for species dependence," *The Journal of Biological Chemistry*, vol. 282, pp. 15894–15902, 2007 [DOI-CrossRef].
- [308] A. Leffler, R. M. Linte, C. Nau, P. Reeh, and A. Babes, "A high-threshold heat-activated channel in cultured rat dorsal root ganglion neurons resembles TRPV2 and is blocked by gadolinium," *The European Journal of Neuroscience*, vol. 26, pp. 12–22, 2007 [DOI-CrossRef].
- [309] A. Schiano Moriello, S. López Chinarro, O. Novo Fernández, J. Eras, P. Amodeo, R. Canela-Garayoa, R. M. Vitale, V. Di Marzo, and L. De Petrocellis, "Elongation of the Hydrophobic Chain as a Molecular Switch: Discovery of Capsaicin Derivatives and Endogenous Lipids as Potent Transient Receptor Potential Vanilloid Channel 2 Antagonists," *Journal of Medicinal Chemistry*, vol. 61, pp. 8255–8281, 2018 [DOI-CrossRef].
- [310] A. Belkacemi, C. F. Trost, R. Tinschert, D. Flormann, M. Malihpour, C. Wagner, M. R. Meyer, A. Beck, and V. Flockerzi, "The TRPV2 channel mediates Ca2+ influx and the Δ9-THC-dependent decrease in osmotic fragility in red blood cells," *Haematologica*, vol. 106, pp. 2246–2250, 2021 [DOI-CrossRef].
- [311] S. Egée and L. Kaestner, "The Transient Receptor Potential Vanilloid Type 2 (TRPV2) Channel-A New Druggable Ca2+ Pathway in Red Cells, Implications for Red Cell Ion Homeostasis," Frontiers in Physiology, vol. 12, p. 677573, 2021 [DOI-CrossRef].
- [312] A. Chari-Bitron and A. Shahar, "Changes in rat erythrocyte membrane induced by delta 1-tetrahydrocannabinol, scanning electron microscope study," *Experientia*, vol. 35, pp. 365–366, 1979 [DOI-CrossRef].
- [313] D. I. Abrams, "The therapeutic effects of Cannabis and cannabinoids: An update from the National Academies of Sciences, Engineering and Medicine report," *European Journal of Internal Medicine*, vol. 49, pp. 7–11, 2018 [DOI-CrossRef].
- [314] L. Rapin, R. Gamaoun, C. El Hage, M. F. Arboleda, and E. Prosk, "Cannabidiol use and effectiveness: Real-world evidence from a Canadian medical cannabis clinic," *Journal of Cannabis Research*, vol. 3, p. 19, 2021 [DOI-CrossRef].
- [315] C. H. Joiner, "Gardos pathway to sickle cell therapies?," *Blood*, vol. 111, pp. 3918–3919, 2008 [DOI-CrossRef].

[316] L. Sforna, A. Megaro, M. Pessia, F. Franciolini, and L. Catacuzzeno, "Structure, Gating and Basic Functions of the Ca2+-activated K Channel of Intermediate Conductance," Current Neuropharmacology, vol. 16, no. 5, pp. 608–617, 2018 [DOI-CrossRef].

- [317] S. Ghanshani, M. Coleman, P. Gustavsson, A. C. Wu, J. J. Gargus, G. A. Gutman, N. Dahl, H. Mohrenweiser, and K. G. Chandy, "Human calcium-activated potassium channel gene KCNN4 maps to chromosome 19q13.2 in the region deleted in diamond-blackfan anemia," *Genomics*, vol. 51, pp. 160–161, 1998 [DOI-CrossRef].
- [318] Y. Jiang, A. Lee, J. Chen, M. Cadene, B. T. Chait, and R. MacKinnon, "Crystal structure and mechanism of a calcium-gated potassium channel," *Nature*, vol. 417, pp. 515–522, 2002 [DOI-CrossRef].
- [319] D. H. Vandorpe, B. E. Shmukler, L. Jiang, B. Lim, J. Maylie, J. P. Adelman, L. de Franceschi, M. D. Cappellini, C. Brugnara, and S. L. Alper, "cDNA cloning and functional characterization of the mouse Ca2+-gated K+ channel, mIK1. Roles in regulatory volume decrease and erythroid differentiation," The Journal of Biological Chemistry, vol. 273, pp. 21542–21553, 1998 [DOI-CrossRef].
- [320] C. M. Fanger, S. Ghanshani, N. J. Logsdon, H. Rauer, K. Kalman, J. Zhou, K. Beckingham, K. G. Chandy, M. D. Cahalan, and J. Aiyar, "Calmodulin mediates calcium-dependent activation of the intermediate conductance KCa channel, IKCa1," *The Journal of Biological Chemistry*, vol. 274, pp. 5746–5754, 1999 [DOI-CrossRef].
- [321] T. Leinders, R. G. Kleef, and H. P. Vijverberg, "Single Ca2+-activated k+ channels in human erythrocytes: Ca2+ dependence of opening frequency but not of open lifetimes," *Biochimica et Biophysica Acta (BBA) Biomembranes*, vol. 1112, pp. 67–74, 1992 [DOI-CrossRef].
- [322] R. Wong and L. C. Schlichter, "PKA reduces the rat and human KCa3.1 current, CaM binding, and Ca2+ signaling, which requires Ser332/334 in the CaM-binding C terminus," *The Journal of Neuroscience: The Official Journal of the Society for Neuroscience*, vol. 34, pp. 13371–13383, 2014 [DOI-CrossRef].
- [323] S. Srivastava, P. Choudhury, Z. Li, G. Liu, V. Nadkarni, K. Ko, W. A. Coetzee, and E. Y. Skolnik, "Phosphatidylinositol 3-phosphate indirectly activates KCa3.1 via 14 amino acids in the carboxy terminus of KCa3.1," *Molecular Biology of the Cell*, vol. 17, pp. 146–154, 2006 [DOI-CrossRef].
- [324] S. Srivastava, Z. Li, L. Lin, G. Liu, K. Ko, W. A. Coetzee, and E. Y. Skolnik, "The phosphatidylinositol 3-phosphate phosphatase myotubularin-related protein 6 (MTMR6) is a negative regulator of the Ca2+-activated K+ channel KCa3.1," *Molecular and Cellular Biology*, vol. 25, pp. 3630–3638, 2005 [DOI-CrossRef].
- [325] H. Klein, L. Garneau, N. T. N. Trinh, A. Privé, F. Dionne, E. Goupil, D. Thuringer, L. Parent, E. Brochiero, and R. Sauvé, "Inhibition of the KCa3.1 channels by AMP-activated protein kinase in human airway epithelial cells," *American Journal of Physiology. Cell Physiology*, vol. 296, pp. C285–295, 2009 [DOI-CrossRef].
- [326] S. Srivastava, O. Zhdanova, L. Di, Z. Li, M. Albaqumi, H. Wulff, and E. Y. Skolnik, "Protein histidine phosphatase 1 negatively regulates CD4 T cells by inhibiting the K+ channel KCa3.1," Proceedings of the National Academy of Sciences of the United States of America, vol. 105, pp. 14442–14446, 2008 [DOI-CrossRef].
- [327] D. C. Devor, A. K. Singh, R. A. Frizzell, and R. J. Bridges, "Modulation of Cl- secretion by benzimidazolones. I. Direct activation of a Ca(2+)-dependent K+ channel," *The American Journal of Physiology*, vol. 271, pp. L775–784, 1996 [DOI-CrossRef].
- [328] H. Wulff and R. Köhler, "Endothelial small-conductance and intermediate-conductance KCa channels: An update on their pharmacology and usefulness as cardiovascular targets," *Journal of Cardiovascular Pharmacology*, vol. 61, pp. 102–112, 2013 [DOI-CrossRef].
- [329] A. Sankaranarayanan, G. Raman, C. Busch, T. Schultz, P. I. Zimin, J. Hoyer, R. Köhler, and H. Wulff, "Naphtho[1,2-d]thiazol-2-ylamine (SKA-31), a new activator of KCa2 and KCa3.1 potassium channels, potentiates the endothelium-derived hyperpolarizing factor response and lowers blood pressure," *Molecular Pharmacology*, vol. 75, pp. 281–295, 2009 [DOI-CrossRef].
- [330] D. Strøbaek, L. Teuber, T. D. Jørgensen, P. K. Ahring, K. Kjaer, R. S. Hansen, S. P. Olesen,

P. Christophersen, and B. Skaaning-Jensen, "Activation of human IK and SK Ca2+ -activated K+ channels by NS309 (6,7-dichloro-1H-indole-2,3-dione 3-oxime)," *Biochimica Et Biophysica Acta*, vol. 1665, pp. 1–5, 2004 [DOI-CrossRef].

- [331] J. C. Ellory, G. B. Nash, P. C. Stone, S. J. Culliford, E. Horwitz, and J. Stuart, "Mode of action and comparative efficacy of pharmacological agents that inhibit calcium-dependent dehydration of sickle cells," *British Journal of Pharmacology*, vol. 106, pp. 972–977, 1992 [DOI-CrossRef].
- [332] C. Brugnara, L. De Franceschi, and S. Alper, "Ca(2+)-activated K+ transport in erythrocytes. Comparison of binding and transport inhibition by scorpion toxins.," *Journal of Biological Chemistry*, vol. 268, pp. 8760–8768, 1993 [DOI-CrossRef].
- [333] C. Brugnara, L. De Franceschi, and S. L. Alper, "Inhibition of Ca(2+)-dependent K+ transport and cell dehydration in sickle erythrocytes by clotrimazole and other imidazole derivatives.," *Journal of Clinical Investigation*, vol. 92, pp. 520–526, 1993 [DOI-CrossRef].
- [334] N. A. Castle, D. O. London, C. Creech, Z. Fajloun, J. W. Stocker, and J.-M. Sabatier, "Maurotoxin: A potent inhibitor of intermediate conductance Ca2+-activated potassium channels," *Molecular Pharmacology*, vol. 63, pp. 409–418, 2003 [DOI-CrossRef].
- [335] D. Wolff, X. Cecchi, A. Spalvins, and M. Canessa, "Charybdotoxin blocks with high affinity the Ca-activated K+ channel of Hb A and Hb S red cells: Individual differences in the number of channels," *The Journal of Membrane Biology*, vol. 106, pp. 243–252, 1988 [DOI-CrossRef].
- [336] O. Scharff and B. Foder, "Halothane inhibits hyperpolarization and potassium channels in human red blood cells," *European Journal of Pharmacology*, vol. 159, pp. 165–173, 1989 [DOI-CrossRef].
- [337] J. Alvarez, M. Montero, and J. Garcia-Sancho, "High affinity inhibition of Ca(2+)-dependent K+ channels by cytochrome P-450 inhibitors," *The Journal of Biological Chemistry*, vol. 267, pp. 11789–11793, 1992.
- [338] H. Wulff, M. J. Miller, W. Hansel, S. Grissmer, M. D. Cahalan, and K. G. Chandy, "Design of a potent and selective inhibitor of the intermediate-conductance Ca2+-activated K+ channel, IKCa1: A potential immunosuppressant," *Proceedings of the National Academy of Sciences of the United States of America*, vol. 97, pp. 8151–8156, 2000 [DOI-CrossRef].
- [339] R. Grygorczyk, W. Schwarz, and H. Passow, "Ca2+-activated K+ channels in human red cells. Comparison of single-channel currents with ion fluxes," *Biophysical Journal*, vol. 45, pp. 693–698, 1984 [DOI-CrossRef].
- [340] L. Kaestner, A. Bogdanova, and S. Egee, "Calcium Channels and Calcium-Regulated Channels in Human Red Blood Cells," *Advances in Experimental Medicine and Biology*, vol. 1131, pp. 625–648, 2020 [DOI-CrossRef].
- [341] I. Andolfo, S. L. Alper, L. De Franceschi, C. Auriemma, R. Russo, L. De Falco, F. Vallefuoco, M. R. Esposito, D. H. Vandorpe, B. E. Shmukler, R. Narayan, D. Montanaro, M. D'Armiento, A. Vetro, I. Limongelli, O. Zuffardi, B. E. Glader, S. L. Schrier, C. Brugnara, G. W. Stewart, J. Delaunay, and A. Iolascon, "Multiple clinical forms of dehydrated hereditary stomatocytosis arise from mutations in PIEZO1," *Blood*, vol. 121, pp. 3925–3935, S1–12, 2013 [DOI-CrossRef].
- [342] E. Glogowska, K. Lezon-Geyda, Y. Maksimova, V. P. Schulz, and P. G. Gallagher, "Mutations in the Gardos channel (KCNN4) are associated with hereditary xerocytosis," *Blood*, vol. 126, pp. 1281–1284, 2015 [DOI-CrossRef].
- [343] R. Rapetti-Mauss, C. Lacoste, V. Picard, C. Guitton, E. Lombard, M. Loosveld, V. Nivaggioni, N. Dasilva, D. Salgado, J.-P. Desvignes, C. Béroud, P. Viout, M. Bernard, O. Soriani, H. Vinti, V. Lacroze, M. Feneant-Thibault, I. Thuret, H. Guizouarn, and C. Badens, "A mutation in the Gardos channel is associated with hereditary xerocytosis," *Blood*, vol. 126, pp. 1273–1280, 2015 [DOI-CrossRef].
- [344] E. Fermo, A. Bogdanova, P. Petkova-Kirova, A. Zaninoni, A. P. Marcello, A. Makhro, P. Hänggi, L. Hertz, J. Danielczok, C. Vercellati, N. Mirra, A. Zanella, A. Cortelezzi, W. Barcellini, L. Kaestner, and P. Bianchi, "'Gardos Channelopathy': A variant of hereditary Stomatocytosis with complex molecular regulation," *Scientific Reports*, vol. 7, p. 1744, 2017 [DOI-CrossRef].

[345] C.-H. Lee and R. MacKinnon, "Activation mechanism of a human SK-calmodulin channel complex elucidated by cryo-EM structures," *Science*, vol. 360, pp. 508–513, 2018 [DOI-CrossRef].

- [346] Y.-W. Nam, M. Downey, M. A. Rahman, M. Cui, and M. Zhang, "Channelopathy of small- and intermediate-conductance Ca2+-activated K+ channels," *Acta Pharmacologica Sinica*, vol. 44, pp. 259–267, 2023 [DOI-CrossRef].
- [347] P. Fatt and B. Katz, "The electrical properties of crustacean muscle fibres," *The Journal of Physiology*, vol. 120, pp. 171–204, 1953 [DOI-CrossRef].
- [348] S. Hagiwara, S. Ozawa, and O. Sand, "Voltage clamp analysis of two inward current mechanisms in the egg cell membrane of a starfish," *The Journal of General Physiology*, vol. 65, pp. 617–644, 1975 [DOI-CrossRef].
- [349] E. Carbone and H. D. Lux, "A low voltage-activated, fully inactivating Ca channel in vertebrate sensory neurones," *Nature*, vol. 310, no. 5977, pp. 501–502, 1984-08-09/0015 [DOI-CrossRef].
- [350] S. A. Fedulova, P. G. Kostyuk, and N. S. Veselovsky, "Two types of calcium channels in the somatic membrane of new-born rat dorsal root ganglion neurones," *The Journal of Physiology*, vol. 359, pp. 431–446, 1985 [DOI-CrossRef].
- [351] D. Hillman, S. Chen, T. T. Aung, B. Cherksey, M. Sugimori, and R. R. Llinás, "Localization of P-type calcium channels in the central nervous system," *Proceedings of the National Academy of Sciences of the United States of America*, vol. 88, pp. 7076–7080, 1991 [DOI-CrossRef].
- [352] M. C. Nowycky, A. P. Fox, and R. W. Tsien, "Three types of neuronal calcium channel with different calcium agonist sensitivity," *Nature*, vol. 316, no. 6027, pp. 440–443, 1985-08-01/0007 [DOI-CrossRef].
- [353] A. Randall and R. W. Tsien, "Pharmacological dissection of multiple types of Ca2+ channel currents in rat cerebellar granule neurons," The Journal of Neuroscience: The Official Journal of the Society for Neuroscience, vol. 15, pp. 2995–3012, 1995 [DOI-CrossRef].
- [354] W. A. Catterall, "Structure and regulation of voltage-gated Ca2+ channels," Annual Review of Cell and Developmental Biology, vol. 16, pp. 521–555, 2000 [DOI-CrossRef].
- [355] A. C. Dolphin, "Beta subunits of voltage-gated calcium channels," *Journal of Bioenergetics and Biomembranes*, vol. 35, pp. 599–620, 2003 [DOI-CrossRef].
- [356] E. A. Ertel, K. P. Campbell, M. M. Harpold, F. Hofmann, Y. Mori, E. Perez-Reyes, A. Schwartz, T. P. Snutch, T. Tanabe, L. Birnbaumer, R. W. Tsien, and W. A. Catterall, "Nomenclature of voltage-gated calcium channels," *Neuron*, vol. 25, pp. 533-535, 2000 [DOI-CrossRef].
- [357] T. P. Snutch and P. B. Reiner, "Ca2+ channels: Diversity of form and function," Current Opinion in Neurobiology, vol. 2, pp. 247–253, 1992 [DOI-CrossRef].
- [358] W. A. Catterall, "Voltage-gated calcium channels," Cold Spring Harbor Perspectives in Biology, vol. 3, p. a003947, 2011 [DOI-CrossRef].
- [359] S. H. Heinemann, H. Terlau, W. Stühmer, K. Imoto, and S. Numa, "Calcium channel characteristics conferred on the sodium channel by single mutations," *Nature*, vol. 356, pp. 441–443, 1992 [DOI-CrossRef].
- [360] W. A. Catterall, M. J. Lenaeus, and T. M. Gamal El-Din, "Structure and Pharmacology of Voltage-Gated Sodium and Calcium Channels," *Annual Review of Pharmacology and Toxicology*, vol. 60, pp. 133–154, 2020 [DOI-CrossRef].
- [361] F. Findeisen and D. L. Minor, Jr., "Progress in the structural understanding of voltage-gated calcium channel (Ca _V) function and modulation," *Channels*, vol. 4, pp. 459–474, 2010 [DOI-CrossRef].
- [362] V. Nimmrich and G. Gross, "P/Q-type calcium channel modulators," *British Journal of Pharmacology*, vol. 167, pp. 741–759, 2012 [DOI-CrossRef].
- [363] R. Llinás, M. Sugimori, J. W. Lin, and B. Cherksey, "Blocking and isolation of a calcium channel from neurons in mammals and cephalopods utilizing a toxin fraction (FTX) from funnel-web spider poison," Proceedings of the National Academy of Sciences of the United States of America, vol. 86, pp. 1689–1693, 1989 [DOI-CrossRef].

[364] R. S. Kass and M. C. Sanguinetti, "Inactivation of calcium channel current in the calf cardiac Purkinje fiber. Evidence for voltage- and calcium-mediated mechanisms.," *The Journal of general physiology*, vol. 84, pp. 705–726, 1984 [DOI-CrossRef].

- [365] B. Hille, "Modulation of ion-channel function by G-protein-coupled receptors," *Trends in Neuro-sciences*, vol. 17, pp. 531–536, 1994 [DOI-CrossRef].
- [366] I. Bezprozvanny, R. H. Scheller, and R. W. Tsien, "Functional impact of syntaxin on gating of N-type and Q-type calcium channels," *Nature*, vol. 378, pp. 623–626, 1995 [DOI-CrossRef].
- [367] H. Zhong, C. T. Yokoyama, T. Scheuer, and W. A. Catterall, "Reciprocal regulation of P/Q-type Ca2+ channels by SNAP-25, syntaxin and synaptotagmin," *Nature Neuroscience*, vol. 2, pp. 939–941, 1999 [DOI-CrossRef].
- [368] M. G. Erickson, B. A. Alseikhan, B. Z. Peterson, and D. T. Yue, "Preassociation of calmodulin with voltage-gated Ca(2+) channels revealed by FRET in single living cells," *Neuron*, vol. 31, pp. 973–985, 2001 [DOI-CrossRef].
- [369] A. Lee, H. Zhou, T. Scheuer, and W. A. Catterall, "Molecular determinants of Ca(2+)/calmodulin-dependent regulation of Ca(v)2.1 channels," *Proceedings of the National Academy of Sciences of the United States of America*, vol. 100, pp. 16059–16064, 2003 [DOI-CrossRef].
- [370] A. Lee, S. T. Wong, D. Gallagher, B. Li, D. R. Storm, T. Scheuer, and W. A. Catterall, "Ca2+/calmodulin binds to and modulates P/Q-type calcium channels," *Nature*, vol. 399, pp. 155–159, 1999 [DOI-CrossRef].
- [371] S. Mochida, A. P. Few, T. Scheuer, and W. A. Catterall, "Regulation of presynaptic Ca(V)2.1 channels by Ca2+ sensor proteins mediates short-term synaptic plasticity," *Neuron*, vol. 57, pp. 210–216, 2008 [DOI-CrossRef].
- [372] M. E. Adams, "Agatoxins: Ion channel specific toxins from the American funnel web spider, Agelenopsis aperta," *Toxicon: Official Journal of the International Society on Toxinology*, vol. 43, pp. 509–525, 2004 [DOI-CrossRef].
- [373] M. E. Adams, I. M. Mintz, M. D. Reily, V. Thanabal, and B. P. Bean, "Structure and properties of omega-agatoxin IVB, a new antagonist of P-type calcium channels," *Molecular Pharmacology*, vol. 44, pp. 681–688, 1993.
- [374] E. Bourinet, T. W. Soong, K. Sutton, S. Slaymaker, E. Mathews, A. Monteil, G. W. Zamponi, J. Nargeot, and T. P. Snutch, "Splicing of alpha 1A subunit gene generates phenotypic variants of P- and Q-type calcium channels," *Nature Neuroscience*, vol. 2, pp. 407–415, 1999 [DOI-CrossRef].
- [375] I. M. Mintz, V. J. Venema, K. M. Swiderek, T. D. Lee, B. P. Bean, and M. E. Adams, "P-type calcium channels blocked by the spider toxin omega-Aga-IVA," *Nature*, vol. 355, pp. 827–829, 1992 [DOI-CrossRef].
- [376] I. M. Mintz, M. E. Adams, and B. P. Bean, "P-type calcium channels in rat central and peripheral neurons," *Neuron*, vol. 9, pp. 85–95, 1992 [DOI-CrossRef].
- [377] G. W. Zamponi, J. Striessnig, A. Koschak, and A. C. Dolphin, "The Physiology, Pathology, and Pharmacology of Voltage-Gated Calcium Channels and Their Future Therapeutic Potential," *Pharmacological Reviews*, vol. 67, pp. 821–870, 2015 [DOI-CrossRef].
- [378] J. G. Danielczok, E. Terriac, L. Hertz, P. Petkova-Kirova, F. Lautenschläger, M. W. Laschke, and L. Kaestner, "Red Blood Cell Passage of Small Capillaries Is Associated with Transient Ca2+-mediated Adaptations," *Frontiers in Physiology*, vol. 8, p. 979, 2017 [DOI-CrossRef].
- [379] M. Föller and F. Lang, "Ion Transport in Eryptosis, the Suicidal Death of Erythrocytes," Frontiers in Cell and Developmental Biology, vol. 8, p. 597, 2020 [DOI-CrossRef].
- [380] A. V. Muravyov and I. A. Tikhomirova, "Role molecular signaling pathways in changes of red blood cell deformability," *Clinical Hemorheology and Microcirculation*, vol. 53, no. 1-2, pp. 45–59, 2013 [DOI-CrossRef].
- [381] P. J. Romero, E. A. Romero, D. Mateu, C. Hernández, and I. Fernández, "Voltage-Dependent Calcium Channels in Young and Old Human Red Cells," *Cell Biochemistry and Biophysics*, vol. 46,

- no. 3, pp. 265–276, 2006 [DOI-CrossRef].
- [382] P. Brandt, E. Ibrahim, G. A. Bruns, and R. L. Neve, "Determination of the nucleotide sequence and chromosomal localization of the ATP2B2 Gene Encoding Human Ca2+-Pumping ATPase Isoform PMCA2," Genomics, vol. 14, pp. 484–487, 1992 [DOI-CrossRef].
- [383] S. Olson, M. G. Wang, E. Carafoli, E. E. Strehler, and O. McBride, "Localization of two genes encoding plasma membrane Ca2+-transporting ATPases to human chromosomes 1q25–32 and 12q21–23," *Genomics*, vol. 9, pp. 629–641, 1991 [DOI-CrossRef].
- [384] M. Wang, H. Yi, H. Hilfiker, E. Carafoli, E. Strehler, and O. McBride, "Localization of two genes encoding plasma membrane Ca²⁺ ATPases isoforms 2 (ATP2B2) and 3 (ATP2B3) to human chromosomes 3p26→p25 and Xq28, respectively," *Cytogenetic and Genome Research*, vol. 67, no. 1, pp. 41–45, 1994 [DOI-CrossRef].
- [385] H. J. Schatzmann, "ATP-dependent Ca++-extrusion from human red cells," *Experientia*, vol. 22, pp. 364–365, 1966 [DOI-CrossRef].
- [386] V. Niggli, P. Ronner, E. Carafoli, and J. T. Penniston, "Effects of calmodulin on the (Ca2+ + Mg2+)ATPase partially purified from erythrocyte membranes," *Archives of Biochemistry and Biophysics*, vol. 198, pp. 124–130, 1979 [DOI-CrossRef].
- [387] G. E. Shull and J. Greeb, "Molecular cloning of two isoforms of the plasma membrane Ca2+-transporting ATPase from rat brain. Structural and functional domains exhibit similarity to Na+,K+- and other cation transport ATPases," *The Journal of Biological Chemistry*, vol. 263, pp. 8646–8657, 1988.
- [388] A. K. Verma, A. G. Filoteo, D. R. Stanford, E. D. Wieben, J. T. Penniston, E. E. Strehler, R. Fischer, R. Heim, G. Vogel, and S. Mathews, "Complete primary structure of a human plasma membrane Ca2+ pump," The Journal of Biological Chemistry, vol. 263, pp. 14152–14159, 1988.
- [389] C. Toyoshima, M. Nakasako, H. Nomura, and H. Ogawa, "Crystal structure of the calcium pump of sarcoplasmic reticulum at 2.6 A resolution," *Nature*, vol. 405, pp. 647–655, 2000 [DOI-CrossRef].
- [390] M. Brini and E. Carafoli, "The plasma membrane Ca²+ ATPase and the plasma membrane sodium calcium exchanger cooperate in the regulation of cell calcium," Cold Spring Harbor Perspectives in Biology, vol. 3, p. a004168, 2011 [DOI-CrossRef].
- [391] E. Zvaritch, P. James, T. Vorherr, R. Falchetto, N. Modyanov, and E. Carafoli, "Mapping of functional domains in the plasma membrane Ca2+ pump using trypsin proteolysis," *Biochemistry*, vol. 29, pp. 8070–8076, 1990 [DOI-CrossRef].
- [392] D. Guerini, B. Pan, and E. Carafoli, "Expression, purification, and characterization of isoform 1 of the plasma membrane Ca2+ pump: Focus on calpain sensitivity," *The Journal of Biological Chemistry*, vol. 278, pp. 38141–38148, 2003 [DOI-CrossRef].
- [393] E. E. Strehler and D. A. Zacharias, "Role of alternative splicing in generating isoform diversity among plasma membrane calcium pumps," *Physiological Reviews*, vol. 81, pp. 21–50, 2001 [DOI-CrossRef].
- [394] T. J. Lynch and W. Y. Cheung, "Human erythrocyte Ca2+-Mg2+-ATPase: Mechanism of stimulation by Ca2+," Archives of Biochemistry and Biophysics, vol. 194, pp. 165–170, 1979 [DOI-CrossRef].
- [395] V. Niggli, J. T. Penniston, and E. Carafoli, "Purification of the (Ca2+-Mg2+)-ATPase from human erythrocyte membranes using a calmodulin affinity column," The Journal of Biological Chemistry, vol. 254, pp. 9955–9958, 1979.
- [396] D. Kosk-Kosicka and T. Bzdega, "Activation of the erythrocyte Ca2+-ATPase by either self-association or interaction with calmodulin," The Journal of Biological Chemistry, vol. 263, pp. 18184–18189, 1988.
- [397] T. Vorherr, T. Kessler, F. Hofmann, and E. Carafoli, "The calmodulin-binding domain mediates the self-association of the plasma membrane Ca2+ pump," *The Journal of Biological Chemistry*, vol. 266, pp. 22–27, 1991.
- [398] T. Boczek, M. Sobolczyk, J. Mackiewicz, M. Lisek, B. Ferenc, F. Guo, and L. Zylinska, "Crosstalk among Calcium ATPases: PMCA, SERCA and SPCA in Mental Diseases," *International Journal*

- of Molecular Sciences, vol. 22, p. 2785, 2021 [DOI-CrossRef].
- [399] J. Krebs, "Structure, Function and Regulation of the Plasma Membrane Calcium Pump in Health and Disease," *International Journal of Molecular Sciences*, vol. 23, p. 1027, 2022 [DOI-CrossRef].
- [400] E. Carafoli, "The calcium pumping ATPase of the plasma membrane," *Annual Review of Physiology*, vol. 53, pp. 531–547, 1991 [DOI-CrossRef].
- [401] M. Brini and E. Carafoli, "Calcium pumps in health and disease," *Physiological Reviews*, vol. 89, pp. 1341–1378, 2009 [DOI-CrossRef].
- [402] V. Niggli, E. Sigel, and E. Carafoli, "The purified Ca2+ pump of human erythrocyte membranes catalyzes an electroneutral Ca2+-H+ exchange in reconstituted liposomal systems," *The Journal of Biological Chemistry*, vol. 257, pp. 2350–2356, 1982.
- [403] M. P. E. Van Heeswijk, J. A. M. Geertsen, and C. H. Van Os, "Kinetic properties of the ATP-dependent Ca2+ pump and the Na+/Ca2+ exchange system in basolateral membranes from rat kidney cortex," *The Journal of Membrane Biology*, vol. 79, pp. 19–31, 1984 [DOI-CrossRef].
- [404] V. Niggli, E. S. Adunyah, and E. Carafoli, "Acidic phospholipids, unsaturated fatty acids, and limited proteolysis mimic the effect of calmodulin on the purified erythrocyte Ca2+ ATPase," *The Journal of Biological Chemistry*, vol. 256, pp. 8588–8592, 1981.
- [405] J. D. Clausen, D. B. McIntosh, D. G. Woolley, and J. P. Andersen, "Modulatory ATP binding affinity in intermediate states of E2P dephosphorylation of sarcoplasmic reticulum Ca2+-ATPase," *The Journal of Biological Chemistry*, vol. 286, pp. 11792–11802, 2011 [DOI-CrossRef].
- [406] I. C. Mangialavori, M. S. Ferreira-Gomes, N. A. Saffioti, R. M. González-Lebrero, R. C. Rossi, and J. P. F. C. Rossi, "Conformational changes produced by ATP binding to the plasma membrane calcium pump," *The Journal of Biological Chemistry*, vol. 288, pp. 31030–31041, 2013 [DOI-CrossRef].
- [407] D. B. McIntosh and P. D. Boyer, "Adenosine 5'-triphosphate modulation of catalytic intermediates of calcium ion activated adenosinetriphosphatase of sarcoplasmic reticulum subsequent to enzyme phosphorylation," *Biochemistry*, vol. 22, pp. 2867–2875, 1983 [DOI-CrossRef].
- [408] A. F. Rega and P. J. Garrahan, *The Ca2+ Pump of Plasma Membranes*. Boca Raton, Fla: CRC Pr. 2. print ed., 1987.
- [409] A. L. Bodley and W. P. Jencks, "Acetyl phosphate as a substrate for the calcium ATPase of sarcoplasmic reticulum," *The Journal of Biological Chemistry*, vol. 262, pp. 13997–14004, 1987.
- [410] P. Champeil and F. Guillain, "Rapid filtration study of the phosphorylation-dependent dissociation of calcium from transport sites of purified sarcoplasmic reticulum ATPase and ATP modulation of the catalytic cycle," *Biochemistry*, vol. 25, pp. 7623–7633, 1986 [DOI-CrossRef].
- [411] J. P. Andersen and J. V. Møller, "The role of Mg2+ and Ca2+ in the simultaneous binding of vanadate and ATP at the phosphorylation site of sarcoplasmic reticulum Ca2+-ATPase," *Biochimica Et Biophysica Acta*, vol. 815, pp. 9–15, 1985 [DOI-CrossRef].
- [412] H. M. Scofano, A. Vieyra, and L. de Meis, "Substrate regulation of the sarcoplasmic reticulum ATPase. Transient kinetic studies," *The Journal of Biological Chemistry*, vol. 254, pp. 10227–10231, 1979.
- [413] M. S. Ferreira-Gomes, R. M. González-Lebrero, M. C. de la Fuente, E. E. Strehler, R. C. Rossi, and J. P. F. C. Rossi, "Calcium occlusion in plasma membrane Ca2+-ATPase," *The Journal of Biological Chemistry*, vol. 286, pp. 32018–32025, 2011 [DOI-CrossRef].
- [414] C. J. Herscher and A. F. Rega, "Pre-steady-state kinetic study of the mechanism of inhibition of the plasma membrane Ca(2+)-ATPase by lanthanum," *Biochemistry*, vol. 35, pp. 14917–14922, 1996 [DOI-CrossRef].
- [415] C. Gatto and M. A. Milanick, "Inhibition of the red blood cell calcium pump by eosin and other fluorescein analogues," *The American Journal of Physiology*, vol. 264, pp. C1577–1586, 1993 [DOI-CrossRef].
- [416] B. D. Roufogalis, Q. Li, V. H. Tran, E. P. W. Kable, and C. C. Duke, "Investigation of plant-derived phenolic compounds as plasma membrane Ca2+-ATPase inhibitors with potential cardiovascular

- activity," no. 3-4, pp. 239-249, 1999 [DOI-CrossRef].
- [417] Y. Dupont and N. Bennett, "Vanadate inhibition of the Ca ²⁺ -dependent conformational change of the sarcoplasmic reticulum Ca ²⁺ -ATPase," FEBS Letters, vol. 139, pp. 237–240, 1982 [DOI-CrossRef].
- [418] I. G. Macara, "Vanadium an element in search of a role," Trends in Biochemical Sciences, vol. 5, pp. 92–94, 1980 [DOI-CrossRef].
- [419] G. H. Bond and P. M. Hudgins, "Inhibition of red cell Ca2+-ATPase by vanadate," *Biochimica Et Biophysica Acta*, vol. 600, pp. 781–790, 1980 [DOI-CrossRef].
- [420] A. Villegas-Mendez, N. Stafford, M. J. Haley, N. E. Pravitasari, F. Baudoin, A. Ali, P. B. S. Asih, J. E. Siregar, E. Baena, D. Syafruddin, K. N. Couper, and D. Oceandy, "The plasma membrane calcium ATPase 4 does not influence parasite levels but partially promotes experimental cerebral malaria during murine blood stage malaria," Malaria Journal, vol. 20, p. 297, 2021 [DOI-CrossRef].
- [421] B. Zámbó, G. Várady, R. Padányi, E. Szabó, A. Németh, T. Langó, Á. Enyedi, and B. Sarkadi, "Decreased calcium pump expression in human erythrocytes is connected to a minor haplotype in the ATP2B4 gene," *Cell Calcium*, vol. 65, pp. 73–79, 2017 [DOI-CrossRef].
- [422] R. Little, M. Zi, S. K. Hammad, L. Nguyen, A. Njegic, S. Kurusamy, S. Prehar, A. L. Armesilla, L. Neyses, C. Austin, and E. J. Cartwright, "Reduced expression of PMCA1 is associated with increased blood pressure with age which is preceded by remodelling of resistance arteries," Aging Cell, vol. 16, pp. 1104–1113, 2017 [DOI-CrossRef].
- [423] D. Polak-Jonkisz, L. Purzyc, K. Laszki-Szczachor, K. Musial, and D. Zwolinska, "The endogenous modulators of Ca2+-Mg2+-dependent ATPase in children with chronic kidney disease (CKD)," Nephrology Dialysis Transplantation, vol. 25, pp. 438-444, 2010 [DOI-CrossRef].
- [424] M. J. Gordon, "The charge on cell membranes," Medical Bulletin (Ann Arbor, Mich.), vol. 25, pp. 170–176, 1959.
- [425] P. G. Lefevre, "The Osmotically Functional Water Content of the Human Erythrocyte," *The Journal of General Physiology*, vol. 47, pp. 585–603, 1964 [DOI-CrossRef].
- [426] T. Teorell, "Permeability properties of erythrocyte ghosts," The Journal of General Physiology, vol. 35, pp. 669–701, 1952 [DOI-CrossRef].
- [427] W. D. Stein, Transport and Diffusion Across Cell Membranes. Elsevier, 1986.
- [428] O. Ariyo and F. Akter, "Anatomy and Physiology of the Neuron," in Neuroscience for Neurosurgeons (F. Akter, N. Emptage, F. Engert, and M. S. Berger, eds.), pp. 72–83, Cambridge University Press, 1 ed., 2024.
- [429] W. A. Catterall, G. Wisedchaisri, and N. Zheng, "The chemical basis for electrical signaling," *Nature Chemical Biology*, vol. 13, pp. 455–463, 2017 [DOI-CrossRef].
- [430] M. H. Grider, R. Jessu, and R. Kabir, "Physiology, Action Potential," in StatPearls, Treasure Island (FL): StatPearls Publishing, 2024.
- [431] P. E. Pack, CliffsAP Biology. Hoboken, NJ: Wiley Pub, 3rd ed ed., 2007.
- [432] W.-G. Choi, R. Hilleary, S. J. Swanson, S.-H. Kim, and S. Gilroy, "Rapid, Long-Distance Electrical and Calcium Signaling in Plants," *Annual Review of Plant Biology*, vol. 67, pp. 287–307, 2016 [DOI-CrossRef].
- [433] A. Prindle, J. Liu, M. Asally, S. Ly, J. Garcia-Ojalvo, and G. M. Süel, "Ion channels enable electrical communication in bacterial communities," *Nature*, vol. 527, pp. 59–63, 2015 [DOI-CrossRef].
- [434] D. E. Goldman, "Potential, impedance, and rectification in membranes," *Journal of General Physiology*, vol. 27, pp. 37–60, 1943 [DOI-CrossRef].
- [435] W. Nernst, "Die elektromotorische Wirksamkeit der Jonen," Zeitschrift für Physikalische Chemie, vol. 4U, pp. 129–181, 1889 [DOI-CrossRef].
- [436] E. J. Warburg, "Studies on Carbonic Acid Compounds and Hydrogen Ion Activities in Blood and Salt Solutions. A Contribution to the Theory of the Equation of Lawrence J. Henderson and K. A. Hasselbach: CHAP. VII," The Biochemical Journal, vol. 16, no. 2, pp. 222–233, 1922 [DOI-CrossRef].

[437] J. C. Freedman and J. F. Hoffman, "Ionic and osmotic equilibria of human red blood cells treated with nystatin," *The Journal of General Physiology*, vol. 74, pp. 157–185, 1979 [DOI-CrossRef].

- [438] U. V. Lassen and O. Sten-Knudsen, "Direct measurements of membrane potential and membrane resistance of human red cells," *The Journal of Physiology*, vol. 195, pp. 681–696, 1968 [DOI-CrossRef].
- [439] F. G. Donnan, "Theorie der Membrangleichgewichte und Membranpotentiale bei Vorhandensein von nicht dialysierenden Elektrolyten. Ein Beitrag zur physikalisch-chemischen Physiologie.," Zeitschrift für Elektrochemie und angewandte physikalische Chemie, vol. 17, pp. 572–581, 1911 [DOI-CrossRef].
- [440] "The Aqueous Electrolyte Solution," in *Developments in Geochemistry*, vol. 11, pp. 53–77, Elsevier, 2007.
- [441] M. M. Gedde and W. H. Huestis, "Membrane potential and human erythrocyte shape," *Biophysical Journal*, vol. 72, pp. 1220–1233, 1997 [DOI-CrossRef].
- [442] R. I. Macey, J. S. Adorante, and F. W. Orme, "Erythrocyte membrane potentials determined by hydrogen ion distribution," *Biochimica Et Biophysica Acta*, vol. 512, pp. 284–295, 1978 [DOI-CrossRef].
- [443] A. W. Jay and A. C. Burton, "Direct measurement of potential difference across the human red blood cell membrane," *Biophysical Journal*, vol. 9, pp. 115–121, 1969 [DOI-CrossRef].
- [444] L. B. Cohen and B. M. Salzberg, "Optical measurement of membrane potential," *Reviews of Physiology, Biochemistry and Pharmacology*, vol. 83, pp. 35–88, 1978 [DOI-CrossRef].
- [445] B. M. Salzberg, H. V. Davila, and L. B. Cohen, "Optical recording of impulses in individual neurones of an invertebrate central nervous system," *Nature*, vol. 246, no. 5434, pp. 508–509, 1973-12-21/0028 [DOI-CrossRef].
- [446] S. B. Knisley, R. K. Justice, W. Kong, and P. L. Johnson, "Ratiometry of transmembrane voltage-sensitive fluorescent dye emission in hearts," *American Journal of Physiology. Heart and Circulatory Physiology*, vol. 279, pp. H1421–1433, 2000 [DOI-CrossRef].
- [447] A. Bullen and P. Saggau, "High-speed, random-access fluorescence microscopy: II. Fast quantitative measurements with voltage-sensitive dyes," *Biophysical Journal*, vol. 76, pp. 2272–2287, 1999 [DOI-CrossRef].
- [448] J. F. Hoffman and P. C. Laris, "Determination of membrane potentials in human and Amphiuma red blood cells by means of fluorescent probe," *The Journal of Physiology*, vol. 239, pp. 519–552, 1974 [DOI-CrossRef].
- [449] T. Klapperstück, D. Glanz, M. Klapperstück, and J. Wohlrab, "Methodological aspects of measuring absolute values of membrane potential in human cells by flow cytometry," *Cytometry. Part A: The Journal of the International Society for Analytical Cytology*, vol. 75, pp. 593–608, 2009 [DOI-CrossRef].
- [450] D. Moersdorf, S. Egee, C. Hahn, B. Hanf, C. Ellory, S. Thomas, and I. Bernhardt, "Transmembrane potential of red blood cells under low ionic strength conditions," Cellular Physiology and Biochemistry: International Journal of Experimental Cellular Physiology, Biochemistry, and Pharmacology, vol. 31, no. 6, pp. 875–882, 2013 [DOI-CrossRef].
- [451] W. Zhang and Z.-y. Zhu, "Structural modification of H histo-blood group antigen," *Blood Transfusion = Trasfusione Del Sangue*, vol. 13, pp. 143–149, 2015 [DOI-CrossRef].
- [452] I. B. Zavodnik, A. Piasecka, K. Szosland, and M. Bryszewska, "Human red blood cell membrane potential and fluidity in glucose solutions," *Scandinavian Journal of Clinical and Laboratory Investigation*, vol. 57, pp. 59–63, 1997 [DOI-CrossRef].
- [453] A. L. Montoya-Navarrete, A. L. Guerrero-Barrera, T. Quezada-Tristán, A. G. Valdivia-Flores, and M. J. Cano-Rábano, "Red blood cells morphology and morphometry in adult, senior, and geriatricians dogs by optical and scanning electron microscopy," *Frontiers in Veterinary Science*, vol. 9, p. 998438, 2022 [DOI-CrossRef].
- [454] S. Kulasekaran, F. Sheeba, J. J. Mammen, B. Saivigneshu, and S. Mohankumar, "Morphology Based Detection of Abnormal Red Blood Cells in Peripheral Blood Smear Images," in 7th WACBE World Congress on Bioengineering 2015 (J. Goh and C. T. Lim, eds.), vol. 52, pp. 57–60, Cham: Springer International Publishing, 2015.

[455] G. Lim H. W., M. Wortis, and R. Mukhopadhyay, "Red Blood Cell Shapes and Shape Transformations: Newtonian Mechanics of a Composite Membrane: Sections 2.5–2.8," in *Soft Matter* (G. Gompper and M. Schick, eds.), pp. 139–204, Wiley, 1 ed., 2008.

- [456] N. M. Geekiyanage, M. A. Balanant, E. Sauret, S. Saha, R. Flower, C. T. Lim, and Y. Gu, "A coarse-grained red blood cell membrane model to study stomatocyte-discocyte-echinocyte morphologies," PLOS ONE, vol. 14, p. e0215447, 2019 [DOI-CrossRef].
- [457] G. Simionato, K. Hinkelmann, R. Chachanidze, P. Bianchi, E. Fermo, R. van Wijk, M. Leonetti, C. Wagner, L. Kaestner, and S. Quint, "Red blood cell phenotyping from 3D confocal images using artificial neural networks," *PLoS computational biology*, vol. 17, p. e1008934, 2021 [DOI-CrossRef].
- [458] L. Barbalato and L. S. Pillarisetty, "Histology, Red Blood Cell," in StatPearls, Treasure Island (FL): StatPearls Publishing, 2024.
- [459] E. Pretorius, O.-O. O. Olumuyiwa-Akeredolu, S. Mbotwe, and J. Bester, "Erythrocytes and their role as health indicator: Using structure in a patient-orientated precision medicine approach," *Blood Reviews*, vol. 30, pp. 263–274, 2016 [DOI-CrossRef].
- [460] J. Ford, "Red blood cell morphology," International Journal of Laboratory Hematology, vol. 35, pp. 351–357, 2013 [DOI-CrossRef].
- [461] E. C. Lynch, "Peripheral Blood Smear," in *Clinical Methods: The History, Physical, and Laboratory Examinations* (H. K. Walker, W. D. Hall, and J. W. Hurst, eds.), Boston: Butterworths, 3rd ed., 1990.
- [462] D. M. W. Karandeniya, D. W. Holmes, E. Sauret, and Y. T. Gu, "A new membrane formulation for modelling the flow of stomatocyte, discocyte, and echinocyte red blood cells," *Biomechanics and Modeling in Mechanobiology*, vol. 21, pp. 899–917, 2022 [DOI-CrossRef].
- [463] S. V. Rudenko, "Erythrocyte morphological states, phases, transitions and trajectories," *Biochimica Et Biophysica Acta*, vol. 1798, pp. 1767–1778, 2010 [DOI-CrossRef].
- [464] K. Tachev, K. Danov, and P. Kralchevsky, "On the mechanism of stomatocyte-echinocyte transformations of red blood cells: Experiment and theoretical model," Colloids and Surfaces B: Biointerfaces, vol. 34, pp. 123–140, 2004 [DOI-CrossRef].
- [465] G. H. W. Lim, A Numerical Study of Morphologies and Morphological Transformations of Human Erythrocyte Based on Membrane Mechanics. Ottawa: Library and Archives Canada = Bibliothèque et Archives Canada, 2006.
- [466] P. Wong, "A basis of echinocytosis and stomatocytosis in the disc-sphere transformations of the erythrocyte," *Journal of Theoretical Biology*, vol. 196, pp. 343–361, 1999 [DOI-CrossRef].
- [467] L. K. Karlsson, M. N. Mottelson, J. Helby, J. Petersen, and A. Glenthøj, "Acquired spherocytosis in the setting of myelodysplasia," *Leukemia Research Reports*, vol. 17, p. 100332, 2022 [DOI-CrossRef].
- [468] M. P. Sheetz and S. J. Singer, "Biological membranes as bilayer couples. A molecular mechanism of drug-erythrocyte interactions," *Proceedings of the National Academy of Sciences of the United States of America*, vol. 71, pp. 4457–4461, 1974 [DOI-CrossRef].
- [469] S. Kim, S. A. Hewlett, C. B. Roth, and J. M. Torkelson, "Confinement effects on glass transition temperature, transition breadth, and expansivity: Comparison of ellipsometry and fluorescence measurements on polystyrene films," *The European Physical Journal E*, vol. 30, p. 83, 2009 [DOI-CrossRef].
- [470] C. R. Hasler, G. R. Owen, W. Brunner, and W. H. Reinhart, "Echinocytosis induced by haemodial-ysis," Nephrology, Dialysis, Transplantation: Official Publication of the European Dialysis and Transplant Association European Renal Association, vol. 13, pp. 3132–3137, 1998 [DOI-CrossRef].
- [471] C. R. Hasler, G. R. Owen, W. Brunner, and W. H. Reinhart, "Echinocytosis induced by haemodial-ysis," Nephrology, Dialysis, Transplantation: Official Publication of the European Dialysis and Transplant Association European Renal Association, vol. 13, pp. 3132–3137, 1998 [DOI-CrossRef].
- [472] H. S. Mallah, M. R. Brown, T. M. Rossi, and R. C. Block, "Parenteral fish oil-associated burr cell anemia," *The Journal of Pediatrics*, vol. 156, pp. 324–326.e1, 2010 [DOI-CrossRef].

[473] W. A. Aherne, "The burr red cell and azotaemia," *Journal of Clinical Pathology*, vol. 10, pp. 252–257, 1957 [DOI-CrossRef].

- [474] J. P. Loge, R. D. Lange, and C. V. Moore, "Characterization of the anemia associated with chronic renal insufficiency," *The American Journal of Medicine*, vol. 24, pp. 4–18, 1958 [DOI-CrossRef].
- [475] H. A. Cynamon, J. N. Isenberg, L. P. Gustavson, and W. K. Gourley, "Erythrocyte lipid alterations in pediatric cholestatic liver disease: Spur cell anemia of infancy," *Journal of Pediatric Gastroenterology and Nutrition*, vol. 4, pp. 542–549, 1985 [DOI-CrossRef].
- [476] R. J. Sokol, M. A. Guggenheim, S. T. Iannaccone, P. E. Barkhaus, C. Miller, A. Silverman, W. F. Balistreri, and J. E. Heubi, "Improved neurologic function after long-term correction of vitamin E deficiency in children with chronic cholestasis," The New England Journal of Medicine, vol. 313, pp. 1580–1586, 1985 [DOI-CrossRef].
- [477] J. F. Flatt and L. J. Bruce, "The Molecular Basis for Altered Cation Permeability in Hereditary Stomatocytic Human Red Blood Cells," *Frontiers in Physiology*, vol. 9, p. 367, 2018 [DOI-CrossRef].
- [478] A. C.-W. Lee, L. Aung, Y. Y. Yip, and C. P.-P. Hia, "Hereditary stomatocytosis: An unusual cause of severe neonatal jaundice," *Singapore Medical Journal*, vol. 59, p. 505, 2018 [DOI-CrossRef].
- [479] S. S. Bandaru, R. B. Killeen, and V. Gupta, "Poikilocytosis," in *StatPearls*, Treasure Island (FL): StatPearls Publishing, 2024.
- [480] B. J. Bain, "Blood cell morphology in health and disease," in *Dacie and Lewis Practical Haematology*, pp. 69–100, Elsevier, 2012.
- [481] R. I. Weed and M. Bessis, "The discocyte-stomatocyte equilibrium of normal and pathologic red cells," *Blood*, vol. 41, pp. 471–475, 1973.
- [482] S. P. Lock, R. S. Smith, and R. M. Hardisty, "Stomatocytosis: A hereditary red cell anomally associated with haemolytic anaemia," *British Journal of Haematology*, vol. 7, pp. 303–314, 1961 [DOI-CrossRef].
- [483] W. Ducrou and R. J. Kimber, "Stomatocytes, haemolytic anaemia and abdominal pain in Mediterranean migrants. Some examples of a new syndrome?," *The Medical Journal of Australia*, vol. 2, pp. 1087–1091, 1969.
- [484] J. M. Jackson, "Stomatocytosis in migrants of Mediterranean origin," *The Medical Journal of Australia*, vol. 1, pp. 939–940, 1969.
- [485] P. G. Gallagher, "Disorders of red cell volume regulation," *Current Opinion in Hematology*, vol. 20, pp. 201–207, 2013 [DOI-CrossRef].
- [486] C. C. Douglass, "Transient Stomatocytosis with Hemolysis: A Previously Unrecognized Complication of Alcoholism," *Annals of Internal Medicine*, vol. 72, p. 159, 1970 [DOI-CrossRef].
- [487] P. Sundd, M. T. Gladwin, and E. M. Novelli, "Pathophysiology of Sickle Cell Disease," *Annual Review of Pathology*, vol. 14, pp. 263–292, 2019 [DOI-CrossRef].
- [488] C. Elendu, D. C. Amaechi, C. E. Alakwe-Ojimba, T. C. Elendu, R. C. Elendu, C. P. Ayabazu, T. O. Aina, O. Aborisade, and J. S. Adenikinju, "Understanding Sickle cell disease: Causes, symptoms, and treatment options," *Medicine*, vol. 102, p. e35237, 2023 [DOI-CrossRef].
- [489] D. C. Rees, T. N. Williams, and M. T. Gladwin, "Sickle-cell disease," Lancet (London, England), vol. 376, pp. 2018–2031, 2010 [DOI-CrossRef].
- [490] H. F. Bunn, "Pathogenesis and treatment of sickle cell disease," *The New England Journal of Medicine*, vol. 337, pp. 762–769, 1997 [DOI-CrossRef].
- [491] L. Pauling and H. A. Itano, "Sickle cell anemia a molecular disease," *Science (New York, N.Y.)*, vol. 110, pp. 543–548, 1949 [DOI-CrossRef].
- [492] R. P. Hebbel, "Ischemia-reperfusion injury in sickle cell anemia: Relationship to acute chest syndrome, endothelial dysfunction, arterial vasculopathy, and inflammatory pain," *Hematology/Oncology Clinics of North America*, vol. 28, pp. 181–198, 2014 [DOI-CrossRef].
- [493] H. Bajwa and H. Basit, "Thalassemia," in StatPearls, Treasure Island (FL): StatPearls Publishing,

2024.

[494] M. Angastiniotis and S. Lobitz, "Thalassemias: An Overview," *International Journal of Neonatal Screening*, vol. 5, p. 16, 2019 [DOI-CrossRef].

- [495] M. D. Cappellini, A. Cohen, J. Porter, A. Taher, and V. Viprakasit, eds., Guidelines for the Management of Transfusion Dependent Thalassaemia (TDT). Nicosia (CY): Thalassaemia International Federation, 3rd ed., 2014.
- [496] J. B. Clegg, M. A. Naughton, and D. J. Weatherall, "An Improved Method for the Characterization of Human Haemoglobin Mutants: Identification of α2β295GLU, Haemoglobin N (Baltimore)," Nature, vol. 207, pp. 945–947, 1965 [DOI-CrossRef].
- [497] D. G. Nathan and R. B. Gunn, "Thalassemia: The consequences of unbalanced hemoglobin synthesis," *The American Journal of Medicine*, vol. 41, pp. 815–830, 1966 [DOI-CrossRef].
- [498] D. J. Weatherall, J. B. Clegg, and M. A. Naughton, "Globin Synthesis in Thalassaemia: An in vitro Study," *Nature*, vol. 208, pp. 1061–1065, 1965 [DOI-CrossRef].
- [499] A. W. Nienhuis and D. G. Nathan, "Pathophysiology and Clinical Manifestations of the β-Thalassemias," Cold Spring Harbor Perspectives in Medicine, vol. 2, p. a011726, 2012 [DOI-CrossRef].
- [500] S. Rivella, "Ineffective erythropoiesis and thalassemias:," Current Opinion in Hematology, vol. 16, pp. 187–194, 2009 [DOI-CrossRef].
- [501] A. Bunyaratvej, S. Sahaphong, N. Bhamarapravati, and P. Wasi, "Quantitative changes of red blood cell shapes in relation to clinical features in beta-thalassemia/HbE disease," American Journal of Clinical Pathology, vol. 83, pp. 555–559, 1985 [DOI-CrossRef].
- [502] C. Körber, A. Wölfler, M. Neubauer, and C. Robier, "Red blood cell morphology in patients with β-thalassemia minor," *Laboratoriums Medizin*, vol. 41, pp. 49–52, 2017 [DOI-CrossRef].
- [503] M. S. Zubairy, "A Very Brief History of Light," in *Optics in Our Time* (M. D. Al-Amri, M. El-Gomati, and M. S. Zubairy, eds.), pp. 3–24, Cham: Springer International Publishing, 2016.
- [504] B. Valeur and M. N. Berberan-Santos, "A Brief History of Fluorescence and Phosphorescence before the Emergence of Quantum Theory," *Journal of Chemical Education*, vol. 88, pp. 731–738, 2011 [DOI-CrossRef].
- [505] S. E. Braslavsky, "Glossary of terms used in photochemistry, 3rd edition (IUPAC Recommendations 2006)," *Pure and Applied Chemistry*, vol. 79, pp. 293–465, 2007 [DOI-CrossRef].
- [506] G. G. Stokes, "XXX. On the change of refrangibility of light," *Philosophical Transactions of the Royal Society of London*, vol. 142, pp. 463–562, 1852 [DOI-CrossRef].
- [507] G. G. Stokes, "XVI. On the change of refrangibility of light.—No. II," *Philosophical Transactions of the Royal Society of London*, vol. 143, pp. 385–396, 1853 [DOI-CrossRef].
- [508] J. Jiang, N. Higashiyama, K.-i. Machida, and G.-y. Adachi, "The luminescent properties of divalent europium complexes of crown ethers and cryptands," *Coordination Chemistry Reviews*, vol. 170, pp. 1–29, 1998 [DOI-CrossRef].
- [509] M. P. Lord, A. L. G. Rees, and M. E. Wise, "The short-period time variation of the luminescence of a zinc sulphide phosphor under ultra-violet excitation," *Proceedings of the Physical Society*, vol. 59, pp. 473–502, 1947 [DOI-CrossRef].
- [510] F. Perrin, "La fluorescence des solutions: Induction moléculaire. Polarisation et durée d'émission. Photochimie," *Annales de Physique*, vol. 10, no. 12, pp. 169–275, 1929 [DOI-CrossRef].
- [511] C. Albrecht, "Joseph R. Lakowicz: Principles of fluorescence spectroscopy, 3rd Edition," Analytical and Bioanalytical Chemistry, vol. 390, pp. 1223–1224, 2008 [DOI-CrossRef].
- [512] A. Jablonski, "Efficiency of Anti-Stokes Fluorescence in Dyes," Nature, vol. 131, pp. 839–840, 1933 [DOI-CrossRef].
- [513] A. Jabłoński, "Über den Mechanismus der Photolumineszenz von Farbstoffphosphoren," Zeitschrift für Physik, vol. 94, pp. 38–46, 1935 [DOI-CrossRef].
- [514] J. W. Verhoeven, "Glossary of terms used in photochemistry (IUPAC Recommendations 1996),"

- Pure and Applied Chemistry, vol. 68, pp. 2223–2286, 1996 [DOI-CrossRef].
- [515] E. Condon, "A Theory of Intensity Distribution in Band Systems," *Physical Review*, vol. 28, pp. 1182–1201, 1926 [DOI-CrossRef].
- [516] E. U. Condon, "Nuclear Motions Associated with Electron Transitions in Diatomic Molecules," *Physical Review*, vol. 32, pp. 858–872, 1928 [DOI-CrossRef].
- [517] J. Franck and E. G. Dymond, "Elementary processes of photochemical reactions," *Transactions of the Faraday Society*, vol. 21, no. February, p. 536, 1926 [DOI-CrossRef].
- [518] "Introduction to Fluorescence," in *Principles of Fluorescence Spectroscopy* (J. R. Lakowicz, ed.), pp. 1–26, Boston, MA: Springer US, 2006.
- [519] D. Dzebo, "Photon Upconversion through Triplet-Triplet Annihilation: Towards Higher Efficiency and Solid State Applications," 2016 [DOI-CrossRef].
- [520] "Fluorophores," in *Principles of Fluorescence Spectroscopy* (J. R. Lakowicz, ed.), pp. 63–95, Boston, MA: Springer US, 2006.
- [521] J. C. Zwinkels, P. C. DeRose, and J. E. Leland, "Spectral Fluorescence Measurements," in *Experimental Methods in the Physical Sciences*, vol. 46, pp. 221–290, Elsevier, 2014.
- [522] R. M. Clegg, "Fluorescence resonance energy transfer," Current Opinion in Biotechnology, vol. 6, pp. 103–110, 1995 [DOI-CrossRef].
- [523] T. Förster, "Mechanisms of energy transfer," in *Comprehensive Biochemistry*, vol. 22, pp. 61–80, Elsevier, 1967.
- [524] R. B. Sekar and A. Periasamy, "Fluorescence resonance energy transfer (FRET) microscopy imaging of live cell protein localizations," *The Journal of Cell Biology*, vol. 160, pp. 629–633, 2003 [DOI-CrossRef].
- [525] M. Y. Berezin and S. Achilefu, "Fluorescence lifetime measurements and biological imaging," *Chemical Reviews*, vol. 110, pp. 2641–2684, 2010 [DOI-CrossRef].
- [526] Y. Chen and A. Periasamy, "Characterization of two-photon excitation fluorescence lifetime imaging microscopy for protein localization," *Microscopy Research and Technique*, vol. 63, pp. 72–80, 2004 [DOI-CrossRef].
- [527] J. C. Stockert and A. Blazquez-Castro, Dyes and Fluorochromes, pp. 61–95. BENTHAM SCIENCE PUBLISHERS, 2017.
- [528] "Introduction to Fluorescence," in *Principles of Fluorescence Spectroscopy* (J. R. Lakowicz, ed.), pp. 1–26, Boston, MA: Springer US, 2006.
- [529] M. Kasha, "Characterization of electronic transitions in complex molecules," *Discussions of the Faraday Society*, vol. 9, p. 14, 1950 [DOI-CrossRef].
- [530] A. Brockes, "Mechanism of whitening and quenching," Environmental Quality and Safety. Supplement, vol. 4, pp. 19–24, 1975.
- [531] R. Badugu, "Fluorescence Sensor Design for Transition Metal Ions: The Role of the PIET Interaction Efficiency," *Journal of Fluorescence*, vol. 15, pp. 71–83, 2005 [DOI-CrossRef].
- [532] K. Cammann, "Sensors and analytical chemistry," *Physical Chemistry Chemical Physics*, vol. 5, no. 23, p. 5159, 2003 [DOI-CrossRef].
- [533] A. De Silva, D. B. Fox, T. S. Moody, and S. M. Weir, "The development of molecular fluorescent switches," *Trends in Biotechnology*, vol. 19, pp. 29–34, 2001 [DOI-CrossRef].
- [534] R. L. Rich and D. G. Myszka, "Survey of the year 2001 commercial optical biosensor literature," Journal of Molecular Recognition, vol. 15, pp. 352–376, 2002 [DOI-CrossRef].
- [535] O. S. Wolfbeis, "Fiber-optic chemical sensors and biosensors," Analytical Chemistry, vol. 74, pp. 2663–2677, 2002 [DOI-CrossRef].
- [536] "Multiphoton Excitation and Microscopy," in Principles of Fluorescence Spectroscopy (J. R. Lakowicz, ed.), pp. 607–621, Boston, MA: Springer US, 2006.

[537] J. Meldolesi, "The development of Ca2+ indicators: A breakthrough in pharmacological research," Trends in Pharmacological Sciences, vol. 25, pp. 172–174, 2004 [DOI-CrossRef].

- [538] T. J. Rink, C. Montecucco, T. R. Hesketh, and R. Y. Tsien, "Lymphocyte membrane potential assessed with fluorescent probes," *Biochimica Et Biophysica Acta*, vol. 595, no. 1, pp. 15–30, 1980 [DOI-CrossRef].
- [539] R. Y. Tsien, "New calcium indicators and buffers with high selectivity against magnesium and protons: Design, synthesis, and properties of prototype structures," *Biochemistry*, vol. 19, pp. 2396–2404, 1980 [DOI-CrossRef].
- [540] X. Zhou, K. J. Belavek, and E. W. Miller, "Origins of Ca2+ Imaging with Fluorescent Indicators," Biochemistry, vol. 60, pp. 3547–3554, 2021 [DOI-CrossRef].
- [541] L. Tian, Y. Yang, L. M. Wysocki, A. C. Arnold, A. Hu, B. Ravichandran, S. M. Sternson, L. L. Looger, and L. D. Lavis, "Selective esterase-ester pair for targeting small molecules with cellular specificity," *Proceedings of the National Academy of Sciences of the United States of America*, vol. 109, pp. 4756–4761, 2012 [DOI-CrossRef].
- [542] R. Y. Tsien, "A non-disruptive technique for loading calcium buffers and indicators into cells," Nature, vol. 290, pp. 527–528, 1981 [DOI-CrossRef].
- [543] G. Grynkiewicz, M. Poenie, and R. Y. Tsien, "A new generation of Ca2+ indicators with greatly improved fluorescence properties," *The Journal of Biological Chemistry*, vol. 260, pp. 3440–3450, 1985.
- [544] I. Johnson, ed., The Molecular Probes Handbook: A Guide to Fluorescent Probes and Labeling Technologies. Carlsbad, California: Life Technologies Corp, 11. ed ed., 2010.
- [545] N. Kresge, R. D. Simoni, and R. L. Hill, "The Chemistry of Fluorescent Indicators: The Work of Roger Y. Tsien," *Journal of Biological Chemistry*, vol. 281, pp. e29–e31, 2006 [DOI-CrossRef].
- [546] M. Poenie, "Alteration of intracellular Fura-2 fluorescence by viscosity: A simple correction," *Cell Calcium*, vol. 11, no. 2-3, pp. 85–91, 1990 [DOI-CrossRef].
- [547] M. W. Roe, J. J. Lemasters, and B. Herman, "Assessment of Fura-2 for measurements of cytosolic free calcium," *Cell Calcium*, vol. 11, no. 2-3, pp. 63–73, 1990 [DOI-CrossRef].
- [548] D. A. Williams and F. S. Fay, "Intracellular calibration of the fluorescent calcium indicator Fura-2," *Cell Calcium*, vol. 11, no. 2-3, pp. 75–83, 1990 [DOI-CrossRef].
- [549] M. Oheim, M. Van 'T Hoff, A. Feltz, A. Zamaleeva, J.-M. Mallet, and M. Collot, "New red-fluorescent calcium indicators for optogenetics, photoactivation and multi-color imaging," *Biochimica et Biophysica Acta (BBA) Molecular Cell Research*, vol. 1843, pp. 2284–2306, 2014 [DOI-CrossRef].
- [550] D. Thomas, S. C. Tovey, T. J. Collins, M. D. Bootman, M. J. Berridge, and P. Lipp, "A comparison of fluorescent Ca2+ indicator properties and their use in measuring elementary and global Ca2+ signals," *Cell Calcium*, vol. 28, pp. 213–223, 2000 [DOI-CrossRef].
- [551] L. B. Dustin, "Ratiometric analysis of calcium mobilization," Clinical and Applied Immunology Reviews, vol. 1, pp. 5–15, 2000 [DOI-CrossRef].
- [552] P. Lipp and E. Niggli, "Ratiometric confocal Ca(2+)-measurements with visible wavelength indicators in isolated cardiac myocytes," *Cell Calcium*, vol. 14, pp. 359–372, 1993 [DOI-CrossRef].
- [553] C. Lohr, "Monitoring neuronal calcium signalling using a new method for ratiometric confocal calcium imaging," *Cell Calcium*, vol. 34, pp. 295–303, 2003 [DOI-CrossRef].
- [554] K. R. Gee, K. A. Brown, W. N. Chen, J. Bishop-Stewart, D. Gray, and I. Johnson, "Chemical and physiological characterization of fluo-4 Ca(2+)-indicator dyes," *Cell Calcium*, vol. 27, pp. 97–106, 2000 [DOI-CrossRef].
- [555] C. H. Lee, D. Poburko, P. Sahota, J. Sandhu, D. O. Ruehlmann, and C. van Breemen, "The mechanism of phenylephrine-mediated [Ca(2+)](i) oscillations underlying tonic contraction in the rabbit inferior vena cava," *The Journal of Physiology*, vol. 534, pp. 641–650, 2001 [DOI-CrossRef].
- [556] J. Chambers, R. S. Ames, D. Bergsma, A. Muir, L. R. Fitzgerald, G. Hervieu, G. M. Dytko, J. J.

Foley, J. Martin, W.-S. Liu, J. Park, C. Ellis, S. Ganguly, S. Konchar, J. Cluderay, R. Leslie, S. Wilson, and H. M. Sarau, "Melanin-concentrating hormone is the cognate ligand for the orphan G-protein-coupled receptor SLC-1," *Nature*, vol. 400, pp. 261–265, 1999 [DOI-CrossRef].

- [557] "Introduction to Fluorescence," in *Principles of Fluorescence Spectroscopy* (J. R. Lakowicz, ed.), pp. 1–26, Boston, MA: Springer US, 2006.
- [558] N. Byrnes, F. Foss, B. Jones, A. Mcdonald, D. Nygren, P. Thapa, and A. Trinidad, *Progress toward Barium Tagging in High Pressure Xenon Gas with Single Molecule Fluorescence Imaging*. 2019.
- [559] R. Y. Tsien and A. Minta, Fluorescent Indicator Dyes for Calcium Working at Long Wavelengths. Google Patents, 1991.
- [560] J. W. Putney, ed., Calcium Signaling. Methods in Signal Transduction, Boca Raton: CRC/Taylor & Francis, 2nd ed ed., 2006.
- [561] W. He and Z. Guo, "Molecular Imaging: Chemistry and Applications," in *Comprehensive Inorganic Chemistry II*, pp. 733–780, Elsevier, 2013.
- [562] M. Sachar, K. E. Anderson, and X. Ma, "Protoporphyrin IX: The Good, the Bad, and the Ugly," *The Journal of Pharmacology and Experimental Therapeutics*, vol. 356, pp. 267–275, 2016 [DOI-CrossRef].
- [563] N. A. Markwardt, N. Haj-Hosseini, B. Hollnburger, H. Stepp, P. Zelenkov, and A. Rühm, "405 nm versus 633 nm for protoporphyrin IX excitation in fluorescence-guided stereotactic biopsy of brain tumors," *Journal of Biophotonics*, vol. 9, pp. 901–912, 2016 [DOI-CrossRef].
- [564] D. Piffaretti, F. Burgio, M. Thelen, A. Kaelin-Lang, P. Paganetti, M. Reinert, and M. L. D'Angelo, "Protoporphyrin IX tracer fluorescence modulation for improved brain tumor cell lines visualization," Journal of Photochemistry and Photobiology B: Biology, vol. 201, p. 111640, 2019 [DOI-CrossRef].
- [565] J. H. Shenk, J. L. Hall, and H. King, "SPECTROPHOTOMETRIC CHARACTERISTICS OF HEMOGLOBINS," *Journal of Biological Chemistry*, vol. 105, pp. 741–752, 1934 [DOI-CrossRef].
- [566] B. Horecker, "THE ABSORPTION SPECTRA OF HEMOGLOBIN AND ITS DERIVATIVES IN THE VISIBLE AND NEAR INFRA-RED REGIONS," Journal of Biological Chemistry, vol. 148, pp. 173–183, 1943 [DOI-CrossRef].
- [567] B. Alpert, D. M. Jameson, and G. Weber, "TRYPTOPHAN EMISSION FROM HUMAN HEMOGLOBIN AND ITS ISOLATED SUBUNITS," *Photochemistry and Photobiology*, vol. 31, pp. 1–4, 1980 [DOI-CrossRef].
- [568] R. E. Hirsch, R. S. Zukin, and R. L. Nagel, "Intrinsic fluorescence emission of intact oxy hemoglobins," Biochemical and Biophysical Research Communications, vol. 93, pp. 432–439, 1980 [DOI-CrossRef].
- [569] S. Gao, X. Lan, Y. Liu, Z. Shen, J. Lu, and X. Ni, "Characteristics of blood fluorescence spectra using low-level, 457.9-nm excitation from Ar+ laser," *Chinese Optics Letters*, vol. 2, pp. 160–161, 2004.
- [570] W. Zheng, D. Li, Y. Zeng, Y. Luo, and J. Y. Qu, "Two-photon excited hemoglobin fluorescence," *Biomedical Optics Express*, vol. 2, pp. 71–79, 2010 [DOI-CrossRef].
- [571] Th. Förster, "Zwischenmolekulare Energiewanderung und Fluoreszenz," Annalen der Physik, vol. 437, pp. 55–75, 1948 [DOI-CrossRef].
- [572] G. Weber and F. J. W. Teale, "Electronic energy transfer in haem proteins," *Discussions of the Faraday Society*, vol. 27, p. 134, 1959 [DOI-CrossRef].
- [573] A. Cu, G. G. Bellah, and D. A. Lightner, "Fluorescence of bilirubin," *Journal of the American Chemical Society*, vol. 97, pp. 2579–2580, 1975 [DOI-CrossRef].
- [574] L. Kaestner, W. Tabellion, E. Weiss, I. Bernhardt, and P. Lipp, "Calcium imaging of individual erythrocytes: Problems and approaches," *Cell Calcium*, vol. 39, pp. 13–19, 2006 [DOI-CrossRef].
- [575] L. Kaestner, A. Juzeniene, and J. Moan, "Erythrocytes-the 'house elves' of photodynamic therapy," Photochemical & Photobiological Sciences: Official Journal of the European Photochemistry Association and the European Society for Photobiology, vol. 3, no. 11-12, pp. 981–989, 2004 [DOI-CrossRef].

[576] Y. Marikovsky, E. Elazar, and D. Danon, "Rabbit erythrocyte survival following diminished sialic acid and ATP depletion," *Mechanisms of Ageing and Development*, vol. 6, pp. 233–240, 1977 [DOI-CrossRef].

- [577] H. Meiselman, E. Evans, and R. Hochmuth, "Membrane mechanical properties of ATP-depleted human erythrocytes," *Blood*, vol. 52, pp. 499–504, 1978 [DOI-CrossRef].
- [578] R. I. Weed, P. L. LaCelle, and E. W. Merrill, "Metabolic dependence of red cell deformability," The Journal of Clinical Investigation, vol. 48, pp. 795–809, 1969 [DOI-CrossRef].
- [579] A. H. Coons, H. J. Creech, and R. N. Jones, "Immunological Properties of an Antibody Containing a Fluorescent Group.," Experimental Biology and Medicine, vol. 47, pp. 200–202, 1941 [DOI-CrossRef].
- [580] A. H. Coons, H. J. Creech, R. N. Jones, and E. Berliner, "The Demonstration of Pneumococcal Antigen in Tissues by the Use of Fluorescent Antibody," *The Journal of Immunology*, vol. 45, pp. 159–170, 1942 [DOI-CrossRef].
- [581] A. H. Coons and M. H. Kaplan, "Localization of antigen in tissue cells; improvements in a method for the detection of antigen by means of fluorescent antibody," *The Journal of Experimental Medicine*, vol. 91, pp. 1–13, 1950 [DOI-CrossRef].
- [582] K. Im, S. Mareninov, M. F. P. Diaz, and W. H. Yong, "An Introduction to Performing Immunofluorescence Staining," Methods in Molecular Biology (Clifton, N.J.), vol. 1897, pp. 299–311, 2019 [DOI-CrossRef].
- [583] D. Gitil, B. H. Landing, and A. Whipple, "The localization of homolgous plasma proteins in the tissues of young human beings as demonstrated with fluorescent antibodies," The Journal of Experimental Medicine, vol. 97, pp. 163–176, 1953 [DOI-CrossRef].
- [584] E. H. Beutner, E. J. Holborow, and G. D. Johnson, "A New Fluorescent Antibody Method: Mixed Antiglobulin Immunofluorescence or Labelled Antigen Indirect Immunofluorescence Staining," Nature, vol. 208, pp. 353–355, 1965 [DOI-CrossRef].
- [585] T. H. Weller and A. H. Coons, "Fluorescent antibody studies with agents of varicella and herpes zoster propagated in vitro," Proceedings of the Society for Experimental Biology and Medicine. Society for Experimental Biology and Medicine (New York, N.Y.), vol. 86, no. 4, pp. 789–794, 1954 [DOI-CrossRef].
- [586] R. A. Goldwasser and C. C. Shepard, "Fluorescent antibody methods in the differentiation of murine and epidemic typhus sera; specificity changes resulting from previous immunization," *Journal of Immunology (Baltimore, Md.: 1950)*, vol. 82, pp. 373–380, 1959.
- [587] P. Klein and P. Burkholder, "Die Darstellung von fixiertem Komplement mit markiertem Antikomplement," *Pathobiology*, vol. 22, no. 5, pp. 729–731, 1959 [DOI-CrossRef].
- [588] T. Matuhasi and M. Usui, "Fluorescent Complement Fixation Technique," Nature, vol. 212, pp. 418–419, 1966 [DOI-CrossRef].
- [589] F. Müller, "Direkter und indirekter Nachweis der Komplementbindung an Virus-Antikörper-Komplexe in der Gewebekultur," *Pathobiology*, vol. 23, no. 5, pp. 712–714, 1960 [DOI-CrossRef].
- [590] M. Shehadul Islam, A. Aryasomayajula, and P. Selvaganapathy, "A Review on Macroscale and Microscale Cell Lysis Methods," *Micromachines*, vol. 8, p. 83, 2017 [DOI-CrossRef].
- [591] S. T. Harrison, "Bacterial cell disruption: A key unit operation in the recovery of intracellular products," *Biotechnology Advances*, vol. 9, pp. 217–240, 1991 [DOI-CrossRef].
- [592] A. E. Galvis, H. E. Fisher, and D. Camerini, "NP-40 Fractionation and Nucleic Acid Extraction in Mammalian Cells," Bio-Protocol, vol. 7, p. e2584, 2017 [DOI-CrossRef].
- [593] J. Sambrook, E. F. Fritsch, T. Maniatis, D. W. Russell, and M. R. Green, Molecular Cloning: A Laboratory Manual. Cold Spring Harbor, NY: Cold Spring Harbor Laboratory Press, 1989.
- [594] J. T. Dodge, C. Mitchell, and D. J. Hanahan, "The preparation and chemical characteristics of hemoglobin-free ghosts of human erythrocytes," Archives of Biochemistry and Biophysics, vol. 100, pp. 119–130, 1963 [DOI-CrossRef].

[595] M. Saleemuddin, U. Zimmermann, and F. Schneeweiss, "Preparation of human erythrocyte ghosts in isotonic solution: Haemoglobin content and polypeptide composition," *Zeitschrift Fur Natur-forschung. Section C, Biosciences*, vol. 32, no. 7-8, pp. 627–631, 1977 [DOI-CrossRef].

- [596] G. Schwoch and H. Passow, "Preparation and properties of human erythrocyte ghosts," *Molecular and Cellular Biochemistry*, vol. 2, pp. 197–218, 1973 [DOI-CrossRef].
- [597] K. M. McKinnon, "Flow Cytometry: An Overview," Current Protocols in Immunology, vol. 120, pp. 5.1.1–5.1.11, 2018 [DOI-CrossRef].
- [598] M. Tzanoudaki and E. Konsta, "Basic Principles of Flow Cytometry," in *Intraoperative Flow Cytometry* (G. Alexiou and G. Vartholomatos, eds.), pp. 9–31, Cham: Springer International Publishing, 2023.
- [599] J. Jansen, M. Qiao, L. Hertz, X. Wang, E. Fermo, A. Zaninoni, R. Colombatti, I. Bernhardt, P. Bianchi, and L. Kaestner, "Mechanistic ion channel interactions in red cells of patients with Gárdos channelopathy," *Blood Advances*, vol. 5, pp. 3303–3308, 2021 [DOI-CrossRef].
- [600] A. Ul-Hamid, Introduction, pp. 1–14. Cham: Springer International Publishing, 2018.
- [601] T. G. Rochow and P. A. Tucker, Definitions, Attributes of Visibility, and General Principles, pp. 23–36. Boston, MA: Springer US, 1994.
- [602] J. Van Zuylen, "The microscopes of Antoni van Leeuwenhoek," *Journal of Microscopy*, vol. 121, pp. 309–328, 1981 [DOI-CrossRef].
- [603] R. F. Egerton, An Introduction to Microscopy, pp. 1–26. Cham: Springer International Publishing, 2016.
- [604] X. Chen, B. Zheng, and H. Liu, "Optical and digital microscopic imaging techniques and applications in pathology," *Analytical Cellular Pathology (Amsterdam)*, vol. 34, no. 1-2, pp. 5–18, 2011 [DOI-CrossRef].
- [605] T. G. Rochow and P. A. Tucker, A Brief History of Microscopy, pp. 1–21. Boston, MA: Springer US, 1994.
- [606] J. W. Lichtman and J.-A. Conchello, "Fluorescence microscopy," Nature Methods, vol. 2, pp. 910–919, 2005 [DOI-CrossRef].
- [607] S. Wang and I. Larina, "High-resolution imaging techniques in tissue engineering," in *Monitoring* and Evaluation of Biomaterials and Their Performance In Vivo, pp. 151–180, Elsevier, 2017.
- [608] J. Jonkman, C. M. Brown, G. D. Wright, K. I. Anderson, and A. J. North, "Tutorial: Guidance for quantitative confocal microscopy," *Nature Protocols*, vol. 15, pp. 1585–1611, 2020 [DOI-CrossRef].
- [609] A. D. Elliott, "Confocal Microscopy: Principles and Modern Practices," Current Protocols in Cytometry, vol. 92, p. e68, 2020 [DOI-CrossRef].
- [610] R. Datta, T. M. Heaster, J. T. Sharick, A. A. Gillette, and M. C. Skala, "Fluorescence lifetime imaging microscopy: Fundamentals and advances in instrumentation, analysis, and applications," *Journal of Biomedical Optics*, vol. 25, pp. 1–43, 2020 [DOI-CrossRef].
- [611] W. Becker, "Fluorescence lifetime imaging techniques and applications," *Journal of Microscopy*, vol. 247, pp. 119–136, 2012 [DOI-CrossRef].
- [612] C. J. De Grauw and H. C. Gerritsen, "Multiple Time-Gate Module for Fluorescence Lifetime Imaging," *Applied Spectroscopy*, vol. 55, pp. 670–678, 2001 [DOI-CrossRef].
- [613] L. Marcu, P. M. W. French, and D. S. Elson, eds., Fluorescence Lifetime Spectroscopy and Imaging: Principles and Applications in Biomedical Diagnostics. Boca Raton: CRC Press, 2015.
- [614] W. Becker, A. Bergmann, G. L. Biscotti, and A. Rueck, "Advanced time-correlated single photon counting techniques for spectroscopy and imaging in biomedical systems," in *Lasers and Applications* in *Science and Engineering* (J. Neev, C. B. Schaffer, and A. Ostendorf, eds.), (San Jose, Ca), p. 104, 2004
- [615] "Time-Domain Lifetime Measurements," in *Principles of Fluorescence Spectroscopy* (J. R. Lakowicz, ed.), pp. 97–155, Boston, MA: Springer US, 2006.

[616] T. Korte and A. Herrmann, "Fluorescence Lifetime Imaging Microscopy by TCSPC (TD-FLIM)," 2017.

- [617] N. Wu, Introduction, vol. 32, pp. 1–13. Berlin, Heidelberg: Springer Berlin Heidelberg, 1997.
- [618] S. Pelet, M. Previte, L. Laiho, and P. C. So, "A Fast Global Fitting Algorithm for Fluorescence Lifetime Imaging Microscopy Based on Image Segmentation," *Biophysical Journal*, vol. 87, pp. 2807–2817, 2004 [DOI-CrossRef].
- [619] W. Becker, The Bh TCSPC Handbook. Becker & Hickl GmbH, 2021.
- [620] A. De Martino and D. De Martino, "An introduction to the maximum entropy approach and its application to inference problems in biology," *Heliyon*, vol. 4, p. e00596, 2018 [DOI-CrossRef].
- [621] R. D. Levie, "Curve Fitting with Least Squares," Critical Reviews in Analytical Chemistry, vol. 30, pp. 59–74, 2000 [DOI-CrossRef].
- [622] K. Molugaram and G. S. Rao, "Curve Fitting," in Statistical Techniques for Transportation Engineering, pp. 281–292, Elsevier, 2017.
- [623] M. Maus, M. Cotlet, J. Hofkens, T. Gensch, F. C. De Schryver, J. Schaffer, and C. A. Seidel, "An experimental comparison of the maximum likelihood estimation and nonlinear least-squares fluorescence lifetime analysis of single molecules," *Analytical Chemistry*, vol. 73, pp. 2078–2086, 2001 [DOI-CrossRef].
- [624] M. Straume, S. G. Frasier-Cadoret, and M. L. Johnson, "Least-Squares Analysis of Fluorescence Data," in *Topics in Fluorescence Spectroscopy* (J. R. Lakowicz, ed.), vol. 2, pp. 177–240, Boston: Kluwer Academic Publishers, 2002.
- [625] H. B. Friedrich and J.-P. Yu, "Combinations of Orthogonal Spectra to Estimate Component Spectra in Multicomponent Mixtures," *Applied Spectroscopy*, vol. 41, pp. 227–234, 1987 [DOI-CrossRef].
- [626] K. Sasaki, S. Kawata, and S. Minami, "Estimation of component spectral curves from unknown mixture spectra," Applied Optics, vol. 23, p. 1955, 1984 [DOI-CrossRef].
- [627] J.-C. Brochon, "[13] Maximum entropy method of data analysis in time-resolved spectroscopy," in Methods in Enzymology, vol. 240, pp. 262–311, Elsevier, 1994.
- [628] J. L. Koenig, Spectroscopy of Polymers. Elsevier, 1999.
- [629] M. Sakata and M. Takata, "The principle of the maximum entropy method," High Pressure Research, vol. 14, pp. 327–333, 1996 [DOI-CrossRef].
- [630] J. E. Noble and M. J. Bailey, "Chapter 8 Quantitation of Protein," in Methods in Enzymology, vol. 463, pp. 73–95, Elsevier, 2009.
- [631] C. N. Pace, F. Vajdos, L. Fee, G. Grimsley, and T. Gray, "How to measure and predict the molar absorption coefficient of a protein," *Protein Science: A Publication of the Protein Society*, vol. 4, pp. 2411–2423, 1995 [DOI-CrossRef].
- [632] M. M. Bradford, "A rapid and sensitive method for the quantitation of microgram quantities of protein utilizing the principle of protein-dye binding," *Analytical Biochemistry*, vol. 72, pp. 248–254, 1976 [DOI-CrossRef].
- [633] N. J. Kruger, The Bradford Method for Protein Quantitation, vol. 32, pp. 9–16. New Jersey: Humana Press, 1994.
- [634] R. Morris, "Spectrophotometry," Current Protocols Essential Laboratory Techniques, vol. 11, 2015 [DOI-CrossRef].
- [635] P. Desjardins, J. B. Hansen, and M. Allen, "Microvolume protein concentration determination using the NanoDrop 2000c spectrophotometer," *Journal of Visualized Experiments: JoVE*, p. 1610, 2009 [DOI-CrossRef].
- [636] A. T. Andrews, Electrophoresis: Theory, Techniques, and Biochemical and Clinical Applications. Monographs on Physical Biochemistry, Oxford: Clarendon Press, 1981.
- [637] M. J. Dunn, Gel Electrophoresis: Proteins. Introduction to Biotechniques, Oxford: BIOS Scientific Publ, 1993.

[638] M. M. Compton, S. A. Lapp, and R. Pedemonte, "Generation of multicolored, prestained molecular weight markers for gel electrophoresis," *Electrophoresis*, vol. 23, pp. 3262–3265, 2002 [DOI-CrossRef].

- [639] A. A. Al-Tubuly, "SDS-PAGE and Western Blotting," Methods in Molecular Medicine, vol. 40, pp. 391–405, 2000 [DOI-CrossRef].
- [640] H. Towbin, T. Staehelin, and J. Gordon, "Electrophoretic transfer of proteins from polyacrylamide gels to nitrocellulose sheets: Procedure and some applications.," *Proceedings of the National Academy of Sciences*, vol. 76, pp. 4350–4354, 1979 [DOI-CrossRef].
- [641] T. Mahmood and P.-C. Yang, "Western blot: Technique, theory, and trouble shooting," *North American Journal of Medical Sciences*, vol. 4, pp. 429–434, 2012 [DOI-CrossRef].
- [642] C. Feo and N. Mohandas, "Role of ATP Depletion on Red Cell Shape and Deformability," in Red Cell Rheology (M. Bessis, S. B. Shohet, and N. Mohandas, eds.), pp. 153–161, Berlin, Heidelberg: Springer Berlin Heidelberg, 1978.
- [643] S. Tuvia, S. Levin, A. Bitler, and R. Korenstein, "Mechanical Fluctuations of the Membrane-Skeleton Are Dependent on F-Actin ATPase in Human Erythrocytes," *The Journal of Cell Biology*, vol. 141, pp. 1551–1561, 1998 [DOI-CrossRef].
- [644] D. Flormann, M. Qiao, N. Murciano, G. Iacono, A. Darras, S. Hof, S. M. Recktenwald, M. G. Rotordam, N. Becker, J. Geisel, C. Wagner, M. Von Lindern, E. Van Den Akker, and L. Kaestner, "Transient receptor potential channel vanilloid type 2 in red cells of cannabis consumer," *American Journal of Hematology*, vol. 97, 2022 [DOI-CrossRef].
- [645] A. Hatem, S. Esperti, N. Murciano, M. Qiao, M. Giustina Rotordam, N. Becker, E. Nader, F. Maurer, L. Pérès, G. Bouyer, L. Kaestner, P. Connes, and S. Egée, "Adverse effects of DELTA-9-TETRAHYDROCANNABINOL on sickle red blood cells," *American Journal of Hematology*, vol. 98, 2023 [DOI-CrossRef].
- [646] J. Albuisson, S. E. Murthy, M. Bandell, B. Coste, H. Louis-dit-Picard, J. Mathur, M. Fénéant-Thibault, G. Tertian, J.-P. De Jaureguiberry, P.-Y. Syfuss, S. Cahalan, L. Garçon, F. Toutain, P. Simon Rohrlich, J. Delaunay, V. Picard, X. Jeunemaitre, and A. Patapoutian, "Dehydrated hereditary stomatocytosis linked to gain-of-function mutations in mechanically activated PIEZO1 ion channels," Nature Communications, vol. 4, p. 1884, 2013 [DOI-CrossRef].
- [647] L. Kaestner, "Channelizing the red blood cell: Molecular biology competes with patch-clamp," Frontiers in Molecular Biosciences, vol. 2, 2015 [DOI-CrossRef].
- [648] R. Zarychanski, V. P. Schulz, B. L. Houston, Y. Maksimova, D. S. Houston, B. Smith, J. Rinehart, and P. G. Gallagher, "Mutations in the mechanotransduction protein PIEZO1 are associated with hereditary xerocytosis," *Blood*, vol. 120, pp. 1908–1915, 2012 [DOI-CrossRef].
- [649] M. Föller, R. S. Kasinathan, S. Koka, C. Lang, E. Shumilina, L. Birnbaumer, F. Lang, and S. M. Huber, "TRPC6 Contributes to the Ca²⁺ Leak of Human Erythrocytes," *Cellular Physiology and Biochemistry*, vol. 21, no. 1-3, pp. 183–192, 2008 [DOI-CrossRef].
- [650] I. Bernhardt and L. Kaestner, "Historical view and some unsolved problems in red blood cell membrane research [in press]," Frontiers in Bioscience Landmark, 2024.
- [651] Y. Yamaguchi, B. Allegrini, R. Rapetti-Mauss, V. Picard, L. Garçon, P. Kohl, O. Soriani, R. Peyronnet, and H. Guizouarn, "Hereditary Xerocytosis: Differential Behavior of PIEZO1 Mutations in the N-Terminal Extracellular Domain Between Red Blood Cells and HEK Cells," Frontiers in Physiology, vol. 12, p. 736585, 2021 [DOI-CrossRef].
- [652] N. Murciano, Characterization Of Ion Channels in Red Blood Cells Using the Automated Patch Clamp. [unpublished thesis], Universität des Saarlandes, Homburg, Saarland, Germany, 2024.
- [653] M. Baunbaek and P. Bennekou, "Evidence for a random entry of Ca2+ into human red cells," Bioelectrochemistry (Amsterdam, Netherlands), vol. 73, pp. 145–150, 2008 [DOI-CrossRef].
- [654] L. Kaestner, X. Wang, L. Hertz, and I. Bernhardt, "Voltage-Activated Ion Channels in Non-excitable Cells-A Viewpoint Regarding Their Physiological Justification," Frontiers in Physiology, vol. 9, p. 450, 2018 [DOI-CrossRef].

[655] M. B. Rust, S. L. Alper, Y. Rudhard, B. E. Shmukler, R. Vicente, C. Brugnara, M. Trudel, T. J. Jentsch, and C. A. Hübner, "Disruption of erythroid K-Cl cotransporters alters erythrocyte volume and partially rescues erythrocyte dehydration in SAD mice," The Journal of Clinical Investigation, vol. 117, pp. 1708–1717, 2007 [DOI-CrossRef].

- [656] D. Monedero Alonso, L. Pérès, A. Hatem, G. Bouyer, and S. Egée, "The Chloride Conductance Inhibitor NS3623 Enhances the Activity of a Non-selective Cation Channel in Hyperpolarizing Conditions," Frontiers in Physiology, vol. 12, p. 743094, 2021 [DOI-CrossRef].
- [657] P. Christophersen and P. Bennekou, "Evidence for a voltage-gated, non-selective cation channel in the human red cell membrane," *Biochimica Et Biophysica Acta*, vol. 1065, pp. 103–106, 1991 [DOI-CrossRef].
- [658] C. Duranton, S. M. Huber, and F. Lang, "Oxidation induces a Cl(-)-dependent cation conductance in human red blood cells," *The Journal of Physiology*, vol. 539, pp. 847–855, 2002 [DOI-CrossRef].
- [659] L. Kaestner, P. Christophersen, I. Bernhardt, and P. Bennekou, "The non-selective voltage-activated cation channel in the human red blood cell membrane: Reconciliation between two conflicting reports and further characterisation," *Bioelectrochemistry (Amsterdam, Netherlands)*, vol. 52, pp. 117–125, 2000 [DOI-CrossRef].
- [660] P. M. MacElveen, "Critical issues in access to data," Communicating Nursing Research, vol. 7, pp. 1–16, 1976.
- [661] R. M. Gopinath and F. F. Vincenzi, "(Ca ²⁺ +Mg ²⁺)-ATPase activity of sickle cell membranes: Decreased activation by red blood cell cytoplasmic activator," *American Journal of Hematology*, vol. 7, pp. 303–312, 1979 [DOI-CrossRef].
- [662] S. K. Ballas and M. J. Marcolina, "Determinants of Red Cell Survival and Erythropoietic Activity in Patients with Sickle Cell Anemia in the Steady State," *Hemoglobin*, vol. 24, pp. 277–286, 2000 [DOI-CrossRef].
- [663] M. M. Barbedo and P. R. McCurdy, "Red Cell Life Span in Sickle Cell Trait," Acta Haematologica, vol. 51, no. 6, pp. 339–343, 1974 [DOI-CrossRef].
- [664] I. V. Pivkin, Z. Peng, G. E. Karniadakis, P. A. Buffet, M. Dao, and S. Suresh, "Biomechanics of red blood cells in human spleen and consequences for physiology and disease," *Proceedings of the National Academy of Sciences*, vol. 113, pp. 7804–7809, 2016 [DOI-CrossRef].
- [665] S. Looareesuwan, M. Ho, Y. Wattanagoon, N. J. White, D. A. Warrell, D. Bunnag, T. Harinasuta, and D. J. Wyler, "Dynamic alteration in splenic function during acute falciparum malaria," The New England Journal of Medicine, vol. 317, pp. 675–679, 1987 [DOI-CrossRef].
- [666] Z. R. Rogers, W. C. Wang, Z. Luo, R. V. Iyer, E. Shalaby-Rana, S. D. Dertinger, B. L. Shulkin, J. H. Miller, B. Files, P. A. Lane, B. W. Thompson, S. T. Miller, R. E. Ware, and BABY HUG, "Biomarkers of splenic function in infants with sickle cell anemia: Baseline data from the BABY HUG Trial," *Blood*, vol. 117, pp. 2614–2617, 2011 [DOI-CrossRef].
- [667] C. Antwi-Boasiako, G. B. Dankwah, R. Aryee, C. Hayfron-Benjamin, E. S. Donkor, and A. D. Campbell, "Oxidative Profile of Patients with Sickle Cell Disease," *Medical Sciences (Basel, Switzerland)*, vol. 7, p. 17, 2019 [DOI-CrossRef].
- [668] E. Fibach and M. Dana, "Oxidative Stress in β-Thalassemia," Molecular Diagnosis & Therapy, vol. 23, pp. 245–261, 2019 [DOI-CrossRef].
- [669] M. A. Mittleman, R. A. Lewis, M. Maclure, J. B. Sherwood, and J. E. Muller, "Triggering Myocardial Infarction by Marijuana," *Circulation*, vol. 103, pp. 2805–2809, 2001 [DOI-CrossRef].
- [670] S. A. Curtis, A. M. Brandow, M. DeVeaux, D. Zeltermam, L. Devine, and J. D. Roberts, "Daily Cannabis Users with Sickle Cell Disease Show Fewer Admissions than Others with Similar Pain Complaints," Cannabis and Cannabinoid Research, vol. 5, no. 3, pp. 255–262, 2020 [DOI-CrossRef].
- [671] M. A. Huestis, "Human Cannabinoid Pharmacokinetics," Chemistry & Biodiversity, vol. 4, pp. 1770–1804, 2007 [DOI-CrossRef].
- [672] A. Almutairi, W. J. Akers, M. Y. Berezin, S. Achilefu, and J. M. J. Fréchet, "Monitoring the

- Biodegradation of Dendritic Near-Infrared Nanoprobes by *in Vivo* Fluorescence Imaging," *Molecular Pharmaceutics*, vol. 5, pp. 1103–1110, 2008 [DOI-CrossRef].
- [673] X. Dai, Z. Yue, M. E. Eccleston, J. Swartling, N. K. Slater, and C. F. Kaminski, "Fluorescence intensity and lifetime imaging of free and micellar-encapsulated doxorubic in living cells," *Nanomedicine: Nanotechnology, Biology and Medicine*, vol. 4, pp. 49–56, 2008 [DOI-CrossRef].
- [674] R. Duncan, "Fluorescence lifetime imaging microscopy (FLIM) to quantify protein–protein interactions inside cells," *Biochemical Society Transactions*, vol. 34, pp. 679–682, 2006 [DOI-CrossRef].
- [675] J. A. Levitt, D. R. Matthews, S. M. Ameer-Beg, and K. Suhling, "Fluorescence lifetime and polarization-resolved imaging in cell biology," *Current Opinion in Biotechnology*, vol. 20, pp. 28–36, 2009 [DOI-CrossRef].
- [676] A. Pliss, X. Peng, L. Liu, A. Kuzmin, Y. Wang, J. Qu, Y. Li, and P. N. Prasad, "Single Cell Assay for Molecular Diagnostics and Medicine: Monitoring Intracellular Concentrations of Macromolecules by Two-photon Fluorescence Lifetime Imaging," *Theranostics*, vol. 5, no. 9, pp. 919–930, 2015 [DOI-CrossRef].
- [677] P. Liu, Z. Zhu, C. Zeng, and G. Nie, "Specific absorption spectra of hemoglobin at different PO2 levels: Potential noninvasive method to detect PO2 in tissues," *Journal of Biomedical Optics*, vol. 17, p. 125002, 2012 [DOI-CrossRef].
- [678] Z. Wang, Y. Zheng, D. Zhao, Z. Zhao, L. Liu, A. Pliss, F. Zhu, J. Liu, J. Qu, and P. Luan, "Applications of fluorescence lifetime imaging in clinical medicine," *Journal of Innovative Optical Health Sciences*, vol. 11, p. 1830001, 2018 [DOI-CrossRef].
- [679] K. Svoboda and R. Yasuda, "Principles of Two-Photon Excitation Microscopy and Its Applications to Neuroscience," *Neuron*, vol. 50, pp. 823–839, 2006 [DOI-CrossRef].
- [680] W. R. Zipfel, R. M. Williams, and W. W. Webb, "Nonlinear magic: Multiphoton microscopy in the biosciences," *Nature Biotechnology*, vol. 21, pp. 1369–1377, 2003 [DOI-CrossRef].
- [681] J. Lakowicz and F. Prendergast, "Detection of Hindered Rotations of 1,6-Diphenyl-1,3,5-Hexatriene in Lipid Bilayers by Differential Polarized Phase Fluorometry," *Biophysical Journal*, vol. 24, pp. 213– 231, 1978 [DOI-CrossRef].
- [682] I. Bezprozvanny, J. Watras, and B. E. Ehrlich, "Bell-shaped calcium-response curves of Ins(1,4,5)P3and calcium-gated channels from endoplasmic reticulum of cerebellum," *Nature*, vol. 351, pp. 751–754, 1991 [DOI-CrossRef].
- [683] E. A. Finch, T. J. Turner, and S. M. Goldin, "Calcium as a coagonist of inositol 1,4,5-trisphosphate-induced calcium release," *Science (New York, N.Y.)*, vol. 252, pp. 443–446, 1991 [DOI-CrossRef].
- [684] E. A. Finch, T. J. Turner, and S. M. Goldin, "Subsecond kinetics of inositol 1,4,5-trisphosphate-induced calcium release reveal rapid potentiation and subsequent inactivation by calcium," *Annals of the New York Academy of Sciences*, vol. 635, pp. 400–403, 1991 [DOI-CrossRef].
- [685] M. Iino, "Biphasic Ca2+ dependence of inositol 1,4,5-trisphosphate-induced Ca release in smooth muscle cells of the guinea pig taenia caeci," The Journal of General Physiology, vol. 95, pp. 1103–1122, 1990 [DOI-CrossRef].
- [686] M. Iino, "Calcium dependent inositol trisphosphate-induced calcium release in the guinea-pig taenia caeci," *Biochemical and Biophysical Research Communications*, vol. 142, pp. 47–52, 1987 [DOI-CrossRef].
- [687] A. Y. Abramov and M. R. Duchen, "Actions of ionomycin, 4-BrA23187 and a novel electrogenic Ca2+ionophore on mitochondria in intact cells," *Cell Calcium*, vol. 33, pp. 101–112, 2003 [DOI-CrossRef].
- [688] D. M. Bers, C. W. Patton, and R. Nuccitelli, "A practical guide to the preparation of Ca(2+) buffers," *Methods in Cell Biology*, vol. 99, pp. 1–26, 2010 [DOI-CrossRef].
- [689] J. A. Squier, M. Müller, G. J. Brakenhoff, and K. R. Wilson, "Third harmonic generation microscopy," Optics Express, vol. 3, p. 315, 1998 [DOI-CrossRef].